Dynamic, Continuous, and Center of Gravity Independent Weighing with a Loader

Vom Fachbereich Maschinenbau und Verfahrenstechnik

der Technischen Universität Kaiserslautern zur Verleihung des akademischen Grades

DOKTOR-INGENIEUR (DR.-ING.)

genehmigte Dissertation

von

DIPL.-ING. FREDERIC BALLAIRE

aus Ludwigshafen

Acknowledgments

Wachstum durch Innovation — EFRE

Contents

Indexes and Symbols

In general, all variables, indexes, and abbreviations are defined directly before they are being used. Otherwise, they are defined in the following tables.

Table 1: Abbreviations and shortcuts

Abbr.	Full form
2D	two-dimensional
BM	boom
BU	bucket
COG, CoG	center of gravity
config	configuration
cf.	compare
DOF	degrees of freedom
DynWeiSys	dynamic weighing system
deg	degree
IMU	inertial measurement unit
LTI	linear time invariant
pos	position
PTFE	polytetrafluoroethylene
rec	record
vs.	versus
w	with
w/o	without

Table 2: General indexes

Index	Property
A	piston side of the hydraulic actuator
B	rod side of the hydraulic actuator
BM	boom
BU	bucket or tool carrier
CogSum	overall center of gravity of several parts
cog	center of gravity
cyl	hydraulic cylinder or hydraulic actuator
g	gravity
i	counter
K	coordinate system
L	load
rod	rod of the hydraulic actuator
P	point in coordinate system or pendulum
piston	piston of the hydraulic actuator
S	sensor in coordinate system
S2	IMU mounted at the chassis
S3	IMU mounted at the boom
S4	IMU mounted at the bucket or tool carrier
sealPiston	piston seal of the hydraulic actuator
sealRod	rod seal of the hydraulic actuator
T	tractor
trans	translation
y	y-component of a vector

Table 3: Latin letters

Symbol	Property	Unit
A	area	m^2
$\boldsymbol{A}$	system matrix of a LTI system	
A_A	hydraulic effective area, piston side of a cylinder	m^2
A_B	hydraulic effective area, rod side of a cylinder	m^2
A_{BM_B}	hydraulic effective area, rod side of the boom cylinder	m^2
A_r	real area of sliding partner's surface contact	m^2
$A_{\delta 1}$	steady state amplification of the disturbance δ_1	
a	acceleration	m/s^2
$\vec{a}$	acceleration vector	m/s^2
a_{cyl}	acceleration of the hydraulic actuator movement	m/s^2
$\vec{a}_L$	acceleration at the payload	m/s^2
B	viscous friction coefficient	Ns/m
$\boldsymbol{B}$	control matrix of a LTI system	
c	amount of joints of a kinematic chain	
$\boldsymbol{C}$	output matrix of a LTI system	
D	diameter	m
D	E.Lehr's damping ratio	
E	Young's modulus	N/m^2
$\boldsymbol{e}$	observer error	
F	force	N
F_{BM_cyl}	force of the boom actuator	N
F_{BU_cyl}	force of the bucket actuator	N
F_C	Coulomb force	N
F_{cogL}	weight force of the payload at its center of gravity	N
F_{cyl}	force of the hydraulic actuator	N
$F_{friction}$	friction force	N
F_g	weight force	N
$\vec{F}_{joint}$	supporting force of the joint	N
F_{normal}	normal force applied in the Hertz theory	N
F_S	stiction force	N
$F_{sealPiston}$	seal load used in the friction modeling	N
$F_{sealRod}$	seal load used in the friction modeling	N
f	mobility of a kinematic chain	
g	gravity	m/s^2

Table 3 – *Continued from previous page*

Symbol	Property	Unit
H	linkage heigt	m
h	height or lever	m
h	height or thickness of fluid film	μm
h_{BM_cyl}	lever of F_{BM_cyl} respective to the joint between chassis and boom	m
h_{mL}	lever of F_{cogL} respective to the joint between chassis and boom	m
J_1	joint between chassis and boom	
J_2	joint between boom and bucket or tool carrier	
j	diminished degrees of freedom of a kinematic chain	
l_{cogSum}	distance between J_1 and overall center of gravity	m
K_1	coordinate system of the inertial system	
K_2	coordinate system of the chassis	
K_3	coordinate system of the boom	
K_4	coordinate system of the bucket or tool carrier	
KS_2	internal coordinate system of the IMU S2	
KS_3	internal coordinate system of the IMU S3	
KS_4	internal coordinate system of the IMU S4	
k_{tanh}	gradient coefficient to determine the switching speed between negative and positive friction	
$k_{1..5}$	coefficients used at the pressure based friction model	
$\boldsymbol{L}$	observer gain	
m	mass	kg
m_{common}	output of the measured payload of a common weighing system	kg
$m_{DynWeiSys}$	output of the measured payload of the "Dynamic Weighing System"	kg
m_L	mass of the measured payload	kg
$m_{payload}$	mass of the true payload	kg
m_{Sum}	overall mass of the front loader	kg
n	amount of parts of a kinematic chain	
p	pressure	bar
p_A	cylinder pressure, piston side	bar
p_B	cylinder pressure, rod side	bar
p_{BM_A}	boom cylinder pressure, piston side	bar

Continued on next page

Table 3 – *Continued from previous page*

Symbol	Property	Unit
p_{BM_B}	boom cylinder pressure, rod side	bar
p_{BU_A}	bucket cylinder pressure, piston side	bar
p_{BU_B}	bucket cylinder pressure, rod side	bar
$\boldsymbol{R}$	transformation matrix	
R	radius	m
R_a	mean roughness index	μm
r	radius	m
$\vec{r}$	position vector	m
$\dot{\vec{r}}$	velocity	m/s
$\ddot{\vec{r}}$	acceleration	m/s^2
$\vec{r}_{cog}$	position vector of the center of gravity in the respective coordinate system	m
$\vec{r}_{CogSum}$	position vector of the overall center of gravity	m
$\vec{r}_N$	vector from joint J$_1$ to joint J$_2$	m
$stroke$	actuator stroke (pin to pin)	m
TQ	torque	Nm
TQ_1	torque at the joint J$_1$ between chassis and boom	Nm
TQ_2	torque at the joint J$_2$ between boom and tool carrier	Nm
$\boldsymbol{u}$	control vector of the plant model	
$\dot{V}_{BM\_A}$	oil flow at cylinder's piston side	m^3/s
$\dot{V}_{BM\_B}$	oil flow at cylinder's rod side	m^3/s
vel	velocity	m/s
vel_{cyl}	actuator or cylinder velocity	m/s
$\dot{x}$	velocity	m/s
$\dot{x}_{stribeck}$	Stribeck velocity	m/s
$\boldsymbol{x}$	state vector of the plant model	
$\boldsymbol{x}_0$	initial state vector	
$\hat{\boldsymbol{x}}$	observer state vector	
$\boldsymbol{y}$	output vector of the plant model	
$\hat{\boldsymbol{y}}$	output vector of the observer	
$[...]_y$	y-component of a vector	
Z_1	boom cylinder stroke (pin to pin)	m
Z_2	bucket cylinder stroke (pin to pin)	m
z_{ss}	steady state deflection used at bristle friction model	μm

Table 4: Greek letters

Symbol	Property	Unit
α	ratio between the hydraulic effective piston and rod area	
$\boldsymbol{\delta}_1$	input disturbance of the observer (offset)	
$\boldsymbol{\delta}_2$	input disturbance of the observer (noise)	
Δp_A	pressure drop in the hydraulic line at piston side	bar
Δp_B	pressure drop in the hydraulic line at rod side	bar
η	dynamic viscosity	$\mathrm{Ns/m^2}$
Θ	moment of inertia	$\mathrm{kgm^2}$
Θ_P	pendulum's moment of inertia	$\mathrm{kgm^2}$
Θ_{Sum}	front loader's over all moment of inertia	$\mathrm{kgm^2}$
λ_o	eigenvalue of the observer	
λ_p	eigenvalue of the plant	
ν	Poisson ratio	
σ_0	average stiffness used at bristle friction model	
σ_1	micro-viscous coefficient used at bristle friction model	
$\sigma(t)$	unit step	
τ	shear stress	$\mathrm{N/mm^2}$
φ	angle	rad
$\dot{\varphi}$	angular velocity	rad/s
$\ddot{\varphi}$	angular acceleration	$\mathrm{rad/s^2}$
φ_{BM}	angle between the boom's coordinate system K_3 and the machine's coordinate system K_2	rad
φ_{BU}	angle between the bucket's or tool carrier's coordinate system K_4 and the machine's coordinate system K_2	rad
φ_{accS2_K2}	angle between IMU S2's acceleration vector and x-axis of coordinate system K_2	rad
φ_{cogSum}	angle between $\vec{r}_{cogSum}$ and boom's x-axis	rad
$\varphi_{mountS3}$	angle between the internal coordinate system of IMU S3 and the x-axis of the respective mounted part, in this case the boom	rad
φ_t	true angle of a plant model	rad

Table 4 – *Continued from previous page*

Symbol	Property	Unit
$\dot{\varphi}_t$	true angular velocity of a plant model	rad/s
$\hat{\varphi}$	observed angle	rad
φ_{tilt}	tilt angle of the machine	rad
ω	angular frequency	1/s
ω_0	undamped angular frequency, eigenfrequency	1/s
ω_D	damped angular frequency	1/s

Abstract

In many industrial applications it is a benefit to measure payload while handling it. For instance, the cost of material loaded on a dump truck in a quarry is generally priced by its weight. In this case, the truck has to pass a stationary scale twice to identify its payload, before and after loading. Measuring weight of the material instantly while loading the truck, increases the efficiency of the process and makes a stationary scale redundant. Moreover, it is necessary to measure weight, for example, to efficiently loading a trailer to its maximum capacity without exceeding the gross load weight. Another example, where a payload measurement is useful, is when filling a biogas plant with a defined mass of organic material. Furthermore, the productivity and efficiency of a dairy farm can be increased by measuring the weight of cattle food in order to supply the right amount of cattle food directly while filling the feeders. Usually, the payload is being handled by a common tractor front loader, wheel loader, or telescopic loader. Hence, it is reasonable to use the loader itself as a scale.

Currently, a variety of loader scales are available on the market. The functionality of most mobile scales is largely identical. The accuracy of the payload measurement is acceptable as long as the measurement is taken at a previous specified loader attachment position during a defined boom up movement. Throughout the measurement process, the machine must not bounce or oscillate and only smooth movements are allowed. To achieve a high accuracy, the center of gravity of the payload must be in a previously defined position. Generally, this is obtained by moving the bucket cylinders to the upper end stroke position and assuming the center of gravity of the payload to be always in the bucket at the same position. This applies to a bucket that is completely filled with bulk material of a constant density such as sand or gravel. If the bucket is only partly filled, the center of gravity position of the payload will vary. Furthermore, with different tools attached, for instance a palette fork or a bale clamp, the center of gravity position of the payload will change. This causes deviations in the payload measurement.

Analyzing these scales revealed that there is a need for an integrated and flexible technical solution for dynamic and continuous weighing of the payload during the operator's work process. This solution needs to be independent of the center of gravity position of the payload which in turn allows the use of any attached tool such as buckets, palette forks, or bale clamps. The payload measurement must be independent of the position and movements of the attachment, as well as independent of the position and its movements of the machine. The calibration process of the scale must be easy to perform and adaptable to

structure changes, such as mounting an additional valve to the boom.

To meet these demands, this thesis deals with the research and development of a mobile loader scale. The underlying theory is concerned with the combination of two models; a static model which deals with the dimensions and actuator forces of the loader; and a multi-body model which deals with accelerations. The static model transfers measured actuator forces into torques at the joints of an open planar kinematic chain which represents the boom and bucket with their joints. The multi-body model transfers actual accelerations of loader movements into forces. These forces in connection with their respective levers, generate torques at the joints as well. These torques are set in relation to each other. Hence, the multi-body model considers a loader without payload. The torques from the static model and the torques from the multi-body model differ from each other so that a calculation of the payload is possible. Measuring accelerations in all axis and providing them to the multi-body model allows to compensate oscillations of the loader movements. Also, tilting of the machine is compensated in this way.

The independence of the measurement of the center of gravity position of the payload is realized by considering the torques at both joints of the open planar kinematic chain which implies the use of the boom and bucket actuator forces. Thus, any tool can be attached without an additional calibration, even a tool with an additional moving arm such as a crane or excavator attachment.

Due to the cylinder and joint friction, the measured actuator forces deviate from the forces which are needed to lift the payload. For instance, the measured actuator force for the same payload will be higher for a boom up movement than at standstill and lower for boom down movement. This disturbs the payload measurement. Hence, friction is estimated with a friction model to counteract these effects.

Usually, scales are categorized and benchmarked by their accuracy. In this case, the accuracy of the payload measurement strongly relies on the accuracy of the models. It is very time consuming to build an accurate multi-body model and identifying all of its parameters. Either the model and its parameters are derived from 3D-CAD data or a real loader is taken apart and each parameter is measured in tests as done in this thesis. A model derived from 3D-CAD data underlies manufacturing tolerances and does not consider changes made to the loader afterwards, such as adding an additional valve to the boom. Deriving the multi-body model by tests requires a lot of effort but is very accurate for one loader. Due to variance in manufacturing outcomes, test results cannot be transfered but have to be conducted for every single machine. This led to the development of

a reduced multi-body model that obtains its parameters partly from 3D-CAD data and partly from a short calibration procedure. In this case, the reduced multi-body model is self-adjusting and covers all manufacturing tolerances. For later changes to the front loader the calibration procedure can easily be redone.

In order to measure payload continuously at any time, the static model and the multi-body model require a continuous position detection of the loader relative to the machine. To obtain a reliable measurement system, which is also easy to retrofit on existing loaders, the position detection is implemented with three inertial measurement units (IMUs) connected to the chassis, boom, tool carrier, or bucket. IMUs consist only of non-moving parts and can be mounted anywhere in a protected position.

Finally, this thesis presents the implementation and testing of the dynamic and continuous mobile scale on an agricultural tractor front loader that measures independently of the center of gravity position of the payload. Further analyses reveal that it is possible to measure payload during the working process with a deviation of 1% of the maximum loading capacity.

Kurzfassung

In vielen industriellen Bereichen ist es vorteilhaft das Gewicht einer Nutzlast während der Abfertigung oder dem Transport zu messen. In einer Mine oder einem Steinbruch werden zum Beispiel die Materialkosten für eine Lastwagenladung für gewöhnlich durch das Gewicht ermittelt. Um das Gewicht der Ladung zu bestimmen, muss der Lastwagen zweimal eine stationäre Waage passieren, vor und nach dem Laden. Wenn man das Gewicht kontinuierlich beim Beladen misst, kann man die Effizienz des gesamten Prozesses steigern und eine stationäre Waage ist überflüssig.

Eine direkte Gewichtsmessung erweist sich auch dann als sinnvoll, wenn man einen Anhänger möglichst effizient beladen möchte ohne dabei das maximale Bruttolastgewicht zu überschreiten. Ein weiteres Beispiel für die Vorteile einer direkten Gewichtsmessung ist das Beschicken einer Biogasanlage mit einer definierten Masse an organischem Material. Eine Steigerung der Produktivität und Effizienz kann auch in einem Viehbetrieb erlangt werden, indem man die richtige Menge an Nahrung direkt während der Befüllung der Futteranlagen abwiegt, anstatt das Gewicht davor auf einer stationären Waage zu wiegen oder einfach nur zu schätzen. In der Regel werden Lasten mit einem Traktor Frontlader, Radlader oder Teleskoplader transportiert. Daher ist es naheliegend den Lader selbst als Waage einzusetzen.

Derzeit sind mehrere verschiedene mobile Lader-Waagen auf dem Markt erhältlich. Die meisten Waagen basieren auf dem selben Funktionsprinzip. Die Genauigkeit dieser Waagen ist nur gegeben, wenn die Messung in einer vorher definierten Schwingenposition und bei einer bestimmten Zylinderverfahrgeschwindigkeit erfolgt. Während des Messvorgangs darf sich die Maschine nicht ruckartig bewegen oder schwingen. Es sind nur sanfte, kontinuierliche Bewegungen erlaubt.

Um eine hohe Genauigkeit der Gewichtsmessung zu erreichen, muss sich der Schwerpunkt der Ladung in einer vorher definierten Position befinden. Im Allgemeinen wird dies erreicht indem die Schaufelzylinder in die obere Endposition gefahren werden. Außerdem gilt die Annahme, dass der Ladungsschwerpunkt sich immer innerhalb der Schaufel und an der gleichen Position befindet. Dies gilt nur dann, wenn die Schaufel vollständig mit Schüttgut von konstanter Dichte gefüllt ist, wie zum Beispiel Sand oder Kies. Die Schwerpunktlage variiert jedoch, wenn die Schaufel nur teilweise gefüllt wird. Wird die Schaufel gegen andere Werkzeuge ausgetauscht, wie zum Beispiel eine Palettengabel oder eine Heuballenzange, so ändert sich die Schwerpunktlage bei jeder neuen Ladungsaufnahme und verursacht Abweichungen in der Gewichtsmessung.

Die Analyse der bestehenden mobilen Lader-Waagen zeigt, dass der Bedarf einer integrierten und flexiblen technischen Lösung einer mobilen Lader-Waage besteht, die kontinuierlich und dynamisch während des Arbeitsvorgangs wiegen kann. Diese Waage muss das Gewicht unabhängig von der Schwerpunktlage der Ladung messen, was den Einsatz beliebiger Werkzeuge, wie zum Beispiel verschiedener Schaufeln, einer Palettengabel oder einer Heuballenzange ermöglicht. Die Gewichtsmessung muss unabhängig von der Schaufel-, Arm- und Maschinenposition oder Bewegung erfolgen. Außerdem muss der Kalibrierungsprozess der Waage einfach durchzuführen und anpassbar sein, um schnell auf Änderungen reagieren zu können, wie zum Beispiel der Montage eines zusätzlichen Ventils auf der Laderschwinge.

Um diesen Anforderungen gerecht zu werden, beschäftigt sich diese Arbeit mit der Forschung und Entwicklung einer mobilen Lader-Waage. Die zugrunde liegende Theorie kombiniert zwei Modelle: Ein statisches Modell, welches die Dimensionen des Laders und die Aktuatorkräfte berücksichtigt und ein Mehrkörpermodell, welches verwendet wird um Beschleunigungen zu verarbeiten. Das statische Modell wandelt gemessene Aktuatorkräfte in Drehmomente an den Gelenken einer offenen, ebenen, kinematischen Kette um, welche die Schwinge und Schaufel mit den jeweiligen Gelenken darstellt. Das Mehrkörpermodell überträgt die aus den Bewegungen des Laders resultierenden Beschleunigungen in Kräfte. Diese Kräfte erzeugen, mit ihren jeweiligen Hebeln, ebenso Drehmomente an den Gelenken. Anschließend werden die Drehmomente aus den verschiedenen Modellen in Relation zueinander gesetzt. Die Drehmomente des Mehrkörpermodells, das die Ladung nicht berücksichtigt, und die Drehmomente des statischen Modells, das mit gemessenen Aktuatorkräften gespeist wird, unterscheiden sich. Aus diesem Unterschied kann nun das Gewicht der Ladung bestimmt werden. Die Schwingungen und Bewegungen des Laders werden kompensiert, da das Mehrkörpermodell mit direkt gemessenen mehrachsigen Beschleunigungen gespeist wird. Ebenso werden Neigungen der Maschine ausgeglichen, die zum Beispiel bei Arbeiten am Hang entstehen.

Durch die Berücksichtigung der Aktuatorkräfte von Schwinge und Schaufel können die Drehmomente an beiden Gelenken der offenen ebenen kinematischen Kette bestimmt werden, wodurch die Gewichtsbestimmung unabhängig der Ladungs-Schwerpunktslage ermöglicht wird. Somit kann jedes Werkzeug oder Anbaugerät ohne zusätzliche Kalibrierung eingesetzt werden. Darüber hinaus kann ein Anbaugerät mit einem zusätzlichen beweglichen Arm eingesetzt werden, ähnlich einem Kran oder einer Grabausrüstung eines Baggers.

Aufgrund der Zylinder- und Gelenkreibung weichen die gemessenen Aktuatorkräfte von den Aktuatorkräften ab, die erforderlich sind die Ladung in Position zu halten. Für die

gleiche Ladung ist, beispielsweise, die gemessene Aktuatorkraft während der Schwingen-aufwärtsbewegung höher und während der Abwärtsbewegung niedriger als bei Stillstand. Dies führt zu Abweichungen in der Gewichtbestimmung. Um diesem Effekt entgegenzuwirken wird die Reibung mithilfe eines Reibmodells abgeschätzt und in der Gewichtsmessung berücksichtigt.

Waagen werden unter anderem anhand ihrer Messgenauigkeit kategorisiert und bewertet. Die Genauigkeit der Gewichtsmessung ist stark abhängig von den Genauigkeiten der Modelle. Es ist sehr zeitaufwendig alle Parameter zu identifizieren, um ein genaues Mehrkörpermodell zu erstellen. Entweder werden das Modell und dessen Parameter von 3D-CAD-Daten abgeleitet oder ein echter Lader wird demontiert und zerlegt und die Parameter werden durch verschiedene Tests bestimmt, wie es in dieser Arbeit erfolgte. Wird ein Modell aus 3D-CAD-Daten abgeleitet, bestehen infolge von Fertigungstoleranzen Abweichungen zur Realität. Außerdem werden keine Änderungen berücksichtigt, die nachträglich am Lader gemacht wurden, wie zum Beispiel das Anbringen eines zusätzlichen Ventils an der Schwinge. Das Identifizieren der Mehrkörpermodellparameter durch Tests ist sehr präzise für einen einzelnen Lader, bedeutet jedoch einen erheblichen Arbeitsaufwand. Aufgrund der Fertigungstoleranzen können die Parameter nicht übertragen werden, sodass die Identifikation für jeden einzelnen Lader erneut durchgeführt werden muss. Auf der Suche nach einem einfacheren und weniger arbeitsaufwendigen Verfahren wurde ein reduziertes Mehrkörpermodell entwickelt, dessen Parameter teilweise von 3D-CAD-Daten abgeleitet werden und teilweise durch ein kurzes Kalibrierverfahren identifiziert werden. Dadurch wird das reduzierte Mehrkörpermodell für jeden Lader automatisch angepasst und deckt alle Fertigungstoleranzen ab. Für spätere Änderungen am Lader kann die Kalibrierung leicht wiederholt werden.

Für das statische Modell und das Mehrkörpermodell ist eine kontinuierliche Positionserfassung der Schwinge und Schaufel zur Maschine nötig, um das Gewicht der Ladung kontinuierlich messen zu können. Ein zuverlässiges Messsystem, das auch einfach an bestehenden Ladern nachgerüstet werden kann, wird mit drei inertialen Messeinheiten (Inertial Measurement Unit, IMU) umgesetzt. Die IMUs sind jeweils an der Maschine, der Schwinge und der Schaufel beziehungsweise dem Geräteträger angebracht. Der Vorteil besteht darin, dass IMUs keine beweglichen Teile beinhalten und an einer beliebigen, vor Zerstörung geschützten, Position angebracht werden können.

Abschließend wurde die mobile Waage als Prototyp an einem Traktor Frontlader installiert. Weitere Analysen zeigen, dass man mit dieser Waage das Gewicht kontinuierlich während des Arbeitsablaufes messen kann. Dies erfolgt mit einer Abweichung von 1% der maximalen Ladekapazität.

1 Introduction

1.1 Motivation

For many loader applications it is a benefit to measure the payload directly while handling it. For instance, the costs of material loaded on a dump truck in a quarry is generally priced by its weight. In this case, the truck has to pass a stationary scale twice to identify its payload, before and after loading. Measuring the weight of the material instantly while loading the truck would increase the efficiency of the process and a stationary scale would be redundant. Also, in many farming tasks it is necessary to measure weight, for example, to efficiently load a trailer with goods to its maximum capacity without exceeding the gross load weight or filling a bio-gas plant with a defined mass of organic material. Generally, a common tractor front loader, wheel loader, or telescopic loader handles the payload. Hence, it is obvious to use the loader itself as a scale.

Using the loader as a scale offers new possibilities for documentation, billing and monitoring the transfer of goods, such as hay bales, palettes, etc. For example, it allows contractors to measure the work in the quantity of the handled payload and change their hourly payment into a merit pay, according to the results or effort or wear of the loader. In addition, by measuring the payload continuously, also discontinuous media, such as seeds, at varying density could be monitored. For instance, precision farming applications demand tracing the spread of seeds or fertilizer on the fields to optimize the yield according to the sowing [Tre02]. Combining a positioning system, like a global navigation satellite system (GNSS), with a continuous payload measurement allows to calculate and to control the mass flow $\dot{m}_{payload}$ of the seeds or fertilizer at any position on the field. Other farming applications are described by [Loa14a] and [Loa14b] where farmers increase their productivity by weighing the feed for dairy cows with a mobile front loader scale. It allows them to supply the exact amount of food to promote the optimum levels of milk productions and to monitor the weight totals of food accurately.

[Vei13] explains that measuring the payload with the loader directly reduces fuel consumption in a mine due to the elimination of under loads and waiting times at the loading site when the truck was overloaded.

Currently, a variety of loader scales is available on the market. The functionality for most mobile scales is largely the same. The accuracy of the payload measurement is good

as long as specific boundary conditions are fulfilled (cf. section 1.2.3). Studying those scales revealed that there is a need for an integrated and flexible technical solution for dynamic and continuous weighing of the payload during the operator's work process. This solution needs to be independent of:

- the center of gravity position of the payload

- the attached tool (e.g. bucket, palette fork, etc.)

- the loader position and its movements

- the vehicle position and its movements.

In order to achieve these goals, this thesis deals with the research and development of a new kind of mobile loader scale.

1.2 State of the Art of Mobile Scales

Currently, several wheel loader and front loader scales are available on the market with an achieved accuracy of class four which corresponds to an ordinary scale [PFR14] [DIN92] (cf. section 5.1.1 for more detailed information on accuracy classes). The technical functionality is generally the same. Differences mostly occur within further processing capacities. This chapter mainly focuses on the technical realization of available scales and their capabilities.

1.2.1 General Functioning

There are several ways to measure the payload attached to the movable boom of a mobile machine, for example, a front loader, wheel loader, telescopic loader, or excavator. Some mobile scales for telescopic loaders measure the bending strain of the long boom to determine the payload. Therefore, strain gauges are applied directly to the boom or mounted by a load cell [Pro12a] [BAR13] [Fli11b]. This kind of scale is not further discussed in this thesis. Most loader scales use the cylinder forces to determine the payload which is usually calculated by measured pressures at the piston and rod sides of the boom cylinders.
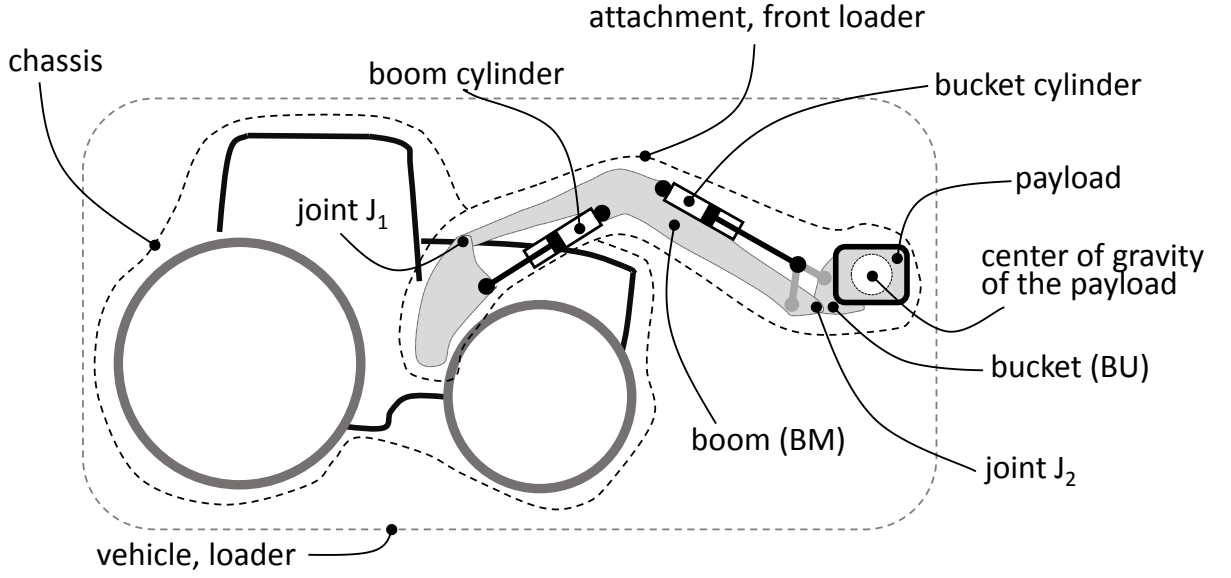
Figure 1.1: Loader description

The payload m_L with its lever h_{mL} and weight $F_{cogL} = -g\, m_L$ generates a torque TQ_1 at the joint J_1 between boom and tractor as shown in figure 1.2. The torque is in balance with the torque generated by the boom cylinder force F_{BM_cyl} and its lever h_{BM_cyl}.

$$F_{cogL}\, h_{mL} = F_{BM\_cyl}\, h_{BM\_cyl} \tag{1.1}$$

Equation (1.1) shows that the cylinder force increases proportionally to the weight of the payload if the levers remain constant. Because the levers h_{mL}, h_{BM_cyl} are functions of the boom or bucket position of the loader, the payload measurement is performed always at the same position or in a small position range.
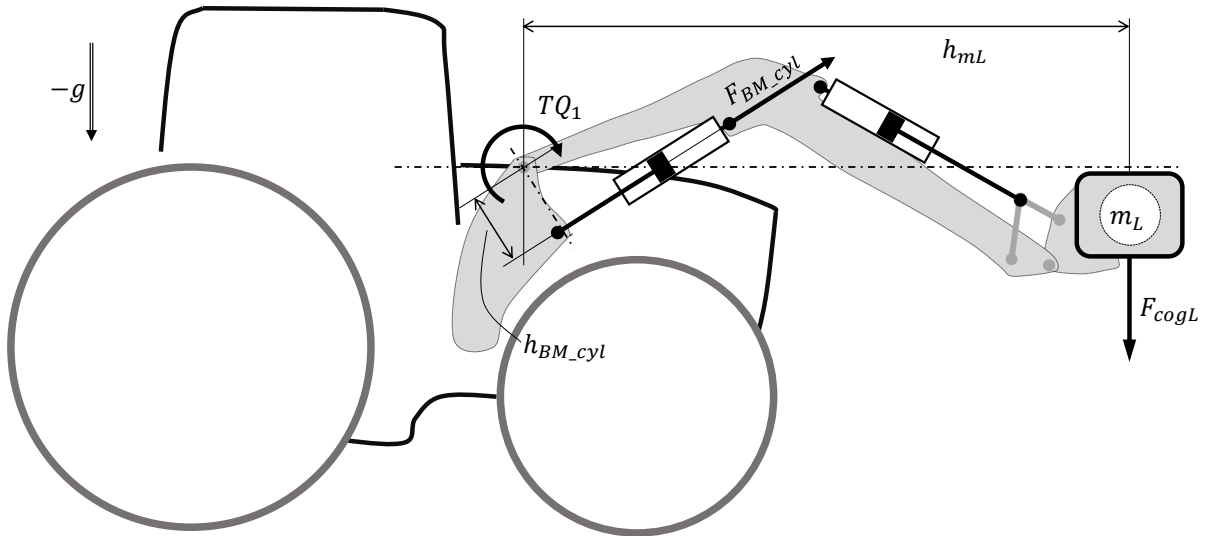
Figure 1.2: Torque balance between the cylinder forces and the payload

Finally, equation (1.2) determines the payload based on the cylinder force.

$$m_L = \left(\frac{h_{BM\_cyl}}{-g\,h_{mL}}\right) F_{BM\_cyl} = kF_{BM\_cyl} \tag{1.2}$$

The constant parameter k is in principle identified by a previous two point calibration with two different known weights m_{L1} and m_{L2}, as described in chapter 1.2.5.

1.2.2 Setup and Components

To measure the payload, the loader is equipped with several sensors. The boom cylinder pressures p_{BM_A} and p_{BM_B} are measured with sensors located in the hydraulic lines between cylinder and valve, as shown in figure 1.3. The cylinder forces can be calculated with the knowledge of the areas of piston and rod sides. However, due to the previous load calibration (cf. section 1.2.5) this is not necessary. It is sufficient to obtain a scaled cylinder force $F_{BM\_cyl_{scaled}}$, from equation (1.3), which is set into relation with the payload and can be calculated with the cylinder ratio between piston area A_A and rod area A_B (ram-ratio, $\alpha = \dfrac{A_A}{A_B}$), mostly in the range of 1.25 to 1.34 [RDS08] [WG08]. The friction is not yet considered.

$$F_{BM\_cyl_{scaled}} = \frac{F_{BM\_cyl}}{A_{BM_B}} = p_{BM\_A}\alpha - p_{BM\_B} \tag{1.3}$$

Furthermore, the boom position is needed. Since the payload measurement is always performed at the same position, it is sufficient to determine, using a proximity switch, if the boom is at the desired measuring position.

In addition, friction has to be considered because the front loader experiences friction in cylinders and bearings. Hence, it is recommended to perform the payload measurement within a defined speed range during a front loader up-movement [Fli11a]. The movement causes sliding friction which is lower than stiction. Thus, the average of a continuous pressure measurement is taken in a small boom position range. The start and end of this position range is often taken with two proximity switches. Moreover, by detecting start and end-time, it is possible to calculate the average speed of the front loader movement [Pro12b]. Some scales, for instance [Loa13], use continuous position detection with angle or stroke sensors instead of proximity switches.
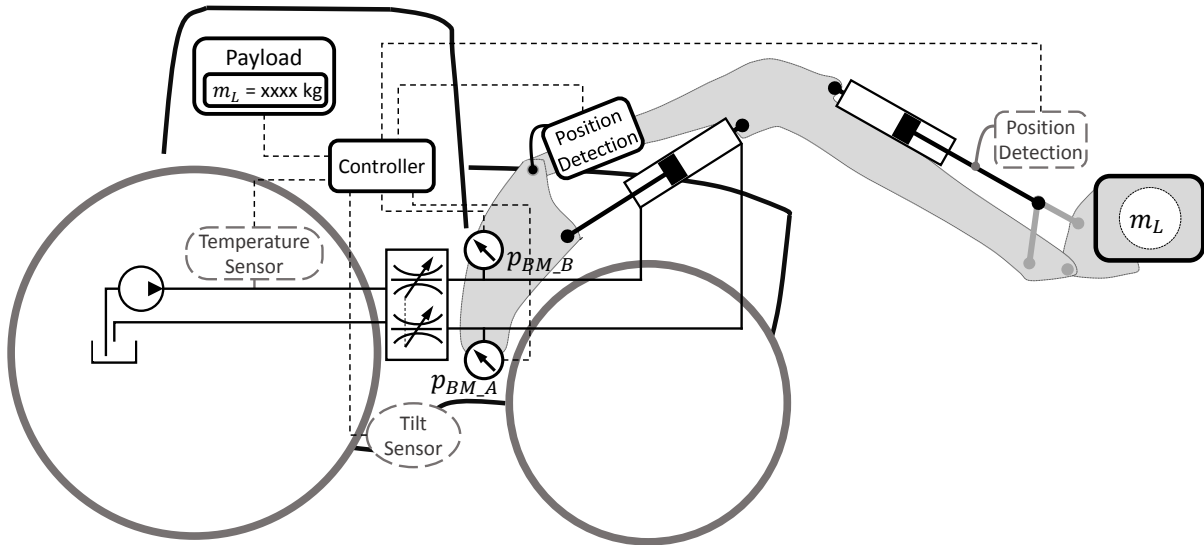
Figure 1.3: Setup and components of a common mobile scale

In addition, some scales, for instance [Loa13] or [Käm12], are equipped with a chassis tilt sensor. The tilt sensor enables a correction of the influences on the payload measurement while working on a slope or to stop the measurement if the tilt angle is too large. Also, hydraulic oil temperature is measured to compensate errors because of pressure drops between sensor and cylinder due to higher oil viscosity. Several scales have an additional bucket position detection, usually a simple proximity switch at the bucket cylinder which detects whether the bucket is in a defined position [Loa13] [RDS08].

Finally, all sensors are connected to a controller to calculate and process the weight. The controller is mostly combined with a user interface in the cab.

1.2.3 Measurement Procedure

In order to receive an accurate payload measurement several conditions and proceedings are needed. First, the operator has to perform several boom up and down movements to warm up the loader and to increase the fluid film between cylinder seal and sliding partner to reduce friction. After the warm up procedure, the scale is ready to measure. For this purpose, the operator has to lift the boom with the loaded bucket at a previously defined speed. As soon as the boom enters the position range of measurement, pressures are recorded and the payload is calculated. The lifting cycle should be smooth and continuous. If the bucket bounces too much, spikes and drops in the pressures lead to a false payload measurement. If the weighing system does not compensate tilts, the loader should operate

on a horizontal surface to avoid deviations caused by the chassis tilt angle.

The center of gravity of the payload is assumed to be always in the same position namely within the bucket. Different bucket positions or even using a different tool like a palette fork causes deviations due to a different lever h_{mL} (cf. equation (1.2)). Hence, it is recommended to turn the bucket during the measurement into a previously defined position, e.g. the upper end position. As mentioned before, some scales use an additional sensor to detect whether the bucket is in the desired position or not [RDS08].

Furthermore, the operator should be aware of greasing the pins and bearings sufficiently and check them for wear or corrosion to allow for a smooth and easy lift cycle. Otherwise, the mechanical friction can increase and be misinterpreted as an extra weight [Agg13].

1.2.4 Hydraulic Oil Viscosity and Friction

The hydraulic oil viscosity is dependent on the oil temperature. Thus, the loader must be warm, that is, the hydraulic oil must be in a constant viscosity range. Due to the fact that the boom performs a movement, oil flows through the hydraulic lines and generates a pressure drop, $\Delta p = f(\dot{V})$. Given that a certain distance exists between pressure sensors and cylinders, the pressures in the cylinders differ from the measurement [WG08] [Wat07].

$$p_{BM\_A_{measured}} = p_{BM\_A} + \Delta p_A$$
$$p_{BM\_B_{measured}} = p_{BM\_B} - \Delta p_B \tag{1.4}$$
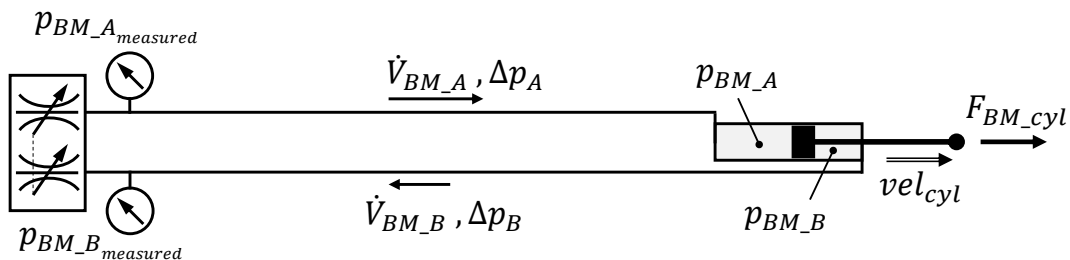
Figure 1.4: Pressure drop in the hydraulic lines due to oil flow

Furthermore, mechanical friction $F_{friction}$ occurs at the cylinders and joints of the attachment. The friction is assumed as load dependent which is further explained in section 2.9. Including the pressure drops and mechanical friction, equation (1.3) results in equation

(1.5) which is proportional to the payload m_L.

$$m_L \sim \frac{F_{BM\_cyl_{measured}}}{A_{BM\_B}} = p_{BM\_A}\alpha - p_{BM\_B} + (\Delta p_A \alpha + \Delta p_B) + \frac{F_{friction}}{A_{BM\_B}} \qquad (1.5)$$

Due to the bracket term which considers the pressure drops because of the oil flow, the measured cylinder force appears higher than it really is and falsifies the payload measurement. The challenge is to define this bracket term for different cylinder speeds at defined oil temperatures by previous calibration procedures and subtract it from the measured cylinder force to correct the payload measurement.

1.2.5 Calibration Procedure

To set the cylinder forces F_{BM_cyl} or $F_{BM\_cyl_{scaled}}$ in relation to the payload, the weighing system has to be calibrated. Before the operator starts the calibration, the hydraulic oil has to be warmed up to normal working conditions to receive a constant oil viscosity. Also, several lifting cycles have to be performed to lubricate the joints and the cylinder rod.

As mentioned before, the calibration is a two point calibration with known payload. It is a reasonable choice to first use the empty loader with zero payload. For the second payload it is recommended to choose a known weight close to the average loading capacity [RDS08]. The payload has to be inside the bucket and the bucket should be in a defined position, generally at the upper end stroke.

During the calibration, lifting cycles are performed for each known payload, e.g. $m_{L1,2}$. While the boom travels through the small measurement range the cylinder force signal is recorded and reduced to a single value $F_{BM\_cyl1,2_{measured}}$. Finally, each cylinder force value is set in relation to the respective payload to calculate the linear interpolated calibration curve as shown in figure 1.5. Due to the load dependency of the mechanical friction, the gradient of the measured calibration curve is reduced. Hence, mechanical friction is considered in the calibration as well as in the subsequent payload measurement. The accuracy of the calibration curve can be increased by additional measurement points with further known payloads.
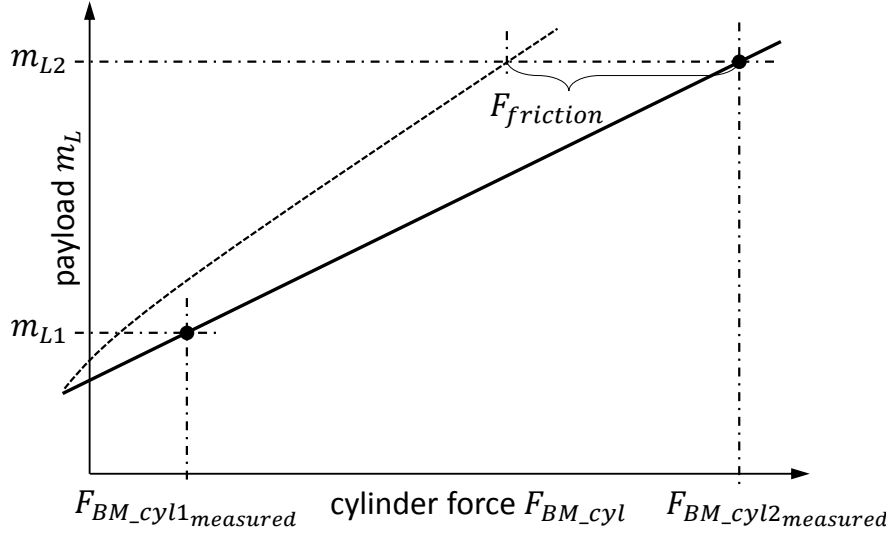
Figure 1.5: Two point calibration

Some manufacturers, for instance [RDS08], distinguish between slow and fast lifting cycles and try to compensate payload deviations that result from pressure drops in the hydraulic lines. As mentioned before, there is a certain distance between the pressure sensors and the cylinders and a pressure drop $\Delta p = f(\dot{V})$, caused by the oil flow, can be measured. Equation (1.6), which originates from equation (1.5), shows that the pressure drop has to be subtracted from the measurement to obtain the cylinder forces.

$$\frac{F_{BM\_cyl}}{A_{BM\_B}} = \frac{F_{BM\_cyl_{measured}}}{A_{BM\_B}} - (\Delta p_A \alpha + \Delta p_B) - \frac{F_{friction}}{A_{BM\_B}} \tag{1.6}$$

The pressure drop can be identified by comparing a very slow lifting cycle to a fast one (cf. appendix A.8). During this procedure, the payload as well as the oil viscosity must not change. Furthermore, the cylinder ratio α has to be known and the friction at a given payload is assumed to be equal for slow and fast movement. Finally, several pressure drops can be identified for different lifting (cylinder) speeds and the deviation, which is due to the pressure drop, can be compensated. Figure 1.6 shows an example of two calibration curves, one for fast and one slow cylinder velocity. Curves for other cylinder speeds can be interpolated or measured as well.
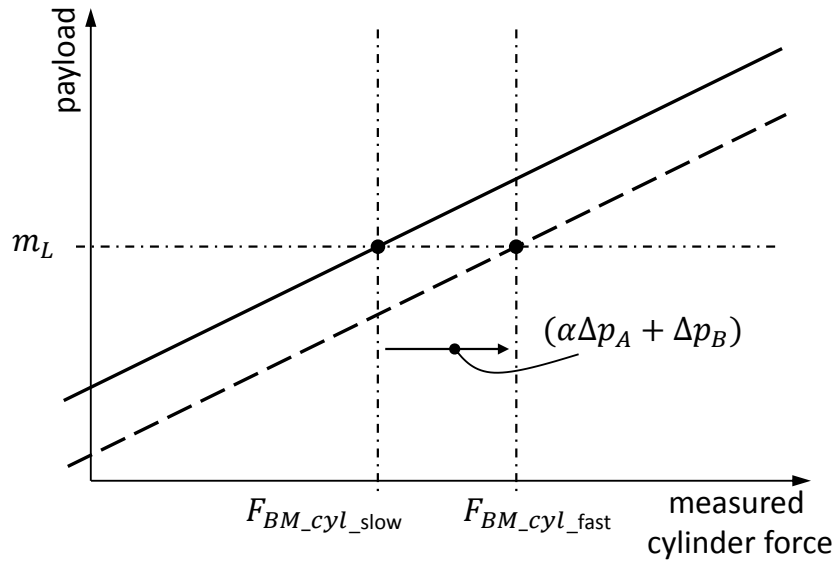
Figure 1.6: Pressure drop compensation

In the figure, the vertical axis is labeled "payload" with m_L marked, and the horizontal axis is "measured cylinder force" with $F_{BM\_cyl\_\text{slow}}$ and $F_{BM\_cyl\_\text{fast}}$ marked. The annotation reads $(\alpha\Delta p_A + \Delta p_B)$.

1.2.6 Current Research

This chapter deals with the current research of mobile scales and their different approaches to increase the performance of mobile scales. In [BBU12] an observer-based payload estimator is introduced. The payload is assumed as a parameter of a dynamic model which will be estimated with an observer. Therefore, a detailed multi-body model of the loader is used. Becker [Bec14] describes a common weighing system with an optimized model based calibration procedure. The calibration procedure is shortened by using a mathematical model. Both approaches require a detailed knowledge of the attachement geometry, parameters, and kinematics.

Kämmerer [Käm12] describes a mobile scale with increased performance and accuracy. It is already implemented and available on the market. The position detection is continuous and the payload can be measured in the range of 10% to 80% lifting height [Pro14]. The basic weighing system is equal to the previously described state of the art but with all additional sensors (cf. figure 1.3). To obtain a high accuracy, the measurement differs from the common ones. The operator starts the measurement procedure by actuating a trigger. In a next step, the boom performs a little, autonomous, slow up and down movement. Due to the friction of the cylinders and joints the measured cylinder forces will be higher for the up movement and lower for the down movement. The absolute amount of friction is assumed to be equal for both movements. Finally, to compensate the friction, the average cylinder force of both movements is taken and set into relation with the payload. During the measurement, the bucket has to be in a defined position at the upper cylinder end-stroke. The end-stroke position is detected by a stroke sensor. Also, the chassis has

to stand still or move slowly [Pro14]. An additional reference is given by [BM13] which is partly subject of this thesis. Hence, it is not further discussed in this section.

1.2.7 Patents

This section summarizes the essential facts of a few patents which are important to mention here. Patent [Fli11a] describes a weighing system which measures the boom cylinder forces by pressures or strain gauges to determine the payload. For this purpose, the generated torques of the weight and the cylinder force at the boom joint are brought into balance. To calculate the effective levers for generating the torques, the attachment kinematics and the boom position have to be known. For the lever and moment of inertia of the weight, the center of gravity of the payload is assumed to be a point mass within the bucket. During the measurement a sensor detects whether the bucket is in the previously defined position. Finally, the torque balance is solved to obtain the payload.

To enable the payload measurement at any boom position, its position is detected continuously through the whole range of movement. Preferably, the boom position sensor is designed as an acceleration sensor with a gyro which measures the gravity vector relatively to the boom. Thus, the boom angle relatively to the chassis can be determined if the chassis is aligned horizontally. Otherwise, the chassis tilt angle is measured with an inclination sensor and considered in the boom position detection. The gyro measures the angular velocity of the boom movement. The angular acceleration is derived from it and is also considered in the torque balance which calculates the payload. Due to lower sliding friction than stiction it is better to measure during the movement which can be detected by the value of the angular velocity. Finally, due to the continuous payload measurement, much data is available for further processing like filtering or averaging.

Patent [Wis00] describes a standard state of the art weighing system which measures the boom cylinder forces using pressures to determine the payload. The system is enhanced by adding acceleration sensors to all parts: chassis, boom and bucket. Preferably, the acceleration sensors are designed to measure accelerations in all three axes which gives the possibility to define a position of each part relative to the gravity. The center of gravity of the payload is assumed to be a point mass within the bucket. If the bucket changes its position, the boom cylinder forces are changing, too, which falsifies the payload measurement. This can be corrected by detecting the positions of boom and bucket. Also, knowing the position allows to compensate the influence of a chassis tilt angle on the payload measurement. If the attachment moves, the acceleration differs from the gravity. Measuring the accelerations directly gives the opportunity to compensate influences of movements on

the payload measurement.

For the sake of completeness, patent [BPH14] has been compiled during the course of this work which covers the topic of this thesis.

1.2.8 Potential for Improvement

Currently available mobile scales for wheel loaders, front loaders, telescopic loaders, or excavators measure the boom cylinder force to determine the payload. Only a few exceptions measure the bending strain of the boom which is not further discussed here. The following list summarizes the facts:

- An initial warm up of the hydraulic oil and several lifting cycles must be performed to lubricate the cylinder seals.

- The payload is measured during a lifting cycle which should be smooth and in a previously defined (calibrated) speed range.

- The measurement is only taken in one position or position range but not continuously. Hence, the operator has to lift the boom until this measurement point or range is reached. An exception is given by [Käm12] (cf. section 1.2.6) which measures at several positions but, thus, the measurement procedure changes to a little, autonomous, slow up and down movement.

- Bouncing of the loader causes spikes and drops in the pressure readings which falsifies the payload measurement. Patent [Wis00] mentions the possibility to compensate the result with measured accelerations.

- To estimate and consider the pressure drop between pressure sensor and cylinder the oil viscosity should match to a previously defined value. To achieve this, a viscosity range is defined at a given oil temperature.

- The center of gravity of the payload is assumed as a point mass within the bucket. Therefore, the bucket has to be in a predefined position usually the upper end position. Variations of the center of gravity position of the payload falsifies the payload measurement. Some loader scales have a position sensor to detect whether the bucket is in the desired position.

- It is important to grease the pins and joints properly and check them for wear. Otherwise, the friction increases and is misinterpreted as an additional weight.

- Proximity switches are often used to detect the position relative to the chassis. If the position is continuously detected, an angle sensor is mounted in the axis of the boom pin and must be protected against damage. In case of a tractor front loader, this could affect the field of view.

- Current mobile scales need an extensive calibration procedure. There are already attempts to reduce this calibration process by using mathematic models (cf. section 1.2.6), but generating these models is very time consuming and generally restricted to one vehicle. For instance, [BBU12] uses a multi-body model of a loader. In this case, changes at the loader are not allowed. For example, if the operator mounts an additional mass to the boom, the real loader differs from the multi-body model and the payload measurement deviates.

In the following, several obvious issues of a common mobile scale are presented which could be enhanced: for instance, the operator must be aware to run the loader smoothly to receive an accurate payload result. If he works on an uneven, bumpy ground, he has to stop traveling which restricts him in his normal work flow. Also, the boom has to be lifted at a defined speed until the measurement position is reached although the work demands different movements.

To calibrate the mobile scale, the loader has to be loaded with several known weights and perform lifting cycles in different conditions. The advantage is that the calibration fits the loader because it has to be done for every loader. The disadvantage is the immense effort to transport the known weights and to perform all test cycles.

It is common to use several tools on one vehicle, for example, a palette fork or a bale clamp in combination with a tractor front loader. Due to the tool, the center of gravity of the payload varies and will not be in a defined position, for example, within the bucket which is turned to the upper end stroke. In this case, the payload measurement is false. The measurement independent of the center of gravity position of the payload allows for the usage of any tool. The net weight of the tool will be measured as payload as well, but can be treated like a tare weight which will be set to zero at the beginning of the working process. In this case, the type of tool is not important. Thus, the payload measurement is independent of the tool in use and the tool could even have an additional arm with a bucket such as an excavator attachment or a crane, like a skidding crane of a forestry machine. The payload measurement independent of the center of gravity position of the payload offers a wide range of opportunities.

In conclusion, it can be said that currently available mobile scales can measure quite

accurately if all required conditions are given (cf. section 1.2.3). For instance, [Pro12b] benchmarked several loader scales. During tests, the payload of a completely filled bucket ($\approx 4t$) was identified with a deviation of $\approx 1\%$, which is the lowest achieved deviation of wheel loader scales. For a half full bucket the deviation increases up to $\approx 8\%$ due to shifting of the center of gravity position of the payload. At tractor front loader scales the lowest achieved deviation turned out to be $\approx 3\%$ for a full bucket ($\approx 600kg$). In [Pro12b] it is advised against measuring payload of a half or quarter full bucket with a tractor front loader due to even higher deviations. This shows that there is still a lot of room for improvements and to increase the performance of a mobile scale.

1.3 Objectives

The goal of this thesis is to develop a mobile scale which measures the weight of the payload lifted with an agricultural tractor front loader or similar vehicle and to provide a continuous signal for further processing. The signal yields the payload as fast as possible after being lifted from the ground. The payload measurement must be accurate in every standard working condition even if the vehicle moves, bounces or travels. It has to be possible to measure continuously in every front boom or bucket position without interrupting the work flow and independent of the center of gravity position of the payload. The influence of the hydraulic oil temperature on the measurement must be minimized. Furthermore, the calibration process should be simplified or eliminated but still provide the opportunity to adjust the weighing system to compensate manufacturing tolerances or structure changes on front loader. For example, if the customer mounts an additional valve to the boom its mass changes and has to be considered for the payload measurement. Moreover, the position detection must be continuous, reliable, easy to mount even for retrofitted weighing systems and easy to protect against damage.

1.4 Approach and Structure of this Thesis

This thesis discusses mainly an agricultural tractor front loader, as an example of all types of loaders, to achieve the previously defined targets. Accordingly, a detailed multi-body model of a common tractor front loader is developed and fed with measured acceleration to calculate reaction forces. All relevant simulation parameters, like inertia or mass, are identified by real tests to reproduce the reality as closely as possible. Furthermore, the loader kinematics is discussed and transferred to a simplified kinematics. An additional static model uses the simplified kinematics combined with a friction model and transfers measured cylinder forces into torques at the joints. Finally, the static model and the multi-

body model are merged to calculate the payload.

In addition, a tractor front loader is equipped to measure all relevant variables and to verify the models. Therefore, measurements of boom and bucket positions, pressures at the cylinders and linear accelerations, angular velocity and angular acceleration at the chassis, boom and bucket are taken. The position detection, as a component of the mobile scale, is implemented by using only the already available acceleration sensors and gyros (Inertial Measurement Unit, IMU) of chassis, boom and bucket. The advantages are that the sensors consist only of non-moving parts and that they can easily be mounted in a protected position.

The identification of the parameters for the multi-body model is very time-consuming and an immense effort is needed. In this case, it is done for a single front loader, because every loader attachment has tolerances the parameter identification must be repeated for every loader. This is not suitable for serial production. Getting these parameters only from 3D-CAD-models is not sufficient due to tolerances. Thus, there is a need for an approach with reduced parameters which can be easily identified by a short and simple procedure. This leads to the development of a reduced multi-body model that fits these requirements. Furthermore, an automatic procedure to identify the parameters of the reduced multi-body model is developed. Finally, the algorithms are tested on a prototype and the results are discussed. The thesis is structured as follows:

- The *Introduction* in chapter 1 shows the motivation and defines the goals and objectives of this thesis by discussing the state of the art of common loader scales.

- Chapter 2, *Technical Basics*, provides a collection of fundamentals that are used in the subsequent main part.

- The main part is divided into two chapters: Chapter 3, *Position Detection* and chapter 4, *Weighing Function*. The loader position is necessary for the weighing function whereas the measurement method is irrelevant for the weighing function. Hence, the *Position Detection* is discussed in a separate chapter. The *Weighing Function* explains the details of the **dynamic, continuous, and center of gravity independent weighing system** which is the main focus of this thesis.

- In chapter 5, *Results*, the weighing function is tested on a prototype and the results are being discussed.

- Finally, chapter 6 completes this thesis with a *Conclusion and Outlook* for further research.

2 Technical Basics

This chapter is a collection of technical fundamentals used in this thesis. The main part, which includes chapter 3 and chapter 4, refers back to this chapter.

2.1 Kinematic Chain

This section gives the basic principles of kinematic chains which are necessary to understand the loader kinematics that are the subject of the following section 2.2. A kinematic chain is a set of rigid bodies (links) coupled by kinematic pairs. The kinematic pairs, also termed as joints, constrain the relative motion of the links [Ang07]. Kinematic chains are divided in open and closed kinematic chains. A closed chain contains at least one loop. An open chain has open attachment points as shown in figure 2.1(b).
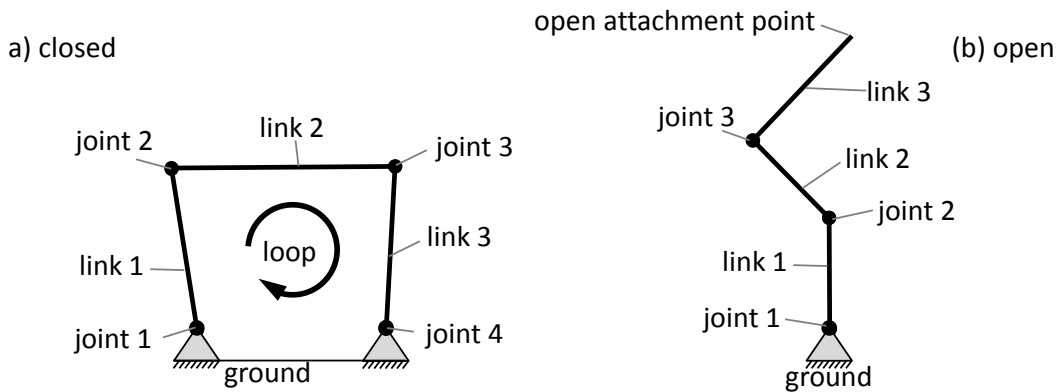
Figure 2.1: Closed and open kinematic chain

A kinematic chain can be analyzed by the degrees of freedom (DOF), which is defined as the amount of input to create a predictable output. In other words, the DOF is the necessary number of link positions which are needed to define the entire position of the whole system. For instance, the closed kinematic chain of figure 2.1 has one DOF and the open chain has three DOFs.

In general, a rigid body has six DOFs, pure translation to all axis x, y, z, and pure rotation around the axis. If the rigid body is connected with a joint to the ground its DOFs are diminished and its mobility is reduced. For example, a revolute joint between the rigid body and the ground allows only rotation around its axis. A second link which is connected via a second revolute joint to the rigid body (first link) could perform rotation and translation. The mobility f of the whole kinematic chain is described with the mobility

table [Mar05] which specifies $f = 3$ for planar chains. The number of DOFs is calculated by the following equation:

$$DOF = (6 - f)n - \sum_{j=f+1}^{5} [(j - f)c_j] \qquad (2.1)$$

Here, the number of linkages equal n, the number of joints per type equal c, and the number of diminished DOFs equal j according to the joint type. For example, a revolute joint has one DOF, that means five DOFs are diminished, hence, $j = 5$. Another example is the closed kinematic chain of figure 2.1(a) which has four joints of one DOF, thus, $j = 5$ and $c_5 = 4$.

The joint order increases by one for every additionally connected link as shown in figure 2.2. For instance, a first order joint connects two links and counts as a single joint $c = 1$. A second order joint connects three links and counts twice, hence, $c = 2$ and so forth [Mar05] [GHSW06].
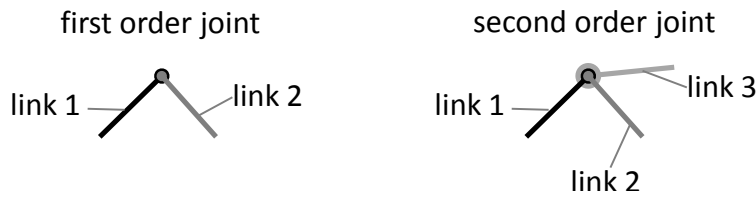
Figure 2.2: Joint order
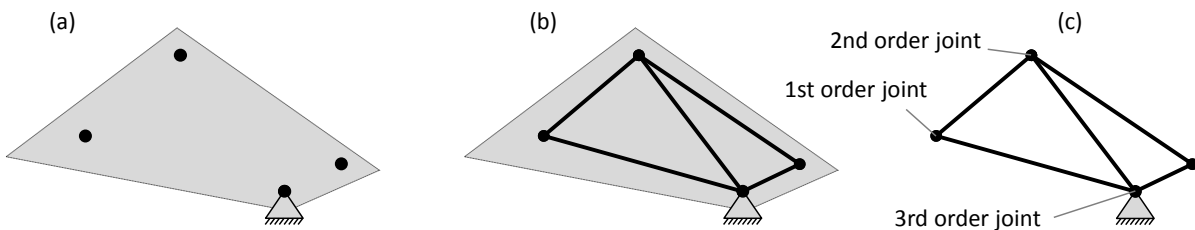
Figure 2.3: Transfer contour to linkage

A link with more than two joints is termed as contour, figure 2.3(a). To calculate the DOFs of the kinematic chain, the contour is transferred into a linkage via connecting the joints of the contour with links, as shown in figure 2.3(b). For the resulting kinematic chain of figure 2.3(c) follows, with $f = 3$, $n = 5$, $c_5 = 7$, and equation (2.1):

$$DOF = (6 - 3)5 - [(5 - 3)7] = 1 \qquad (2.2)$$

2.2 Loader Kinematics

This section analyzes the kinematics of loaders. The loaders shown here in 2D represent commonly 80% of the available loaders.

2.2.1 Non Self-Leveling

Figure 2.4 shows a standard **non self-leveling tractor front loader** which is used in this thesis. After transferring the boom contour into a linkage, the number of revolute joints is given by two first order joints, three second order joints, two third order joints, and one forth order joint. The two (double-)cylinders are considered as prismatic linear first order joints, hence $c_5 = 40$. With $f = 3$, $j = 5$, and $n = 14$ equation (2.1) results in two DOFs. Thus, the front loader is comparable to an open planar kinematic chain with two degrees of freedom [Cra05] [Ang07].
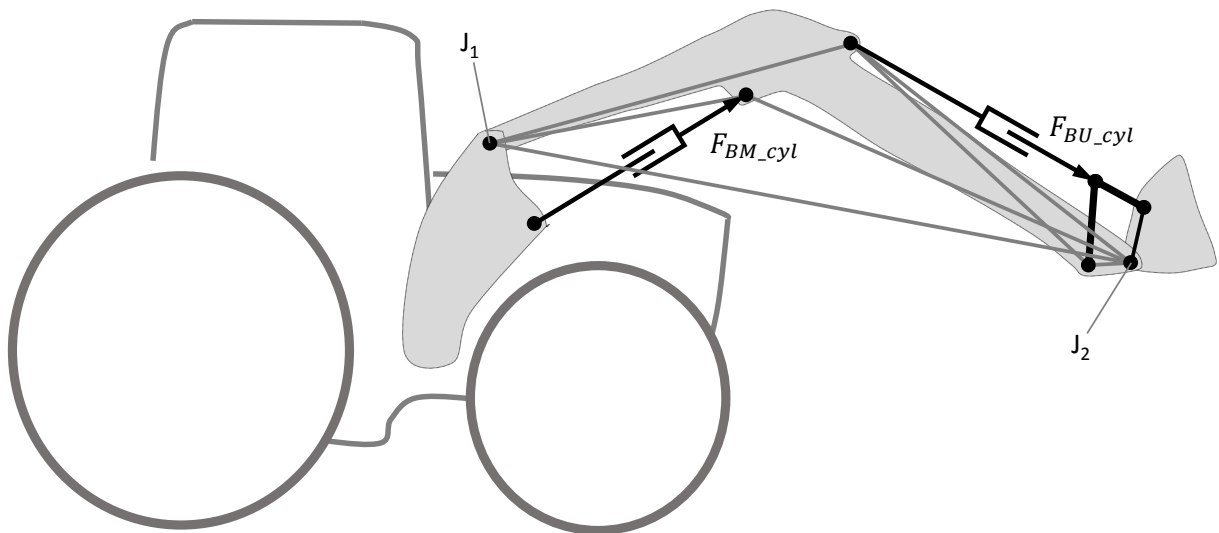
Figure 2.4: Kinematic chain of a tractor front loader

The task of the loader kinematics is to bring the bucket into the desired position and to convert the cylinder forces F into torques TQ at the main joints J_1 and J_2. In regard to the bucket position, the kinematics can be reduced to a simple kinematic chain as shown in figure 2.5. The simplified kinematic chain also has two DOFs: the angle φ_{BM} of the boom relative to the chassis and the angle φ_{BU} between chassis and bucket. The simplified kinematic chain of the loader is the basis for the further discussion and is valid for all front loaders with two DOFs.
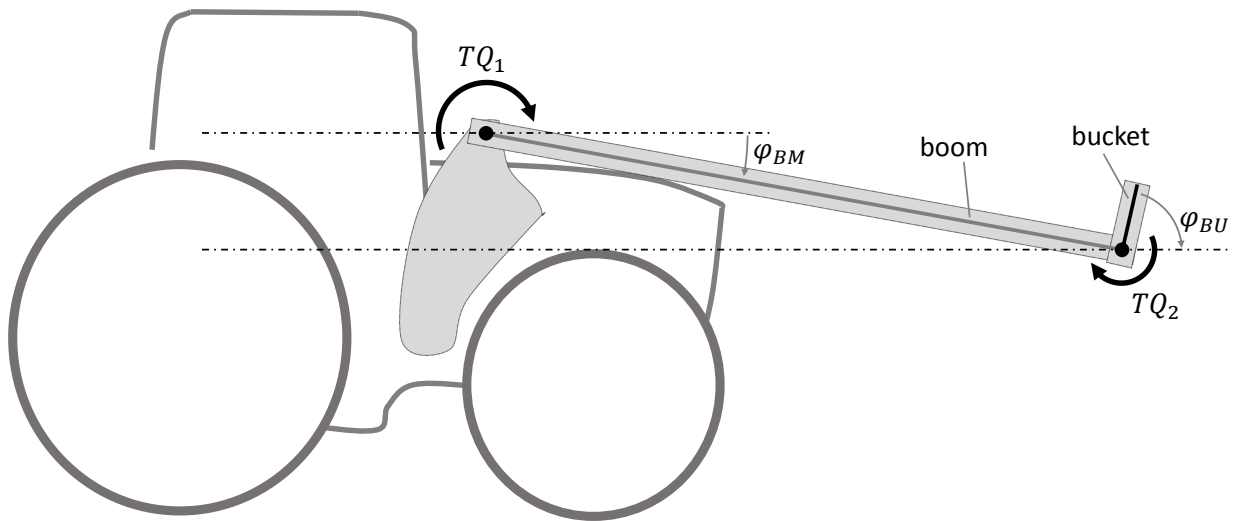
Figure 2.5: Simplified kinematic chain of a tractor front loader

2.2.2 Mechanical Self-Leveling

The front loader as depicted in figure 2.4 is a **non self-leveling** front loader. This implies that the bucket angle φ_{BU} changes if the boom angle φ_{BM} changes. Usually, this is undesirable, such that the operator needs to manually adjust the implement. For instance, a palette fork must move parallel to the ground to pick and carry load.

Hence, several loaders have a **self-leveling** option. That means the bucket angle φ_{BU} remains almost constant regardless of the boom angle φ_{BM}. The key idea is to shift the mounting point of the bucket cylinder proportionally to the boom angle to avoid the influence of φ_{BM} on φ_{BU}. A common way to achieve this is to add additional linkages to the loader. This does not change the loaders DOFs, hence, it could be also transferred to the simplified kinematics of figure 2.5. Only the transfer of the cylinder forces into torques at the joints needs a little more effort. Self-leveling loaders generate the torque at the boom joint by the boom cylinder forces and by the bucket cylinder forces via the additional linkage. This is contrary to non self-leveling loaders, where the torque at the boom joint is only generated by the boom cylinder forces.

In the following, a few examples of mechanical self-leveling loaders are presented. For the sake of completeness tractor front loaders are presented as well as wheel loaders. Figure 2.6 shows the kinematics of a mechanical self-leveling tractor front loader where the additional linkage is on top of the boom [Dee14a]. The additional linkage of the loader in figure 2.6 restricts the operator's field of view, hence, figure 2.7 shows an optimization where the additional linkage is below or inside the boom structure [Wil14].
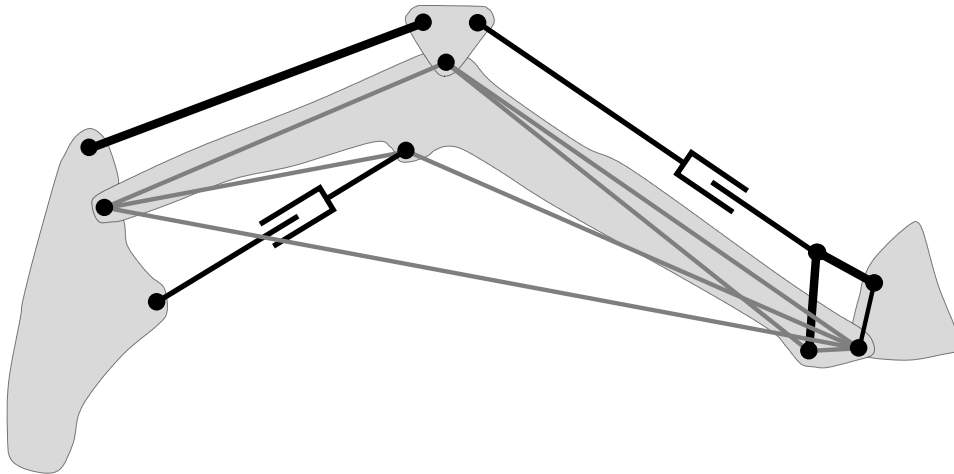
Figure 2.6: Mechanical self-leveling tractor front loader, linkage on top
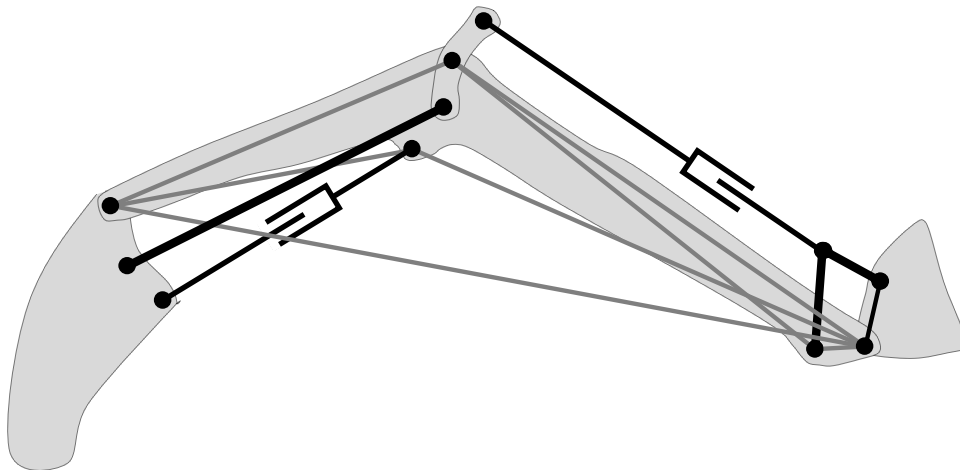
Figure 2.7: Mechanical self-leveling tractor front loader, linkage below

Also, wheel loaders have self-leveling kinematics which are generally realized with a bell crank (Z-kinematics). Due to the rear engine installation of wheel loaders more space is available in the front than at a tractor. This allows to mount the cylinders directly to the chassis and allows to build the boom stiffer. At tractor front loaders, the bucket cylinders generally pull. Whereas, at wheel loaders the bucket cylinder pushes to turn the bucket upward which increases the break out force of the bucket. There a several ways to actuate the bell crank. Figure 2.8 shows two examples of common wheel loader kinematics with the bell crank actuated from above and from below the boom [Dee14b] [Vol14].
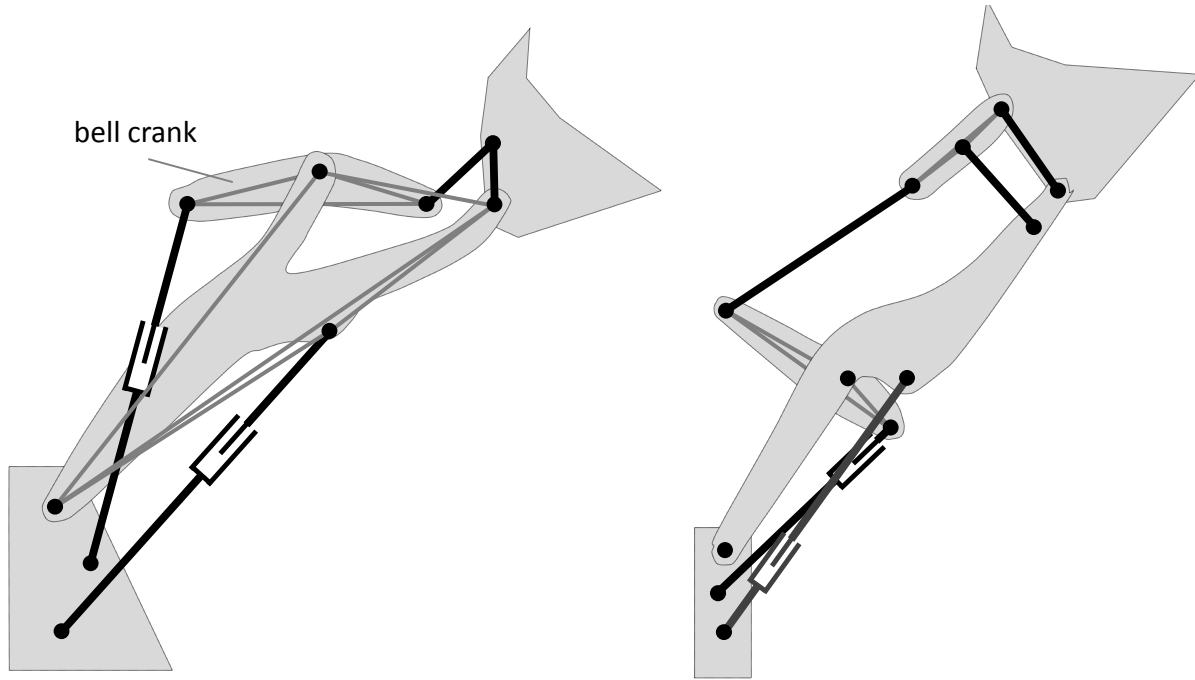
Figure 2.8: Wheel loader kinematics

For the sake of completeness, it must be mentioned that there are even more ways to implement self-leveling, for instance "hydraulic self-leveling" or "electronic self-leveling" which are not further discussed here [Dee15].

2.3 Coordinate Systems

All coordinate systems used in this thesis are right handed Cartesian systems. The coordinate system of the earth K_1 is assumed as inertial. The non-inertial vehicle coordinate system K_2 of the tractor is adopted from [DIN13] and [Ise06]. The x-axis points horizontally forward. The y-axis is rectangular to the x-axis and points to the left side and the z-axis points upward. The location of the origin is chosen in the middle between the left and right boom joints J_1 directly on the pin axis which allows further simplifications. Because the front loader consists of several parts, each part has its own coordinate system. For example, the boom has the coordinate system K_3 and the bucket has the coordinate system K_4 as shown in figure 2.9.

The angle convention of yaw, roll, and pitch is according to the right handed system: clockwise is defined as positive (corkscrew rule). This also defines the sign of the boom and bucket angular velocity $\dot{\varphi}_{BM}, \dot{\varphi}_{BU}$. Upward movement is defined negative and downward movement is defined positive.
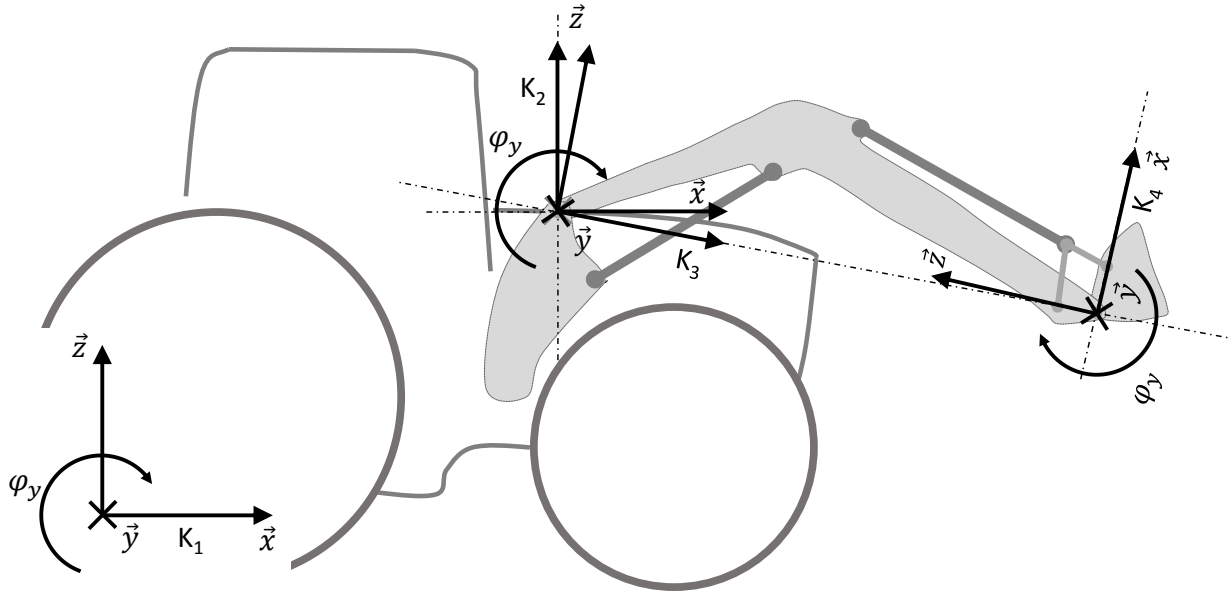
Figure 2.9: Coordinate systems

2.4 Coordinate Transformation

This section describes the basics of coordinate transformation as used in this thesis and refers to the sources [Hol07] [DH11] [HSG99]. Furthermore, the nomenclature of the following sections is defined here. If vectors are assigned to the same coordinate system they can be summed and subtracted in any order. Otherwise, they first have to be transformed to the same coordinate system.

For example, in equation (2.24) the vectors $[...\vec{r}_{3K4} + \vec{r}_{4P}...]$ are combined. In practice, the vectors are assigned to the most reasonable coordinate system. For instance, the vector $\vec{r}_{3K4}$ is assigned to the boom coordinate system K_3, indexed $\vec{r}_{3K4[K3]}$ and vector $\vec{r}_{4P}$ to the bucket coordinate system K_4, indexed $\vec{r}_{4P[K4]}$.

To assign them to the same coordinate system, vector $\vec{r}_{4P[K4]}$ has to be transformed to $\vec{r}_{4P[K3]}$ with the transformation matrix $\underset{K3}{\overset{K4}{\downarrow}} \boldsymbol{R}$ or the other way around $\vec{r}_{3K4[K3]}$ to $\vec{r}_{3K4[K4]}$ with $\underset{K4}{\overset{K3}{\downarrow}} \boldsymbol{R}$.

The front loader consists of several parts. Each part has its own coordinate system. If the origins of the coordinate systems are within the joints the transformation to different systems is only achieved by a rotation with Cardan angle φ around the y-axis, as shown in figure 2.10.
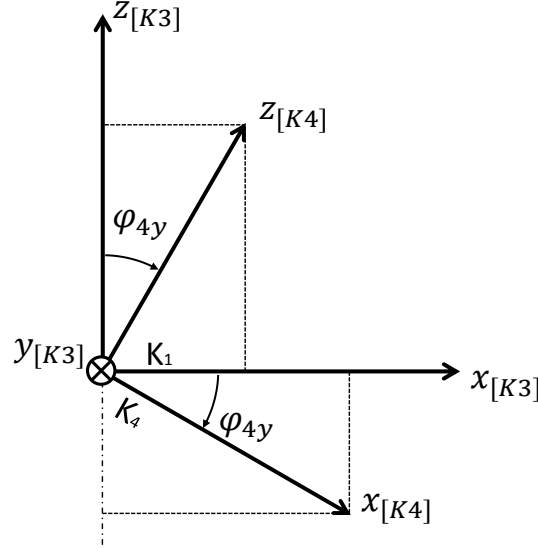
Figure 2.10: Transformation from K$_4$ to K$_3$

The transformation matrix $\underset{K3}{\overset{K4}{\downarrow}} \boldsymbol{R}$ is composed as follows with $\vec{r} = \begin{bmatrix} x \\ y \\ z \end{bmatrix}$:

$$
\begin{aligned}
x_{[\mathrm{K3}]} &= x_{[\mathrm{K4}]} \cdot \cos\varphi_{4y} & &+y_{[\mathrm{K4}]} \cdot 0 & &+z_{[\mathrm{K4}]} \cdot \sin\varphi_{4y} \\
y_{[\mathrm{K3}]} &= x_{[\mathrm{K4}]} \cdot 0 & &+y_{[\mathrm{K4}]} \cdot 1 & &+z_{[\mathrm{K4}]} \cdot 0 \\
z_{[\mathrm{K3}]} &= x_{[\mathrm{K4}]} \cdot (-\sin\varphi_{4y}) & &+y_{[\mathrm{K4}]} \cdot 0 & &+z_{[\mathrm{K4}]} \cdot \cos\varphi_{4y}
\end{aligned}
\tag{2.3}
$$

$$
\begin{bmatrix} x \\ y \\ z \end{bmatrix}_{[\mathrm{K3}]} = \begin{bmatrix} \cos\varphi_{4y} & 0 & \sin\varphi_{4y} \\ 0 & 1 & 0 \\ (-\sin\varphi_{4y}) & 0 & \cos\varphi_{4y} \end{bmatrix} \cdot \begin{bmatrix} x \\ y \\ z \end{bmatrix}_{[\mathrm{K4}]}
\tag{2.4}
$$

$$
\vec{r}_{[\mathrm{K3}]} = \underset{K3}{\overset{K4}{\downarrow}}\boldsymbol{R} \cdot \vec{r}_{[\mathrm{K4}]}
\tag{2.5}
$$

Because $\underset{K3}{\overset{K4}{\downarrow}}\boldsymbol{R}$ is a rotational matrix, it is orthonormal, hence, the following rules can be applied:

$$
\left(\underset{K3}{\overset{K4}{\downarrow}}\boldsymbol{R} \right)^{T} = \left(\underset{K3}{\overset{K4}{\downarrow}}\boldsymbol{R} \right)^{-1} = \left(\underset{K4}{\overset{K3}{\downarrow}}\boldsymbol{R} \right)
\tag{2.6}
$$

The reverse transformation is given by

$$
\left(\underset{K3}{\overset{K4}{\downarrow}}\boldsymbol{R} \right)^{-1} \cdot \vec{r}_{[\mathrm{K3}]} = \left(\underset{K3}{\overset{K4}{\downarrow}}\boldsymbol{R} \right)^{-1} \left(\underset{K3}{\overset{K4}{\downarrow}}\boldsymbol{R} \right) \cdot \vec{r}_{[\mathrm{K4}]} = \vec{r}_{[\mathrm{K4}]}
\tag{2.7}
$$

The transformation with rotation angle $\varphi = \varphi_{3y}$ will later be applied to equation (2.22), which is shown in advance in equation (2.8).

$$
\begin{aligned}
\ddot{\vec{r}}_{1P} = {}& \ddot{\vec{r}}_{1S2} + \dot{\vec{\varphi}}_2 \times (\dot{\vec{\varphi}}_2 \times (\vec{r}_{2K3} + \underset{K2}{\overset{K3}{\downarrow}} \boldsymbol{R} \cdot \vec{r}_{3P} - \vec{r}_{2S2})) + \ddot{\vec{\varphi}}_2 \times (\vec{r}_{2K3} + \underset{K2}{\overset{K3}{\downarrow}} \boldsymbol{R} \cdot \vec{r}_{3P} - \vec{r}_{2S2}) \\
& + 2(\dot{\vec{\varphi}}_2 \times (\dot{\vec{\varphi}}_3 \times \underset{K2}{\overset{K3}{\downarrow}} \boldsymbol{R} \cdot \vec{r}_{3P})) + \dot{\vec{\varphi}}_3 \times (\dot{\vec{\varphi}}_3 \times \underset{K2}{\overset{K3}{\downarrow}} \boldsymbol{R} \cdot \vec{r}_{3P}) + (\ddot{\vec{\varphi}}_3 \times \underset{K2}{\overset{K3}{\downarrow}} \boldsymbol{R} \cdot \vec{r}_{3P})
\end{aligned}
\tag{2.8}
$$

2.5 Data Acquisition and Sensor Description

A tractor front loader was equipped with a controller, four pressure sensors, and three inertial measurement units (IMU, acceleration sensors combined with gyros $S2, S3, S4$), as shown in figure 2.11, in order to collect the relevant data for this thesis (cf. section 3.3).
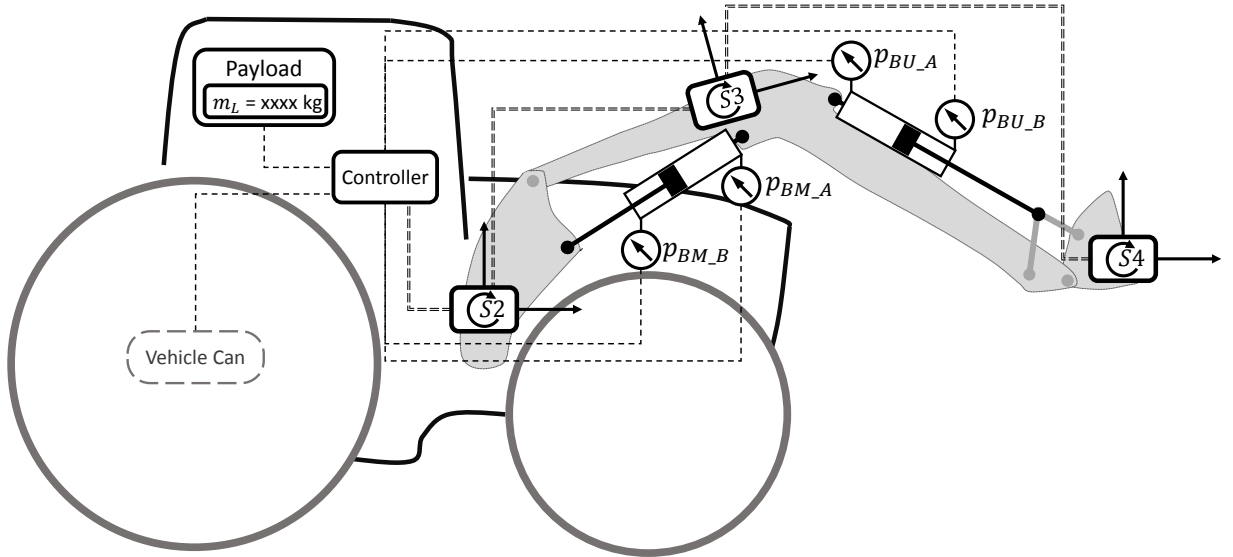
Figure 2.11: Instrumentation

The IMU $S2$ is connected to the chassis of the tractor, $S3$ to the boom, and $S4$ to the bucket or tool carrier (cf. table A.4 in the appendix). The IMUs $S2$, $S3$, $S4$ are micro electromechanical systems (MEMS) as used in vehicle stability systems and are connected via a CAN bus with the controller [Con14b] [Con14a]. The IMUs used in this work measure the acceleration $\vec{a}$ in the x- and z-axis and the angular velocity $\dot{\varphi}$ in y-axis. In addition, IMU $S2$ measures angular velocity in the z-axis. The angular acceleration $\ddot{\varphi}$ is derived inside the IMU controller. The outputs of the IMUs are termed as $\vec{a}_{Si}$, $\dot{\vec{\varphi}}_{Si}$, and $\ddot{\vec{\varphi}}_{Si}$ with $i = 2, 3, 4$. All signals are sent to the CAN bus with a sampling rate of 100Hz. If the angular acceleration is not derived inside the IMU the sampling rate should be higher to provide enough data for the derivation within the controller. An efficient and simple method is given by [KK87]. The bucket IMU $S4$ should be shockproof due to higher accelerations and angular velocities during front loader work compared to IMU $S2$ or $S3$.

The pressure sensors measure cylinder pressures at the piston and at the rod side of the boom and bucket cylinders. The best way to do this, is by measuring the pressure directly within the cylinder to avoid pressure drop deviations due to oil flow. This could not be realized. Thus, the sensors are connected with a T-fitting and a 90 degree knee fitting (size: 13/16"-16UN) in the hydraulic line just next to the cylinder ports. This keeps the deviation of the pressure drop due to the oil flow negligibly small. The sensors deliver an analogous voltage signal and are connected directly to the controller. For this reason the pressure readings are transferred faster than the accelerations from the CAN bus. Given that the signals of all sensors are used for further calculations, they have to be synchronized first. Hence, the analogous pressure inputs are provided with a time lag.

Additionally, the hydraulic oil temperature or engine speed, for example, are derived from the vehicle CAN bus. Finally, all data is processed in a real time controller to calculate the payload with a sample time of 10 milliseconds. The used controller is a real time rapid prototyping system (dSPACE MicroAutoBox2 [dSP14]) which is programmed directly with Matlab/Simulink. It enables, among other things, recording variables and debugging while simultaneously displaying the variables on a notebook (see also section A.2 in the appendix).

2.6 Accelerations

This section summarizes the essentials of accelerations as a basis of this thesis and refers to the sources [Hon93][Sch07][Nol06][HSG99]. The *Position Detection* of chapter 3 as well as the *Weighing Function* of chapter 4 are parameterized with continuously measured accelerations. This requires a comprehensive understanding and detailed explanation. In the following, the accelerations of any point, which is referenced to different coordinate systems, are explained in general. In a second step, the point is associated with the loader and represents, for example, the center of gravity of a specific part. Finally, this section explains how to calculate the acceleration of this point by measuring accelerations at a different position. For reasons of clarity and ease of comprehension, all figures in this section are based on two dimensions. In addition, vector $\vec{r}_1(t)$ will be written as $\vec{r}_1$. For further calculations, all vectors have to be first transformed to the same coordinate system, e.g. $\vec{r}_{1P} = \vec{r}_{1K2} + \underset{K1}{\overset{K2}{\downarrow}} \boldsymbol{R}\, \vec{r}_{2P}$ (cf. figure 2.13). In addition, the transformation matrices $\underset{K*}{\overset{K*}{\downarrow}} \boldsymbol{R}$ in the equations of this chapter are omitted for reasons of clarity.

The coordinate system K_1 (see figure 2.12) is an inertial system also known as inertial

frame. A moving point P of this coordinate system is defined by the position vector $\vec{r}_{1P}$. The velocity and acceleration of this point P is defined as follows:

$$\dot{\vec{r}}_{1P} = \frac{\partial \vec{r}_{1P}}{\partial t} \tag{2.9}$$

$$\ddot{\vec{r}}_{1P} = \frac{\partial^2 \vec{r}_{1P}}{\partial t^2} \tag{2.10}$$
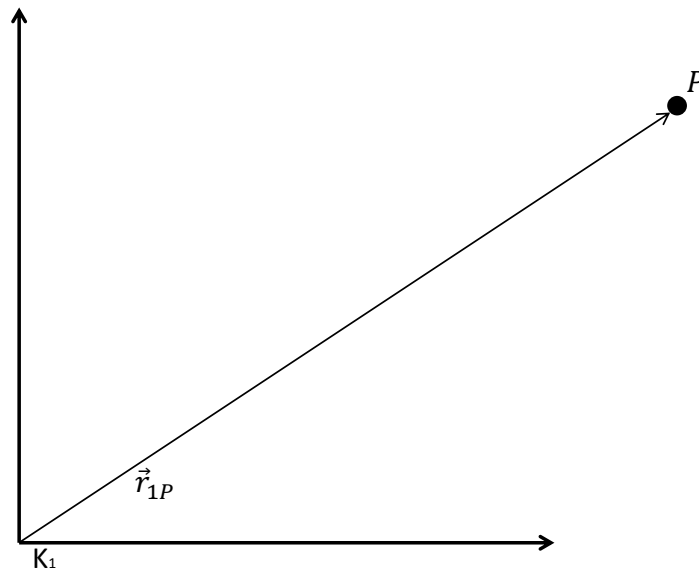
Figure 2.12: Point P in inertial system K_1

2.6.1 Non-Inertial System K_2

The coordinate system K_2 moves relative to coordinate system K_1 and is called a non-inertial system. The location of K_2 within K_1 is determined by the position vector $\vec{r}_{1K2}$ and the rotation vector $\vec{\varphi}_2$, as shown in figure 2.13.
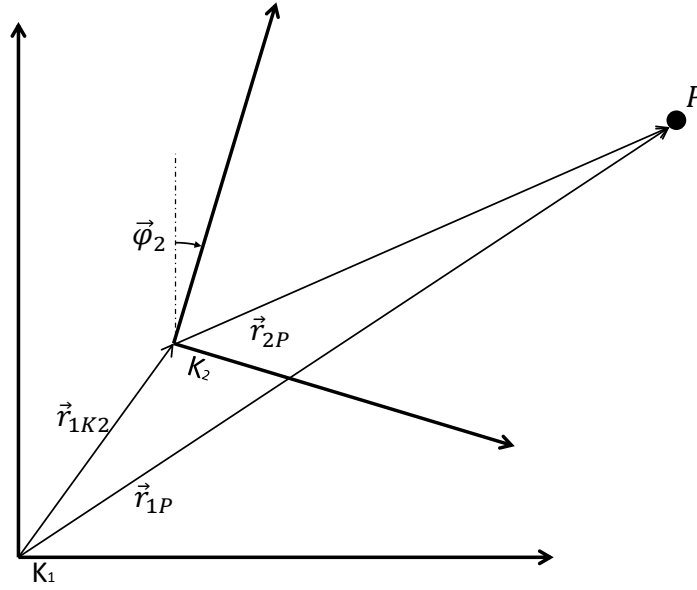
Figure 2.13: Point P in non-inertial system K_2

The position vector of point P referenced to K_2 is called Vector $\vec{r}_{2P}$. If it is referenced to K_1 it is called $\vec{r}_{1P}$. Consequently, it follows that:

$$\vec{r}_{1P} = \vec{r}_{1K2} + \vec{r}_{2P} \tag{2.11}$$

$$\dot{\vec{r}}_{1P} = \dot{\vec{r}}_{1K2} + \dot{\vec{r}}_{2P} + (\dot{\vec{\varphi}}_2 \times \vec{r}_{2P}) \tag{2.12}$$

$$\ddot{\vec{r}}_{1P} = \ddot{\vec{r}}_{1K2} + \ddot{\vec{r}}_{2P} + 2(\dot{\vec{\varphi}}_2 \times \dot{\vec{r}}_{2P}) + \dot{\vec{\varphi}}_2 \times (\dot{\vec{\varphi}}_2 \times \vec{r}_{2P}) + (\ddot{\vec{\varphi}}_2 \times \vec{r}_{2P}) \tag{2.13}$$

The terms of equation (2.13) are defined as follows:

- $\left[\ddot{\vec{r}}_{1K2} + \ddot{\vec{r}}_{2P}\right]$ is the translational acceleration of point P.

- $\left[2(\dot{\vec{\varphi}}_2 \times \dot{\vec{r}}_{2P})\right]$ is the Coriolis acceleration which affects point P and is generated by the relative movement between K_2 and K_1.

- $\left[\dot{\vec{\varphi}}_2 \times (\dot{\vec{\varphi}}_2 \times \vec{r}_{2P}) + (\ddot{\vec{\varphi}}_2 \times \vec{r}_{2P})\right]$ is the acceleration induced by the rotation of K_2 relative to K_1.

2.6.2 Non-Inertial System K_3

In the following scenario, a non-inertial system K_3 moves relative to the non-inertial system K_2; and K_2 moves relative to K_1. The location of K_3 within K_2 is determined by the position vector $\vec{r}_{2K3}$ and the rotation vector $\vec{\varphi}_3$, as shown in figure 2.14.

Figure 2.14: Point P in non-inertial system K_3

The position vector of point P referenced to K_3 is called Vector $\vec{r}_{3P}$. If it is referenced to K_1 it is still called $\vec{r}_{1P}$. Thus, the following equations are valid:

$$\vec{r}_{1P} = \vec{r}_{1K2} + \vec{r}_{2P}$$

$$= \vec{r}_{1K2} + \vec{r}_{2K3} + \vec{r}_{3P} \tag{2.14}$$

$$\dot{\vec{r}}_{1P} = \dot{\vec{r}}_{1K2} + \dot{\vec{r}}_{2K3} + \dot{\vec{r}}_{3P} + (\dot{\vec{\varphi}}_3 \times \vec{r}_{3P}) + (\dot{\vec{\varphi}}_2 \times (\vec{r}_{2K3} + \vec{r}_{3P})) \tag{2.15}$$

$$\ddot{\vec{r}}_{1P} = \ddot{\vec{r}}_{1K2} + \ddot{\vec{r}}_{2K3} + \ddot{\vec{r}}_3 + 2(\dot{\vec{\varphi}}_3 \times \dot{\vec{r}}_{3P}) + \dot{\vec{\varphi}}_3 \times (\dot{\vec{\varphi}}_3 \times \vec{r}_{3P}) + (\ddot{\vec{\varphi}}_3 \times \vec{r}_{3P})$$
$$+ 2(\dot{\vec{\varphi}}_2 \times [\dot{\vec{r}}_{2K3} + \dot{\vec{r}}_{3P} + (\dot{\vec{\varphi}}_3 \times \vec{r}_{3P})]) + \dot{\vec{\varphi}}_2 \times (\dot{\vec{\varphi}}_2 \times (\vec{r}_{2K3} + \vec{r}_{3P})) + \ddot{\vec{\varphi}}_2 \times (\vec{r}_{2K3} + \vec{r}_{3P})$$
$$\tag{2.16}$$

The terms of equation (2.16) are defined as follows:

- $\left[\ddot{\vec{r}}_{1K2} + \ddot{\vec{r}}_{2K3} + \ddot{\vec{r}}_{3P} \right]$ is the translational acceleration of point P.

- $\left[2(\dot{\vec{\varphi}}_3 \times \dot{\vec{r}}_{3P}) \right]$ is the Coriolis acceleration which affects point P and is generated by the relative movement between K_3 and K_2.

- $\left[\dot{\vec{\varphi}}_3 \times (\dot{\vec{\varphi}}_3 \times \vec{r}_{3P}) + (\ddot{\vec{\varphi}}_3 \times \vec{r}_{3P}) \right]$ is the acceleration induced by the rotation of K_3 relative to K_2.

- $\left[2(\dot{\vec{\varphi}}_2 \times [\dot{\vec{r}}_{2K3} + \dot{\vec{r}}_{3P} + (\dot{\vec{\varphi}}_3 \times \vec{r}_{3P})]) \right]$ is the Coriolis acceleration which affects point P and is generated by the relative movement between K_2 and K_1.

- $\left[\dot{\vec{\varphi}}_2 \times (\dot{\vec{\varphi}}_2 \times (\vec{r}_{2K3} + \vec{r}_{3P})) + \ddot{\vec{\varphi}}_2 \times (\vec{r}_{2K3} + \vec{r}_{3P}) \right]$ is the acceleration induced by the rotation of K_2 relative to K_1.

2.6.3 Non-Inertial System K_4

For the sake of completeness the procedure is repeated once more with a further non-inertial system K_4 which moves relative to K_3 as shown in figure 2.15. The location of K_4 within K_3 is determined by the position vector $\vec{r}_{3K4}$ and the rotation vector $\vec{\varphi}_4$. The position vecto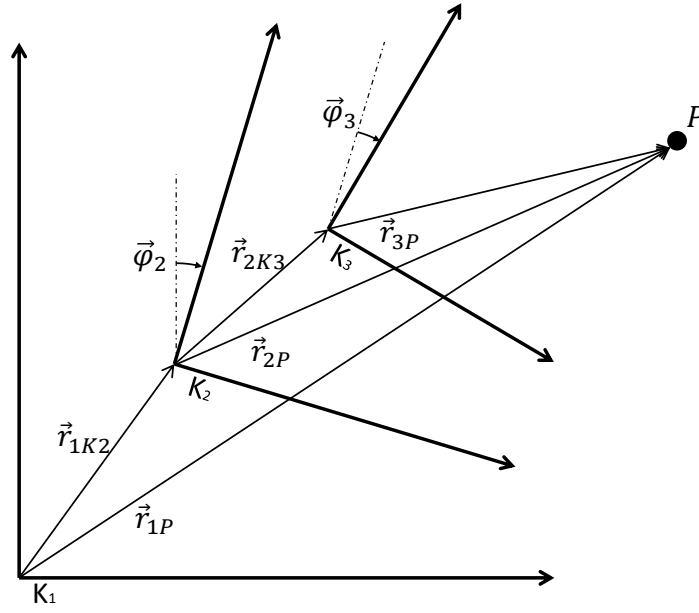r of point P referenced to K_4 is called Vector $\vec{r}_{4P}$. Its reference to K_1 is still called $\vec{r}_{1P}$. The acceleration of point P is given by the following equation (2.17).
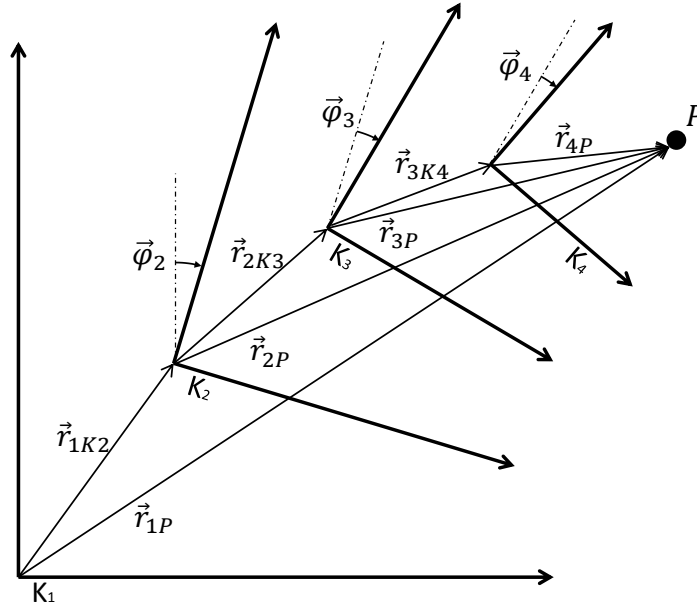
Figure 2.15: Point P in non-inertial system K_4

$$
\begin{aligned}
\ddot{\vec{r}}_{1P} = {} & \ddot{\vec{r}}_{1K2} + \ddot{\vec{r}}_{2K3} + \ddot{\vec{r}}_{3K4} + \ddot{\vec{r}}_{4P} + 2(\dot{\vec{\varphi}}_4 \times \dot{\vec{r}}_{4P}) + \dot{\vec{\varphi}}_4 \times (\dot{\vec{\varphi}}_4 \times \vec{r}_{4P}) + (\ddot{\vec{\varphi}}_4 \times \vec{r}_{4P}) \\
& + 2(\dot{\vec{\varphi}}_3 \times [\dot{\vec{r}}_{3K4} + \dot{\vec{r}}_{4P} + (\dot{\vec{\varphi}}_4 \times \vec{r}_{4P})]) + \dot{\vec{\varphi}}_3 \times \dot{\vec{\varphi}}_3 \times (\vec{r}_{3K4} + \vec{r}_{4P}) + \ddot{\vec{\varphi}}_3 \times (\vec{r}_{3K4} + \vec{r}_{4P}) \\
& + 2(\dot{\vec{\varphi}}_2 \times [\dot{\vec{r}}_{2K3} + \dot{\vec{r}}_{3K4} + \dot{\vec{r}}_{4P} + (\dot{\vec{\varphi}}_4 \times \vec{r}_{4P}) + \dot{\vec{\varphi}}_3 \times (\vec{r}_{3K4} + \vec{r}_{4P})]) \\
& + \dot{\vec{\varphi}}_2 \times (\dot{\vec{\varphi}}_2 \times (\vec{r}_{2K3} + \vec{r}_{3K4} + \vec{r}_{4P})) + \ddot{\vec{\varphi}}_2 \times (\vec{r}_{2K3} + \vec{r}_{3K4} + \vec{r}_{4P})
\end{aligned}
\tag{2.17}
$$

2.6.4 Acceleration at the Tractor

The following sections explain how to calculate the acceleration at a different position that varies from the inertial measurement unit position (IMU, acceleration sensors with gyros). The inertial coordinate system K_1, as illustrated in section 2.6.1, represents the earth. The non-inertial coordinate system K_2 is attached to the tractor which moves relative to the earth. The accelerations which occur due to the movements of the tractor can be measured with an IMU $S2$. Usually, it is not possible to measure the acceleration at any point P.

For instance, the acceleration at the center of gravity of the tractor is needed which is located in the middle of the gear but the only possibility to mount an IMU is outside the gear.

Accordingly, equation (2.13) is now applied to represent the acceleration $\ddot{\vec{r}}_{1P}$ at point P.

$$\ddot{\vec{r}}_{1P} = \ddot{\vec{r}}_{1K2} + \ddot{\vec{r}}_{2P} + 2(\dot{\vec{\varphi}}_2 \times \dot{\vec{r}}_{2P}) + \dot{\vec{\varphi}}_2 \times (\dot{\vec{\varphi}}_2 \times \vec{r}_{2P}) + (\ddot{\vec{\varphi}}_2 \times \vec{r}_{2P}) \qquad (2.18)$$

Moreover, equation (2.13) is applied to represent the acceleration $\ddot{\vec{r}}_{1S2}$ at the IMU position $S2$.

$$\ddot{\vec{r}}_{1S2} = \ddot{\vec{r}}_{1K2} + \ddot{\vec{r}}_{2S2} + 2(\dot{\vec{\varphi}}_2 \times \dot{\vec{r}}_{2S2}) + \dot{\vec{\varphi}}_2 \times (\dot{\vec{\varphi}}_2 \times \vec{r}_{2S2}) + (\ddot{\vec{\varphi}}_2 \times \vec{r}_{2S2}) \qquad (2.19)$$

$$\Rightarrow \ddot{\vec{r}}_{1K2} = \ddot{\vec{r}}_{1S2} - \ddot{\vec{r}}_{2S2} - 2(\dot{\vec{\varphi}}_2 \times \dot{\vec{r}}_{2S2}) - \dot{\vec{\varphi}}_2 \times (\dot{\vec{\varphi}}_2 \times \vec{r}_{2S2}) - (\ddot{\vec{\varphi}}_2 \times \vec{r}_{2S2})$$

Given that the chassis of the tractor is assumed as a rigid body, the vectors $\vec{r}_{2S2}$ and $\vec{r}_{2P}$ are constant over time. If point P is assigned to the center of gravity, the IMU $S2$ and the center of gravity P do not change their position relative to the tractor and its coordinate system K$_2$, see figure 2.16. Hence, the acceleration and the velocity will be zero, $\ddot{\vec{r}}_{2S2} = \ddot{\vec{r}}_{2P} = \dot{\vec{r}}_{2S2} = \dot{\vec{r}}_{2P} = 0$. Merging equation (2.19) into equation (2.18) yields the following expression:

$$\ddot{\vec{r}}_{1P} = \ddot{\vec{r}}_{1S2} + \dot{\vec{\varphi}}_2 \times \left(\dot{\vec{\varphi}}_2 \times [\vec{r}_{2P} - \vec{r}_{2S2}]\right) + \ddot{\vec{\varphi}}_2 \times [\vec{r}_{2P} - \vec{r}_{2S2}]$$

$$\ddot{\vec{r}}_{1P} = \ddot{\vec{r}}_{1S2} + \dot{\vec{\varphi}}_2 \times \left(\dot{\vec{\varphi}}_2 \times [\vec{r}_{S2P}]\right) + \ddot{\vec{\varphi}}_2 \times [\vec{r}_{S2P}] \qquad (2.20)$$

Figure 2.16: Calculated acceleration for any point at a rigid body

The acceleration $\ddot{\vec{r}}_{1S2}$ is measured with the IMU $S2$. The variables $\dot{\vec{\varphi}}_2$ and $\ddot{\vec{\varphi}}_2$ are the angular velocity and angular acceleration of the tractor chassis. They are constant at any position of a rigid body and can be measured directly with IMU $S2$, hence $\dot{\vec{\varphi}}_2 = \dot{\vec{\varphi}}_{S2}$ and $\ddot{\vec{\varphi}}_2 = \ddot{\vec{\varphi}}_{S2}$. The vector $\vec{r}_{S2P}$ points from the IMU to point P, which is the point in question where the acceleration is calculated, for instance, the center of gravity. It is irrelevant for vector $\vec{r}_{S2P}$ whether the origin of K_2 is at the center of rotation, as displayed in figure 2.16, or not. It is important that the vector is referenced to the coordinate system where the acceleration is measured, here K_2, otherwise, it has to be transformed.

2.6.5 Acceleration at the Front Loader

The boom (BM) is mounted to the chassis by the rotational joint J_1, which allows relative movement to each other. The non-inertial coordinate system K_3 is connected to the boom. The bucket or tool carrier (BU) is mounted to the boom by the rotational joint J_2. The non-inertial coordinate system K_4 is referenced to the bucket.

By locating the origin of the coordinate system within the joints, K_3 only performs a rotation relative to K_2. Also, K_4 performs rotation relative to K_3 and no translation. This results in $\dot{\vec{r}}_{2K3} = \ddot{\vec{r}}_{2K3} = 0$ and $\dot{\vec{r}}_{3K4} = \ddot{\vec{r}}_{3K4} = 0$.

2.6.5.1 Acceleration at the Boom

In this section, the acceleration is measured with an IMU $S2$ located at the tractor chassis but it is calculated for a point P which is located at the boom, see figure 2.17.
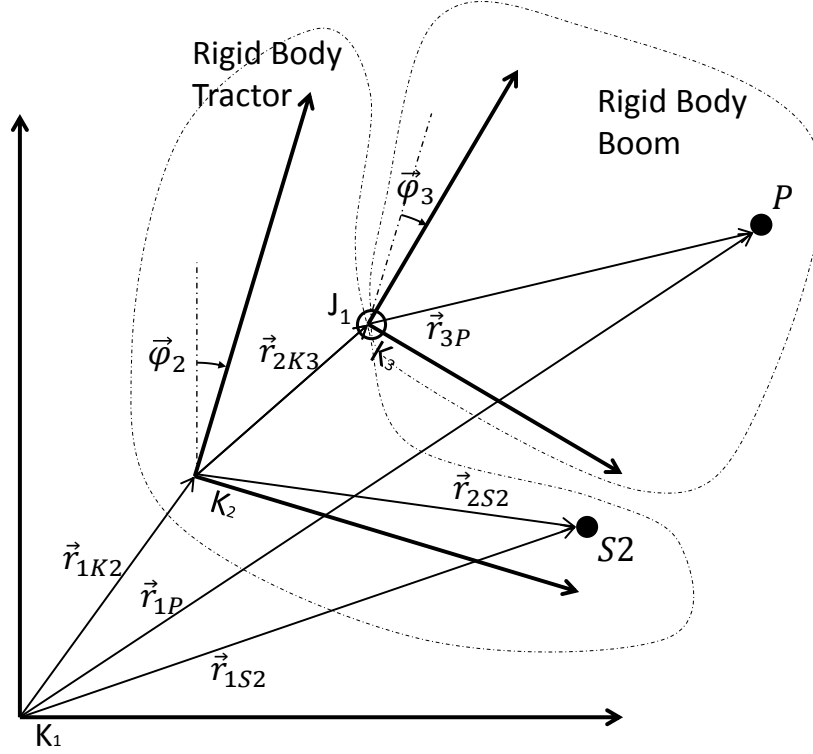
Figure 2.17: Calculated acceleration for any point at the boom

The following conditions are applied. The boom is assumed as a rigid body and $\vec{r}_{3P}$ does not change over time. Hence, the derivatives will be zero, $\dot{\vec{r}}_{3P} = \ddot{\vec{r}}_{3P} = 0$ and equation (2.16) is simplified to the following equation.

$$
\begin{aligned}
\ddot{\vec{r}}_{1P} = {} & \ddot{\vec{r}}_{1K2} + \dot{\vec{\varphi}}_2 \times (\dot{\vec{\varphi}}_2 \times (\vec{r}_{2K3} + \vec{r}_{3P})) + \ddot{\vec{\varphi}}_2 \times (\vec{r}_{2K3} + \vec{r}_{3P}) \\
& + 2(\dot{\vec{\varphi}}_2 \times (\dot{\vec{\varphi}}_3 \times \vec{r}_{3P})) + \dot{\vec{\varphi}}_3 \times (\dot{\vec{\varphi}}_3 \times \vec{r}_{3P}) + (\ddot{\vec{\varphi}}_3 \times \vec{r}_{3P})
\end{aligned}
\tag{2.21}
$$

Because the IMU is located in K_2 at the chassis, the variable $\ddot{\vec{r}}_{1K2}$ is substituted by equation (2.19) which results in:

$$
\begin{aligned}
\ddot{\vec{r}}_{1P} = {} & \ddot{\vec{r}}_{1S2} + \dot{\vec{\varphi}}_2 \times (\dot{\vec{\varphi}}_2 \times (\vec{r}_{2K3} + \vec{r}_{3P} - \vec{r}_{2S2})) + \ddot{\vec{\varphi}}_2 \times (\vec{r}_{2K3} + \vec{r}_{3P} - \vec{r}_{2S2}) \\
& + 2(\dot{\vec{\varphi}}_2 \times (\dot{\vec{\varphi}}_3 \times \vec{r}_{3P})) + \dot{\vec{\varphi}}_3 \times (\dot{\vec{\varphi}}_3 \times \vec{r}_{3P}) + (\ddot{\vec{\varphi}}_3 \times \vec{r}_{3P})
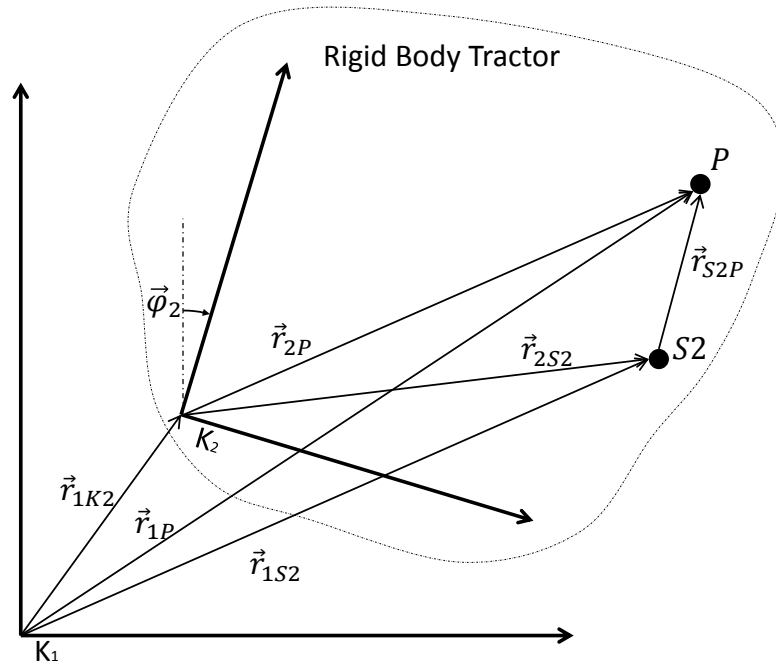\end{aligned}
\tag{2.22}
$$

A closer look at equation (2.22) reveals that the acceleration of P consists of several parts.

- $\left[\ddot{\vec{r}}_{1S2} + \dot{\vec{\varphi}}_2 \times (\dot{\vec{\varphi}}_2 \times (\vec{r}_{2K3} + \vec{r}_{3P} - \vec{r}_{2S2})) + \ddot{\vec{\varphi}}_2 \times (\vec{r}_{2K3} + \vec{r}_{3P} - \vec{r}_{2S2})\right]$ is analog to equation (2.20) and considers the system as a rigid body.

31

- $\left[2(\dot{\vec{\varphi}}_2 \times (\dot{\vec{\varphi}}_3 \times \vec{r}_{3P}))\right]$ is the Coriolis acceleration.

- $\left[\dot{\vec{\varphi}}_3 \times (\dot{\vec{\varphi}}_3 \times \vec{r}_{3P}) + (\ddot{\vec{\varphi}}_3 \times \vec{r}_{3P})\right]$ is the acceleration induced by the rotation of the boom (K_3) relative to the chassis (K_2).

To add up vectors, they must be transformed to the same coordinate system. For instance, to sum up $(\vec{r}_{2K3} + \vec{r}_{3P})$, $\vec{r}_{3P}$ which belongs to K_3 is transformed to the coordinate system K_2. The variables $\dot{\vec{\varphi}}_3$ and $\ddot{\vec{\varphi}}_3$ are the relative angular velocity and angular acceleration between boom and chassis, hence, they are measured with IMU $S2$ and $S3$: $\dot{\vec{\varphi}}_3 = \dot{\vec{\varphi}}_{S3} - \dot{\vec{\varphi}}_{S2}$ and $\ddot{\vec{\varphi}}_3 = \ddot{\vec{\varphi}}_{S3} - \ddot{\vec{\varphi}}_{S2}$.

2.6.5.2 Acceleration at the Bucket

In this section, the acceleration is measured with an IMU $S2$ at the tractor chassis K_2, but calculated for a point P which is located at the bucket or tool carrier K_4, see figure 2.18. The origin of the bucket coordinate system K_4 is at the joint J_2 and the bucket is considered as a rigid body. Thus, the variables $\dot{\vec{r}}_{4P} = \ddot{\vec{r}}_{4P} = 0$ are zero and the previously mentioned conditions $\dot{\vec{r}}_{2K3} = \ddot{\vec{r}}_{2K3} = 0$ and $\dot{\vec{r}}_{3K4} = \ddot{\vec{r}}_{3K4} = 0$ are valid. The acceleration is calculated as follows:

$$
\begin{aligned}
\ddot{\vec{r}}_{1P} = {} & \ddot{\vec{r}}_{1S2} + \dot{\vec{\varphi}}_2 \times (\dot{\vec{\varphi}}_2 \times (\vec{r}_{2K3} + \vec{r}_{3K4} + \vec{r}_{4P} - \vec{r}_{2S2})) + \ddot{\vec{\varphi}}_2 \times (\vec{r}_{2K3} + \vec{r}_{3K4} + \vec{r}_{4P} - \vec{r}_{2S2}) \\
& + 2(\dot{\vec{\varphi}}_3 \times (\dot{\vec{\varphi}}_4 \times \vec{r}_{4P})) + 2(\dot{\vec{\varphi}}_2 \times [\dot{\vec{\varphi}}_4 \times \vec{r}_{4P} + \dot{\vec{\varphi}}_3 \times (\vec{r}_{3K4} + \vec{r}_{4P})]) \\
& + \dot{\vec{\varphi}}_3 \times (\dot{\vec{\varphi}}_3 \times (\vec{r}_{3K4} + \vec{r}_{4P})) + \ddot{\vec{\varphi}}_3 \times (\vec{r}_{3K4} + \vec{r}_{4P}) \\
& + \dot{\vec{\varphi}}_4 \times (\dot{\vec{\varphi}}_4 \times \vec{r}_{4P}) \ + \ \ddot{\vec{\varphi}}_4 \times \vec{r}_{4P}
\end{aligned}
$$

$$(2.23)$$

The acceleration $\ddot{\vec{r}}_{1P}$ calculated in equation (2.23) is a summation of several parts.

- $\left[\ddot{\vec{r}}_{1S2} + \dot{\vec{\varphi}}_2 \times (\dot{\vec{\varphi}}_2 \times (\vec{r}_{2K3} + \vec{r}_{3K4} + \vec{r}_{4P} - \vec{r}_{2S2})) + \ddot{\vec{\varphi}}_2 \times (\vec{r}_{2K3} + \vec{r}_{3K4} + \vec{r}_{4P} - \vec{r}_{2S2})\right]$ is analog to equation (2.20) and considers the system as a rigid body.

- $\left[2(\dot{\vec{\varphi}}_3 \times (\dot{\vec{\varphi}}_4 \times \vec{r}_{4P})) + 2(\dot{\vec{\varphi}}_2 \times [\dot{\vec{\varphi}}_4 \times \vec{r}_{4P} + \dot{\vec{\varphi}}_3 \times (\vec{r}_{3K4} + \vec{r}_{4P})])\right]$ is the Coriolis acceleration.

- $\left[\dot{\vec{\varphi}}_3 \times (\dot{\vec{\varphi}}_3 \times (\vec{r}_{3K4} + \vec{r}_{4P})) + \ddot{\vec{\varphi}}_3 \times (\vec{r}_{3K4} + \vec{r}_{4P})\right]$ is the acceleration induced by the rotation of the boom (K_3) relative to the chassis (K_2).

- $\left[\dot{\vec{\varphi}}_4 \times (\dot{\vec{\varphi}}_4 \times \vec{r}_{4P}) \ + \ \ddot{\vec{\varphi}}_4 \times \vec{r}_{4P}\right]$ is the acceleration induced by the rotation of the bucket (K_4) relative to the boom (K_3).
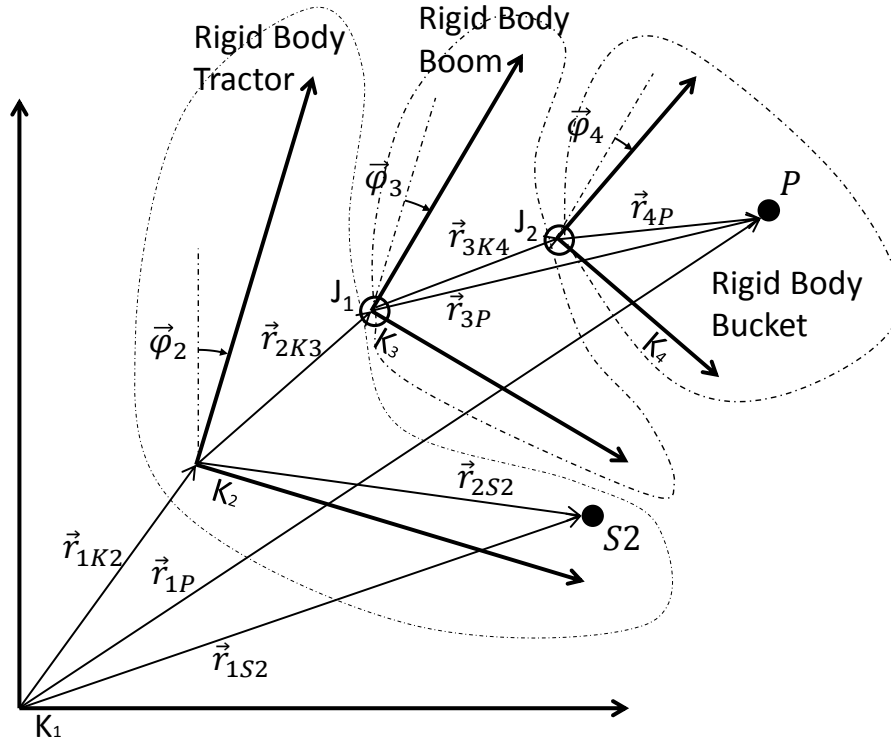
Figure 2.18: Calculated acceleration for any point at the bucket

As in the previous section, to sum up vectors, they have to be transformed to the same coordinate system K_2. The variables $\dot{\vec{\varphi}}_4$ and $\ddot{\vec{\varphi}}_4$ are the relative angular velocity and angular acceleration between bucket and boom, hence, they are measured with IMU $S3$ and $S4$: $\dot{\vec{\varphi}}_4 = \dot{\vec{\varphi}}_{S4} - \dot{\vec{\varphi}}_{S3}$ and $\ddot{\vec{\varphi}}_4 = \ddot{\vec{\varphi}}_{S4} - \ddot{\vec{\varphi}}_{S3}$.

2.6.5.3 Acceleration at the Bucket, Measured with an IMU at the Boom

If the acceleration is measured with an IMU $S3$ at the boom K_3 but calculated at a point P, which is located at the bucket or tool carrier K_4 (see figure 2.19), there is only one joint between the two coordinate systems and it is basically the same scenario as in section 2.6.5.1 *Acceleration at the Boom.* Therefore, equation (2.22) is transformed to match this situation:

$$\begin{aligned}
\ddot{\vec{r}}_{1P} = {} & \ddot{\vec{r}}_{1S3} + (\dot{\vec{\varphi}}_2 + \dot{\vec{\varphi}}_3) \times ((\dot{\vec{\varphi}}_2 + \dot{\vec{\varphi}}_3) \times (\vec{r}_{3K4} + \vec{r}_{4P} - \vec{r}_{3S3})) \\
& + (\ddot{\vec{\varphi}}_2 + \ddot{\vec{\varphi}}_3) \times (\vec{r}_{3K4} + \vec{r}_{4P} - \vec{r}_{3S3}) \\
& + 2((\dot{\vec{\varphi}}_2 + \dot{\vec{\varphi}}_3) \times (\dot{\vec{\varphi}}_4 \times \vec{r}_{4P})) + \dot{\vec{\varphi}}_4 \times (\dot{\vec{\varphi}}_4 \times \vec{r}_{4P}) + (\ddot{\vec{\varphi}}_4 \times \vec{r}_{4P})
\end{aligned} \qquad (2.24)$$
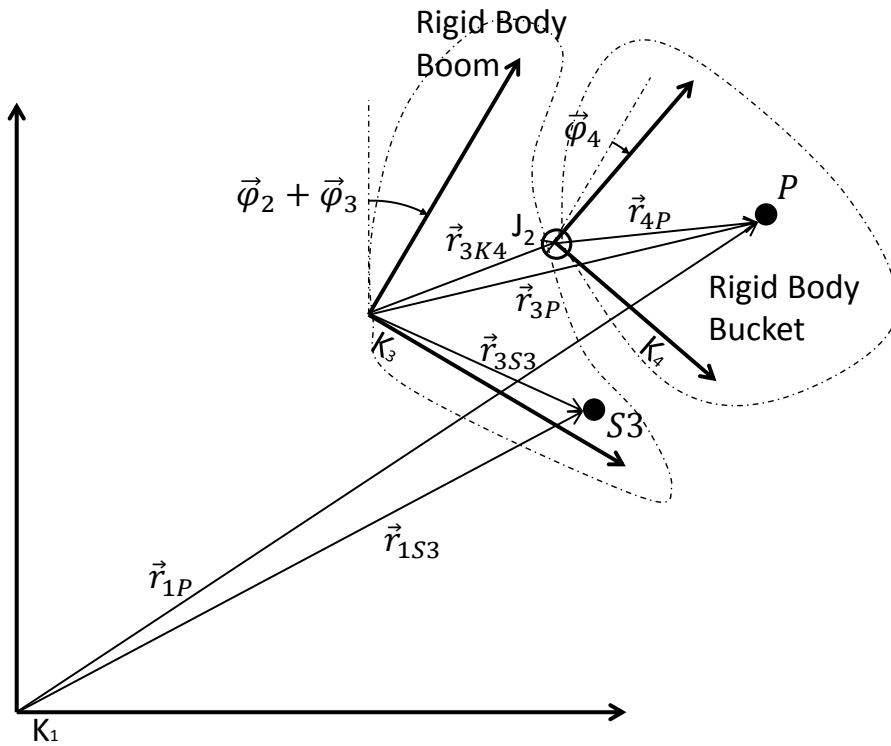
Figure 2.19: Calculated acceleration for any point at the bucket

The angular velocity $(\dot{\vec{\varphi}}_2 + \dot{\vec{\varphi}}_3 = \dot{\vec{\varphi}}_{S3})$ and angular acceleration $(\ddot{\vec{\varphi}}_2 + \ddot{\vec{\varphi}}_3 = \ddot{\vec{\varphi}}_{S3})$ are relative to the earth K_1 and are equal to the absolute values measured with the IMU $S3$ located at the boom.

2.6.6 Gravity

For the sake of completeness and better understanding gravity is shortly mentioned here. Gravity is referenced to the tractor which means that it points "upwards". For clarification, the following example is given. The tractor is accelerated upwards with one g in a non-gravity environment to receive the same mass-forces effects as on earth. On earth, an IMU mounted at the tractor measures an upward pointing gravity vector during standstill. If the tractor starts moving upwards, the acceleration is added to the gravity vector.

2.7 Mass and Center of Gravity

For the multi-body model of section 4.2 the parameters like mass, center of gravity position, and moment of inertia of each part are required. This section serves to define the nomenclature and determines how the parameters are identified in this thesis.

There are different ways to identify the mass m and center of gravity position $\vec{r}_{cog}$ of

a part. A part is defined as a rigid body with all stiff-mounted add-ons, such as brackets. The boom-part, for instance, includes all hoses, fittings and pins. In order to not consider a pin twice, it has to be determined to which part it belongs. One approach is to add a density to 3D-CAD solids. This allows for the determination of the mass of a part and its center of gravity position. If the part consists of several individual parts, the overall mass has to be accumulated ($\sum m_i$) and the overall center of gravity position is defined by equation (2.25).

$$\vec{r}_{cog} = \frac{\sum m_i \vec{r}_{cog\_i}}{\sum m_i} \tag{2.25}$$

All individual center of gravity positions $\vec{r}_{cog\_i}$ of each individual part need to be assigned to the same coordinate system. This method is easy to accomplish with current CAD systems but the effort increases with the amount of individual parts. The major difficulty is to assign the appropriate density to each part. Also, deviations from the real part occur due to manufacturing tolerances.

In this thesis is the mass of each front loader part measured with a scale in order to avoid these deviations. The identification of the center of gravity is done as shown in figure 2.20. Each part is hung up in different positions and the perpendicular is dropped from the pivot point. The intersection of the perpendicular lines is the position of the center of gravity [1]. The front loader is assumed as symmetrical to the xz-plane. Hence, the center of gravity position is only measured for x and z coordinates in the coordinate system of the respective part. For instance, the vector $\vec{r}_{cogBM}$ of the boom is referenced to coordinate system K_3. The mass and center of gravity position of each part of the front loader are listed in the appendix in table A.2.

---

[1] A hydraulic cylinder consists of two parts, the cylinder and the rod. Appendix A.1 describes a procedure to define the center of gravity of both parts without disassembling the cylinder.
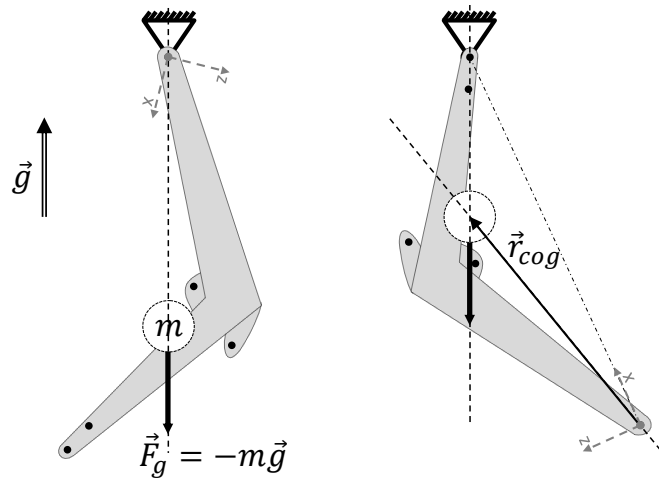
Figure 2.20: Center of gravity identification

2.8 Moment of Inertia

This chapter explains how the moments of inertia of each part are identified as it is required for the multi-body model in section 4.2. To obtain a high accuracy, the real moments of inertia are measured by tests and not calculated with 3D-CAD data. For instance, the inertia of the boom is considered at the current status with all mounted parts like hydraulic lines, fittings, pins, etc, and even oil within the hydraulic lines. Identifying the moments of inertia in the same quality with 3D-CAD data would require an immense effort. Only moments of inertia Θ_y in y-axis are significant which are parallel to the axes of the boom and bucket joints. This is due to the fact that the accelerated Θ_y generates torques around the y-axis which is supported by the cylinders of the front loader. Torques around the other axes are supported directly by the joints and are irrelevant for further processing. Furthermore, the moment of inertia in the y-axis is only needed for the principal axis of inertia (main axis, cf. section 4.2.2.3). All parameters identified in this thesis are listed in the appendix in table A.2.

To identify the moment of inertia Θ_i by tests each part is hung up as a pendulum. As an example, the boom of the front loader is hung up and swings as depicted in figure 2.21. Due to the friction of the joints, it performs a damped oscillation which is measured with an inertial measurement unit (see section A.2 in the appendix). The damping of the air resistance is neglected.
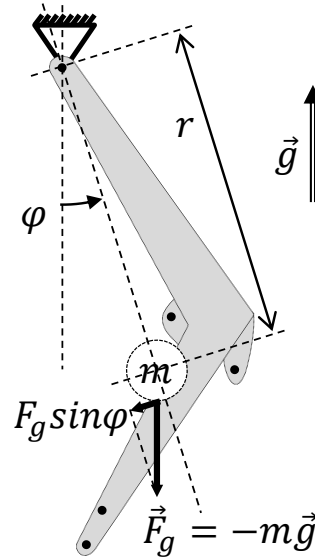
Figure 2.21: Pendulum

The differential equation of an undamped pendulum is given with the mass m of the pendulum, the gravity g, the distance r between joint and the center of gravity of the pendulum, and the eigenfrequency ω_0:

$$\Theta_p \ddot{\varphi} - mgr \sin \varphi = 0 \quad \text{with} \quad \varphi = \hat{\varphi} \sin (\omega_0 t) \tag{2.26}$$

For small φ ($\sin \varphi \approx \varphi$) equation (2.26) can be solved to obtain the moment of inertia Θ_p of the pendulum.

$$\Theta_p = \sqrt{\frac{mgr}{\omega_0^2}} \tag{2.27}$$

In order to obtain a higher accuracy of the moment of inertia the damping of the pendulum is considered. Hence, the eigenfrequency ω_0 is substituted with $\omega_0 = \omega_D/\sqrt{1 - D^2}$ in which $\omega_D = 2\pi/T_D$ is directly received by measuring the oscillation period T_D [DH11] [Krä84]. This turns equation (2.27) into:

$$\Theta_p = \sqrt{\frac{mgr}{\omega_D^2}(1 - D^2)} \tag{2.28}$$

The damping ratio D (E. Lehr's damping ratio [DH11]) is given by

$$D = \frac{1}{2\pi n} \ln \left(\frac{q_k}{q_{k+n}} \right) \tag{2.29}$$

in which n is the number of oscillations and q the amplitude. In practice, the oscillations n

are counted until the amplitude is half of the amplitude at the beginning, $q_{k+n} = 0.5q_k$ which results in $D = \dfrac{1}{2\pi n} \ln(2)$ [DH11].

The moment of inertia Θ_p refers to the pendulum joint. Finally, the Huygens-Steiner theorem has to be subtracted to obtain the moment of inertia Θ in the principal axis.

$$\Theta = \Theta_p - mr^2 \tag{2.30}$$

Further references are given by [WNB$^+$06] and [HSG99].

2.9 Friction

Friction and lubrication have a strong influence on the performance and behavior of the front loader. The friction is generated in the joints and the hydraulic cylinders and influences the payload measurement. In order to predict friction, a detailed understanding of where and how friction is generated is essential. This will be discussed in the following sections.

2.9.1 Seal Friction

A common hydraulic actuator consists of two main parts, the cylinder and the piston. Both parts move relatively to each other. The contact points between both parts are the seals. Hence, the mechanical friction at the hydraulic cylinders is only generated by the seals. A common differential, double acting cylinder, as it is used for tractor front loaders and wheel loaders, generally has at least two seals: a piston seal, which is mostly symmetrical in both directions, and a rod seal. The rod seal is often combined with a wiper to clean the rod and to prevent dirt to destroy the seal. A seal in its mounted position, for example the rod seal, is already pre-loaded and presses against the rod. While operating the cylinder, it is loaded with the working pressure p (up to 200bar for agricultural tractors or even up to 300bar or more for construction equipment) and the seal is pressed with even higher forces towards the rod. Figure 2.22 shows the contact pressure of a seal to a non-moving rod without and with the working pressure p.
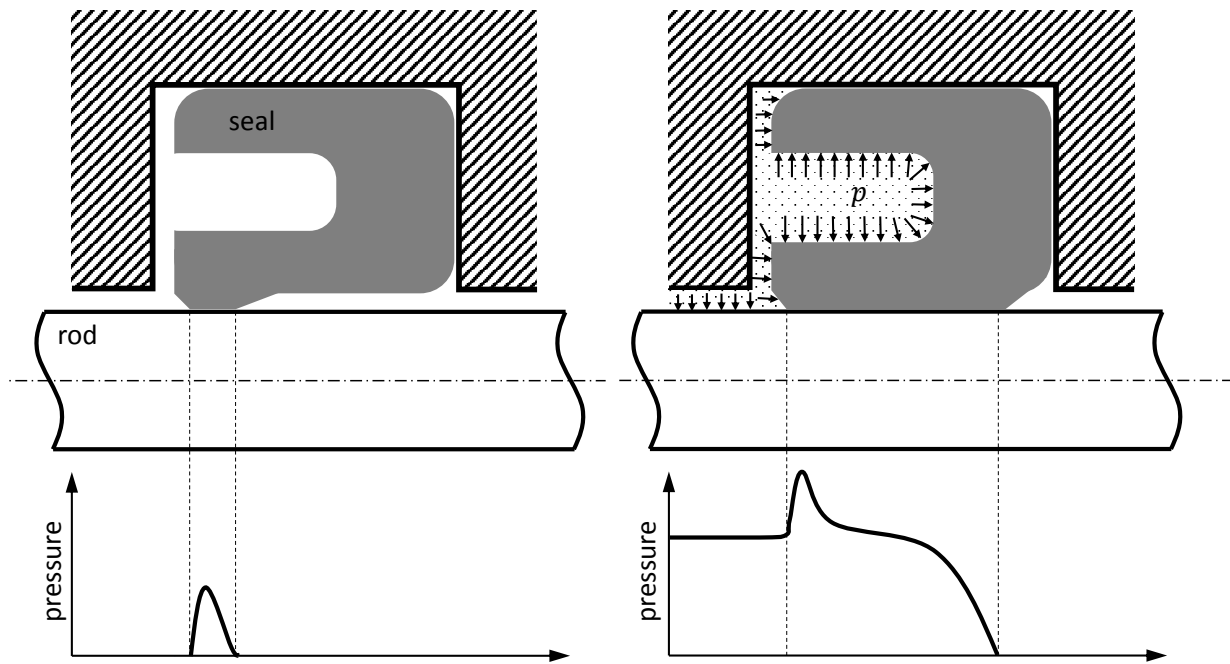
Figure 2.22: Seal without and with working pressure, based on [Mer14]

For dry friction it is well known that the higher the sliding parts are pressed onto each other the higher is the friction force. In case of hydraulic cylinders, the seals are lubricated with a fluid film which has to be taken into account.

2.9.2 Lubrication

The surface of the rod as well as the cylinder wall are surrounded by the hydraulic fluid and a fluid film sticks to it by adhesion. If the surface moves, the fluid film moves as well and tows further fluid molecules by cohesion. As a result, the fluid will be pumped with hydrodynamic pressure between seal and rod or seal and cylinder wall and creates a lubrication film [MN13] [Bau11] [HEN14].

At high actuator velocities and not too high loads the lubrication film completely separates the sliding parts which is called full fluid film lubrication. The remaining friction force is generated by the shear stress τ in the fluid film with its thickness h, dynamic viscosity η and the cylinder speed vel_{cyl} [Mer14] .

$$\tau = \eta \frac{\mathrm{d}(vel_{cyl})}{\mathrm{d}(h)} \tag{2.31}$$

To allow full fluid film lubrication, the fluid film has to be thicker than the roughness of the seal and cylinder surface, $h >> R_a$ (cf. appendix A.4).

At lower actuator velocities or higher loads, the hydrodynamic pressure is not high enough to completely separate the sliding parts. In this situation, a mixed lubrication regime exists where part of the load is supported directly by the contact points of the surfaces and produces mixed friction, $h \approx R_a$. At even lower actuator velocities or higher loads, the generated hydrodynamic pressure becomes insignificant and the load is mostly supported by the contact points of the surfaces (asperities). This lubrication regime is called boundary lubrication and causes static friction or stiction. The different kinds of friction are often described in a Stribeck curve, as shown in figure 2.23.
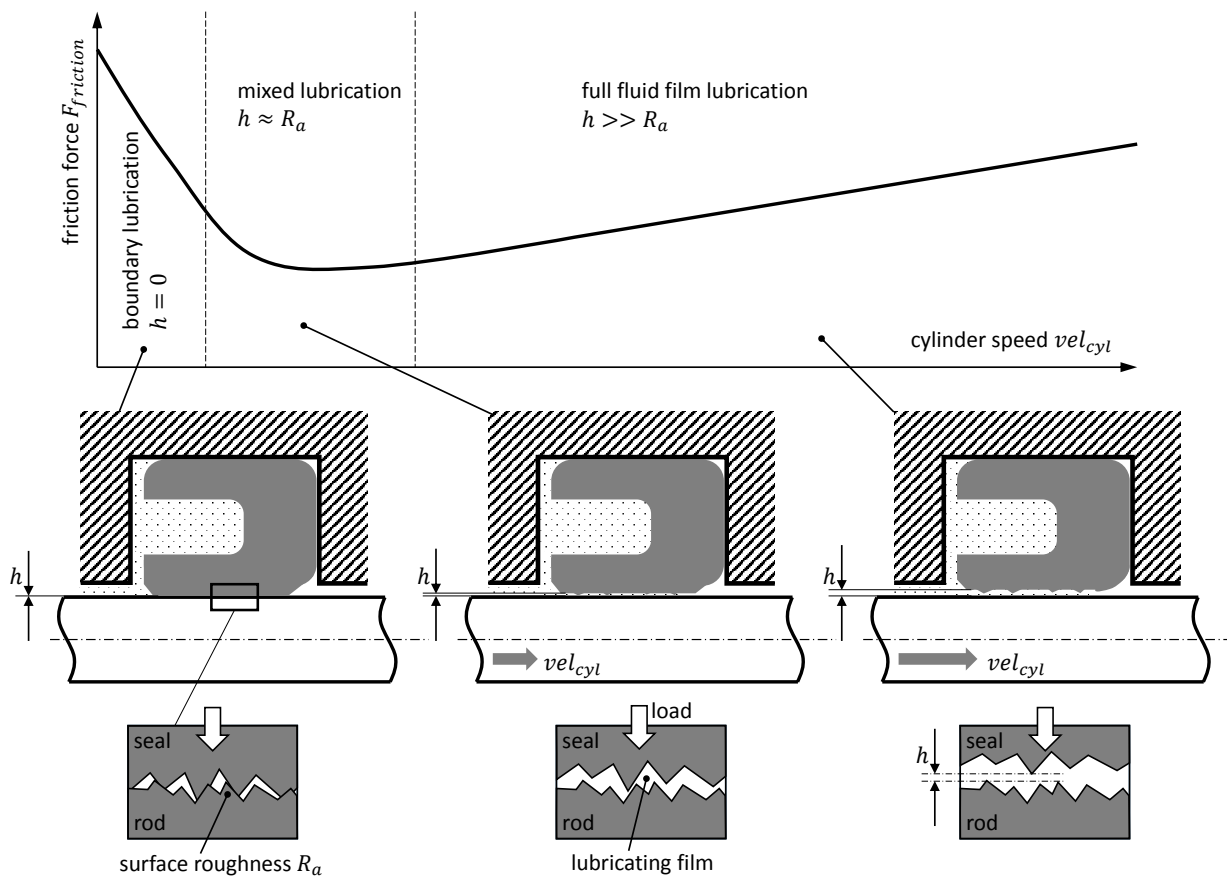
Figure 2.23: Friction force at different cylinder speeds, based on [GRU11]

The thickness of the lubricating film of the rod seal must be very small on order to avoid leakage. Also, the cylinders velocity vel_{cyl} of a front loader during operation are generally slow and within the range of 0.010 to 0.110m/s. Therefore, the seal is always in the mixed or boundary lubrication regime and the load is supported by the asperities of the surfaces [GRU11].

When two surfaces under boundary or mixed lubrication are brought very close together, they actually touch at an extremely small number of points. In other words, their real area of contact is an extremely small fraction of their apparent contact area. A load dependency

for this situation can be described with the multi-asperity-contact model by Bowden and Tabor [BT39]. They showed that the force of friction between two sliding surfaces strongly depends on the real area of contact A_r and on the shear strength τ of the adhesion or boundary lubricant in this area.

$$F_{friction} = \tau A_r \tag{2.32}$$

The real area of contact A_r increases with the load. Bowden and Tabor described the asperities idealized as spherically shaped with radius R and Young's modulus E_1. The asperities are pressed against a flat surface with Young's modulus E_2, as shown in figure 2.24. Their contact radius r can be determined by the Hertz theory [HC12].

$$r = \left(\frac{3F_{normal}R}{2E^*}\right)^{\frac{1}{3}}; \quad E^* = 2\frac{E_1 E_2}{(1-\nu_1{}^2)E_2 + (1-\nu_2{}^2)E_1}; \quad r << R \tag{2.33}$$

The real area of contact A_r of a single asperity is calculated by πr^2 which leads to the following equation:

$$F_{friction} = \tau\pi \left(\frac{3R}{2E^*}\right)^{\frac{2}{3}} F_{normal}^{\frac{2}{3}} \tag{2.34}$$
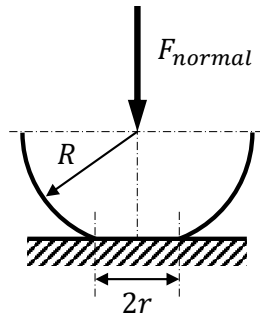
Figure 2.24: Area of contact

Equation (2.34) contradicts the Amontons 1st law, which states $F_{friction} = \mu F_{normal}$. Archard [Arc53] recognized that there is no contradiction between an elastic single asperity model and Amontons 1st law. Instead of assuming a constant number of asperities, as Bowden and Taylor did, Archard assumed the load dependency of the number of asperities. He stated that the higher the load the higher is the amount of junctions of contact, which leads to the proportionality $F_{friction} \sim F_{normal}$ and is conform with Amontons 1st law. Greenwood and Williamson [GW66] further improved the method with a Gaussian and exponential distribution of asperities [NAS71] [Ove07].

The asperity model makes it possible to explain that friction depends on the real area of contact. Due to the fact that the Hertz theory is only valid for $r << R$ it is assumed

that the area of contact of a single asperity must be much smaller than the asperity itself. Hence, the previous asperity model can only be applied to hard materials with linear elastic material properties, e.g. as used for bearings. But many cylinder seals are made out of polyurethane or PTFE-rings, which are much softer than steel. However, measurements with increasing loads have shown an increasing friction force at the seal (cf. figure 4.8). This is due to the fact that at low load the seal ring is not completely in contact with the sealing surface [MN13]. If the load increases, the contact area of the seal increases as well, as is shown in figure 2.22. Hence, analog to the multi-asperity-model for hard materials, the friction force increases with the real area of contact of the sealing surface.

2.9.3 Bearing Friction

The joints at the front loader are equipped with slide bearings lubricated with grease. Their sliding speed is quite low. For example, the relative boom movement $\dot{\varphi}_{BM}$ is in a speed range from 0 to 0.5 rad/s which results in a maximum relative speed of 8.8 mm/s between the sliding parts of a 35 mm diameter bearing. Thus, the bearings run in boundary or mixed lubrication and the same assumptions as in section 2.9.2 can be applied.

2.9.4 Friction Models

In order to predict friction, several friction models are introduced in this section. Generally, these models can be split into steady state friction models and dynamic friction models which consider time based effects. If the conditions like relative velocity or pressure between the sliding partners are constant over the time the dynamic friction model becomes a steady state friction model. A special steady state friction model is the pressure based friction model which is introduced in section 2.9.4.3.

2.9.4.1 Steady State Friction Model

Generally, friction can be split up into different components, as displayed in figure 2.25, where the friction force $F_{friction}$ is shown as a function of the velocity $\dot{x}$ between the sliding parts. The viscous friction is induced by the fluid film and assumed to be proportional to the velocity with the viscous friction coefficient B. The Coulomb friction is independent of the velocity, thus, shown as constant. This can be explained, for example, by the braking force of a car disk brake, which remains constant at the same actuating force regardless of the wheel speed. The Stribeck effect describes friction at low velocities, which decreases exponentially to zero from the difference of the stiction force F_S and the Coulomb force F_C. The total friction in figure 2.25 is the sum of the viscous friction, Stribeck friction, and Coulomb friction [HO11] [Str02].
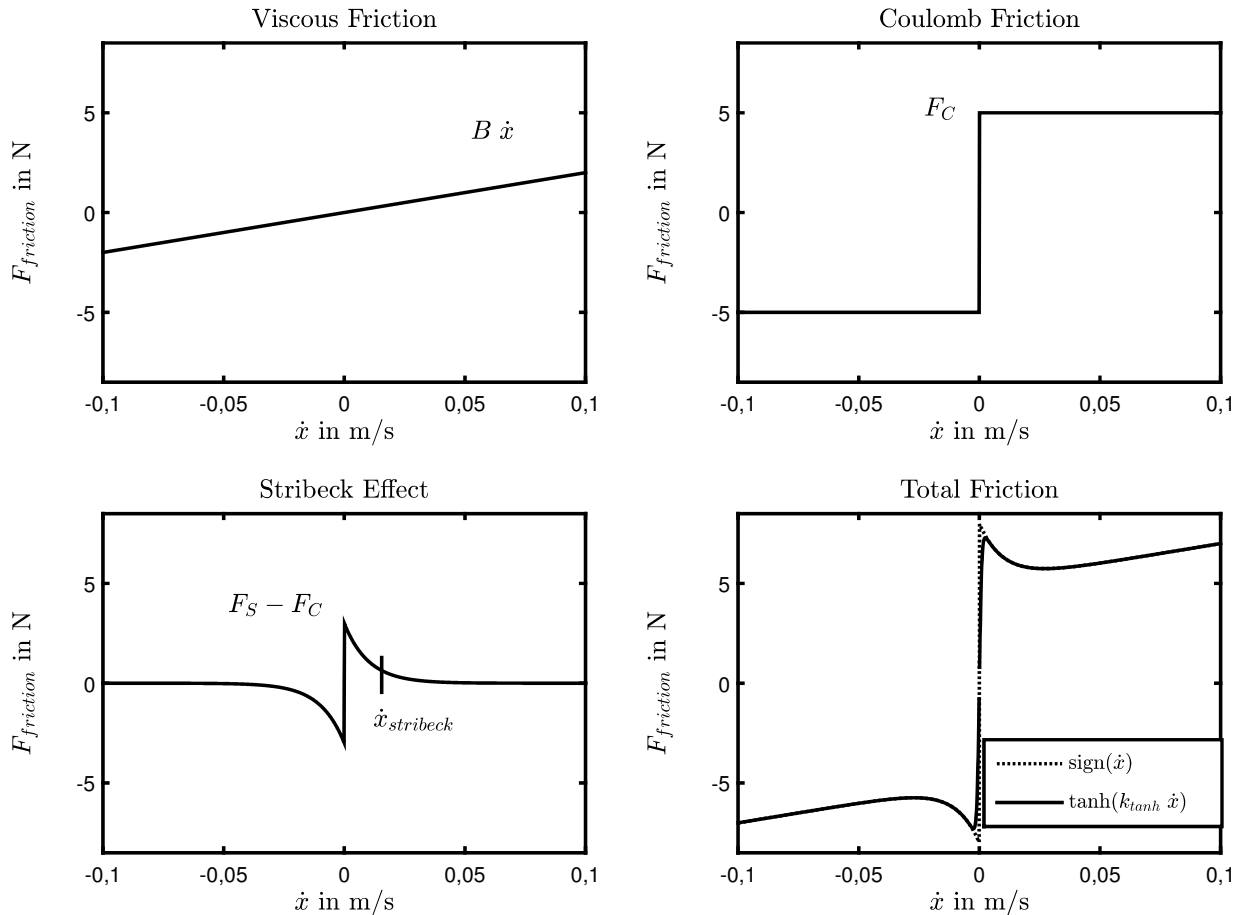
Figure 2.25: Friction characteristics

Bo and Pavelescu, [AHDdW94], [BP82], adopt and linearize an exponential model of the following form which describes the curve of the total friction.

$$F_{friction} = \text{sign}\left(\dot{x}\right)\left(F_C + (F_S - F_C)\, e^{-\left(\frac{\dot{x}}{\dot{x}_{stribeck}}\right)^{\delta}}\right) + B\,\dot{x} \qquad (2.35)$$

The Stribeck velocity $\dot{x}_{stribeck}$ and the exponent δ are empirical parameters. For example, Bo and Pavelescu find a range from $\delta = 1/2$ to 1, Armstrong-Hélouvry find $\delta = 2$, which is also known as the Gaussian model and a very large δ was cited by Fuller [AHDdW94].

Due to the dependence of the sign of the velocity, friction force is discontinuous at zero velocity which bears some problems by using this model in simulation or analysis. Hence, a lot of effort was done to describe the friction in this situation. A solution is introduced by using the tanh-function instead of the sign-function with a coefficient k_{tanh} that determines how fast the function changes from near -1 to near 1 [ASB05]. This turns equation (2.35)

into the following term:

$$F_{friction} = \tanh\left(k_{tanh}\dot{x}\right)\left(F_C + (F_S - F_C)\,e^{-\left(\frac{\dot{x}}{\dot{x}_{stribeck}}\right)^{\delta}}\right) + B\,\dot{x} \qquad (2.36)$$

2.9.4.2 Dynamic Friction Model

Friction is known to have a memory-dependent behavior. Phenomena such as pre-displacement, rate-dependence, and hysteresis have been experimentally identified and are reproduced only by models with memory that include dynamics [AdW08]. Hence, the consistent further development of steady state friction models are dynamic friction models. In steady conditions, dynamic friction models are equal to steady state models.

A common state of the art friction model is the LuGre model [Ols96], which contains only a few parameters, and, thus, can easily be adapted to experimental data. It is able to model the Stribeck effect and hysteresis loops. Another aspect of this model is the ability to simulate the deformation of the asperity junctions and the elastic, spring-like pre-displacement [HO11]. In the LuGre model, asperity junctions are considered as bristles, as shown in figure 2.26. One surface has rigid bristles; the other surface has elastic ones. If a tangential force is applied, the bristles deflect like springs and the friction force rises. If the force is large enough, some of the bristles deflect to an extend that they slip off each other. New contacts are formed and as long as the two surfaces continue to move the process goes on. The relative velocity $\dot{x}$ between the surfaces determines the amount of lubricant that is pumped in between them and how far they are pushed apart (cf. chapter 2.9.2). At high velocities, the surfaces are further away from each other and the bristles deflect less before they slip. This corresponds to the Stribeck effect and to different lubrication regimes. For motion with constant velocity, friction reaches a steady state value [AdW08].
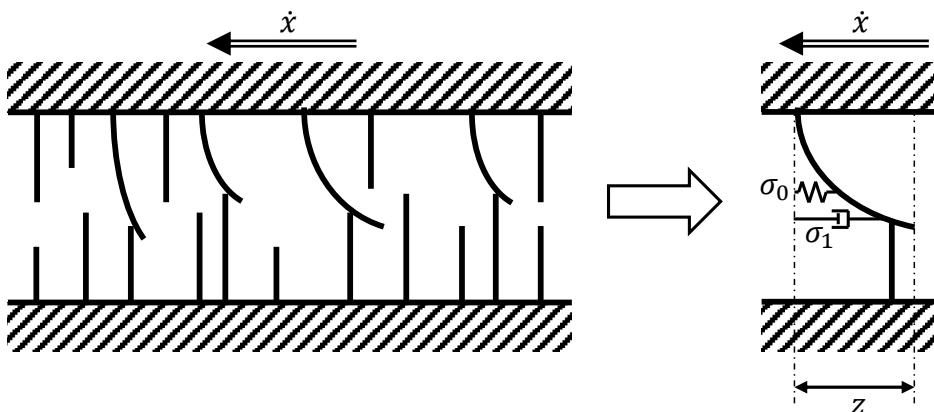

Figure 2.26: Bristle modeling, based on [Ols96]

The LuGre model is based on a single bristle which represents the average behavior and which can never slip off. The parameter σ_0 is the average stiffness of the bristles; the parameter σ_1 is the micro-viscous coefficient which is equivalent to a damping coefficient. The friction force is described in equation (2.37) with the viscous friction term $B\dot{x}$.

$$F_{friction} = \sigma_0 z + \sigma_1 \dot{z} + B\dot{x} \qquad (2.37)$$

The deflection of the elastic bristle is denoted by z and modeled by the following equation.

$$\dot{z} = \dot{x} - \frac{|\dot{x}|}{g(\dot{x})} z \qquad (2.38)$$

The function $g(\dot{x})$ is described as follows.

$$g(\dot{x}) = \frac{1}{\sigma_0} \left(F_C + (F_S - F_C) e^{-\left(\frac{\dot{x}}{\dot{x}_{stribeck}}\right)^{\delta}} \right) \qquad (2.39)$$

The steady state friction force $F_{friction,ss}$ arises when the velocity $\dot{x}$ is held constant. Thus, the deflection rate will be zero $\dot{z} = 0$ and the steady state deflection z_{ss} is described by the following equation:

$$z_{ss} = \frac{\dot{x}}{|\dot{x}|} g(\dot{x}) = \text{sign}(\dot{x}) g(\dot{x}) \qquad (2.40)$$

This turns equation (2.37) into the following term which is equal to equation (2.35) of the steady state friction model.

$$\begin{aligned} F_{friction,ss} &= \sigma_0 z_{ss} + B\dot{x} \\ &= \sigma_0 \, \text{sign}(\dot{x}) g(\dot{x}) + B\dot{x} \\ &= \text{sign}(\dot{x}) \left(F_C + (F_S - F_C) e^{-\left(\frac{\dot{x}}{\dot{x}_{stribeck}}\right)^{\delta}} \right) + B\dot{x} \end{aligned} \qquad (2.41)$$

In conclusion, the dynamic friction models such as the LuGre are able to model phenomena like pre-displacement, rate-dependence, and hysteresis. In steady state conditions, they are equal to a steady state model. In real time applications it must be mentioned that, a high sample rate is needed to run a dynamic friction model on a controller, which is due to the fast transient response of pre-displacement.

2.9.4.3 Pressure Based Model

The pressure based friction model is a steady state friction model especially developed for hydraulic applications. It is also possible to combine the pressure based friction model with the previously described friction models, for instance, by replacing the Coulomb friction.

Bonchis et al. [BCR99] formulated a friction model for asymmetric hydraulic cylinders using the chamber pressures and the piston velocity.

$$F_{friction} = k_1 p_A + k_2 p_B + k_3 e^{k_4 vel_{cyl}} + k_5 vel_{cyl} \tag{2.42}$$

The coefficients k_{1-5} are determined by [BCR99] for several particular cases. The closest fit to the real measurement was achieved by using all coefficients. Nearly the same fit was obtained by setting coefficient $k_4 = 0$. If coefficient k_5 was neglected, the loss of accuracy was less than 1%. With previous simplifications, equation (2.42) turns into the following term:

$$F_{friction} = k_1 p_A + k_2 p_B + k_3 \tag{2.43}$$
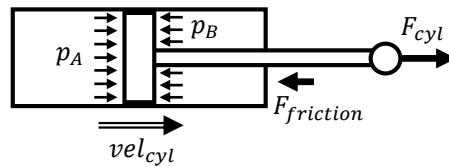

Figure 2.27: Asymmetric hydraulic cylinder

In equation (2.43), all velocity dependent terms are neglected. However, in real applications the back-up pressure of the return oil increases with the actuator velocity. This effect increases the pressure of the whole system and affects the previous equation. Thus, the velocity is still considered indirectly with the pressure (cf. figure 4.7).

3 Position Detection

The angular position of the front loader is required to calculate the vectors which are used in the subsequently discussed weighing algorithm of chapter 4. There are several ways to detect the position of the front loader relative to the machine, for instance, by measuring the actuator length with stroke sensors or by detecting the boom and bucket angle with rotary sensors. The implementation of the position detection is irrelevant for the weighing algorithm, hence, the position detection is discussed separately in this chapter.

This thesis pursues an approach that uses inertial measurement units (IMUs), also known as acceleration sensors combined with gyros, to detect the position of the front loader. The IMUs' advantages are that they consist of non-moving parts and that they can be mounted individually in a protected position at boom, bucket, or tool carrier. For this purpose, the position of the front loader relative to the tractor is defined by the angle φ_{BM} between boom and tractor chassis and by the angle φ_{BU} between bucket or tool carrier and tractor chassis. Thus, the angle φ_{BM} is equal to the rotation angle φ_{3y} between the coordinate system K_2 and K_3 (cf. figure 2.18). The angle $\varphi_{BU} = \varphi_{3y} + \varphi_{4y}$ is the rotation of the coordinate system K_4 relative to K_2. With the knowledge of these angles, all other variables such as the cylinder strokes can be derived. To receive these angles, the accelerations at the chassis, boom, and bucket are measured and compared to each other. Therefore, the front loader is equipped with three IMUs (cf. section A.3.3).

- The IMU $S2$ is mounted to the chassis and assigned to the tractor coordinate system K_2.

- The IMU $S3$ is mounted to the boom and assigned to the boom coordinate system K_3.

- The IMU $S4$ is mounted to the bucket or tool carrier and assigned to the bucket coordinate system K_4.

3.1 Angle between Chassis and Boom

To determine the angle φ_{BM}, the acceleration vector $\vec{a}_{S3} = \ddot{\vec{r}}_{S3}$ is measured in the boom coordinate system K_3 using IMU $S3$. At the same time, the acceleration vector $\vec{a}_{S2} = \ddot{\vec{r}}_{S2}$ is measured in the chassis coordinate system K_2 using IMU $S2$. In a next step, the acceleration vector $\vec{a}_{S2} = \ddot{\vec{r}}_{S2}$ is calculated for the IMU position of $S3$ using equation (2.22), which results in $\vec{a}_{S3byS2}$ of equation (3.1). Equation (3.1) includes $\vec{r}_{2K3} = \vec{0}$, the angular

velocity $\dot{\vec{\varphi}}_{S2}$, and angular acceleration $\ddot{\vec{\varphi}}_{S2}$ of IMU $S2$. Basically, the same acceleration is measured in two coordinate systems with two IMUs.

$$
\begin{aligned}
\vec{a}_{S3byS2} = {} & \ddot{\vec{r}}_{S2} + \dot{\vec{\varphi}}_{S2} \times (\dot{\vec{\varphi}}_{S2} \times (\underset{K2}{\overset{K3}{\downarrow \boldsymbol{R}}}\, \vec{r}_{S3} - \vec{r}_{S2})) + \ddot{\vec{\varphi}}_{S2} \times (\underset{K2}{\overset{K3}{\downarrow \boldsymbol{R}}}\, \vec{r}_{S3} - \vec{r}_{S2}) \\
& + 2(\dot{\vec{\varphi}}_{S2} \times (\dot{\vec{\varphi}}_{BM} \times \underset{K2}{\overset{K3}{\downarrow \boldsymbol{R}}}\, \vec{r}_{S3})) + \dot{\vec{\varphi}}_{BM} \times (\dot{\vec{\varphi}}_{BM} \times \underset{K2}{\overset{K3}{\downarrow \boldsymbol{R}}}\, \vec{r}_{S3}) + (\ddot{\vec{\varphi}}_{BM} \times \underset{K2}{\overset{K3}{\downarrow \boldsymbol{R}}}\, \vec{r}_{S3})
\end{aligned}
\tag{3.1}
$$

Because the coordinate systems are rotated against each other, the acceleration vectors point in different directions for each coordinate system. For instance, the direction of the acceleration vector $\vec{a}_{S3byS2}$ is defined by the angle φ_{accS2_K2} between the x-axis of K_2 and $\vec{a}_{S3byS2}$. The desired angle φ_{BM} results by subtracting direction φ_{accS2_K2} from direction φ_{accS2_K3} as shown in figure 3.1. With the scalar product the angle φ_{BM} is calculated in the range of $-\pi < \varphi_{BM} < \pi$ as follows:

$$
\varphi_{BM} = - \operatorname{sign}\left([\vec{a}_{S3byS2} \times \vec{a}_{S3}]_y\right) \arccos\left(\frac{\vec{a}_{S3byS2} \cdot \vec{a}_{S3}}{|\vec{a}_{S3byS2}||\vec{a}_{S3}|}\right)
\tag{3.2}
$$
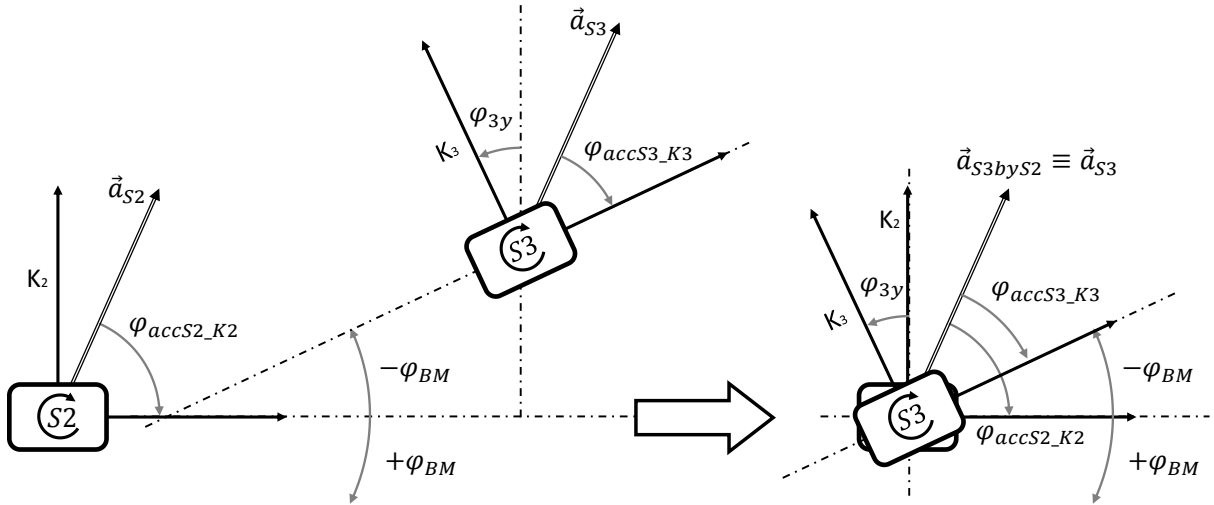
Figure 3.1: Acceleration vectors at IMUs $S2$ and $S3$

As shown in equation (3.1), the position vector $\vec{r}_{S3}$ of IMU $S3$ must be transformed to the coordinate system K_2 with $\underset{K2}{\overset{K3}{\downarrow \boldsymbol{R}}}$. Thus, the demanded angle φ_{BM} is needed in advance to calculate the transformation matrix as described in section 2.4. Because of the continuous position detection, which runs on an electronic control unit with a sample time of a few milliseconds, the angle is provided by the previous calculation step. The angle starts with an initial value at zero which causes a small deviation for the first few cycles.

3.2 Angle between Chassis and Bucket

The angle φ_{BU} between chassis and boom is calculated in the same way as φ_{BM} in the previous chapter 3.1 but with the acceleration vectors of $S3$ and $S4$ and equation (2.24) (cf. equation (4.24)). The angle φ_{BU} is a sum of the angle φ_{BM} and the angle φ_{4y} between boom and bucket, $\varphi_{BU} = \varphi_{BM} + \varphi_{4y}$.

It is also possible to calculate φ_{BU} directly by using the acceleration vectors of $S2$ and $S4$ and equation (2.23). In this case, there will be a higher deviation due to one additional joint between the IMUs which performs relative movements. In addition, a longer distance between the two IMUs causes a higher influence on φ_{BU} because of a noise corrupted angular velocity and acceleration signal (cf. equation (2.23) and equation (2.24), distance $(\vec{r}_{2K3} + \vec{r}_{3K4} + \vec{r}_{4P} - \vec{r}_{2S2})$ vs. $(\vec{r}_{3K4} + \vec{r}_{4P} - \vec{r}_{3S3})$).

3.3 Interchangeability and Sensor Configuration

It is irrelevant whether the accelerations are calculated at the IMU position of $S3$ as in section 3.1 or vice versa at the IMU position of $S2$. With both methods, it is possible to obtain the angle. In order to transfer a measured acceleration to another position using equation (2.22), the angular velocities and angular accelerations have to be measured. Hence, it is obvious to mount an inertial measurement unit $S3$ to the boom that provides accelerations, angular velocity and derived angular acceleration for all axis. With these signals, the accelerations at the IMU positions $S2$ and $S4$ of chassis and bucket can be calculated. In this case, it is sufficient if IMUs $S2$ and $S4$ provide accelerations for all axis and angular velocity and acceleration only around the y-axis. Furthermore, the accelerations, angular velocities, and angular accelerations for all axis of the boom IMU $S3$ are needed for the dynamic weighing in chapter 4.

3.4 Continuous Angle Function

A continuous position angle is needed for further calculations. Depending on the kinematics and the coordinate systems of the front loader the measured position angle φ_{BM} or φ_{BU} overshoot π and the angle is a discontinuous function and jumps to $-\pi$.

To prevent the angle to switch from $+\pi$ to $-\pi$, a start angle φ_{start} is defined, which is outside of the movement range. For example, if φ_{start} is larger than $-\pi$ but the output of equation (3.2) is smaller than φ_{start}, the value of 2π has to be added, as shown in figure 3.2. Thus, the angle is continuous in the range from φ_{start} to $\varphi_{start} + 2\pi$.
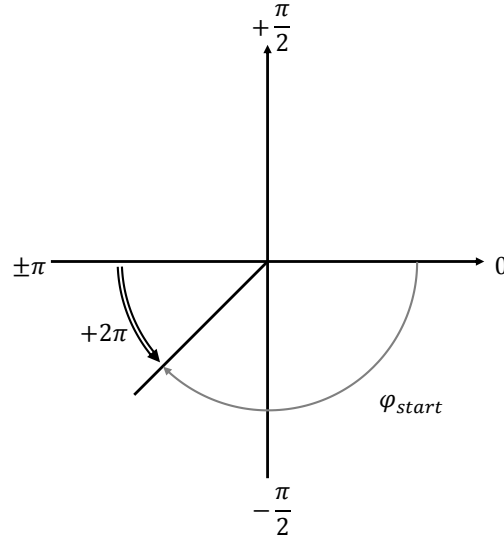
Figure 3.2: Continuous position angle

3.5 IMU Mounting Correction

Each acceleration sensor has its own internal sensor coordinate system, which is generally not the coordinate system of the part. For instance, the internal coordinate system K_{S3} of IMU $S3$ is rotated with angle $\varphi_{mountS3}$ against the boom coordinate system K_3, as shown in figure 3.3. To receive accelerations directly in the boom coordinate system K_3, the acceleration vector of $S3$ first has to be transformed with $\varphi_{mountS3}$, as described in chapter 2.4.

To determine the mounting angle $\varphi_{mountS3}$, the boom has to be adjusted horizontally. Due to the gravity, the angle φ_{accS3_K3} between the acceleration vector $\vec{a}$ and the x-axis of the boom coordinate system K_3 must be $\pi/2$.

$$\varphi_{accS3\_K3} = \frac{\pi}{2} \tag{3.3}$$

Due to the mounting angle $\varphi_{mountS3}$, IMU $S3$ measures a different angle $\varphi_{accS3\_KS3} \neq \varphi_{accS3\_K3}$ in the coordinate system K_{S3}. This results in equation (3.4), which can be solved for $\varphi_{mountS3}$.

$$\varphi_{mountS3} + \varphi_{accS3\_KS3} = \frac{\pi}{2} \tag{3.4}$$
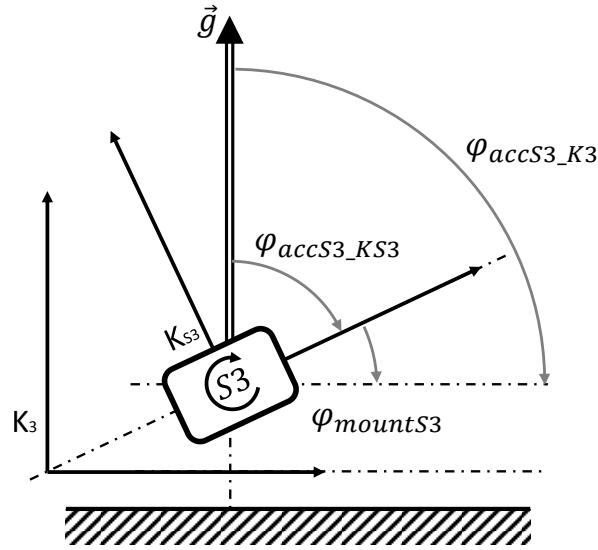
Figure 3.3: Mounting angle

The mounting angles of IMU $S2$ and $S4$, $\varphi_{mountS2}$ and $\varphi_{mountS4}$, are determined by the known angle φ_{BM} and φ_{BU} at the cylinder end-stroke position and the previously defined $\varphi_{mountS3}$. Alternatively, they can be determined in the same way as $\varphi_{mountS3}$ by adjusting the x-axis of the tractor and the bucket coordinate system horizontally.

3.6 IMU Output Correction

The accuracy of the previous calculation is highly dependent on the accuracy of the acceleration sensor output. In this thesis, during standstill of the front loader, the acceleration sensor output varies from the gravity. In this case, the sensor outputs must be corrected for each axis by adding corresponding factors or offsets. These values can be obtained by aligning the IMU with different previously defined angles relative to the gravity and comparing the actual acceleration output with the gravity.

3.7 Signal filtering

The average output of the previous angle calculation in section 3.1 et sqq. is very accurate but the signal is quite noisy ($\varphi_{measured}$ in figure 3.4). A low-pass filter would provide a reliable front loader position but due to the phase shift the position detection will be slow which makes it difficult to use it for further processing.

Another approach is to calculate the angle by integrating the angular rates. Here, the angular velocities $\dot{\vec{\varphi}}$ are measured with gyros and the relative angular velocities between

chassis and boom $\dot{\varphi}_{BM_y}$ and boom and bucket $\dot{\varphi}_{BU_y}$ are calculated ($\dot{\varphi}_{measured}$ in figure 3.4). Depending on the quality of the gyro, the sensor signal is disturbed by an offset. Hence, the integrated angular velocities produce a precise angle, but due to the offset the angle is drifting, as shown figure 3.4. To use the advantages of both methods and to receive a precise and accurate angle signal (see figure 3.5) the angle $\varphi_{measured}$ of the previous angle calculation of chapter 3.1 and the angle of the integrated angular rates $\dot{\varphi}_{measured}$ are merged together with an observer.
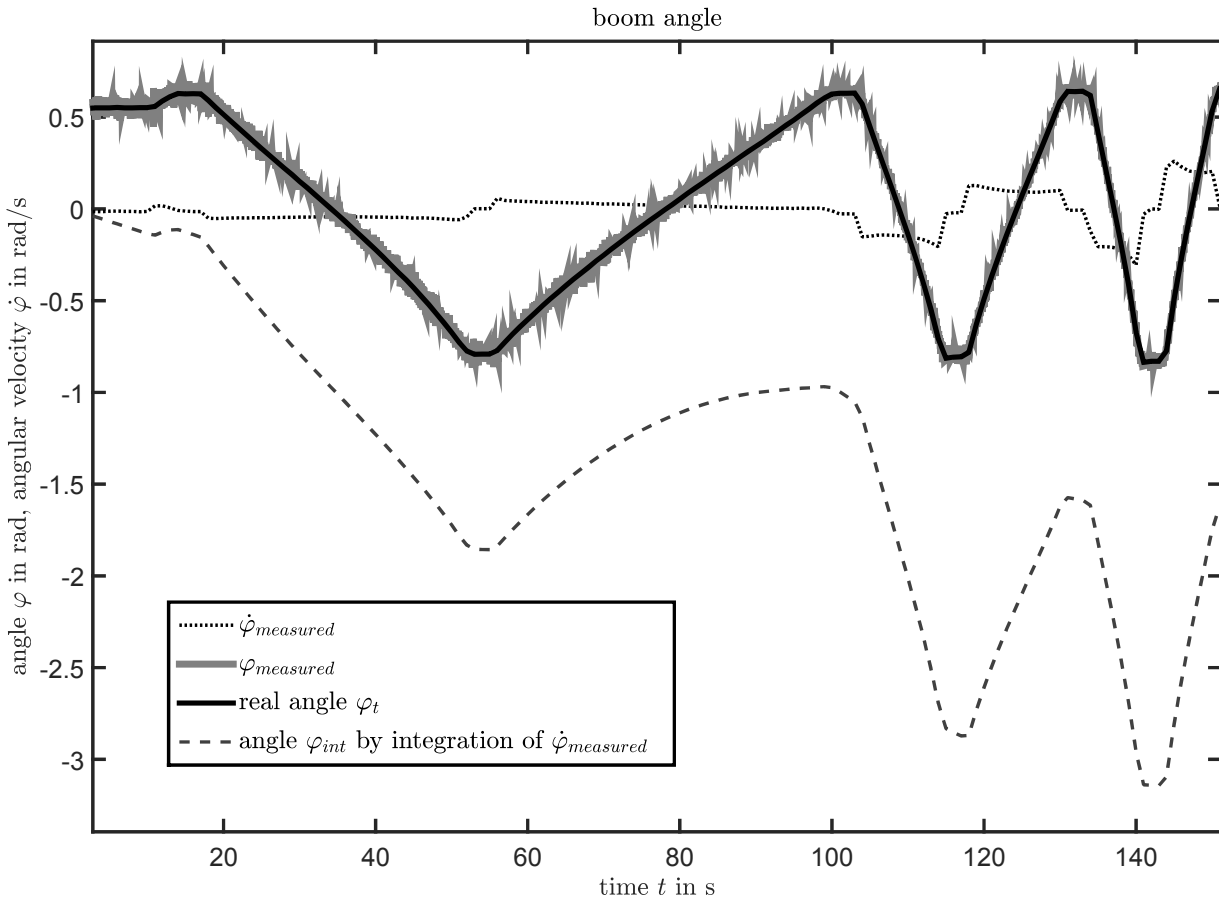
Figure 3.4: Angle drift
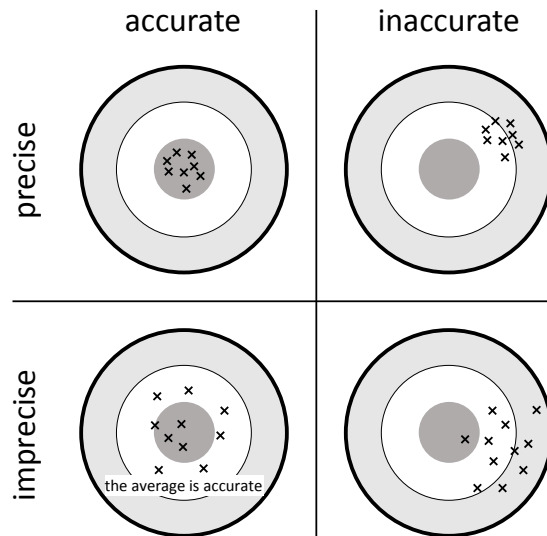
Figure 3.5: Accurate vs. precise

3.7.1 Observer

In order to merge the position angle $\varphi_{measured}$ of the previous angle calculation of chapter 3.1 with the angle of the integrated angular rates $\dot{\varphi}_{measured}$, a closer look is taken at the Luenberger observer [Lun06]. The approach of the Luenberger observer is to run a model parallel to the plant and to reproduce the state vector $\boldsymbol{x}$ of the plant with the observed state vector $\hat{\boldsymbol{x}}$ of the model, see figure 3.6. Hence, the model and the plant have the same control vector $\boldsymbol{u}$ as input. Due to different initial states the output $\hat{\boldsymbol{y}}$ of the model deviates from the output $\boldsymbol{y}$ of the plant. The Luenberger observer uses the difference $(\boldsymbol{y} - \hat{\boldsymbol{y}})$ as feedback to correct the deviations of the model.
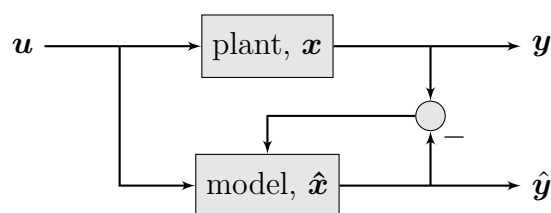
Figure 3.6: Observer

The mathematical description in the time domain of the plant is given by equation (3.5). The plant has the control vector $\boldsymbol{u}$ as input, vector $\boldsymbol{y}$ as output, and internal state variables, which are merged into a state vector $\boldsymbol{x}$.

$$\begin{aligned} \dot{\boldsymbol{x}} &= \boldsymbol{A}\boldsymbol{x} + \boldsymbol{B}\boldsymbol{u} \,, \quad \boldsymbol{x} \in \mathbb{R}^{n \times 1},\ \boldsymbol{A} \in \mathbb{R}^{n \times n},\ \boldsymbol{B} \in \mathbb{R}^{n \times k} \\ \boldsymbol{y} &= \boldsymbol{C}\boldsymbol{x} \end{aligned} \tag{3.5}$$

Ideally, the mathematical behavior of the model is the same as that of the plant. But, due to inaccuracies of the matrices $\boldsymbol{A}$,$\boldsymbol{B}$, and $\boldsymbol{C}$ and the lack of knowledge of the initial state $\boldsymbol{x}_0$, the output of the model deviates from the output of the plant. The observer uses the feedback of the deviation to adjust the state vector $\hat{\boldsymbol{x}}$ of the model to the state vector $\boldsymbol{x}$ of the plant. Hence, the observer contains an additional input term, that includes these deviations, also called estimation error, $(\boldsymbol{y} - \hat{\boldsymbol{y}})$. The input $\boldsymbol{u}, \boldsymbol{y}$ of the observer is generally measured and corrupted by disturbances $\boldsymbol{\delta}$ which results in equation (3.6)

$$\begin{aligned} \boldsymbol{u}_{measured} &= \boldsymbol{u} + \boldsymbol{\delta}_1 \\ \boldsymbol{y}_{measured} &= \boldsymbol{y} + \boldsymbol{\delta}_2 \end{aligned} \tag{3.6}$$

The observer output $\hat{\boldsymbol{y}}$ is continuously corrected. To adjust the amplification of the correction, the estimation error is multiplied by the observer gain $\boldsymbol{L}$. Finally, the mathematical description in the time domain of the observer is given by equation (3.7) [Oga02].

$$\begin{aligned} \dot{\hat{\boldsymbol{x}}} &= \boldsymbol{A}\hat{\boldsymbol{x}} + \boldsymbol{B}\boldsymbol{u}_{measured} + \boldsymbol{L}(\boldsymbol{y}_{measured} - \hat{\boldsymbol{y}}) \\ &= \boldsymbol{A}\hat{\boldsymbol{x}} + \boldsymbol{B}\boldsymbol{u} + \boldsymbol{L}(\boldsymbol{y} - \hat{\boldsymbol{y}}) + \boldsymbol{B}\boldsymbol{\delta}_1 + \boldsymbol{L}\boldsymbol{\delta}_2 \ , \\ \hat{\boldsymbol{y}} &= \boldsymbol{C}\hat{\boldsymbol{x}} \end{aligned} \tag{3.7}$$

Figure 3.7 shows the Luenberger observer [Lun06], which estimates the state variables based on the measurements of the output variables $\boldsymbol{y}_{measured}$ and the control variables $\boldsymbol{u}_{measured}$. In order to determine the observer gain $\boldsymbol{L}$, the observer error equation is introduced: $\boldsymbol{e} = \boldsymbol{x} - \hat{\boldsymbol{x}}$, which is derived in respect to time:

$$\begin{aligned} \dot{\boldsymbol{e}} &= \dot{\boldsymbol{x}} - \dot{\hat{\boldsymbol{x}}} \\ &= \boldsymbol{A}\boldsymbol{x} + \boldsymbol{B}\boldsymbol{u} - (\boldsymbol{A}\hat{\boldsymbol{x}} + \boldsymbol{B}\boldsymbol{u}_{measured} + \boldsymbol{L}(\boldsymbol{y}_{measured} - \hat{\boldsymbol{y}})) \\ &= \boldsymbol{A}\boldsymbol{x} + \boldsymbol{B}\boldsymbol{u} - \boldsymbol{A}\hat{\boldsymbol{x}} - \boldsymbol{B}(\boldsymbol{u} + \boldsymbol{\delta}_1) - \boldsymbol{L}(\boldsymbol{y} + \boldsymbol{\delta}_2 - \hat{\boldsymbol{y}}) \\ &= (\boldsymbol{A} - \boldsymbol{L}\boldsymbol{C})\boldsymbol{e} - \boldsymbol{B}\boldsymbol{\delta}_1 - \boldsymbol{L}\boldsymbol{\delta}_2 \end{aligned} \tag{3.8}$$

The observer error can be considered as a state variable of a dynamic system. Given that the measurement disturbances, $\boldsymbol{\delta}_1$ and $\boldsymbol{\delta}_2$, are zero, the observer error $\boldsymbol{e}$ converges to zero if the matrix $(\boldsymbol{A} - \boldsymbol{L}\boldsymbol{C})$ is stable. Accordingly, all their eigenvalues λ_{o_i} are negative.

$$\lim_{t \to \infty} \|e(t)\| = 0 \tag{3.9}$$

If the system $(\boldsymbol{A},\boldsymbol{C})$ is completely observable, it is possible to choose matrix $\boldsymbol{L}$ so that $(\boldsymbol{A} - \boldsymbol{L}\boldsymbol{C})$ can have any desired eigenvalues λ_{o_i}. Matrix $\boldsymbol{L}$ must be chosen in a way that the eigenvalues λ_{o_i} of $(\boldsymbol{A} - \boldsymbol{L}\boldsymbol{C})$ are on the left side of the dominant eigenvalues λ_{p_i} of the plant [Föl94] [Lun06].
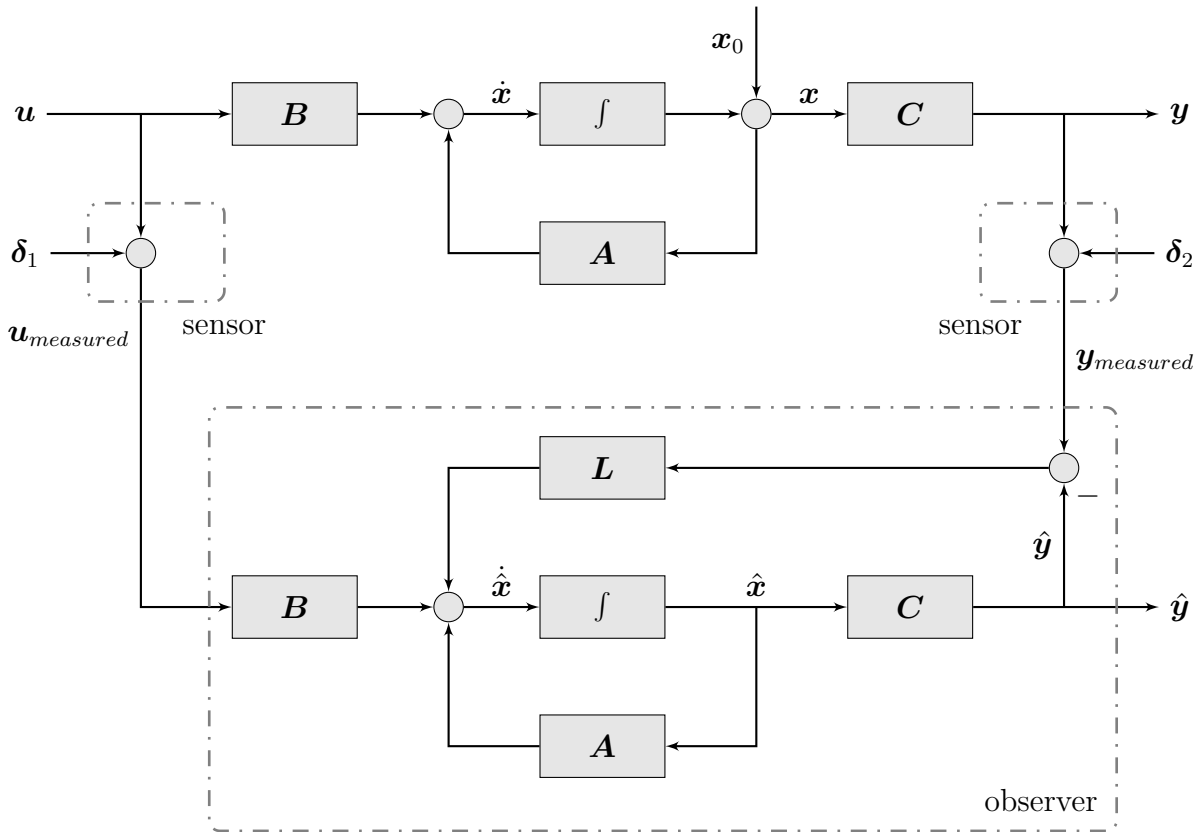
Figure 3.7: Luenberger observer

3.7.1.1 Plant model

In the case of the position detection of the front loader, the input of the plant is the true angular velocity $\dot{\varphi}_t$ and the output is the true angle φ_t of the respective front loader part. The observer runs with only a single state variable and all matrices become 1×1-matrices (scalars), $\boldsymbol{A}, \boldsymbol{B}, \boldsymbol{C}, \boldsymbol{L} \to A, B, C, L$. The plant, as a linear time invariant (LTI) system with $A = 0$, $B = 1$, $C = 1$ is written in the time domain and $\circ\!\!-\!\!\bullet$ the frequency domain.

$$
\begin{aligned}
\dot{\varphi} = A\varphi + B\dot{\varphi}_t \quad &\circ\!\!-\!\!\bullet \quad s\varphi(s) = A\varphi(s) + B\dot{\varphi}_t(s) \\
\varphi_t = C\varphi \quad &\circ\!\!-\!\!\bullet \quad \varphi_t(s) = C\varphi(s)
\end{aligned}
\tag{3.10}
$$

The transfer function of plant $P(s)$ is given below with the eigenvalue $\lambda_p = 0$:

$$
P(s) = \frac{\varphi_t(s)}{\dot{\varphi}_t(s)} = \frac{CB}{s - A} = \frac{1}{s}
\tag{3.11}
$$

3.7.1.2 Observer model

The input of the observer corresponds to the measured angular velocity and the angle of the respective front loader part. The gyros measure the true angular velocity $\dot{\varphi}_t$, which is

corrupted by an offset error δ_1 and it follows $\dot{\varphi}_{measured} = \dot{\varphi}_t + \delta_1$. The true position angle φ_t is detected by the direction of the acceleration vectors of chapter 3.1 and the measured angle signal is disturbed by a noise error, $\varphi_{measured} = \varphi_t + \delta_2$. The position detection observer is written in the time domain as:

$$
\begin{aligned}
\dot{\hat{\varphi}} &= A\hat{\varphi} + B\dot{\varphi}_{measured} + L(\varphi_{measured} - \hat{y}) \\
&= A\hat{\varphi} + B\dot{\varphi}_t + L(\varphi_t - \hat{y}) + B\delta_1 + L\delta_2 , \\
\hat{y} &= C\hat{\varphi}
\end{aligned}
\tag{3.12}
$$

In this case, the observer output $\hat{y}$ is equivalent to $\hat{\varphi}$ which is the filtered angle signal of the respective front loader part, see figure 3.8.
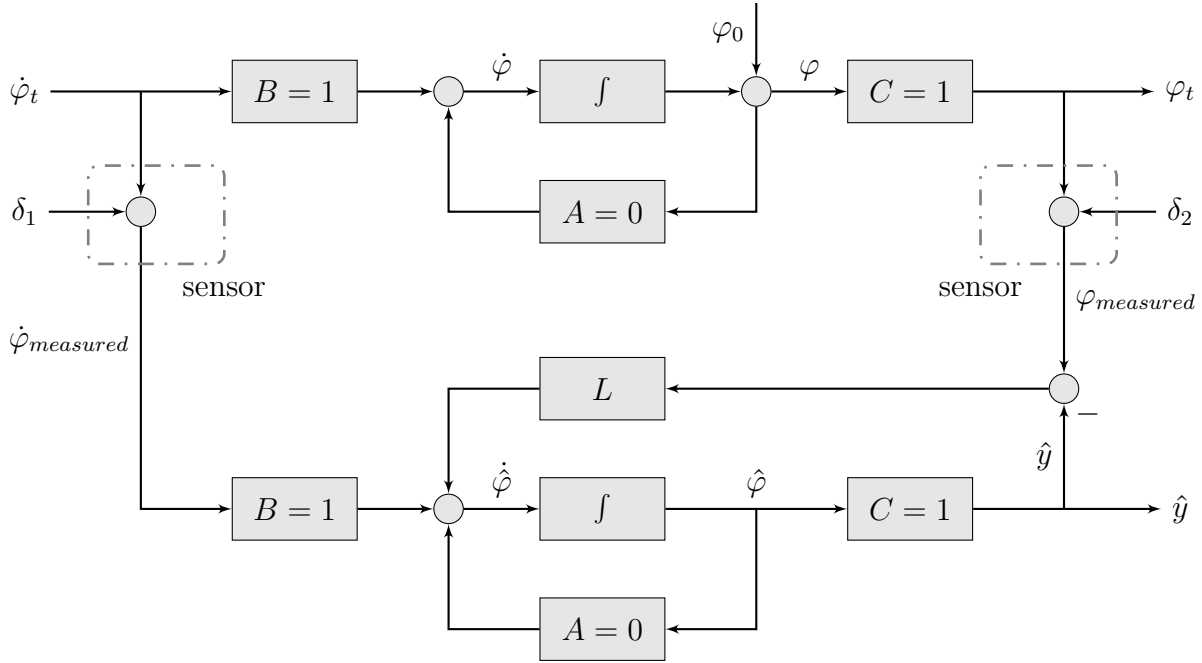
Figure 3.8: Observer for signal filtering

As mentioned above, to define the observer gain L the eigenvalue λ_o of $(A - LC)$ must be chosen on the left side of the eigenvalue of the plant λ_p which is zero. Hence, the observer error is given by the following linear differential equation:

$$
\dot{e}(t) = (A - LC)e(t) - B\delta_1 - L\delta_2
\tag{3.13}
$$

The homogeneous solution of the observer error is given by the following equations [Lun08]:

$$
\begin{aligned}
e(t) &= k \exp(\lambda_o t) \\
\dot{e}(t) &= k\lambda_o \exp(\lambda_o t)
\end{aligned}
\tag{3.14}
$$

If equations (3.14) are inserted into the homogeneous differential equation (3.13) ($\delta_1 = \delta_2 = 0$) and it is given that $A = 0$ and $C = 1$, the observer gain L is determined by the chosen eigenvalue λ_o.

$$\lambda_o = (A - LC) = -L \tag{3.15}$$

3.7.1.3 Observer Gain

This section discusses the effect of different observer gains for $L > 0$ on the observer output $\hat{\varphi}$. Therefore, equation (3.12) is transferred to the frequency domain.

$$\circ\!\!-\!\!\bullet \quad s\hat{\varphi}(s) = A\hat{\varphi}(s) + Bs\varphi_t(s) + L\varphi_t(s) - LC\hat{\varphi}(s) + B\delta_1(s) + L\delta_2(s) \tag{3.16}$$

Solving equation (3.16) for $\hat{\varphi}(s)$ results in equation (3.17).

$$\hat{\varphi}(s) = \frac{1}{s + LC - A}\left(B\left(s + \frac{L}{B}\right)\varphi_t(s) + B\delta_1(s) + L\delta_2(s)\right) \tag{3.17}$$

With $A = 0$, $B = 1$, $C = 1$ equation (3.17) results in equation (3.18).

$$\hat{\varphi}(s) = \varphi_t(s) + \frac{1}{s + L}\delta_1(s) + \frac{L}{s + L}\delta_2(s) \tag{3.18}$$

Since equation (3.18) is a LTI system, the influence of the disturbances δ_1 and δ_2 on the output signal can be analyzed separately. This is evident from the two separate transfer functions:

$$\frac{\hat{\varphi}(s)}{\delta_1(s)} = \frac{1}{s + L} \quad \text{and} \quad \frac{\hat{\varphi}(s)}{\delta_2(s)} = \frac{L}{s + L} \quad .$$

The steady state amplification $A_{\delta 1}$ of $\dfrac{\hat{\varphi}(s)}{\delta_1(s)}$ can be analyzed by applying the final value theorem with a unit step $\sigma(t) = \begin{cases} 0 \text{ for } t < 0 \\ 1 \text{ for } t \geq 0 \end{cases}$, equation (3.19).

$$A_{\delta 1} = \lim_{s \to 0} s \frac{\hat{\varphi}(s)}{\delta_1(s)} \frac{1}{s} = \lim_{s \to 0} \frac{1}{s + L} \frac{s}{s} = \frac{1}{L} \tag{3.19}$$

The steady-state amplification $A_{\delta 1}$ of $\dfrac{\hat{\varphi}(s)}{\delta_1(s)}$ increases if L decreases, see figure 3.9. In order to decrease the influence of the offset disturbance δ_1 on the observer output $\hat{\varphi}$, the amplification must be low. Hence, it is recommended to choose a high value for L with at least $L > 1$.
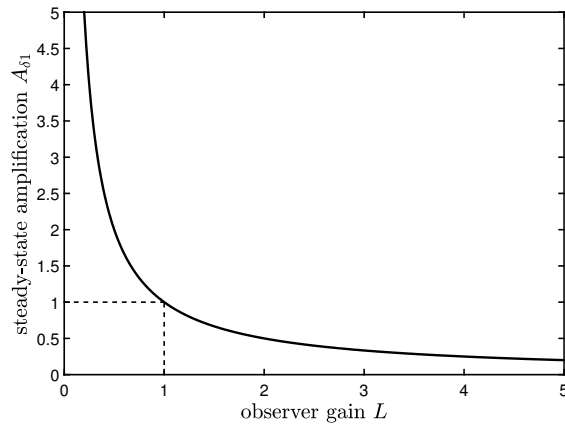
Figure 3.9: Steady state amplification

The transfer function $\dfrac{\hat{\varphi}(s)}{\delta_2(s)}$ represents a low pass filter, whose amplitude starts at the 0dB-level. Its cutoff frequency decreases with decreasing L. Because δ_2 is a noise disturbance, it is recommended to use a low cut-off frequency to remove the noise from the observer output $\hat{\varphi}$. Hence, L should be low.
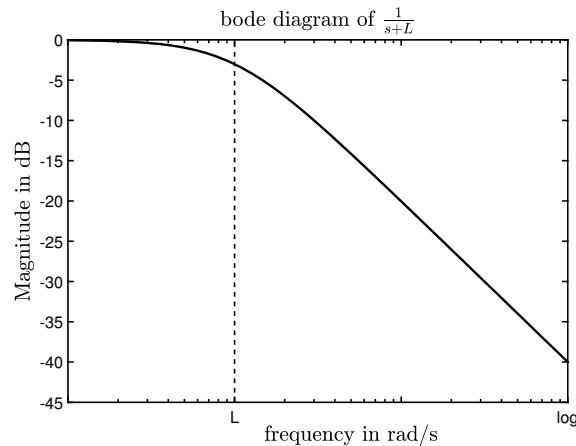
Figure 3.10: Low pass filter with cutoff frequency at L

In conclusion, a high value for L produces an observer output angle signal $\hat{\varphi}$ with a low offset disturbance δ_1 but is corrupted by noise. Conversely, a low value for L has a low noise disturbance δ_2 but is corrupted by the offset.

Figure 3.11 shows the observer output angle $\hat{\varphi}$ for different observer gains L: the higher the gain, the higher the influence of the disturbance noise δ_2. If the gain is low, the offset δ_1 of the gyro influences the observer output. Based on experiments, the gain was chosen as $L = 2.5$.
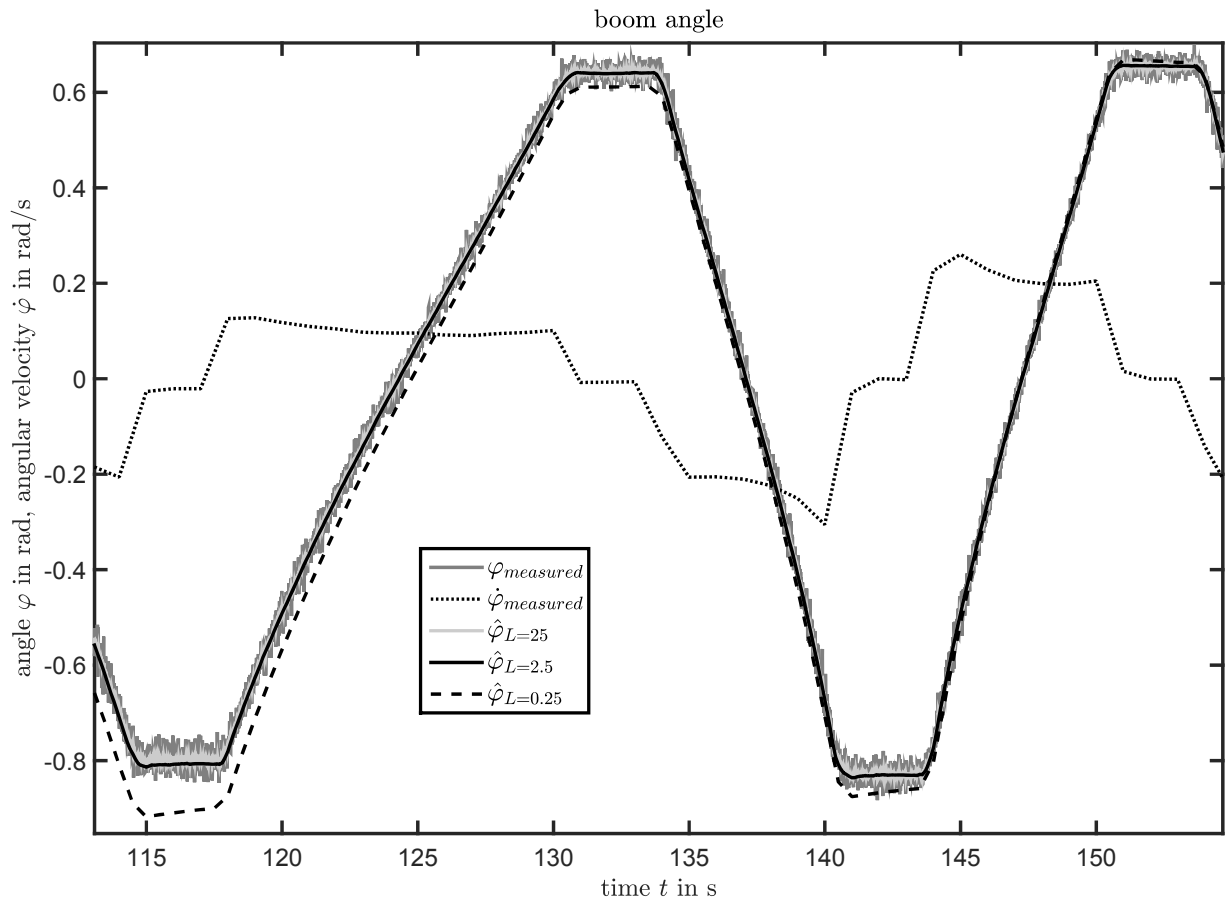
Figure 3.11: Variations of observer gain L

3.8 Cylinder Stroke to Angle Conversion

The cylinder strokes, which are defined from pin to pin, are needed for further processing. They are derived from the position angles φ_{BM} and φ_{BU}. Figure 3.12 shows the relevant dimensions and variables of the front loader for the calculation of the cylinder strokes.
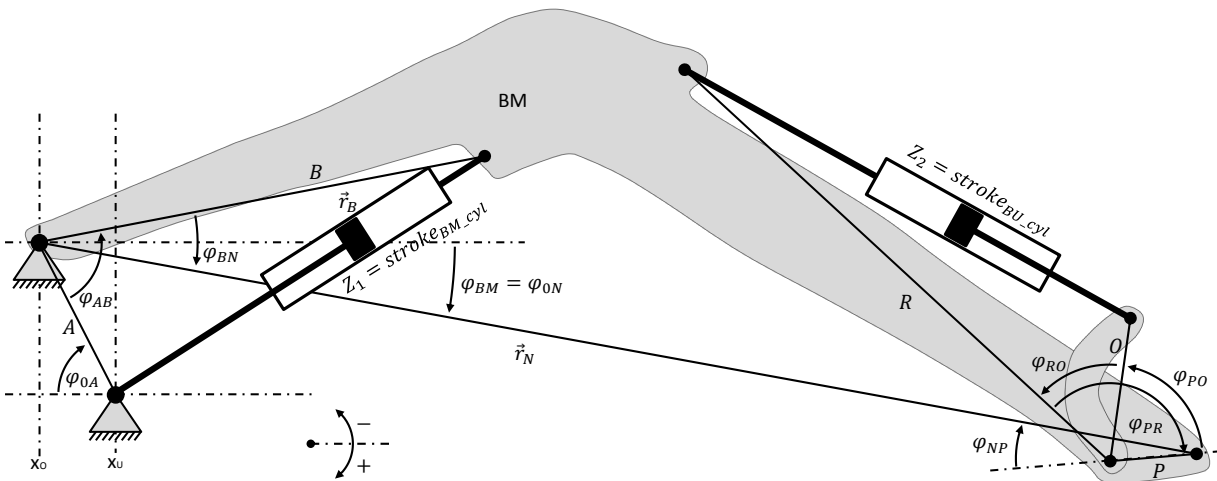
Figure 3.12: Cylinder strokes

With the knowledge of the constant front loader dimensions the strokes Z_1 and Z_2 of the boom and bucket cylinders are calculated by the law of cosines:

$$Z_1 = \sqrt{A^2 + B^2 - 2AB \cos \varphi_{AB}} \tag{3.20}$$

$$Z_2 = \sqrt{O^2 + R^2 - 2RO \cos \varphi_{RO}} \tag{3.21}$$

The angle $\varphi_{AB} = -\varphi_{0A} + \varphi_{0N} - \varphi_{BN}$ is derived from the boom position angle $\varphi_{BM} = \varphi_{0N}$ and the constants $\varphi_{0A}, \varphi_{BN}$. The angle $\varphi_{RO} = -\varphi_{PR} - \varphi_{PO}$ is deduced from the constant φ_{PR} and the bucket linkage, as described in the following section.

3.9 Bucket Linkage Calculation

The bucket cylinder is connected to the tool carrier by a linkage to transfer the linear motion of the cylinder into a rotation around the joint of the tool carrier. Also, due to the gear ratio of the linkage the angle of movement of the bucket or tool carrier is larger than without linkage.

To calculate the cylinder stroke, the linkage of the tipping link O and the bucket link I have to be considered first, see figure 3.13. Hence, the inputs of the linkage are the measured position angles $\varphi_{BU} = \varphi_{0K}$, $\varphi_{BM} = \varphi_{0N}$ and the output is φ_{PO}.
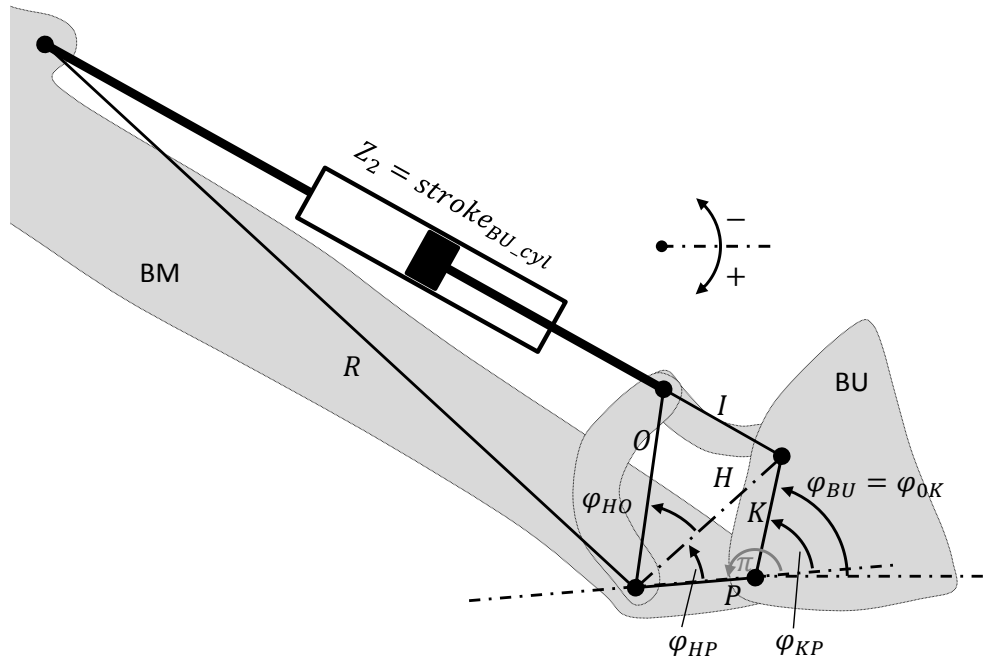
Figure 3.13: Bucket linkage

At first, the angle $\varphi_{KP} = -\varphi_{0N} + \varphi_{NP} + \varphi_{0K}$ has to be calculated to receive the linkage height H (cf. figure 3.12, 3.13).

$$H = \sqrt{K^2 + P^2 - 2KP\cos\left(\pi - \varphi_{KP}\right)} \tag{3.22}$$

With the knowledge of the height the angles φ_{HP}, φ_{HO} are calculated,

$$
\begin{aligned}
\varphi_{HP} &= \arccos\left(\frac{P^2 + H^2 - K^2}{2PH}\right) \\
\varphi_{HO} &= \arccos\left(\frac{O^2 + H^2 - I^2}{2OH}\right)
\end{aligned}
\tag{3.23}
$$

Finally, the demanded angle is $\varphi_{PO} = \varphi_{HP} + \varphi_{HO}$. Additional linkage calculations are described in the references [Hol07] [Tan06].

4 Weighing Function

The dynamic, continuous, and center of gravity independent weighing system describes the approach of a mobile scale that measures payload continuously in standard working conditions of a loader. The result is independent of the center of gravity of the payload and machine movements. In order to achieve this goal, the approach combines two major models. On the one hand, cylinder forces are measured continuously and transferred to torques by using a **static model**. On the other hand, a **multi-body model** of the front loader is created to generate cylinder forces and torques on the joints based on continuously measured accelerations. The output of both models are merged together. The deviation between the two models is the basis for the payload calculation. Splitting the weighing approach into two models provides transferability to different kind of loaders. Thus, only the static model has to be adapted to a different loader. The multi-body model is reduced and parameterized with a calibration function which is explained later in section 4.6.2.

The proceeding and structure of this chapter is illustrated in figure 4.1. First, the **static model** is described which uses the cylinder forces to calculate torques at the front loader main joints. The static model is subject to friction, hence, the friction modeling is explained in detail. Secondly, a detailed **multi-body model** is discussed which is used to transform measured accelerations into torques at the loader joints. Thirdly, the static model and the multi-body model are merged to calculate the **payload** m_L, which is illustrated with a simplified example. Fourthly, it is explained how the algorithms are **simplified and implemented** in order to run them on a real time controller that is applied on a tractor prototype.

The multi-body model is very detailed in order to achieve high accuracy. The parameter identification of the multi-body model consumes a lot of time and effort. The subsequent mounting of an additional part to the front loader makes it necessary to identify the parameters again. Additionally, in serial production each front loader is subject to tolerances, which requires to identify the parameters for each front loader separately. Because this is difficult to accomplish, a **reduced multi-body model** is developed which obtains its parameters from CAD and a short calibration procedure. This calibration procedure can also be automated.
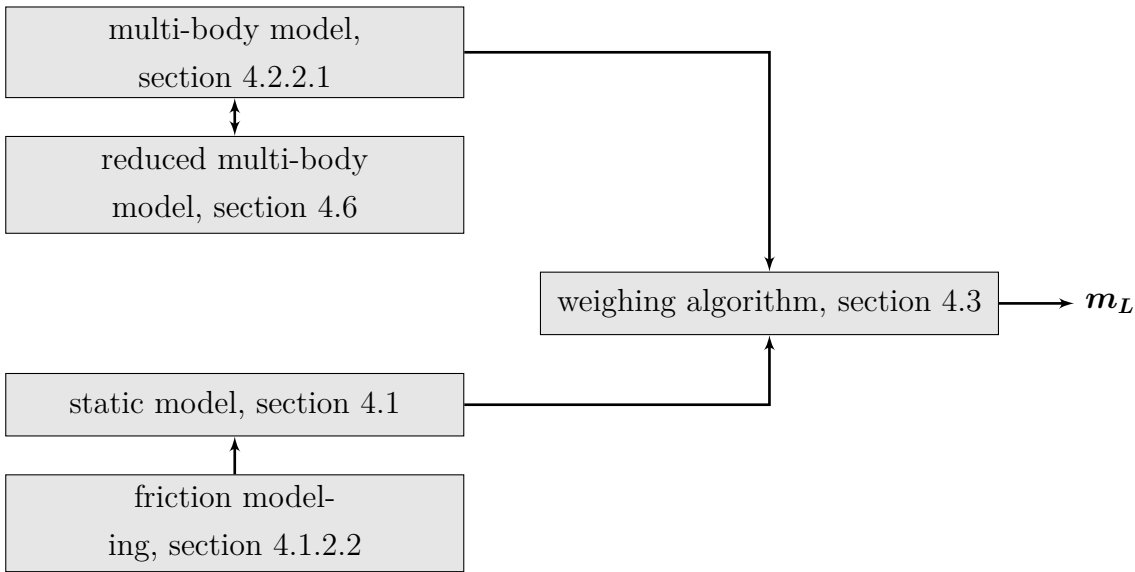
Figure 4.1: Structure of the weighing function

4.1 Static Model

The static model is used to transfer continuously measured cylinder forces into torques at the front loader main joints. In order to achieve this, the cylinder forces, which include friction, are considered as quasi-static condition. Thus, the static calculations are performed on the front loader structure, which allows to transfer the real front loader kinematics into simplified front loader kinematics. The simplified front loader kinematics is an open, planar kinematic chain which consists of three segments: the chassis (T), the boom (BM) and the bucket or tool carrier (BU). Each segment is connected to the next one by a rotational joint. The torques at the joints keep the kinematic front loader chain in position.

Figure 4.2a shows a standard non-self-leveling front loader kinematics. The cylinders, here shown as arrows e.g. $stroke_{BM\_cyl}$, can be treated as prismatic joints. Below, in figure 4.2b, the simplified loader kinematic model is shown.
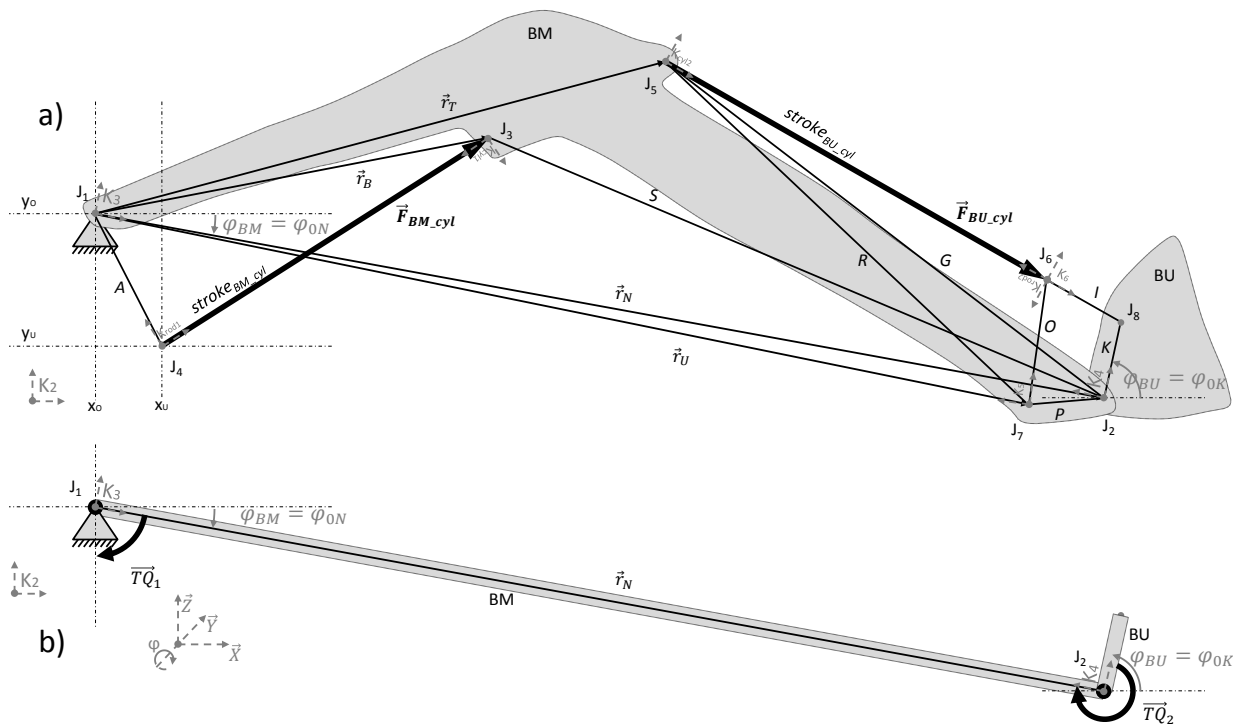
Figure 4.2: Front loader kinematics

The static model of the loader deals with all dimensions and cylinder forces. With the knowledge of the constraints and positions, the cylinder forces $\vec{F}_{BM\_cyl}$ and $\vec{F}_{BU\_cyl}$ can be transferred into torques, $\vec{TQ}_1$ and $\vec{TQ}_2$, at the joints J_1 between tractor and boom or J_2 between boom and bucket. As a result, the inputs are forces and outputs are torques on a simplified loader kinematic. Any kind of front loader can be used for this approach whether it is self-leveling or non-self-leveling, as long as it is transferred into the simplified loader kinematics.

4.1.1 Cylinder Forces

As mentioned before, the static model transfers continuously measured cylinder forces into torques at the main joints of the loader. The applied method in this thesis calculates the cylinder forces F_{cyl} by measuring hydraulic pressures in the cylinders. It is very important to measure these pressures as closely as possible to the cylinder. This reduces influences of pressure drop between sensor and cylinder, which is generated by the oil flow due to the oil viscosity. it is even better to measure inside the cylinder or on a separate cylinder port. This procedure helps to completely avoid the influence of pressure drop. Since the oil viscosity is dependent on the hydraulic oil temperature, the disturbances of both variables have a reduced influence on the measured cylinder force.

The force F_{cyl} of the hydraulic differential cylinders

$$F_{cyl} = p_A A_A - p_B A_B - F_{friction} - m a_{cyl} \qquad (4.1)$$

is calculated by the pressures p and the respective area A at the piston side "$_A$" and the rod side "$_B$", see figure 4.3. The parameters of the cylinders are specified in table A.5 in the appendix.

Due to the sealing, the cylinder force is reduced by the friction $F_{friction}$, which is explained in-depth in chapter 2.9.1. During movement, the inertial force $m a_{cyl}$ has to be considered, too. In this thesis, the inertial force is considered by the multi-body model. Hence, the cylinder will be treated without mass.
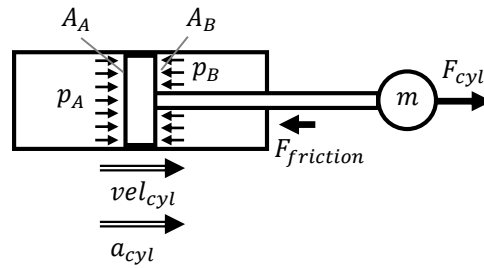
Figure 4.3: Cylinder force

If the cylinder is at the minimum or maximum end-stroke position, as shown in figure 4.4, it is not possible to measure F_{cyl} by the hydraulic pressures. In this case, the forces are partly supported by the cylinder walls. If the cylinder is close to the end-stroke and equipped with an end-stroke damping, it is also not possible to measure F_{cyl}.
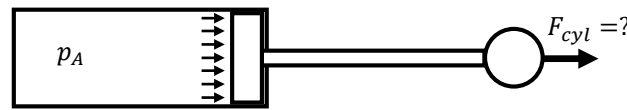
Figure 4.4: Cylinder end-stroke

To measure the cylinder force continuously, the end-stroke positions have to be avoided. See also [Fin06], [WG08], and [Wat07].

A preferable alternative method is to measure F_{cyl} with strain gauges applied on a homogeneous position of the cylinder rod. This approach avoids the influence of the cylinder seal friction on the actuator force measurement. It is meaningful to reduce parts between the point of measuring and the joint, where the torque is calculated. For instance, the torque at the bucket joint J_2 is calculated by measuring the bucket cylinder forces. To

calculate this torque, the bucket linkage with all its joints has to be considered. It can be said that the less pivots have to be considered in the calculation the less friction disturbs the result. Accordingly, the strain gauges could be applied directly at the upper bucket linkage (figure 4.2 (a) part I). A further advantage of this method is that the force measurement can be performed in every cylinder position even in the end-stroke position. The disadvantage of this method is the time-consuming bonding and calibration of the strain gauges. Moreover, the calibration of the strain gauges requires a test bench, which applies known test loads to the cylinder.

4.1.2 Friction

The payload measurement is performed dynamically, hence, friction in the cylinders and joints or bearings have to be taken into account. The friction at the joints and hydraulic cylinders is different for each front loader. This is caused by many aspects, for example, by manufacturing tolerances, by wear due to the number of operation hours, or by temperature.

4.1.2.1 Approach of Friction Modeling

Friction compensation is a very basic problem of the payload weighing system. There are different methods to consider friction. A common way is to design friction with a dynamic friction model as described in section 2.9.4.2. If the system is in a steady condition, for instance, when the actuator does not accelerate, the dynamic friction model is equal to the steady state friction model as described in section 2.9.4.1. The dynamic friction model needs a high sample rate to model the transient response of pre-displacement which makes it difficult to implement the dynamic friction model for a common real time controller.

A friction observer as described in [TASLH08] is inappropriate for the weighing system because, generally, a dynamic model with known inertial mass is needed. A friction observer calculates the friction force with the knowledge of the input actuator force and the acceleration of the inertial mass. If the mass changes, the system experiences different accelerations which are concluded as a different friction force instead of a different mass. In this case, the mass (payload) changes permanently and has to be calculated. Hence the friction force must be modeled. The accuracy of the friction is strongly related to the accuracy of friction model parameters, which are generally obtained from empirical data. Hence, it is meaningful to reduce the parameters to those which are easy to identify in tests.

In order to consider friction, this thesis develops a steady state friction model which is based on the "Pressure Based Model" of section 2.9.4.3. The friction model is parameter-

ized with data which is obtained from tests with the loader. Basically, the Coulomb friction in the steady state friction model (cf. section 2.9.4.1) is replaced by the "Pressure Based Model". The stiction is not considered because measurements show that stiction is insignificantly low except directly after longer standstill of the loader. This can be explained by the decreasing lubrication film between the sliding partners when standing still. Also, measurements show that the cylinder forces change during standstill (cf. section A.6). For example, after moving the boom upward the seal friction acts against the movement, which is downward. During standstill, the cylinder drifts downward which causes the seal friction to act upward. Because the drift is too small to detect, it is not possible to define the direction of the friction. For this reason, it is not yet possible to consider friction during standstill of the front loader. Hence, stiction is not considered. Also, the viscous friction, which is dependent on the actuator velocity, is neglected. However, the influence of the actuator velocity is considered indirectly as explained in the following section.

4.1.2.2 Procedure of Friction Modeling

The total friction is a sum of bearing frictions and seal frictions. The friction generated by the bearings is low compared to the total friction (cf. section A.10). Thus, the cylinder seals are primarily responsible for the friction and the total friction is treated as if it is only related to the cylinders.

It is assumed that the amount of friction is symmetrical. That means the absolute friction of a boom down movement is the same as of a boom up movement as long as the load and the corresponding cylinder pressures remain constant. This assumption is based on the friction of the piston seals, which are built symmetrically in both directions, and due to the bearings, which ideally have the same amount of friction no matter in which direction they turn (cf. section 2.9.3). The rod seal is built asymmetrically. Therefore, the friction of the rod seal also varies from in- to out-movement of the actuator. This is simplified by treating friction of the rod seal symmetrically.

In order to identify the overall friction the tractor needs to stand still and only the front loader moves up and down with a constant cylinder velocity. Due to the quasi-static condition, all acceleration terms will be zero and the force balance will be as follows (cf. figure 4.5):

$$F_{cyl\_raw} = F_{cyl} - F_{friction} \tag{4.2}$$

The raw cylinder force F_{cyl_raw} is calculated by the cylinder pressures p_A, p_B and its area dimensions A_A, A_B. (index "$_A$" stands for the piston side and index "$_B$" stands for the

rod side)

$$F_{cyl\_raw} = F_A - F_B = p_A A_A - p_B A_B \tag{4.3}$$
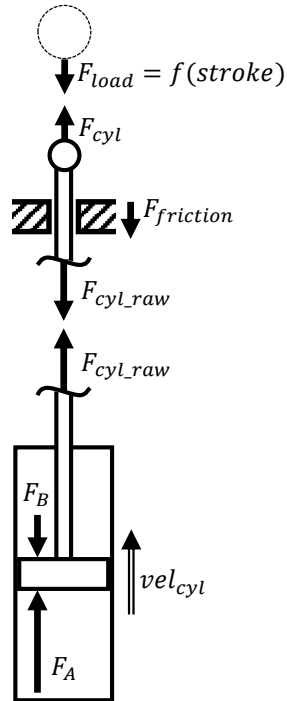
Figure 4.5: Cylinder force

The mass of the front loader and the position of the tractor are constant during the measurement. Hence, the force F_{load}, and along with it F_{cyl}, are only functions of the loader position or cylinder stroke. To evaluate the friction, several up and down cycles with different cylinder velocities vel_{cyl} are performed. During the movement, pressures are recorded and the force F_{cyl_raw} is calculated, as displayed in figure 4.6.
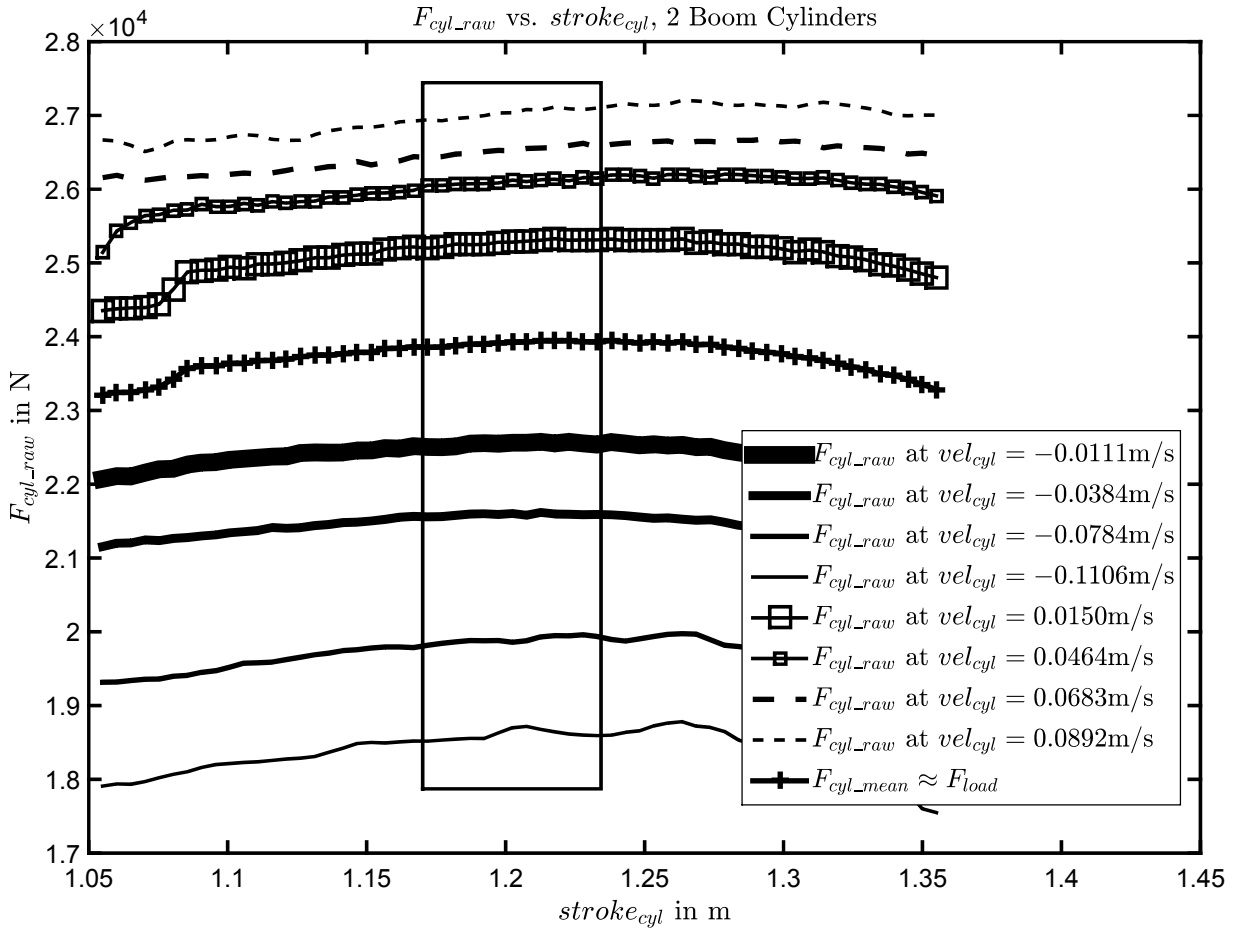
Figure 4.6: Cylinder force over boom cylinder stroke

The friction wants to hold the front loader in its position and works against the movement. If the cylinder speed is positive $vel_{cyl} > 0$, the boom moves upward and the measured cylinder force F_{cyl_raw} is higher than the force F_{load} due to the friction. If the boom moves downward the cylinder force is lower than F_{load}.

The force F_{load} can be obtained by the multi-body model of the front loader, but the model is not accurate enough. Also, due to manufacturing tolerances, the model parameters slightly change at different front loaders. Thus, the boom of the empty front loader is moved up and down very slowly ($vel_{cyl} \approx 0.015 \text{m/s}$) and the force F_{load} is approximated by the mean value of the forces F_{cyl_raw} for up and down movement.

$$F_{load} \approx F_{cyl\_mean} = \frac{F_{cyl\_raw\ up\ slow} + F_{cyl\_raw\ down\ slow}}{2} \qquad (4.4)$$

The approximated force F_{load} is more accurate if the difference between the raw forces $F_{cyl\_raw\ up/down\ slow}$ is kept as small as possible. This can be achieved by moving the front

loader very slowly and without a payload or attached tool. The faster the movement is the higher are the pressures because the return-to-tank pressure will be backed up, as shown in figure 4.7, and the friction at the sealing increases with the pressure (cf. chapter 2.9.1).
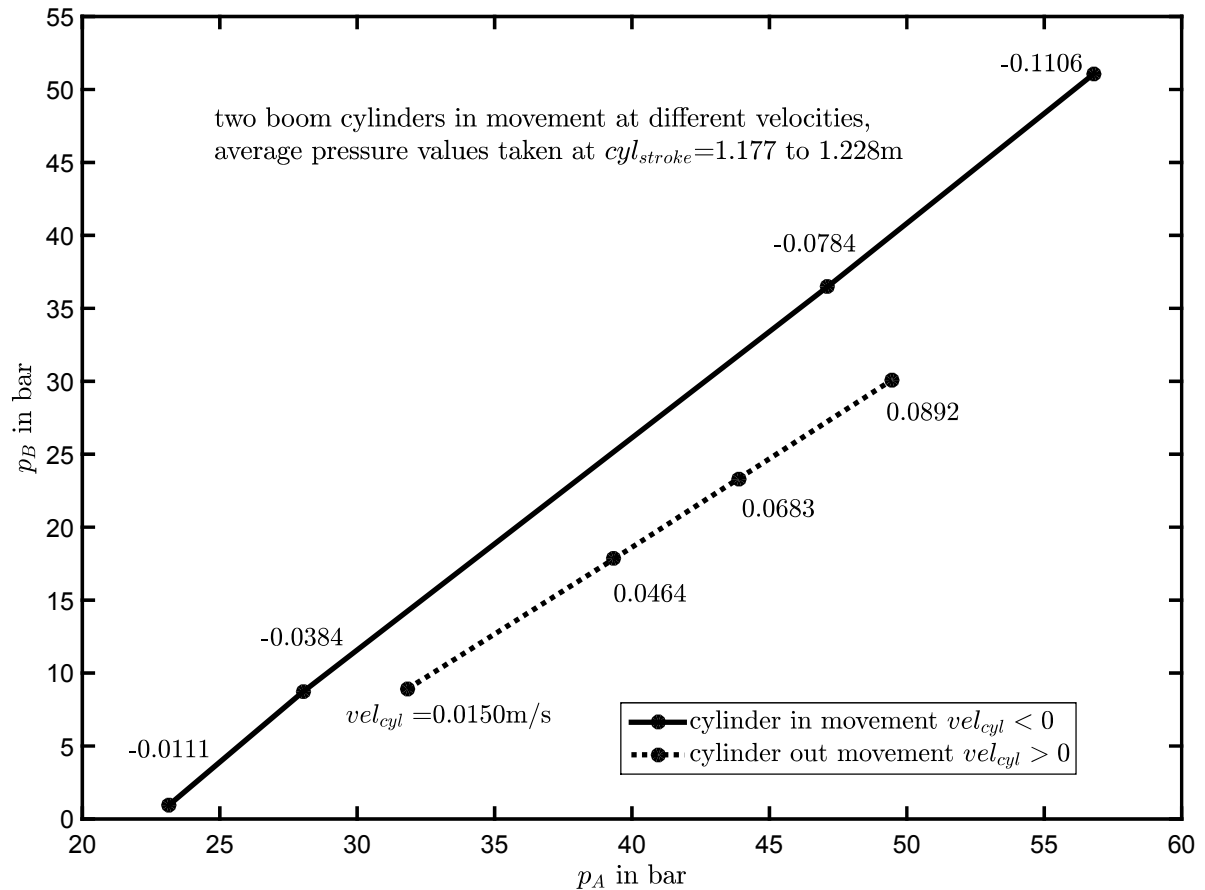
Figure 4.7: Different pressures at different cylinder velocities

In addition, the friction rises with the payload and higher payloads generate higher pressures. Hence, it is obvious to model the friction as a function of pressures,

$$F_{friction} = k_1 p_A + k_2 p_B + k_3 \tag{4.5}$$

with constant factors k_i which are derived from the pressure based model as described in chapter 2.9.4.3. The factor k_3 results from the mounting preload of the seals. As mentioned above, the boom is moved up- and downward at different cylinder velocities that cause different pressures. For these movements, the friction is set into relation with the corresponding cylinder pressures, as shown in figure 4.8. For this purpose, the friction force is calculated by the following equation.

$$F_{friction} = F_{cyl\_raw} - F_{load} \approx F_{cyl\_raw} - F_{cyl\_mean} \tag{4.6}$$

To avoid influences of acceleration and deceleration of the front loader movements on the measurement, the start and end of the movement is not taken into account. Hence, the cylinder forces of equation (4.6) are only considered in a small range of movement which is indicated by the box in figure 4.6. Inside the box, a smooth and fluent movement is guaranteed.
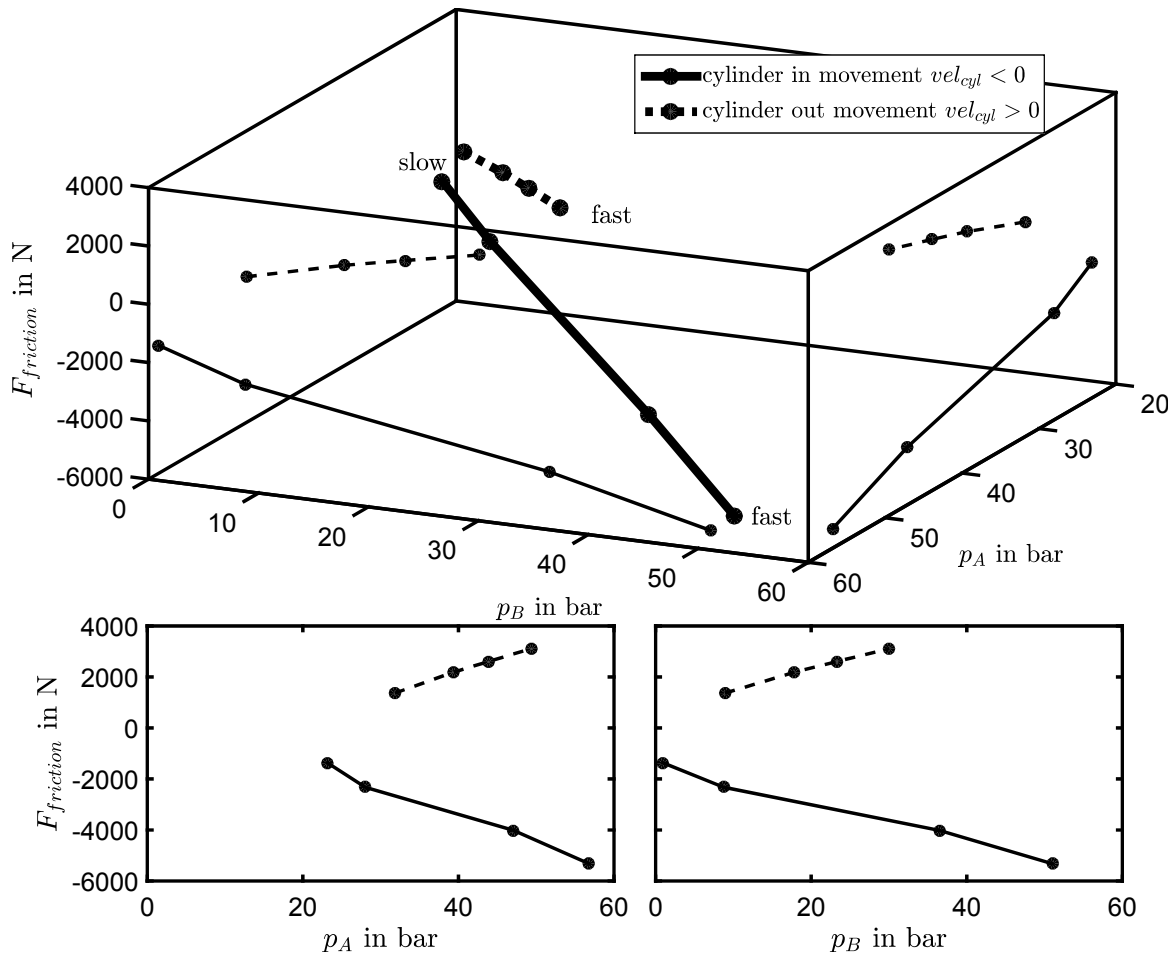
Figure 4.8: Different friction force at different pressure

This is the first step to generate a pressure based friction characteristic. To receive more measurement points, the bucket cylinders are taken into account as well. Friction is different for cylinders with different dimensions although the pressure is the same. In order to handle different cylinder dimensions with the friction model, an approach using seal loads $F_{sealPiston}$ and $F_{sealRod}$ is introduced. The approach is based on the assumption that the material of the seal is compressed by facing hydraulic pressure that causes a seal load. Due to the elastic property of the seal the pressure is transformed into a normal force in direction of the cylinder wall or rod as shown in a close-up view in figure 4.9. This allows to adopt Amontons 1st law and the friction force is expressed proportional to the seal load

(cf. section 2.9.2). For example, $F_{sealRod}$ is calculated as follows:

$$F_{sealRod} = p_B A_{sealRod} = p_B \frac{\pi}{4}(D_{seal}^2 - D_{rod}^2) \tag{4.7}$$

The effective area $A_{sealRod}$ of the seal, which faces the hydraulic pressure p_B, is explained in figure 4.9.
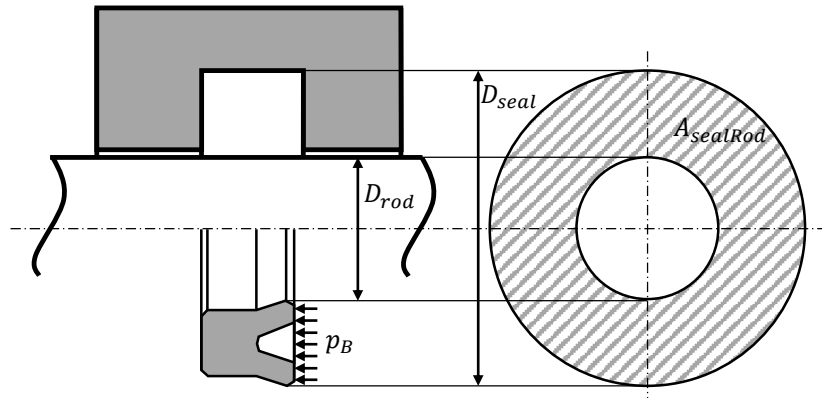
Figure 4.9: Area to calculate the seal load

The piston seal load $F_{sealPiston}$ is calculated in the same way. Due to the symmetrical construction of the piston seal the hydraulic pressure is applied from both sides, but only the higher pressure of the rod or piston side is considered. The higher pressure pushes the seal or the loading ring against the edge of the groove. In addition to the lower pressure, the seal is also supported by the groove (F_{groove}) at the low pressure side, as shown in figure 4.10. Hence, the relevant force is equal to the force applied by the higher pressure.
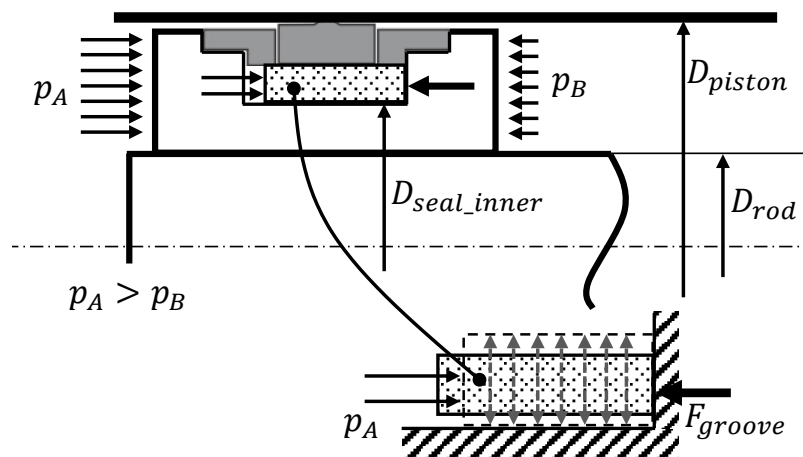
Figure 4.10: Piston seal support at the low pressure side

The previous assumptions turn equation (4.5) into equation (4.8).

$$F_{friction} = k_1 F_{sealPiston} + k_2 F_{sealRod} + k_3 \tag{4.8}$$

To determine the factors k_1 to k_3, several measurements are taken with the boom and bucket cylinders and with different seal loads. To increase the amount of measurement points to evaluate the factors k_1 to k_3, the absolute value of the measured friction is used which turns equation (4.6) into the following expression:

$$F_{friction\_measured} = |F_{cyl\_raw} - F_{cyl\_mean}| \tag{4.9}$$

In figure 4.11 all measurement points are displayed and linearly approximated with the plane.

$$F_{friction} = 0.12 F_{sealPiston} + 0.07 F_{sealRod} + 700 \tag{4.10}$$

Equation (4.10) represents the approximated friction.
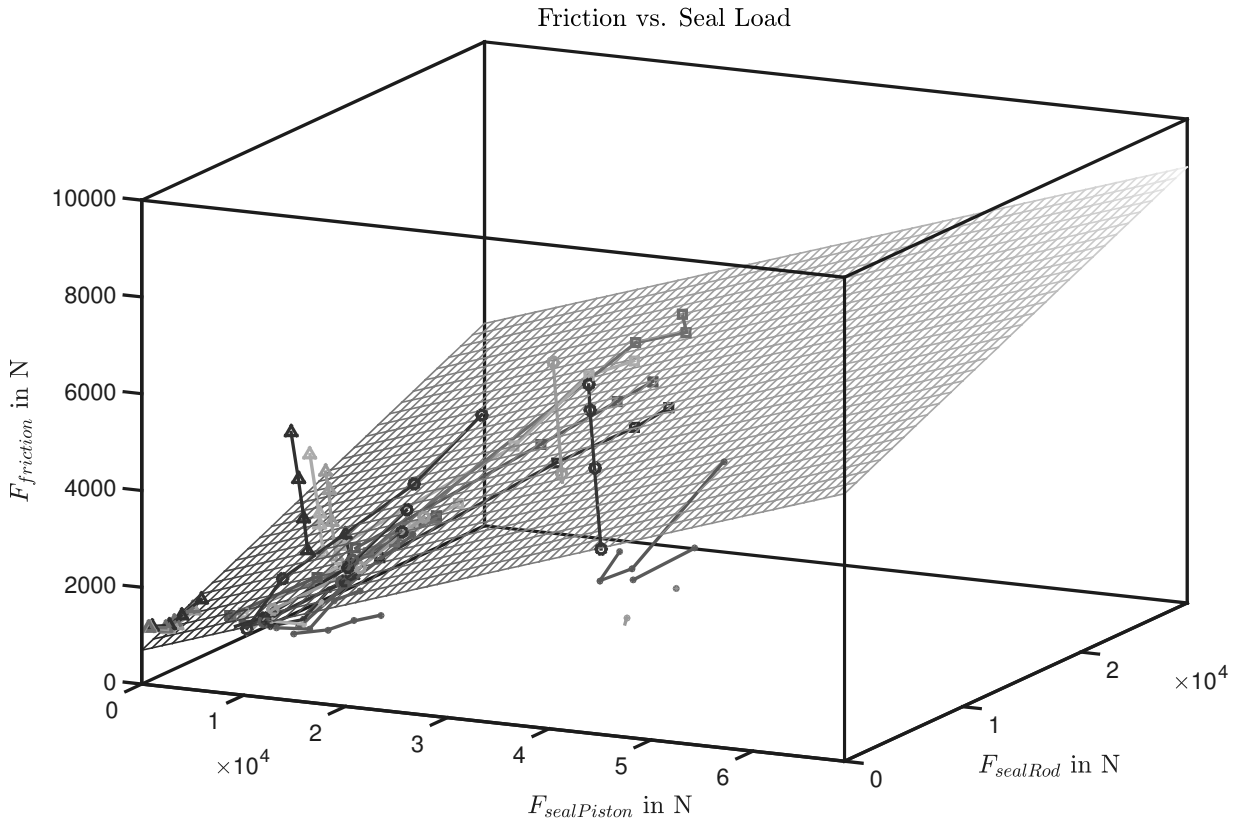
Figure 4.11: Cylinder friction

The friction modeling of the front loader is only applied during cylinder movements. The stiction at standstill is not considered because of some non predictable settlement effects, which are described in appendix A.6. Thus, only a steady state friction model is applied (cf. chapter 2.9.4). The final friction, as it is used in this thesis, is given by equation (4.11). Here, the friction is modeled by the tanh-function for velocities close to zero .

$$F_{friction} = \tanh\left(k_{tanh} vel_{cyl}\right) \left(0.12 F_{sealPiston} + 0.07 F_{sealRod} + 700\right) \tag{4.11}$$

4.1.3 Torque Calculation

The static model is used to calculate torques at the joints. Basically, the previously discussed cylinder forces F_{cyl} are multiplied with their effective lever h. Since the structure of the front loader is a planar kinematic chain, only the torque in the y-axis, TQ_y, is calculated. Hence, the complete torque vector is given by: $\vec{TQ} = \begin{bmatrix} 0 \\ TQ_y \\ 0 \end{bmatrix}$.

All the relevant geometric dimensions of the following sections are specified in table A.3.

4.1.3.1 Torque at the First Joint

Figure 4.12 shows the boom cylinder with its length Z_1 in its mounting position. The distance A is given by the joints of the mounting positions that connect the front loader to the chassis. The distance B is between the cylinder mounting at the boom and the main joint J_1. The angle φ_{AB} corresponds to the boom position relative to the chassis and is given by the position detection. In the following, the calculation of the torque $\vec{TQ}_1$ at the first joint J_1 is described.
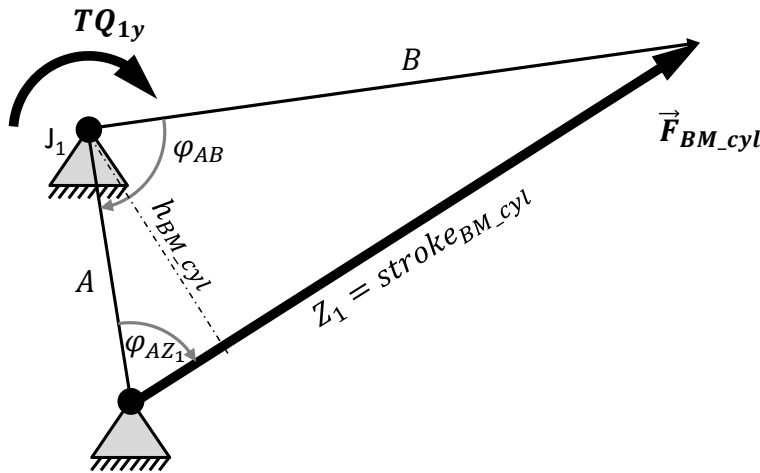
Figure 4.12: Torque at the first joint

The law of sine for the triangle A, B, Z_1 is given by:

$$\frac{\sin(\varphi_{AB})}{Z_1} = \frac{\sin(\varphi_{AZ_1})}{B} \tag{4.12}$$

The effective lever h_{BMcyl} of the actuator in respect to the first joint is calculated with the sine of φ_{AZ_1}.

$$\sin(\varphi_{AZ_1}) = \frac{h_{BMcyl}}{A} \tag{4.13}$$

Finally, the torque TQ_{1_y} is calculated with the force $\vec{F}_{BMcyl}$ and its effective lever.

$$TQ_{1_y} = -|\vec{F}_{BMcyl}|h_{BMcyl} = -|\vec{F}_{BMcyl}|\frac{AB\sin(\varphi_{AB})}{Z_1} \tag{4.14}$$

4.1.3.2 Torque at the Second Joint

Figure 4.13 shows the bucket cylinder with its length Z_2 and its absolute force $|\vec{F}_{BUcyl}|$ connected to the bucket linkage (cf. chapter 3.9). All angles φ are derived from the position detection. The force $|\vec{F}_I|$ has to be calculated first to obtain the torque $\vec{TQ}_2$ at the second joint J_2. Chapter 4.1.1 mentions to measure force as closely as possible at the joint in order to reduce friction influences. This could be done by applying strain gauges directly on the link I. In this thesis, the cylinder forces are used to calculate torques at the joints. Therefore, the force $|\vec{F}_I|$ is obtained by the force equilibrium as shown in figure 4.13.
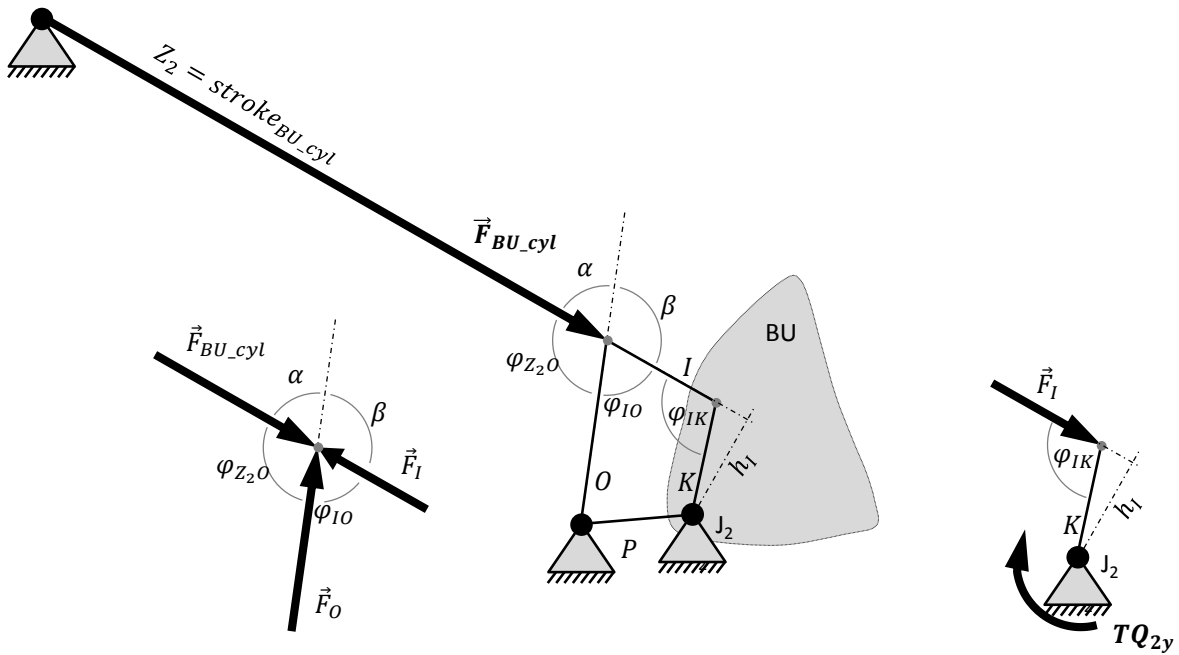
Figure 4.13: Torque at the second joint

The force equilibrium is described by the following formula:

$$|\vec{F}_{BUcyl}|\sin(\varphi_{Z_2O}) = |\vec{F}_I|\sin(\varphi_{IO}) \tag{4.15}$$

The effective lever h_I of the actuator related to the second joint is calculated with the sine of φ_{IK}.

$$h_I = K\sin(\varphi_{IK}) \tag{4.16}$$

Finally, the torque TQ_{2_y} is calculated by the force and its effective lever.

$$TQ_{2_y} = -|\vec{F}_I| h_I = -|\vec{F}_{BUcyl}| \frac{\sin(\varphi_{Z_2O})}{\sin(\varphi_{IO})} K \sin(\varphi_{IK}) \tag{4.17}$$

4.2 Multi-Body Model of a Front Loader

The multi-body model is used to turn continuously measured accelerations into the resulting torques at the front loader main joints J_1 and J_2. At first, it is important to look at the composition of a front loader. A front loader consists of several parts. Each part has its own mass m, center of gravity $\vec{r}_{cog}$, and moment of inertia Θ and is connected via joints to the next part. A common front loader can be simplified by an open, planar kinematic chain with two degrees of freedom (DOFs), as described in chapter 2.2. Thus, only a two dimensional multi-body model is considered.

Figure 4.14 illustrates the multi-body model of the two-dimensional front loader as discussed in this thesis. It consists of eight links, also termed as parts, which are described in table 4.1. Each part has its own coordinate system with the origin positioned in an axis of a joint. For instance, the boom has the coordinate system K_3 and the bucket cylinder the coordinate system K_{cyl2}. The masses m are shown as a point mass in the center of gravity of each part.
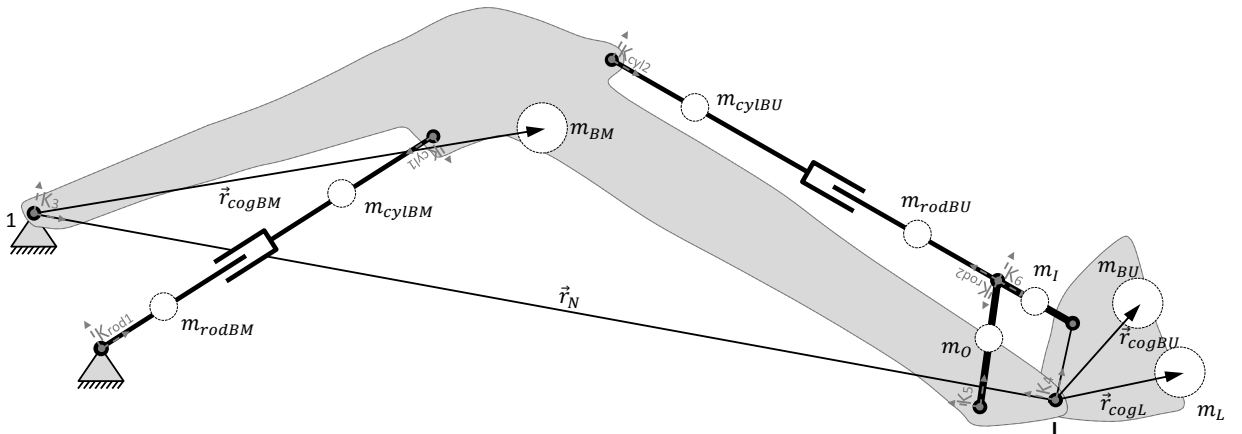
Figure 4.14: Full multi-body model of a front loader

Part (i)	Full form	Coordinate sys.
BM	boom	K3
BU	bucket	K4
I	bucket link of the bucket linkage	K6
O	tipping link of the bucket linkage	K5
cylBM	cylinder of the boom actuator	Kcyl1
rodBM	rod of the boom actuator	Krod1
cylBU	cylinder of the bucket actuator	Kcyl2
rodBU	rod of the bucket actuator	Krod2
L	payload	K4

Table 4.1: Parts of the multi-body model

The mass of the payload is of course unknown and is the variable that is being searched for. In order to achieve this, the payload and its unknown center of gravity position have to be considered in the following equations.

4.2.1 Differential Equations

A common loader has two DOFs (cf. chapter 2.2). Hence, two equations are formulated in order to calculate the torques at the main joints of the loader. In order to achieve this, the proceeding is first discussed in general and then transferred to the front loader.

Every part (i) of the front loader with its mass m_i is impacted by an acceleration $\vec{a}_i$ at its center of gravity which results in a force $\vec{F}_i = -m_i \vec{a}_i$, as shown in figure 4.15. This force has to be supported and generates a force $\vec{F}_{Joint}$ and a torque $\vec{TQ}$ at the front loader joints. The torque of a single part

$$\vec{TQ}_i = \vec{r}_{cog\,i} \times \vec{F}_i + \Theta_i \ddot{\vec{\varphi}}_i \tag{4.18}$$

is a sum of the torque induced by the force $\vec{F}_i$ with its respective lever $\vec{r}_{cog\,i}$, and the torque produced by the angular acceleration $\ddot{\vec{\varphi}}_i$, and the moment of inertia Θ_i along the main axis. The vector $\vec{r}_{cog\,i}$ always points from the joint to the center of gravity of the relevant part (i).
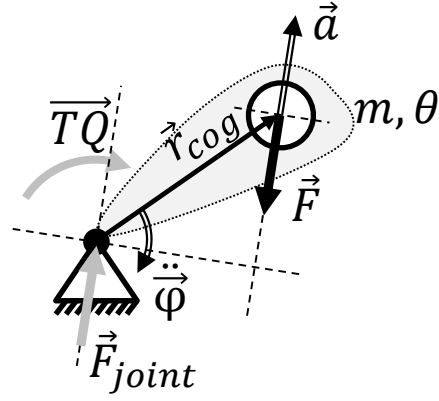
Figure 4.15: Forces at the joint

This calculation is repeated for every part of the front loader at the first joint between tractor and boom and the second joint between boom and bucket. For example, the torque generated by the boom at the first joint yields

$$\vec{TQ}_{BM_{J1}} = \vec{r}_{cogBM} \times (-m_{BM}\vec{a}_{BM}) + \Theta_{BM}\ddot{\vec{\varphi}}_{BM} \tag{4.19}$$

The final torque calculation for all parts at the first joint is as follows:

$$-\vec{TQ}_1 = (\vec{TQ}_{BM}+\vec{TQ}_{BU}+\vec{TQ}_I+\vec{TQ}_O+\vec{TQ}_{cylBM}+\vec{TQ}_{rodBM}+\vec{TQ}_{cylBU}+\vec{TQ}_{rodBU}+\vec{TQ}_L)_{J1} \tag{4.20}$$

As an example, at the second joint, the torque generated only by the bucket yields

$$\vec{TQ}_{BU_{J2}} = \vec{r}_{cogBU} \times (-m_{BU}\vec{a}_{BU}) + \Theta_{BU}\ddot{\vec{\varphi}}_{BU} \tag{4.21}$$

For all relevant parts, the torque at the second joint results in:

$$-\vec{TQ}_2 = (\vec{TQ}_{BU} + \vec{TQ}_I + \vec{TQ}_O + \vec{TQ}_{cylBU} + \vec{TQ}_{rodBU} + \vec{TQ}_L)_{J2} \tag{4.22}$$

The inertial force of the cylinders and the bucket linkage is split up to calculate the torque at the joints. For example, the inertial force of the boom cylinder is partly supported by the chassis and partly supported by the boom. Only the force supported by the boom affects the torque at the first joint, as shown in section A.11.

4.2.2 Parameters

This section explains how to obtain the parameters for the multi-body model. The parameters of the static model are given by dimensions which are defined in table A.3.2 and cylinder forces which are explained before in section 4.1.1.

As mentioned before, the multi-body model is used to transfer measured accelerations into resulting torques at the front loader main joints. Hence, the translational acceleration, angular acceleration, and angular velocity are measured continuously with an IMU. Furthermore, the position of the front loader is needed, which is continuously provided by the position detection as described in chapter 3. The relative movements and accelerations between the loader parts are necessary to calculate the accelerations for each center of gravity, as explained in the following section. These relative movements and accelerations can be derived from the position detection. Alternatively, they can be continuously measured by subtracting the angular velocities and angular accelerations of different IMUs as applied in this thesis. All other parameters such as masses, inertia, and dimensions are constants and defined once before installing the weighing system.

4.2.2.1 Accelerations

The acceleration $\vec{a}$ can be measured with a sensor at any position. The accelerations $\vec{a}_i$ for each center of gravity are calculated with the knowledge of the angular velocity $\dot{\varphi}$, angular acceleration $\ddot{\varphi}$, center of gravity positions, and front loader movements. For example, section 2.6.4 demonstrates the calculation of the acceleration for any point at the tractor with IMU $S2$. In this thesis, the boom IMU $S3$ is used to calculate the accelerations $\vec{a}_i$ for each center of gravity of the front loader as illustrated in figure 4.16. As an example, equation (2.20) is converted to calculate the acceleration $\vec{a}_P$ with IMU $S3$ for any point at the boom:

$$\vec{a}_P = \ddot{\vec{r}}_{1P} = \ddot{\vec{r}}_{1S3} + \dot{\vec{\varphi}}_{S3} \times \left(\dot{\vec{\varphi}}_{S3} \times [\vec{r}_{3P} - \vec{r}_{3S3}] \right) + \ddot{\vec{\varphi}}_{S3} \times [\vec{r}_{3P} - \vec{r}_{3S3}]$$

$$\vec{a}_P = \ddot{\vec{r}}_{1P} = \ddot{\vec{r}}_{1S3} + \dot{\vec{\varphi}}_{S3} \times \left(\dot{\vec{\varphi}}_{2} \times [\vec{r}_{S3P}] \right) + \ddot{\vec{\varphi}}_{S3} \times [\vec{r}_{S3P}] \tag{4.23}$$
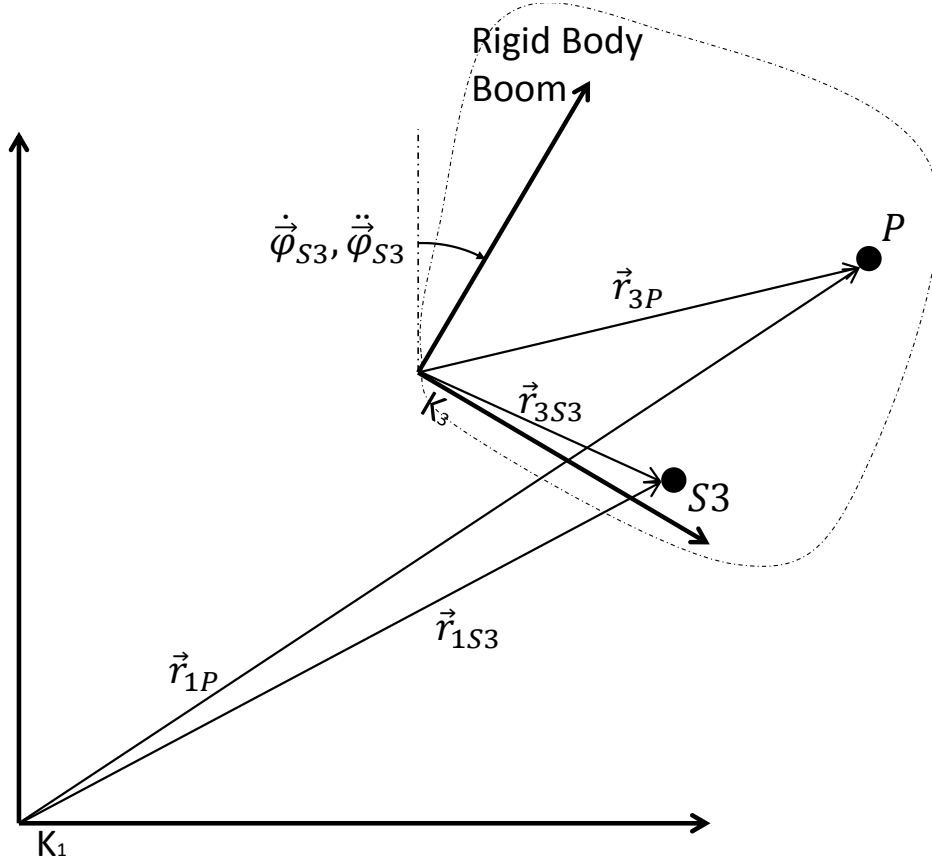
Figure 4.16: Acceleration calculated for any point at the boom

If a joint lies between the IMU and the desired point, the relative movement must be taken into account. For instance, to calculate the acceleration $\vec{a}_P$ at other parts, like on the bucket, the relative movements have to be considered as shown in figure 2.19 in section 2.6.5.3. Equation (2.24), simplified for an acceleration at the bucket, turns into:

$$
\begin{aligned}
\vec{a}_P = \ddot{\vec{r}}_{1P} = \ddot{\vec{r}}_{1S3} &+ (\dot{\vec{\varphi}}_{S3}) \times \left((\dot{\vec{\varphi}}_{S3}) \times [\vec{r}_{S3P}] \right) + (\ddot{\vec{\varphi}}_{S3}) \times [\vec{r}_{S3P}] \\
&+ 2((\dot{\vec{\varphi}}_{S3}) \times (\dot{\vec{\varphi}}_4 \times \vec{r}_{4P})) + \dot{\vec{\varphi}}_4 \times (\dot{\vec{\varphi}}_4 \times \vec{r}_{4P}) + (\ddot{\vec{\varphi}}_4 \times \vec{r}_{4P})
\end{aligned}
\tag{4.24}
$$

The acceleration $\ddot{\vec{r}}_{1S3} = \vec{a}_{S3}$, angular velocity $\dot{\vec{\varphi}}_{S3}$, and angular acceleration $\ddot{\vec{\varphi}}_{S3}$ are directly measured with the IMU $S3$. The relative angular velocity $\dot{\vec{\varphi}}_4$ and the relative angular acceleration $\ddot{\vec{\varphi}}_4$ between bucket and boom can be derived from the position detection or can be continuously measured by subtracting the angular velocities and angular accelerations of IMU $S3$ from IMU $S4$ (e.g. $\dot{\vec{\varphi}}_{S4} - \dot{\vec{\varphi}}_{S3}$).

A disadvantage is that summing several sensor values increases the deviation because every sensor value deviates from the true value. To reduce deviations due to an inaccurate angular velocity or angular acceleration signal it is advantageous to minimize the distance

$[\vec{r}_{S3P}]$ between IMU and the point, where the acceleration is calculated for. For the purpose of this thesis, it is better to place the IMU directly at the center of gravity or at least close to it at the same part. In order to simplify the calculation, the following rule is applied. If the IMU is mounted at a different part, as in equation (4.24), and the relative movement is slow between both parts, the acceleration terms, which consider relative movement, can be neglected for small parts.

The acceleration $\vec{a}_L$ of the payload cannot be defined accurately, because the exact center of gravity position $\vec{r}_{cogL\_exact}$ of the payload is unknown. Nevertheless, the center of gravity position of the payload will be close to the bucket or attachment carrier. Therefore, the acceleration $\vec{a}_L$ is calculated with an approximated center of gravity position $\vec{r}_{cogL\_exact} \approx \vec{r}_{cogL}$ as shown in equation (4.25). This procedure is acceptable, because deviations only arise if the payload experiences angular velocities or angular accelerations (see also equation (4.36)).

$$\vec{a}_{L[K3]} = \ddot{\vec{a}}_{S3} + (\dot{\vec{\varphi}}_{S3}) \times \left((\dot{\vec{\varphi}}_{S3}) \times [\underset{K3}{\downarrow}\overset{K4}{\boldsymbol{R}}\,\vec{r}_{cogL} + \vec{r}_N - \vec{r}_{S3}] \right) + (\ddot{\vec{\varphi}}_{S3}) \times [\underset{K3}{\downarrow}\overset{K4}{\boldsymbol{R}}\,\vec{r}_{cogL} + \vec{r}_N - \vec{r}_{S3}]$$

$$+ \, 2((\dot{\vec{\varphi}}_{S3}) \times (\dot{\vec{\varphi}}_4 \times \underset{K3}{\downarrow}\overset{K4}{\boldsymbol{R}}\,\vec{r}_{cogL})) + \dot{\vec{\varphi}}_4 \times (\dot{\vec{\varphi}}_4 \times \underset{K3}{\downarrow}\overset{K4}{\boldsymbol{R}}\,\vec{r}_{cogL}) + (\ddot{\vec{\varphi}}_4 \times \underset{K3}{\downarrow}\overset{K4}{\boldsymbol{R}}\,\vec{r}_{cogL})$$

$$(4.25)$$

It is assumed that the payload is rigidly connected to the bucket or tool carrier. The acceleration $\vec{a}_L$ of a swinging payload, for example, a load hanging on a chain, cannot be approximated by this approach. In this case, the payload has to be in a steady condition, which means that the payload must not oscillate. An approach to deal with oscillating payloads is to use the average of the calculated payload over a few cycles.

As mentioned before, the front loader is simplified to a planar, open kinematic chain and only movements in the x-z-plane are considered. Therefore, it is sufficient to define only accelerations in the x- and z-direction for each center of gravity.

4.2.2.2 Mass, Center of Gravity, and Inertia of a Part

The mass m, the center of gravity $\vec{r}_{cog}$, and the inertia Θ of a part are constant, as long as the part is not modified. A part is defined as a rigid body including all stiff mounted add-ons, such as brackets. The boom part, for instance, includes all hoses, fittings and pins. To obtain an accurate multi-body model, a standard series front loader is taken apart as shown in figure A.4. For each part the parameters like the mass, the inertia and the center of gravity are measured as described in section 2.7 *Mass and Center of Gravity*

and section 2.8 *Moment of Inertia.* Because the front loader is equal to a planar kinematic chain, the moments of inertia are only considered in the main axis in y-direction. The parameters of the front loader used in this thesis are defined in table A.2 in section A.3.1.

Identifying the parameters by tests is very time-consuming but it is also very accurate. The multi-body model exactly describes the front loader used in this thesis. Thus, the multi-body model serves as a reference for subsequent developments. A disadvantage of this approach is that adding an additional weight to a part falsifies the previously measured parameters and they must be identified again. For example, mounting an additional valve to the boom shifts the center of gravity position and finally falsifies the payload measurement. Identifying the parameters again is very time-consuming. Hence, a reduced multi-body model is presented later in section 4.6.1, whose parameters are identified during a short calibration procedure. The weighing algorithm is first developed with the accurate full multi-body model, which provides a basis for subsequent simplifications.

The inertia Θ is only defined for the main axis of the parts. The effects of the parallel axis theorem, also known as Huygens-Steiner theorem, are already considered as long as only the accelerations at the center of gravity are used,which is discussed in the following section 4.2.2.3.

4.2.2.3 Considering the Parallel Axis Theorem

The differential equation for a part of section 4.2.1 uses only the moment of inertia Θ_i along the main axis. The parallel axis theorem, also known as Huygens-Steiner theorem, is already considered in the torque calculation as long as the translational acceleration $\vec{a}_i$ is referenced to the center of gravity of the respective part. Hence, only the moment of inertia in the y-main axis is relevant. This fact that the parallel axis theorem is already considered in the torque calculation explains a closer look at a driven pendulum in a non-gravity environment, as shown in figure 4.17.

The movement as well as the acceleration of a pendulum are split into a translational (figure 4.17b) and a rotational (figure 4.17c) part. The translational acceleration $\vec{a}$ is measured at the center of gravity and the rotational acceleration $\ddot{\vec{\varphi}}$ can be measured anywhere at the pendulum.
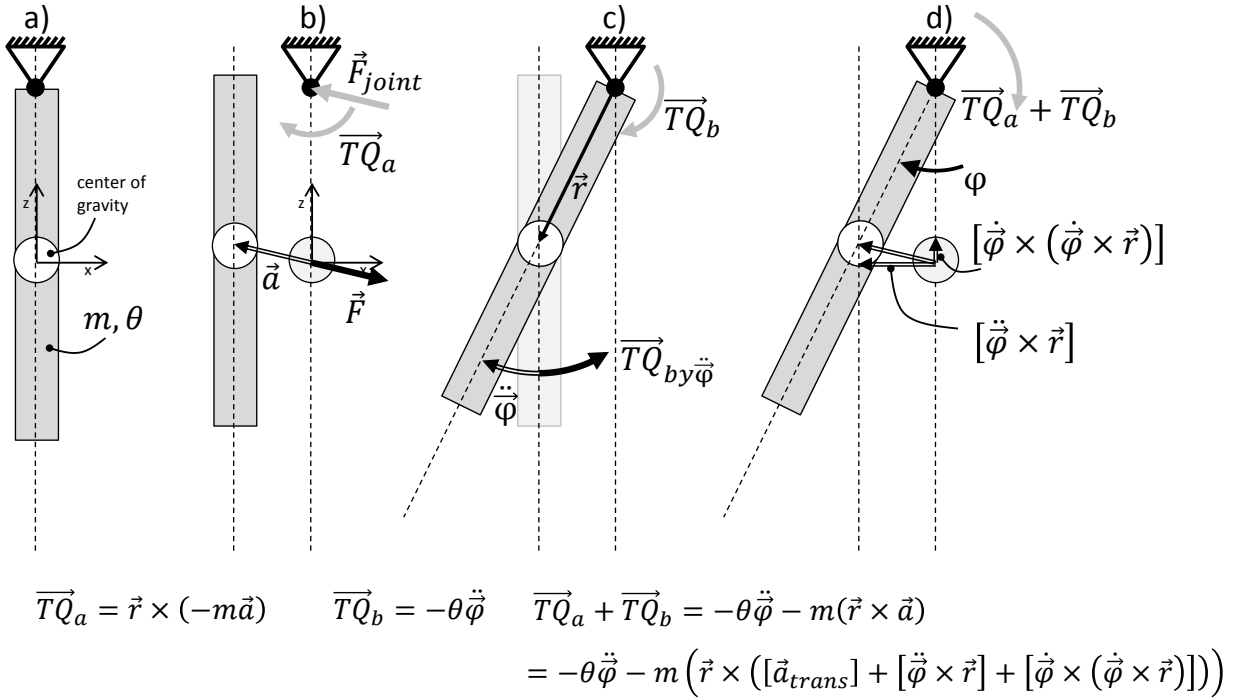
$$\overrightarrow{TQ_a} = \vec{r} \times (-m\vec{a}) \qquad \overrightarrow{TQ_b} = -\theta\ddot{\vec{\varphi}} \qquad \overrightarrow{TQ_a} + \overrightarrow{TQ_b} = -\theta\ddot{\vec{\varphi}} - m(\vec{r} \times \vec{a})$$

$$= -\theta\ddot{\vec{\varphi}} - m\left(\vec{r} \times \left([\vec{a}_{trans}] + [\ddot{\vec{\varphi}} \times \vec{r}] + [\dot{\vec{\varphi}} \times (\dot{\vec{\varphi}} \times \vec{r})]\right)\right)$$

Figure 4.17: Driven pendulum in non-gravity environment

The rotational acceleration $\ddot{\vec{\varphi}}$ generates $\overrightarrow{TQ_b} = -\Theta\ddot{\vec{\varphi}}$ using the moment of inertia Θ along the main axis (figure 4.17c). The acceleration $\vec{a}$ (figure 4.17b) at the center of gravity generates $\overrightarrow{TQ_a} = -m(\vec{r} \times \vec{a})$. The acceleration $\vec{a}$ splits into several terms (figure 4.17d). The first term $\vec{a}_{trans}$ is the translational acceleration of the whole system, the pendulum, and its support. In this non-gravity example $\vec{a}_{trans}$ is set to zero and just mentioned for the sake of completeness. The term $[\dot{\vec{\varphi}} \times (\dot{\vec{\varphi}} \times \vec{r})]$ is the centripetal acceleration and points, in case of a pendulum, directly to the joint. The resulting force does not generate a torque. The term $[\ddot{\vec{\varphi}} \times \vec{r}]$ is the acceleration of the center of gravity due to the rotation. Compared to the momentum theorem $TQ = (\Theta + mr^2)\ddot{\varphi}$ for a part that does not rotate around its main axis, the term $m(\vec{r} \times [\ddot{\vec{\varphi}} \times \vec{r}])$ results in the parallel axis theorem $mr^2\ddot{\varphi}$ [HSG99].

In reality, the front loader does not only rotate around its joints. For example, if the tractor is tilting, additional rotations superpose movements of the front loader. For this reason, further terms, like the Coriolis acceleration, are added to the acceleration, as described in chapter 2.6.

4.3 Weighing Algorithm

This section explains the weighing algorithm using the example of a tractor front loader. The distinctive feature of this approach is the independence of the center of gravity posi-

tion of the payload, which is achieved by considering the torque equilibrium at two joints of an open, planar kinematic chain. Thus, it is possible, to apply the weighing algorithm also on other systems similar to an open, planar kinematic chain with at least two joints such as an excavator arm or a loader crane. In addition, the weighing system compensates disturbances that arise from tractor or front loader movements by considering continuously measured accelerations.

In order to achieve this, two equilibrium equations are formed using the torque output of the multi-body model and torque output of the static model. These equations correspond to the first joint J_1 between tractor and boom and to the second joint J_2 between boom and bucket. As an example, the multi-body model is simplified and combined with the simplified kinematic chain of the static model, as shown in figure 4.18. For reasons of clarity, only the boom and the bucket are considered here. Terms of smaller parts are not mentioned.
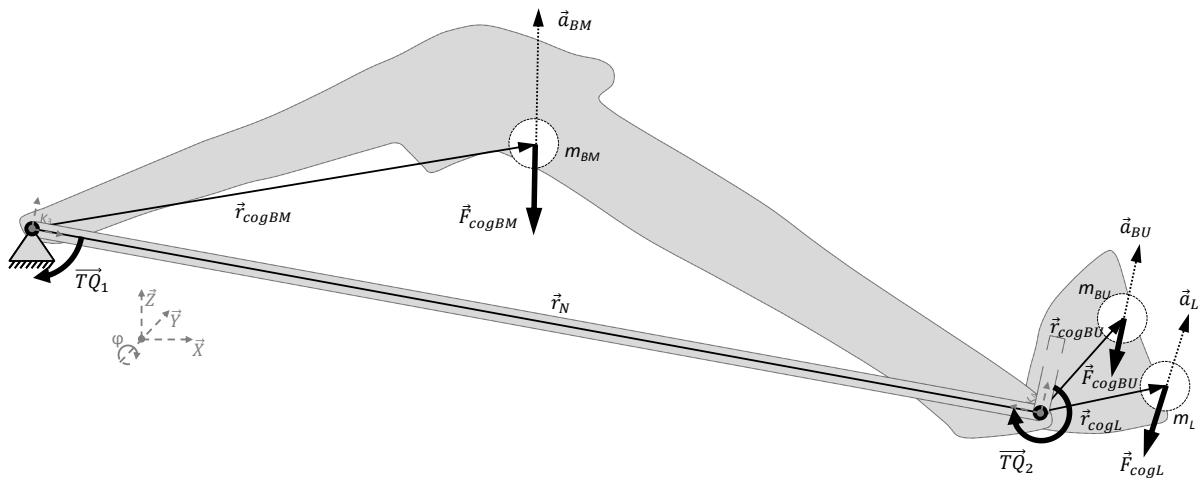
Figure 4.18: Simplified model for the torque equilibrium

The torque output of the static model is set into relation with the torque output of the multi-body model which generates torques through inertial forces and their respective levers. The levers are defined by vectors $\vec{r}_{cog}$, that point from the respective joint to the center of gravity of the relevant part as described in chapter 4.2.1.

All vectors are referenced to their corresponding part and not to a global inertial coordinate system. For example, $\vec{r}_{cogBM}$ is referenced to the boom coordinate system, which implies that $\vec{r}_{cogBM}$ is constant. To add or subtract a vector, it has to be transformed to the same coordinate system K, as shown in chapter 2.4.

For instance: $\vec{r}_{coordinatesystem3} = \underset{K3}{\overset{K4}{\downarrow}} \boldsymbol{R} \cdot \vec{r}_{coordinatensystem4}$

4.3.1 Torque Equilibrium at the First Joint

The torque equilibrium at the first joint is created as follows:

$$
\begin{aligned}
0 = \vec{TQ}_1 &+ [\vec{r}_{cogBM} \times (-m_{BM} \cdot \vec{a}_{BM})] \\
&+ [(\underset{K3}{\overset{K4}{\downarrow}}\!\!\boldsymbol{R} \cdot \vec{r}_{cogBU} + \vec{r}_N) \times (-m_{BU} \cdot \underset{K3}{\overset{K4}{\downarrow}}\!\!\boldsymbol{R} \cdot \vec{a}_{BU})] \\
&+ [(\underset{K3}{\overset{K4}{\downarrow}}\!\!\boldsymbol{R} \cdot \vec{r}_{cogL} + \vec{r}_N) \times (-m_L \cdot \underset{K3}{\overset{K4}{\downarrow}}\!\!\boldsymbol{R} \cdot \vec{a}_L)] \\
&- \Theta_{BM}\ddot{\vec{\varphi}}_{S3} - (\Theta_{BU} + \Theta_L)\ddot{\vec{\varphi}}_{S4}
\end{aligned}
\tag{4.26}
$$

The cross product is bilinear and the distributive law can be applied. Hence, it can be rearranged:

$$
\begin{aligned}
0 = \vec{TQ}_1 &+ [\vec{r}_{cogBM} \times (-m_{BM} \cdot \vec{a}_{BM})] \\
&+ [\underset{K3}{\overset{K4}{\downarrow}}\!\!\boldsymbol{R} \cdot \vec{r}_{cogBU} \times (-m_{BU} \cdot \underset{K3}{\overset{K4}{\downarrow}}\!\!\boldsymbol{R} \cdot \vec{a}_{BU})] + [\vec{r}_N \times (-m_{BU} \cdot \underset{K3}{\overset{K4}{\downarrow}}\!\!\boldsymbol{R} \cdot \vec{a}_{BU})] \\
&+ [\underset{K3}{\overset{K4}{\downarrow}}\!\!\boldsymbol{R} \cdot \vec{r}_{cogL} \times (-m_L \cdot \underset{K3}{\overset{K4}{\downarrow}}\!\!\boldsymbol{R} \cdot \vec{a}_L)] + [\vec{r}_N \times (-m_L \cdot \underset{K3}{\overset{K4}{\downarrow}}\!\!\boldsymbol{R} \cdot \vec{a}_L)] \\
&- \Theta_{BM}\ddot{\vec{\varphi}}_{S3} - (\Theta_{BU} + \Theta_L)\ddot{\vec{\varphi}}_{S4}
\end{aligned}
\tag{4.27}
$$

The transformation of coordinates is a rotation around the y-axis. Thus, the cross product of the transformed vectors is equal to the non-transformed vectors and equation (4.27) can be simplified to the following term:

$$
\begin{aligned}
0 = \vec{TQ}_1 &+ [\vec{r}_{cogBM} \times (-m_{BM} \cdot \vec{a}_{BM})] \\
&+ \underline{[\vec{r}_{cogBU} \times (-m_{BU} \cdot \vec{a}_{BU})]} + [\vec{r}_N \times (-m_{BU} \cdot \underset{K3}{\overset{K4}{\downarrow}}\!\!\boldsymbol{R} \cdot \vec{a}_{BU})] \\
&+ \underline{[\vec{r}_{cogL} \times (-m_L \cdot \vec{a}_L)]} + [\vec{r}_N \times (-m_L \cdot \underset{K3}{\overset{K4}{\downarrow}}\!\!\boldsymbol{R} \cdot \vec{a}_L)] \\
&- \Theta_{BM}\ddot{\vec{\varphi}}_{S3} - \underline{(\Theta_{BU} + \Theta_L)\ddot{\vec{\varphi}}_{S4}}
\end{aligned}
\tag{4.28}
$$

4.3.2 Torque Equilibrium at the Second Joint

The torque equilibrium at the second joint is given by the following equation:

$$
\begin{aligned}
0 = \vec{TQ}_2 &+ [\vec{r}_{cogBU} \times (-m_{BU} \cdot \vec{a}_{BU})] + [\vec{r}_{cogL} \times (-m_L \cdot \vec{a}_L)] \\
&- (\Theta_{BU} + \Theta_L)\ddot{\vec{\varphi}}_{S4}
\end{aligned}
\tag{4.29}
$$

The rearranged equation (4.29) turns into the following term, where all <u>underlined</u> terms are equal to the <u>underlined</u> terms of equation (4.28):

$$\underline{[\vec{r}_{cogBU} \times (-m_{BU} \cdot \vec{a}_{BU})]} + \underline{[\vec{r}_{cogL} \times (-m_L \cdot \vec{a}_L)]} - \underline{(\Theta_{BU} + \Theta_L)\ddot{\vec{\varphi}}_{S4}} = -\vec{TQ}_2 \qquad (4.30)$$

4.3.3 Payload Calculation

To obtain the payload m_L, the following procedure is applied. Equation (4.30) is inserted into equation (4.28) which yields the following result:

$$
\begin{aligned}
0 = \vec{TQ}_1 &+ [\vec{r}_{cogBM} \times (-m_{BM} \cdot \vec{a}_{BM})] \\
&+ [\vec{r}_N \times (-m_{BU} \cdot \overset{K4}{\underset{K3}{\downarrow}}\boldsymbol{R} \cdot \vec{a}_{BU})] \\
&+ [\vec{r}_N \times (-m_L \cdot \overset{K4}{\underset{K3}{\downarrow}}\boldsymbol{R} \cdot \vec{a}_L)] \\
&- \Theta_{BM}\ddot{\vec{\varphi}}_{S3} - \vec{TQ}_2
\end{aligned}
\qquad (4.31)
$$

The equation is rearranged and results into:

$$
\begin{aligned}
m_L \cdot \left[\vec{r}_N \times (\overset{K4}{\underset{K3}{\downarrow}}\boldsymbol{R} \cdot \vec{a}_L)\right] = \\
\left[\vec{TQ}_1 - \vec{TQ}_2 - m_{BM} \cdot [\vec{r}_{cogBM} \times \vec{a}_{BM}] - m_{BU} \cdot [\vec{r}_N \times (\overset{K4}{\underset{K3}{\downarrow}}\boldsymbol{R} \cdot \vec{a}_{BU})] - \Theta_{BM}\ddot{\vec{\varphi}}_{S3})\right]
\end{aligned}
\qquad (4.32)
$$

Since the front loader is similar to an open, planar kinematic chain, every joint has only one degree of freedom, namely the rotation along the y-axis. Thus, only torques in the y-direction are considered and all terms turn into vectors of the following form $\vec{TQ} = \begin{bmatrix} 0 \\ TQ_y \\ 0 \end{bmatrix}$.

By only taking the y-component of the torque vector TQ_y, the equation (4.32) can be solved to calculate the payload m_L.

$$m_L = \frac{TQ_{num}}{TQ_{denum}} \qquad (4.33)$$

with

$$
\begin{aligned}
TQ_{num} = \\
\left[\vec{TQ}_1 - \vec{TQ}_2 - m_{BM} \cdot [\vec{r}_{cogBM} \times \vec{a}_{BM}] - m_{BU} \cdot [\vec{r}_N \times (\overset{K4}{\underset{K3}{\downarrow}}\boldsymbol{R} \cdot \vec{a}_{BU})] - \Theta_{BM}\ddot{\vec{\varphi}}_{S3}\right]_y
\end{aligned}
\qquad (4.34)
$$

and with

$$TQ_{denum} = \left[\vec{r}_N \times (\underset{K3}{\overset{K4}{\downarrow}} \boldsymbol{R} \cdot \vec{a}_L) \right]_y \tag{4.35}$$

At first glance, the payload is only dependent on dimensions related to the boom, like $\vec{r}_{cogBM}$ and $\vec{r}_N$, which is the distance between the two main joints. A closer examination reveals that, in order to calculate the acceleration at the bucket, the distance between the center of gravity of the bucket and the IMU is needed. Additionally, in order to calculate the acceleration at the payload, as shown in equation (4.36), the distance between the center of gravity of the payload and the IMU is necessary, which is of course unknown. Hence, the center of gravity position of the payload is approximated, as described in section 4.2.2.1.

If the distances between the IMU and the center of gravity of the payload are not defined correctly, deviations of the payload measurement occur only if the machine or the front loader experiences angular velocities or angular accelerations. Otherwise, all ~~crossed~~ terms of equation (4.36) will become zero and the acceleration at the bucket or payload is equal to the translational acceleration of IMU$S3$, $\vec{a}_{S3} = \ddot{\vec{r}}_{1S3}$. (cf. equation (4.25))

$$\vec{a}_L = \underset{K4}{\overset{K3}{\downarrow}} \boldsymbol{R} \left[\ddot{\vec{a}}_{S3} + (\dot{\bcancel{\vec{\beta}_{S3}}}) \times \left((\dot{\bcancel{\vec{\beta}_{S3}}}) \times [\vec{r}_{S3cogL}] \right) + (\ddot{\bcancel{\vec{\beta}_{S3}}}) \times [\vec{r}_{S3cogL}] \right.$$

$$\left. + 2((\dot{\bcancel{\vec{\beta}_{S3}}}) \times (\dot{\bcancel{\vec{\beta}_4}} \times \underset{K3}{\overset{K4}{\downarrow}} \boldsymbol{R} \, \vec{r}_{cogL})) + \dot{\bcancel{\vec{\beta}_4}} \times (\dot{\bcancel{\vec{\beta}_4}} \times \underset{K3}{\overset{K4}{\downarrow}} \boldsymbol{R} \, \vec{r}_{cogL}) + (\ddot{\bcancel{\vec{\beta}_4}} \times \underset{K3}{\overset{K4}{\downarrow}} \boldsymbol{R} \, \vec{r}_{cogL}) \right]$$

$$\tag{4.36}$$

With $[\vec{r}_{S3cogL}] = [-\vec{r}_{S3} + \vec{r}_N + \underset{K3}{\overset{K4}{\downarrow}} \boldsymbol{R} \, \vec{r}_{cogL}]$ (see figure 4.18 and figure A.6).

The mass of the bucket or tool carrier is considered by m_{BU}. Accordingly, the scale displays zero as weight of an empty bucket or tool carrier. If the bucket mass is not considered, ~~m_{BU}~~, the scale displays an offset for an empty bucket. The offset is equal to the bucket mass m_{BU} and must be handled as tare.

4.4 Roll and Pitch Angle of the Machine

In normal work conditions, the tractor is pitching and rolling. Here, accelerations at the front loader will also point in the y-direction. The resulting forces in the y-direction are directly supported by the joints and are not measureable by the cylinder forces. For this reason, the outputs of the static model are only torques in the y-axis, which are generated by inertial forces in the x- or z-direction. The torques obtained by the multi-body model

have components on all axis. As mentioned in section 4.3.3, only torques in the y-axis are considered. In this way, the deviation, which is induced by rolling of the machine, is compensated.
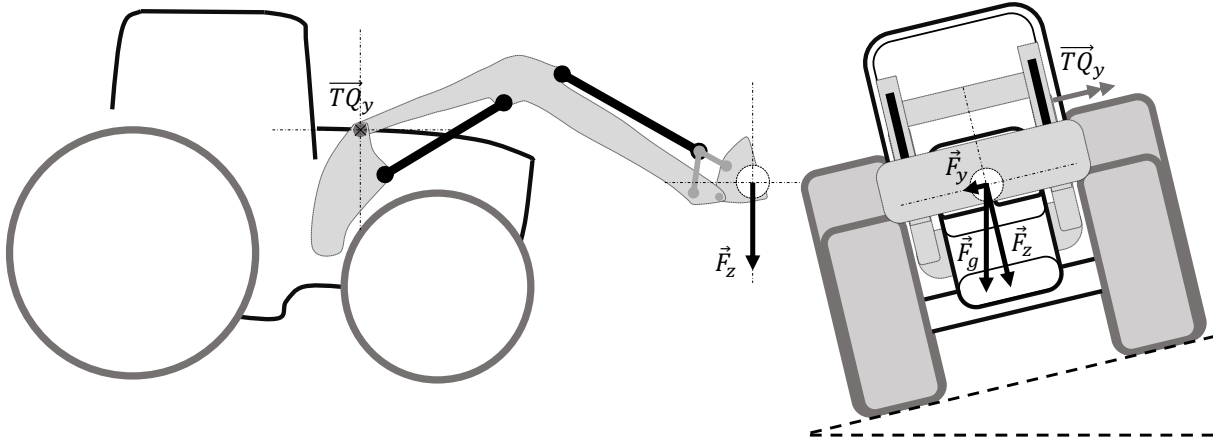

Figure 4.19: Roll compensation

A mathematical explanation of the previous statement is given as follows. Figure 4.19 shows a roll-tilted tractor during standstill. The torque TQ_y of the static model is only generated by $\vec{F}_z$, which is of course smaller than $\vec{F}_g$. To merge the static model with the multi-body model, TQ_x and TQ_z from the multi-body model have to be set to zero. Solving the first part of equation (4.18) results in equation (4.37) in which TQ_x and TQ_z are ~~crossed out~~. It reveals that only accelerations in x and z-direction are considered for TQ_y. Accelerations in y-direction have no influence on TQ_y.

$$\vec{TQ} = \vec{r} \times \vec{F} = \vec{r} \times m\vec{a} = m \begin{bmatrix} r_x \\ r_y \\ r_z \end{bmatrix} \times \begin{bmatrix} a_x \\ a_y \\ a_z \end{bmatrix} = m \begin{bmatrix} \cancel{r_y a_z - r_z a_y} \\ r_z a_x - r_x a_z \\ \cancel{r_x a_y - r_y a_x} \end{bmatrix} \tag{4.37}$$

If the roll-tilt angle is too large, the force $\vec{F}_y$ generates a higher friction torque at the joints, which can falsify the result.

A pitch angle of the machine, for example when the machine stands up- or downward on a slope, is compensated in any case because it is only a rotation around the y-axis and only affects the accelerations in x- and z-direction, which are measured to generate the torque TQ_y. Finally, it can be said that rolling and pitching of the machine has no influence on the payload measurement.

4.5 Implementation

This section describes the weighing algorithm as implemented at the prototype. To allow plausibility checks during the early stage of development, the torque from the multi-body model and from the static model need to be comparable. Hence, equation (4.30) and equation (4.28) are transformed, in order to obtain comparable torque values from the multi-body model and torque values from the static model for each joint J_1 and J_2. For reasons of clarity, the vectors are not indexed with the respective coordinate system. In this section, every vector is transformed to the same coordinate system, here to the boom coordinate system K_3. For instance, $\underset{K3}{\downarrow}\overset{K4}{\boldsymbol{R}} \cdot \vec{a}_{BU}$ is now written as $\vec{a}_{BU}$.

Subtracting equation (4.30) from equation (4.28) generates the following term:

$$
\begin{aligned}
0 = \vec{TQ}_1 - \vec{TQ}_2 \\
+ [\vec{r}_{cogBM} \times (-m_{BM} \cdot \vec{a}_{BM})] + [\vec{r}_{cogBU} \times (-m_{BU} \cdot \vec{a}_{BU})] \\
+ [\vec{r}_N \times (-m_{BU} \cdot \vec{a}_{BU})] + \underline{[\vec{r}_{cogL} \times (-m_L \cdot \vec{a}_L)]} \\
+ \underline{\underline{[\vec{r}_N \times (-m_L \cdot \vec{a}_L)]}} - \Theta_{BM}\ddot{\vec{\varphi}}_{S3} - (\Theta_{BU} + \Theta_L)\ddot{\vec{\varphi}}_{S4} \\
- \left[[\vec{r}_{cogBU} \times (-m_{BU} \cdot \vec{a}_{BU})] + \underline{[\vec{r}_{cogL} \times (-m_L \cdot \vec{a}_L)]} - (\Theta_{BU} + \Theta_L)\ddot{\vec{\varphi}}_{S4} \right]
\end{aligned}
\tag{4.38}
$$

The previous equation is simplified to the following expression:

$$
\begin{aligned}
0 = \vec{TQ}_1 - \vec{TQ}_2 + \underline{\underline{[\vec{r}_N \times (-m_L \cdot \vec{a}_L)]}} \\
+ \left\{ [\vec{r}_{cogBM} \times (-m_{BM} \cdot \vec{a}_{BM})] + [\vec{r}_{cogBU} \times (-m_{BU} \cdot \vec{a}_{BU})] \right. \\
\left. + [\vec{r}_N \times (-m_{BU} \cdot \vec{a}_{BU})] - \Theta_{BM}\ddot{\vec{\varphi}}_{S3} - (\Theta_{BU} + \Theta_L)\ddot{\vec{\varphi}}_{S4} \right\} \\
- \left\{ [\vec{r}_{cogBU} \times (-m_{BU} \cdot \vec{a}_{BU})] - (\Theta_{BU} + \Theta_L)\ddot{\vec{\varphi}}_{S4} \right\}
\end{aligned}
\tag{4.39}
$$

The terms in the curly brackets are replaced by the expressions $\vec{TQ}_{1\,by\,acc}$ and $\vec{TQ}_{2\,by\,acc}$:

$$
\underline{\underline{[\vec{r}_N \times (m_L \cdot \vec{a}_L)]}} = \vec{TQ}_1 - \vec{TQ}_2 + \left\{ \vec{TQ}_{1\,by\,acc} \right\} - \left\{ \vec{TQ}_{2\,by\,acc} \right\}
\tag{4.40}
$$

The expressions $\vec{TQ}_{1\,by\,acc}$ and $\vec{TQ}_{2\,by\,acc}$ are obtained from the multi-body model. They include all individual torques caused by every part of the front loader, such as cylinders or links from the bucket linkage. An example of the different parts of the front loader with

their center of gravity is shown in figure 4.14. $\vec{TQ}_1$ and $\vec{TQ}_2$ are replaced by

$$
\begin{aligned}
\vec{TQ}_1 &= -\vec{TQ}_{1\,meas} \\
\vec{TQ}_2 &= -\vec{TQ}_{2\,meas}
\end{aligned}
\tag{4.41}
$$

$\vec{TQ}_{1\,meas}$ and $\vec{TQ}_{2\,meas}$ are calculated by the static model with measured cylinder forces. The negative value is used to easily compare them to the torques of the multi-body model. For example, $\vec{TQ}_{1\,meas} = \vec{TQ}_{1\,by\,acc}$ or $\vec{TQ}_{2\,meas} = \vec{TQ}_{2\,by\,acc}$ applies to a front loader without payload.

4.5.1 Payload

The payload is calculated by solving equation (4.40) to m_L. It is not possible to divide two vectors by each other, but in case of a planar kinematic chain, like the front loader, torque has only a y-component, hence, only the y-components are divided by each other.

$$
m_L = \frac{\left[-\vec{TQ}_{1\,meas} + \vec{TQ}_{2\,meas} + \vec{TQ}_{1\,by\,acc} - \vec{TQ}_{2\,by\,acc}\right]_y}{\left[\vec{r}_N \times \vec{a}_L\right]_y}
\tag{4.42}
$$

4.5.2 Simplifications

In the following, several further simplifications are described, that serve to ease the implementation at the tractor front loader.

4.5.2.1 Moments of Inertia

As mentioned in chapter 4.2.2.1, the accelerations $\vec{a}_i$ are referenced to the center of gravity of each part. Thus, the torque influence of the moment of inertia Θ is low compared to other torque terms (cf. equation (4.39)). Hence, only the moments of inertia from big parts, such as boom or tool carrier, are considered whereas moments of inertia of small parts, for instance links of the bucket linkage, are not considered.

4.5.2.2 Oil Mass

The oil was drained before measuring the cylinder mass for the multi-body model. In operation, the oil volume in the cylinders changes and, thereby, the mass of the cylinder changes as well. Given that the cylinders are not too big, the oil mass in the cylinders is not considered. In the reduced multi-body model (chapter 4.6.1) the oil mass is considered.

4.5.2.3 Hoses

Flexible hoses are used to transfer the hydraulic power from the tractor to the cylinders of the front loader. The hoses are fixed to the front loader and are bent to follow the movements of the front loader. These bending forces influence the torques TQ_1 at joint J_1 between chassis and boom and TQ_2 at joint J_2 between boom and bucket. Due to the fact that the hoses are quite thin, the bending forces are low and not considered.

4.5.2.4 Relative Movements

An IMU is mounted at a given position. The output of the IMU is used to calculate the acceleration at the center of gravity for each part as shown in chapter 2.6. In case of a front loader, the parts are moving relative to each other. For instance, the bucket or tool carrier moves relative to the boom, which causes Coriolis accelerations and further rotational accelerations, as described in equation (2.22). Since relative movements are slow compared to the overall movement, the front loader is treated as a rigid body and Coriolis accelerations and further rotational accelerations are not considered for smaller parts. For bigger parts, like the tool carrier or the payload, Coriolis acceleration and further rotational accelerations must be considered. The IMU can be mounted anywhere at the tractor but in order to reduce relative movements between mounting position and the relevant part as well as to minimize deviations, the IMU is mounted at the boom (IMU $S3$).

4.5.2.5 Acceleration Sensor Position and Output

Chapter 2.6 describes how to transfer accelerations from one point to another. At a rigid body, equation (4.43) calculates an acceleration $\vec{a}$ for any point P, measured at IMU position S (cf. equation (2.20)). The distance between IMU and point P is given by the vector $\vec{r}_{SP}$.

$$\vec{a} = \ddot{\vec{r}}_{1P} = \ddot{\vec{r}}_{1S} + \dot{\vec{\varphi}}_2 \times \left(\dot{\vec{\varphi}}_2 \times [\vec{r}_{SP}] \right) + \ddot{\vec{\varphi}}_2 \times [\vec{r}_{SP}] \tag{4.43}$$

If equation (4.43) is solved, it results in equation (4.44).

$$\vec{a} = \begin{bmatrix} \ddot{r}_{1S_x} \\ \ddot{r}_{1S_y} \\ \ddot{r}_{1S_z} \end{bmatrix} + \begin{bmatrix} \dot{\varphi}_{2_y}(\dot{\varphi}_{2_x}r_{SP_y} - \dot{\varphi}_{2_y}r_{SP_x}) - \dot{\varphi}_{2_z}(\dot{\varphi}_{2_z}r_{SP_x} - \dot{\varphi}_{2_x}r_{SP_z}) \\ \dot{\varphi}_{2_z}(\dot{\varphi}_{2_y}r_{SP_z} - \dot{\varphi}_{2_z}r_{SP_y}) - \dot{\varphi}_{2_x}(\dot{\varphi}_{2_x}r_{SP_y} - \dot{\varphi}_{2_y}r_{SP_x}) \\ \dot{\varphi}_{2_x}(\dot{\varphi}_{2_z}r_{SP_x} - \dot{\varphi}_{2_x}r_{SP_z}) - \dot{\varphi}_{2_y}(\dot{\varphi}_{2_y}r_{SP_z} - \dot{\varphi}_{2_z}r_{SP_y}) \end{bmatrix} + \begin{bmatrix} \ddot{\varphi}_{2_y}r_{SP_z} - \ddot{\varphi}_{2_z}r_{SP_y} \\ \ddot{\varphi}_{2_z}r_{SP_x} - \ddot{\varphi}_{2_x}r_{SP_z} \\ \ddot{\varphi}_{2_x}r_{SP_y} - \ddot{\varphi}_{2_y}r_{SP_x} \end{bmatrix}$$
$$\tag{4.44}$$

Forces in the y-direction are supported directly by the front loader joints. Hence, accelerations in the y-direction have no influence and are not considered (~~crossed out~~).

The IMU $S3$ used in this thesis has only three degrees of freedom. It measures accelerations in the x- and z-direction, rotational velocity, and rotational acceleration along the y-axis. Therefore, $\dot{\varphi}_{2_x}$, $\dot{\varphi}_{2_z}$ and $\ddot{\varphi}_{2_x}$, $\ddot{\varphi}_{2_z}$ are not measured and set to zero. This influences equation (4.44) and the terms marked with a dashed underline become zero:

$$\vec{a} = \begin{bmatrix} \ddot{r}_{1S_x} \\ 0 \\ \ddot{r}_{1S_z} \end{bmatrix} + \begin{bmatrix} \dot{\varphi}_{2_y}(-\dot{\varphi}_{2_y} r_{SP_x}) \\ 0 \\ -\dot{\varphi}_{2_y}(\dot{\varphi}_{2_y} r_{SP_z}) \end{bmatrix} + \begin{bmatrix} \ddot{\varphi}_{2_y} r_{SP_z} \\ 0 \\ -\ddot{\varphi}_{2_y} r_{SP_x} \end{bmatrix} \qquad (4.45)$$

To minimize the deviations caused by the missing or disturbed angular velocities and accelerations, the vector $\vec{r}_{SP}$ has to be minimized. This requires a position of the acceleration sensor close to the center of gravity. The multi-body model has several centers of gravity. Because of this, the IMU position should be chosen between the center of gravity of the biggest part, usually the boom, and the estimated center of gravity of the payload. In chapter 4.6.1, all centers of gravity are summarized in a single one. This determines the IMU position between the summarized center of gravity and the bucket where the estimated center of gravity of the payload is located.

4.6 Optimized Model for Simple Parameter Identification

One major goal of this thesis is to avoid the extensive calibration process of current mobile scales, which makes it difficult to install them in serial production. However, the opportunity must be provided to adjust the weighing system to compensate manufacturing tolerances or front loader structure changes. For example, if an additional part is mounted to the boom, its mass changes and has to be considered in the payload measurement, which requires to tune or to re-calibrate the loader scale.

The full multi-body model as described in section 4.2 requires all masses, center of gravity positions and inertias of each part. It is very labor-intensive and time-consuming to identify these parameters. In this thesis, a standard series front loader is taken apart as shown in figure A.4 and for every part the mass, moment of inertia, and center of gravity position is measured as described in section 2.7 and section 2.8. In serial production, these parameters are subject to tolerance and they will vary for each loader, which makes it necessary to identify these parameters for each loader. This is not feasible for larger productions. Hence, the multi-body model needs to be modified in a way that the parameters can be easily identified. To achieve this, the approach of the reduced multi-body model and its parameter identification is discussed in the following sections.

4.6.1 Reduced Multi-Body Model

A reduced multi-body model is developed, whose parameters can be measured by a short calibration procedure on each front loader. The full multi-body model is still used as a reference for later comparison. On the basis of the section *Payload Calculation*, a closer look at equation (4.32) reveals that many parameters are constant. These parameters are marked with an <u>underline</u> in equation (4.46):

$$m_L \cdot \left[\vec{r}_N \times (\underset{K3}{\overset{K4}{\downarrow}} \boldsymbol{R} \cdot \vec{a}_L) \right] =$$
$$\left[\vec{TQ}_1 - \vec{TQ}_2 - \underline{m_{BM}} \cdot [\underline{\vec{r}_{cogBM}} \times \vec{a}_{BM}] - \underline{m_{BU}} \cdot [\underline{\vec{r}_N} \times (\underset{K3}{\overset{K4}{\downarrow}} \boldsymbol{R} \cdot \vec{a}_{BU})] - \underline{\Theta_{BM}} \ddot{\vec{\varphi}}_{S3} \right] \tag{4.46}$$

The masses and the respective center of gravity vectors remain constant. The masses connected to the second joint, like m_{BU} only depend on vector $\vec{r}_N$. Thus, it is obvious to sum up all single masses to obtain m_{Sum} and to merge the centers of gravity to receive $\vec{r}_{cogSum}$. As mentioned in 4.5.2.1, the influence of the moment of inertia is low as long as the acceleration $\vec{a}_{Sum}$ is referenced to the center of gravity. Therefore, all moments of inertia Θ_i of all parts are combined and replaced by a beam with the length and height of the front loader structure and with the equivalent mass of all parts (cf. equation (A.13)).

$$\Theta_{Sum} = \frac{1}{12}(m_{Sum} - m_{BU})\left((length_{BM})^2 + (height_{BM})^2\right) \tag{4.47}$$

The weighing algorithm is independent of the moment of inertia of parts connected to the second joint J_2. For example, the moment of inertia of the payload Θ_L and of the bucket Θ_{BU} do not appear in equation (4.46). Their effects are only measurable in $\vec{TQ}_1$ and $\vec{TQ}_2$. For this reason, in order to calculate Θ_{Sum}, the mass of the bucket m_{BU} must be subtracted from m_{Sum}. With these assumptions, equation (4.46) turns into the following equation:

$$m_L \cdot \left[\vec{r}_N \times (\underset{K3}{\overset{K4}{\downarrow}} \boldsymbol{R} \cdot \vec{a}_L) \right] = \vec{TQ}_1 - \vec{TQ}_2 - m_{Sum} \cdot [\vec{r}_{cogSum} \times \vec{a}_{Sum}] - \Theta_{Sum}\ddot{\vec{\varphi}}_{S3} \tag{4.48}$$

Figure 4.20 illustrates equation (4.48) for a front loader without payload, $m_L = 0$. In figure 4.20 a) to c) the generated torque of m_{BU} at the first joint is substituted by removing the lever $\vec{r}_{cogBU}$ and adding a torque $\vec{TQ}_2$. From now on, the generated torque of m_{BU} depends only on vector $\vec{r}_N$. Given that vector $\vec{r}_N$ belongs to the boom and is constant and that vector $\vec{r}_{cogBM}$ is constant, the centers of gravity can be merged to receive $\vec{r}_{cogSum}$. The moment of inertia is implied by the square box as shown in figure 4.20 d). The torque $\vec{TQ}_2$ is obtained by the static model as described in chapter 4.1.3.2 and, finally, equation (4.48) is solved to receive the payload m_L as described in chapter 4.3.3.
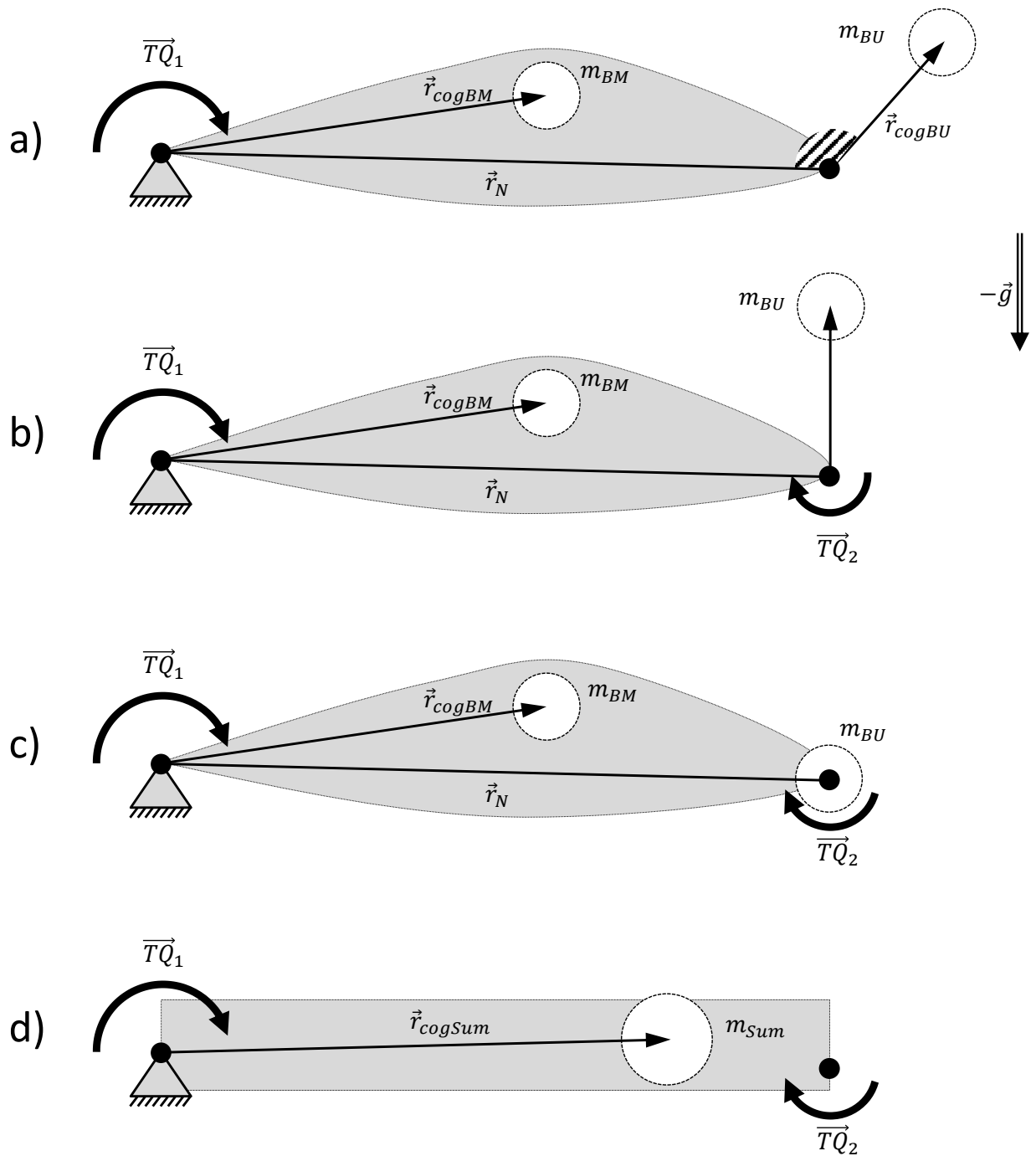
Figure 4.20: Reduced multi-body model

4.6.2 Parameter Identification

Apart from some geometric data, only the position $\vec{r}_{cogSum}$ of the merged center of gravity and the sum of all masses m_{Sum} must be identified for the reduced multi-body model. The total mass of all front loader parts m_{sum} can be received from CAD data or by weighing the completely empty front loader. Generally, tractor front loaders can be demounted. Thus, measuring the weight of a tractor front loader can easily be performed.

The merged center of gravity has to be defined in the boom coordinate system K_3 given by

$$\vec{r}_{cogSum} = l_{cogSum} \begin{bmatrix} \cos(\varphi_{cogSum}) \\ 0 \\ -\sin(\varphi_{cogSum}) \end{bmatrix} \quad \text{with} \quad l_{cogSum} = |\vec{r}_{cogSum}| \qquad (4.49)$$

Note that the angle in figure 4.21 is negative (counterclockwise). Hence, the third component is negative too, $(-)\sin(\varphi_{cogSum})$.
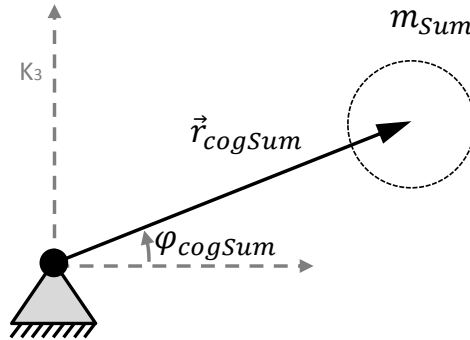

Figure 4.21: Merged center of gravity in boom coordinates

To define the center of gravity position $\vec{r}_{cogSum}$ sufficiently, the distance l_{cogSum} and the angle φ_{cogSum} are needed. To identify these parameters, the empty front loader performs a slow boom movement. During the movement, the torques $\vec{TQ}_1$ and $\vec{TQ}_2$ are recorded. Due to the slow movement, the measurement is nearly stationary and the only acceleration is given by the gravity. Equation (4.48) for an empty front loader with $m_L = 0$ and in quasi-static condition with $\ddot{\vec{\varphi}} = 0$ results in the following expression:

$$m_{Sum} \cdot [\vec{r}_{cogSum} \times \vec{a}_{Sum}] = \vec{TQ}_1 - \vec{TQ}_2 \qquad (4.50)$$

If the tractor stands on a horizontal surface, the gravity g points only in z-direction of the tractor coordinate system K_2. In order to substitute the acceleration $\vec{a}_{Sum}$ by the gravity

g in equation (4.50), the gravity has to be transformed to the boom coordinate system K_3.

$$
\underset{K3}{\overset{K2}{\downarrow}}\boldsymbol{R} \cdot \begin{bmatrix} 0 \\ 0 \\ g \end{bmatrix} = \begin{bmatrix} \cos\varphi_{BM} & 0 & -\sin\varphi_{BM} \\ 0 & 1 & 0 \\ \sin\varphi_{BM} & 0 & \cos\varphi_{BM} \end{bmatrix} \begin{bmatrix} 0 \\ 0 \\ g \end{bmatrix} = \begin{bmatrix} -\sin(\varphi_{BM})g \\ 0 \\ \cos(\varphi_{BM})g \end{bmatrix} \tag{4.51}
$$

Equation (4.50) merged with equation (4.51) leads to the torque formula:

$$
m_{Sum} \cdot l_{cogSum} \cdot g[\sin(\varphi_{cogSum})\sin(\varphi_{BM}) - \cos(\varphi_{cogSum})\cos(\varphi_{BM})] = [\vec{TQ}_1 - \vec{TQ}_2]_y \tag{4.52}
$$

The x- and z-components of formula (4.52) are zero and can be ignored because of the planar kinematic chain. The lowest torque $[\vec{TQ}_1 - \vec{TQ}_2]_y$ (or the highest of $[\vec{TQ}_{1meas} - \vec{TQ}_{2meas}]_y = -[\vec{TQ}_1 - \vec{TQ}_2]_y$) is generated when the vector $\vec{r}_{cogSum}$ points rectangular to $\vec{a}_{Sum}$, in this case the gravity, as shown in figure 4.22. This occurs if, and only if the angle $-\varphi_{cogSum}$ is equal to φ_{BM},

$$
-\varphi_{cogSum} = \varphi_{BM} \tag{4.53}
$$

which turns the first bracket term of equation (4.52) to $[\sin(\varphi_{cogSum})...\cos(\varphi_{BM})] = -1$.
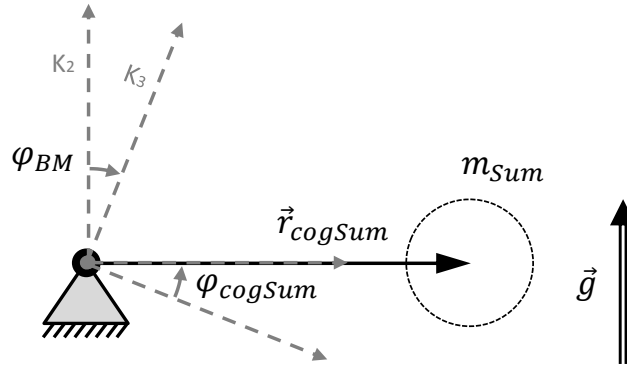

Figure 4.22: Generating the highest torque

By measuring the lowest torque $\min[\vec{TQ}_1 - \vec{TQ}_2]$ or the highest $\max[\vec{TQ}_{1meas} - \vec{TQ}_{2meas}]$ at $-\varphi_{cogSum} = \varphi_{BM}$ and in addition with the knowledge of m_{Sum}, equation (4.52) can be solved to receive the distance l_{cogSum} and to calculate the center of gravity position $\vec{r}_{cogSum}$.

$$
l_{cogSum} = \left| \frac{\min[\vec{TQ}_1 - \vec{TQ}_2]_y}{-m_{Sum} \cdot g} \right| = \left| \frac{\max[\vec{TQ}_{1meas} - \vec{TQ}_{2meas}]_y}{-m_{Sum} \cdot g} \right| \tag{4.54}
$$

4.6.3 Tractor Tilt Correction

Under normal conditions the x-axis of the tractor in coordinate system K_2 is not parallel to the ground and the machine is tilted by the angle φ_{tilt}. As in the previous section, the lowest torque $\min[\vec{TQ}_1 - \vec{TQ}_2]_y$ (highest with TQ_{meas}) is generated when vector $\vec{r}_{cogSum}$ points rectangular to the gravity, as shown in figure 4.23. This is fulfilled if the following equation is achieved:

$$- \varphi_{cogSum} = \varphi_{BM} + \varphi_{tilt} \tag{4.55}$$
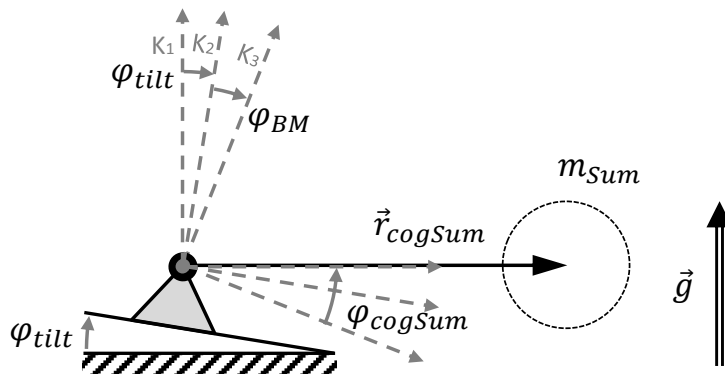
Figure 4.23: Generating the highest torque - tilted machine

The angle φ_{tilt} can be measured by an inclination sensor or by the acceleration sensor itself, as described in appendix A.5.

Figure 4.24 shows torque curves $[\vec{TQ}_{1meas} - \vec{TQ}_{2meas}]$ over the boom angle φ_{BM}, which are recorded during boom movements at different machine tilt angles. To obtain the angle φ_{cogSum}, the angle φ_{BM} at the maximum of the curve has to be determined first. If the tractor stands on a horizontal ground, the x-axis of coordinate system K_2 is parallel to the ground, and the angle φ_{cogSum} is obtained by equation (4.53). Otherwise, the tilt angle φ_{tilt} must be considered, and φ_{cogSum} is obtained by equation (4.55).
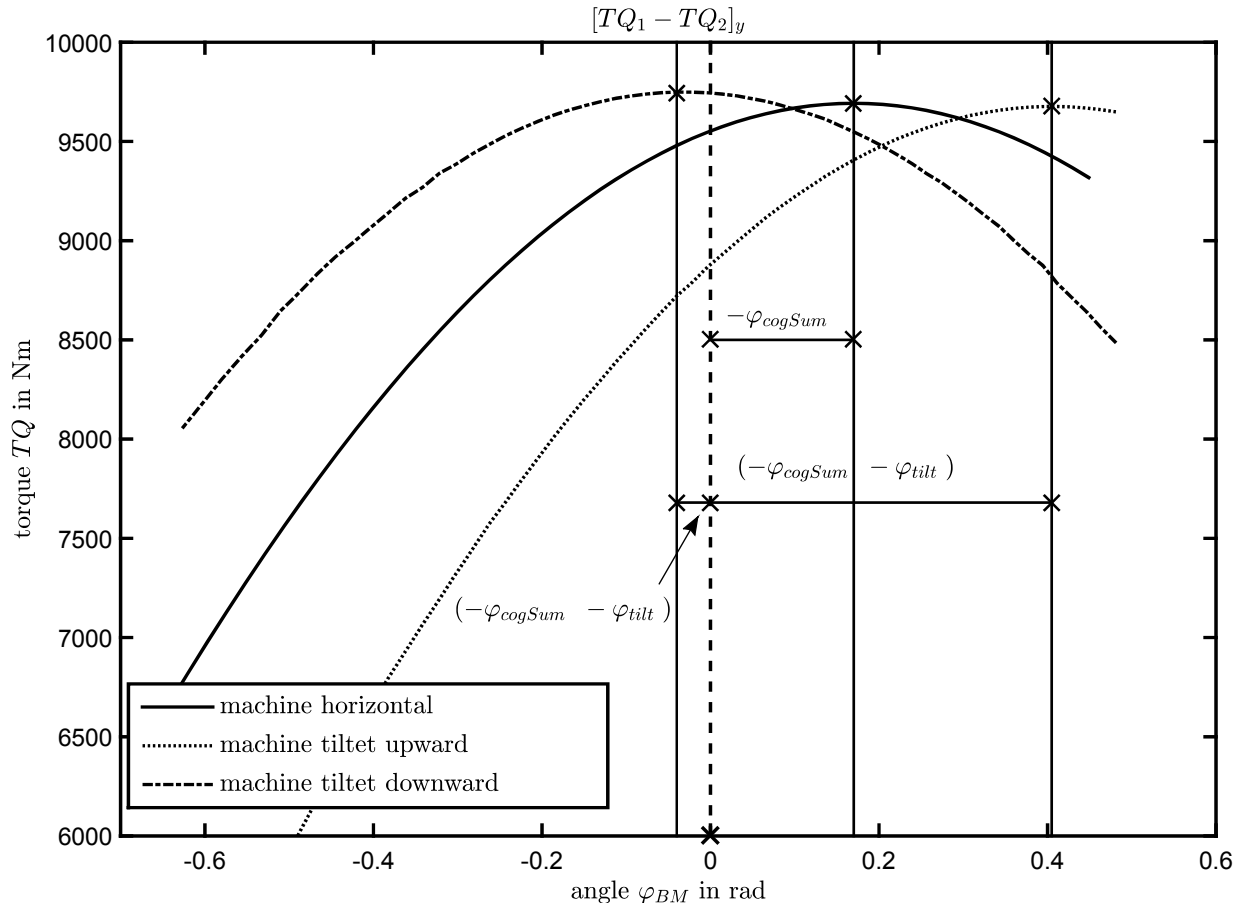
Figure 4.24: Torque curves for different tilt angles

4.6.4 Torque Measurement

As mentioned in chapter 4.1.1, the actuator forces and with it the torques are measured by cylinder pressures (cf. section 4.1.3). During the calculation of the merged center of gravity, the friction is not yet compensated and the torque measurement varies between up and down movement of the boom. To receive acceptable values for the torque TQ_1, both movements have to be taken into account. To keep the friction low, the boom has to perform a very slow up and down movement. The higher the cylinder velocity, the higher is the return pressure. The goal is to keep the pressures, which are generated by the oil flow, as low as possible because the cylinder friction is mainly a function of pressures (cf. chapter 2.9) and the cylinders have the largest share of the total friction.

The bucket cylinders do not perform a movement, but their force is also changing when the boom moves. In this case, the torque TQ_2 is affected by stiction. To keep the influence low, it is recommended to reduce the torque TQ_2 by removing the tool and to adjust the tool carrier to a proper position which generates almost zero forces on the bucket cylinders.

Figure 4.25 shows a torque measurement of slow movements of a front loader without a tool. It is assumed that the amount of friction is equal for both directions due to the symmetric piston seal (cf. chapter 4.1.2.2). To receive the torque without friction, the mean value of up- and down movement is calculated.
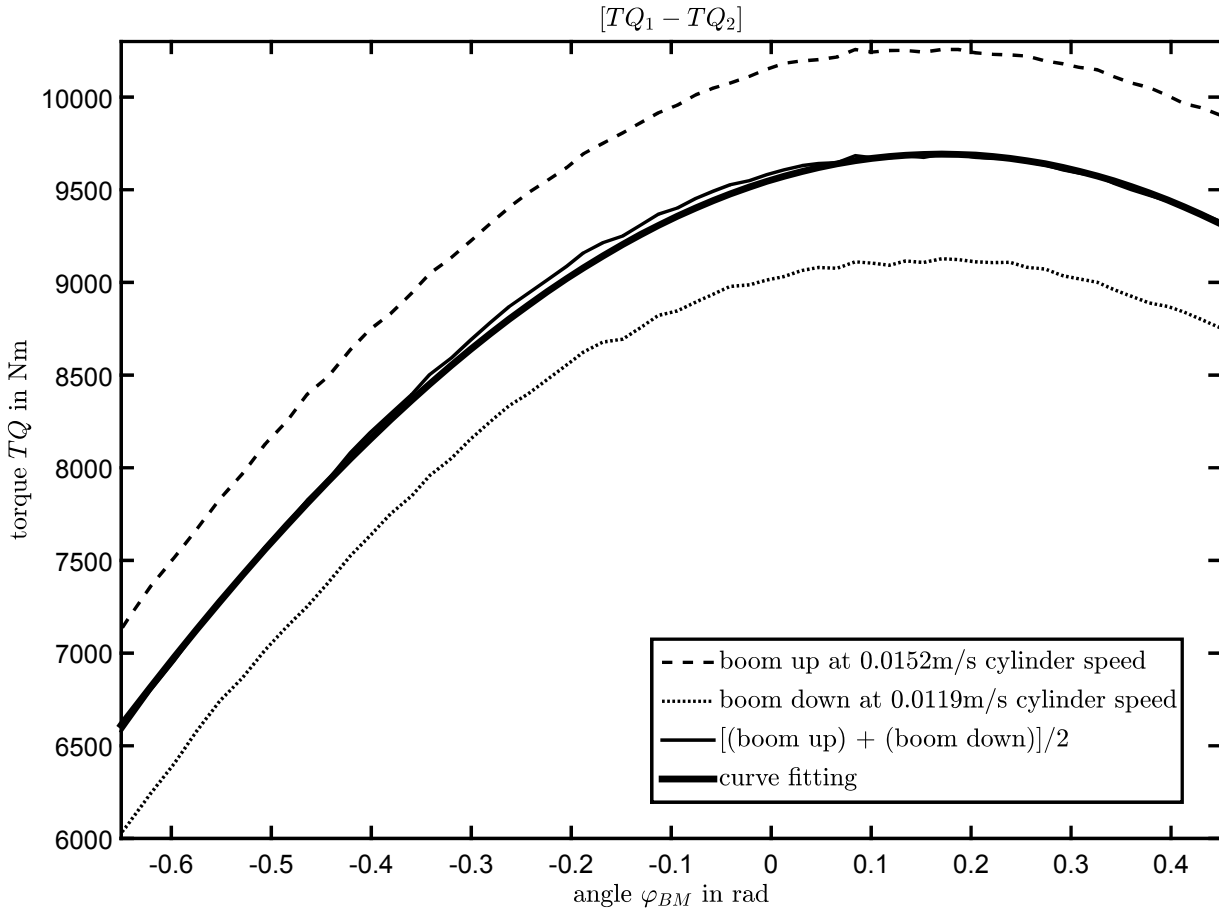

Figure 4.25: Torque measurement with friction

Finally, the mean value curve is fitted with a shifted cosine function,
$$f(\varphi) = \max |\bar{TQ}_1 - \bar{TQ}_2|_{fitted} \cos \left(\varphi - [\varphi_{BM@maxPosition\_fitted} - \varphi_{tilt}]\right),$$ to calculate the maximum torque for the merged center of gravity calculation of the previous section.

4.6.5 Deviation of the Total Loader Mass

The total mass of the front loader m_{Sum} obtained from CAD-data will not be accurate and can vary by a few kilograms. If the merged center of gravity position is defined with an incorrect mass m_{Sum}, the lever l_{cogSum} is incorrect, too. Given that the maximum torque and the gravity are constant, equation (4.56) shows the mathematical correlation between

mass m_{Sum} and lever l_{cogSum} (cf. equation (4.54)).

$$l_{cogSum} = \frac{1}{m_{Sum}} \left| \frac{\max |\vec{TQ}_1 - \vec{TQ}_2|}{-g} \right| \Rightarrow m_{Sum}\, l_{cogSum} = constant \qquad (4.56)$$

To investigate the influence of an incorrect mass and lever on the merged center of gravity position, the torque is calculated as in section 4.2.1 and solved for TQ_y. Equation (4.18) merged with equation (4.49) results in:

$$\begin{aligned}
TQ_y &= [\vec{r} \times \vec{F}]_y + \Theta \ddot{\varphi}_y = -m_{Sum}[\vec{r}_{cogSum} \times \vec{a}]_y + \Theta_{Sum}\ddot{\varphi}_y \\
&= -m_{Sum}l_{cogSum}[-\sin(\varphi_{cogSum})a_x - \cos(\varphi_{cogSum})a_z] + \Theta_{Sum}\ddot{\varphi}_y \qquad (4.57) \\
&= constant[-\sin(\varphi_{cogSum})a_x - \cos(\varphi_{cogSum})a_z] + \Theta_{Sum}\ddot{\varphi}_y
\end{aligned}$$

Equation (4.57) shows that an incorrect mass has no influence on the torques as long as the front loader accelerates only translational. Only if rotational accelerations affect the front loader, becomes the second term $\Theta_{Sum}\ddot{\varphi}_y$ relevant and generates a deviation because the moment of inertia Θ_{Sum} is compiled with an incorrect mass m_{Sum} (cf. equation (4.47)). Also, accelerations a_x and a_z are calculated at the incorrect center of gravity position. Equation (2.20) shows that, for translational accelerations, there is no influence on a_x and a_z. For rotational accelerations and movements, there is a deviation dependent on the distance between the IMU and the incorrect center of gravity position.

Figure 4.26 shows several payload measurements of the same front loader work simulation. The loader is moved very abruptly to generate a strong and extreme pitching of the machine. For each measurement the center of gravity is calculated (calibrated) in a different way. For one measurement the center of gravity is calculated with the correct mass $m_{Sum} = m_{front\ loader}$ and for two other measurements the centers of gravity are calculated with the incorrect mass $m_{Sum} = m_{front\ loader} \pm m_{disturb}$.
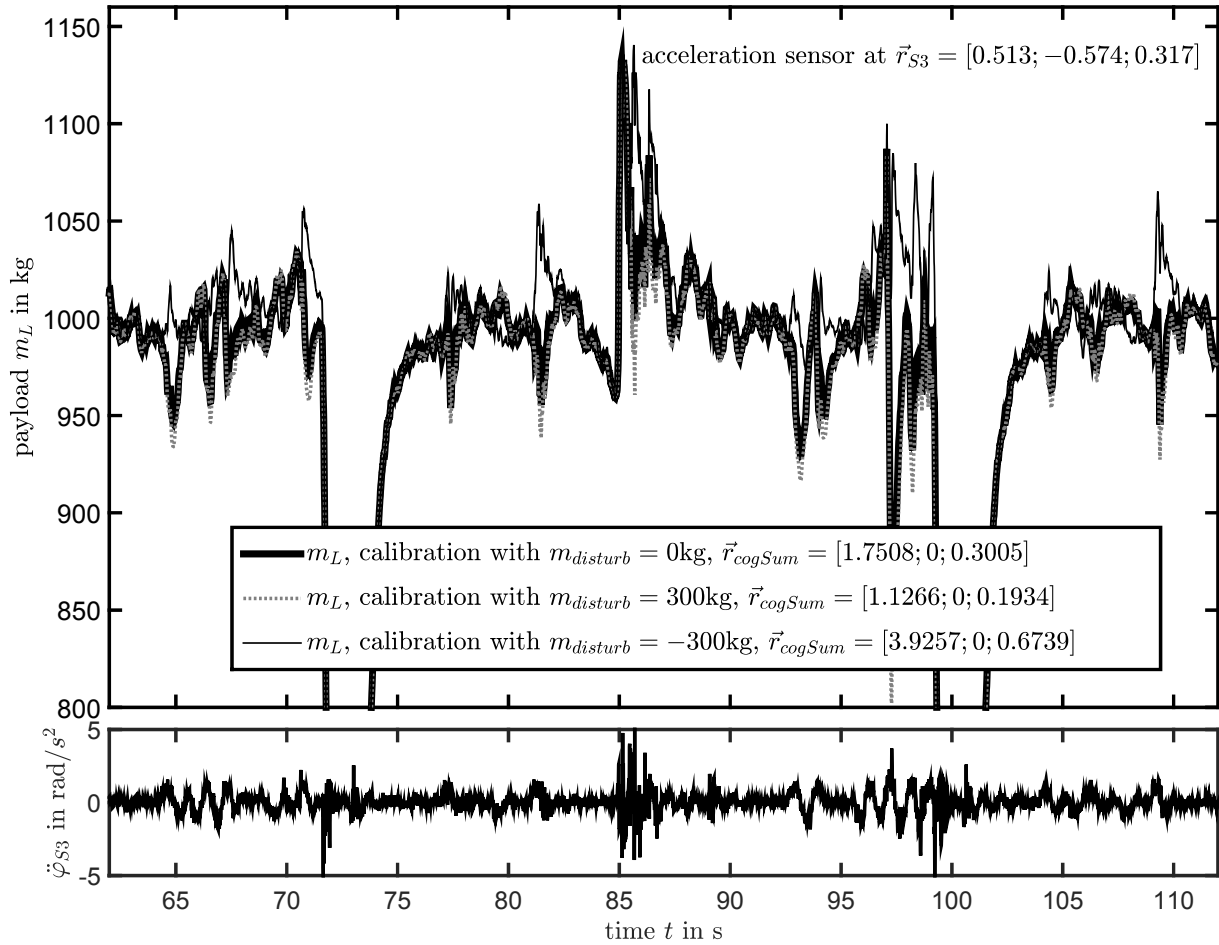
Figure 4.26: Payload measurement in extreme conditions with incorrect m_{Sum} and $\vec{r}_{cogSum}$

The greater the distance between sensor and incorrect center of gravity $(\vec{r}_{cogSum} - \vec{r}_{S3})$, the greater are the deviations at high boom pitch accelerations $\ddot{\varphi}_{S3\_y}$. The measurement in figure 4.26 was done in extreme conditions with high pitch rates, thus, the influence of an incorrect m_{Sum} and $\vec{r}_{cogSum}$ is low under normal conditions. Also, the obtained mass $m_{Sum} = m_{front\ loader} \pm m_{disturb}$ from the CAD-model is generally more accurate, here $m_{disturb} = \pm 300 \text{kg}$ is more than 50% of the front loader mass $m_{front\ loader} = 541 \text{kg}$.

4.6.6 Deviation Compared to the Full Multi-Body Model

4.6.6.1 Merged Center of Gravity Position

The approach to merge the center of gravity positions to receive $\vec{r}_{cogSum}$ is only valid for rigidly mounted parts that are connected to the boom or tool carrier (BU). In this thesis, however, this approach is also applied to parts that are not rigidly mounted to the boom or tool carrier. Some parts change their center of gravity positions during the front loader movements relative to the boom or tool carrier. For instance, the boom cylinders will change their position relative to the boom during movements. For the reduced multi-body

model all masses are summed up and the center of gravity positions are merged together into $\vec{r}_{CogSum}$. Due to the cylinders or the linkage, the measured center of gravity position $\vec{r}_{CogSum\_measured}$ deviates slightly from the real center of gravity position $\vec{r}_{CogSum\_precise}$ of the full multi-body model.

Figure 4.27 shows the precise center of gravity position $r_{CogSum\_precise}$, that changes due to front loader movements indicated by the cylinder strokes. The boom cylinder strokes vary from 0.915m to 1.495m and the bucket cylinder strokes vary from 1.135m to 1.665m (pin to pin). All center of gravity positions are located within an area with the dimensions of 62*35mm. Considering that the distance of the boom from joint J_1 to joint J_2 measures 2.95m, the center of gravity positions vary only about ≈2%.[1]
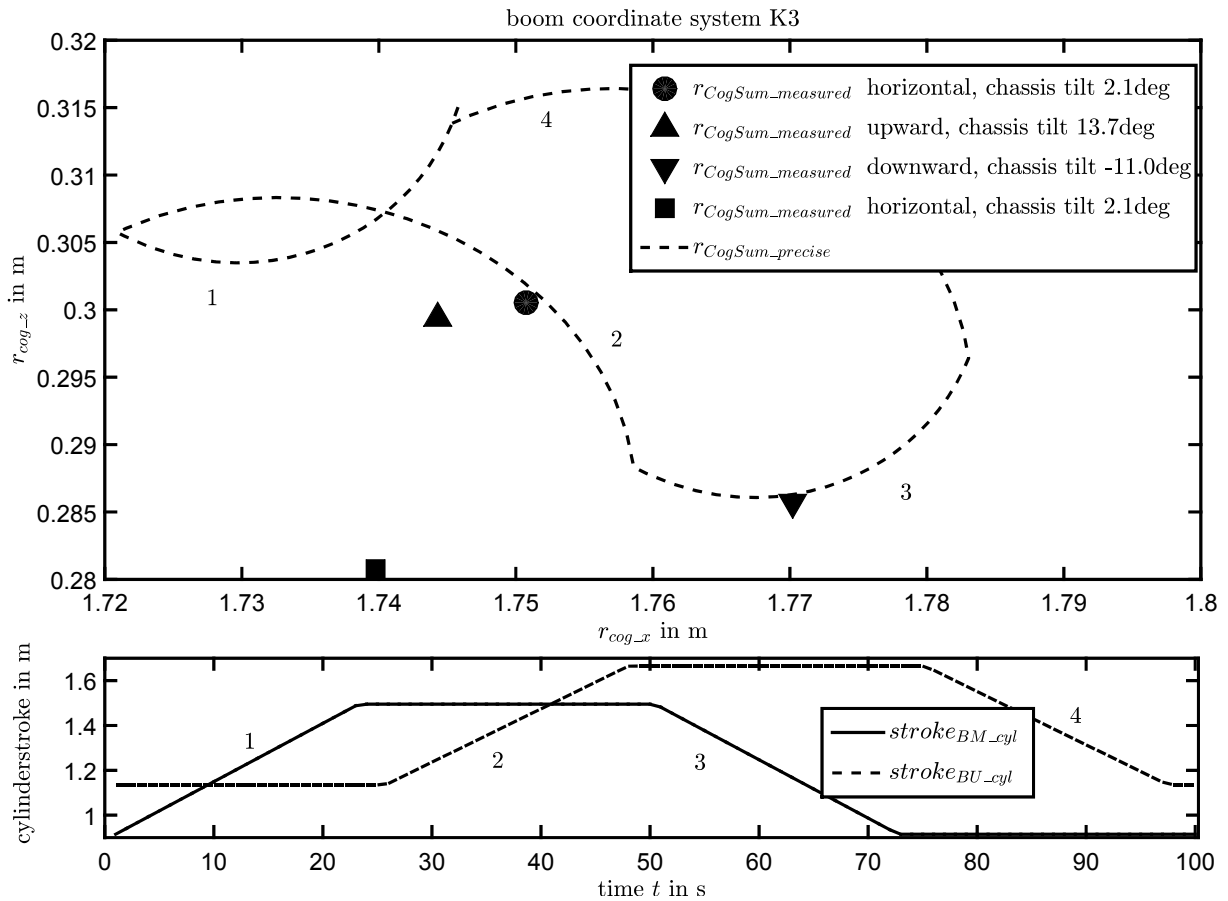

Figure 4.27: Centers of gravity in K_3, multi-body model vs. measurement

Additionally, figure 4.27 shows the merged center of gravity position $r_{CogSum\_measured}$, which is measured by calibration procedures at different tractor tilt angles. Due to limited measurement accuracy, the measured center of gravity position varies for different measurements. For instance, in figure 4.27 four center of gravity positions $r_{CogSum\_measured}$

---

[1]In this case, the tool carrier is referenced as a point mass as shown in figure 4.20 c).

are shown from different measurements with three different machine tilt angles (horizontal, upward, and downward). All center of gravity positions are located within an area with the dimensions of approximately 30*20mm. The maximum deviation is about 30mm, which is about 1% of the boom length.

Finally, in figure 4.28 two payload measurements of a loading cycle are compared. The payload is once calculated with the measured center of gravity position of the reduced multi-body model and once calculated with the precise center of gravity of the full multi-body model. The figure illustrates that the graphs are almost completely aligned. It can be said that the influence of merging the center of gravity on the payload measurement is negligibly small.
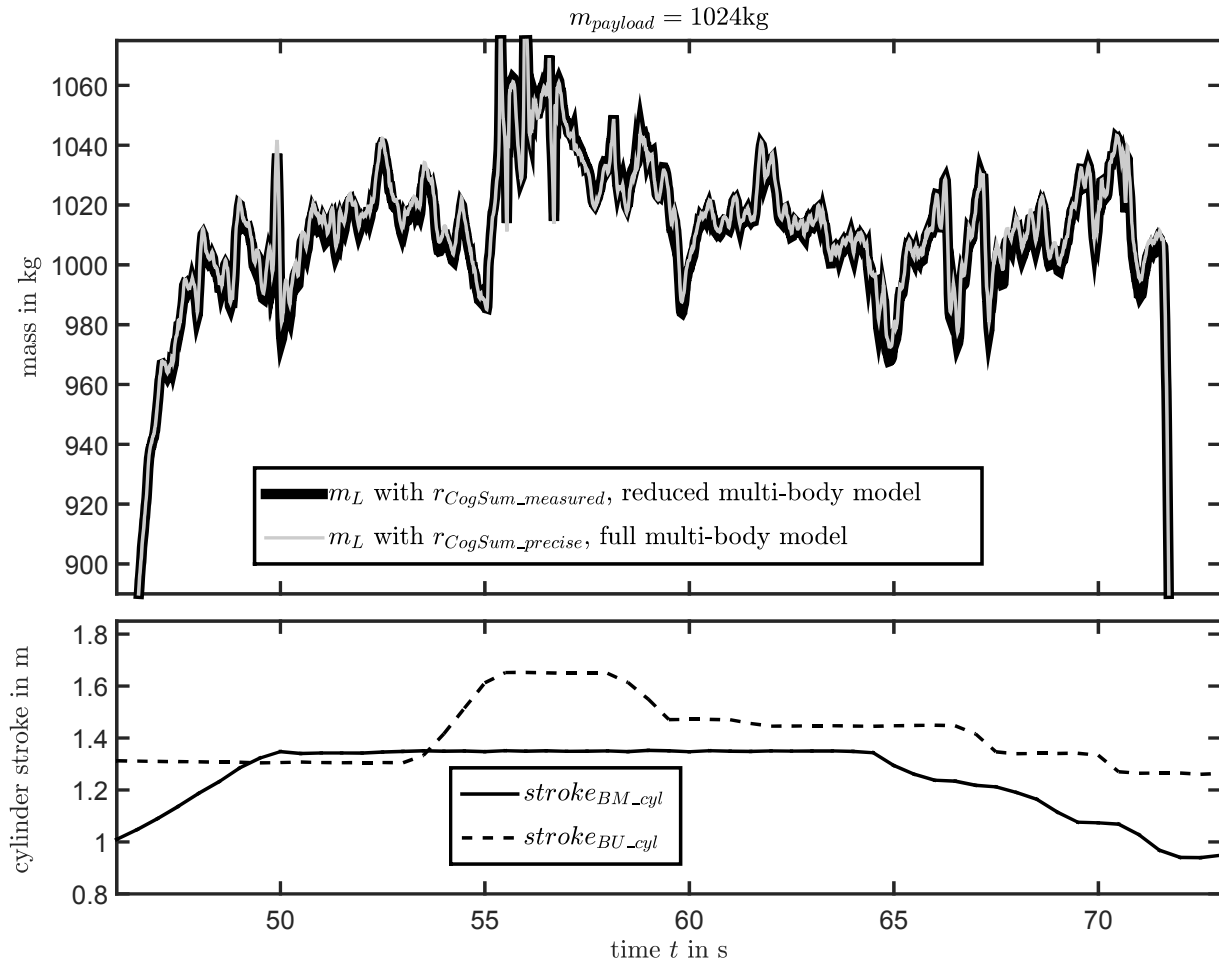

Figure 4.28: Payload measurement with reduced and full multi-body model

4.6.6.2 Estimated Moment of Inertia

The moment of inertia of the boom is estimated by assuming the boom structure as a box as described in section 4.6.1. Figure 4.29 compares the estimated inertia $\Theta_{sumEstimated}$

with the real inertia $\Theta_{sumReal}$ which changes from 259 to 334kgm^2 for different cylinder positions. The mean value is 296kgm^2. Hence, the mean deviation is 44kgm^2, which is approximately 15% of $\Theta_{sumReal}$.

The moment of inertia only influences the payload measurement if the boom experiences an angular acceleration. Under rough work conditions, the angular acceleration peaks are approximately 3rad/s^2, which results in an absolute mean error of $\approx$0.12kNm for the torque measurement at the boom joint J$_1$. For a payload of 1t the torque at J$_1$ is around $TQ_1 \approx$ 15kNm, hence the error is negligibly small.
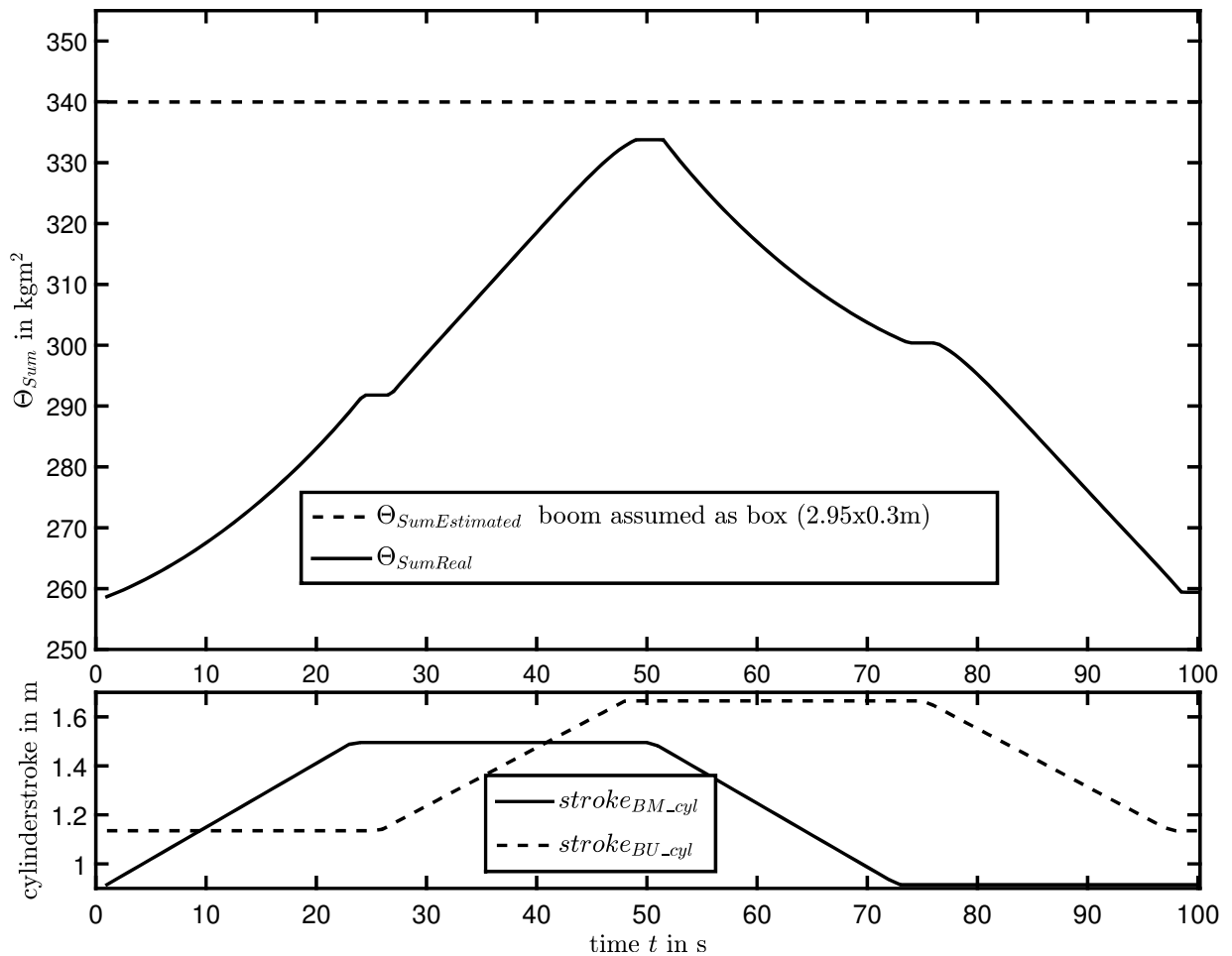

Figure 4.29: Estimated vs. real moment of inertia

Figure 4.30 illustrates that the influence of Θ_{Sum} on the payload measurement is negligibly small. It shows a measurement of a rough working condition with and without considering the moment of inertia Θ_{Sum}. Only at high angular acceleration of the boom deviates the payload measurement slightly.
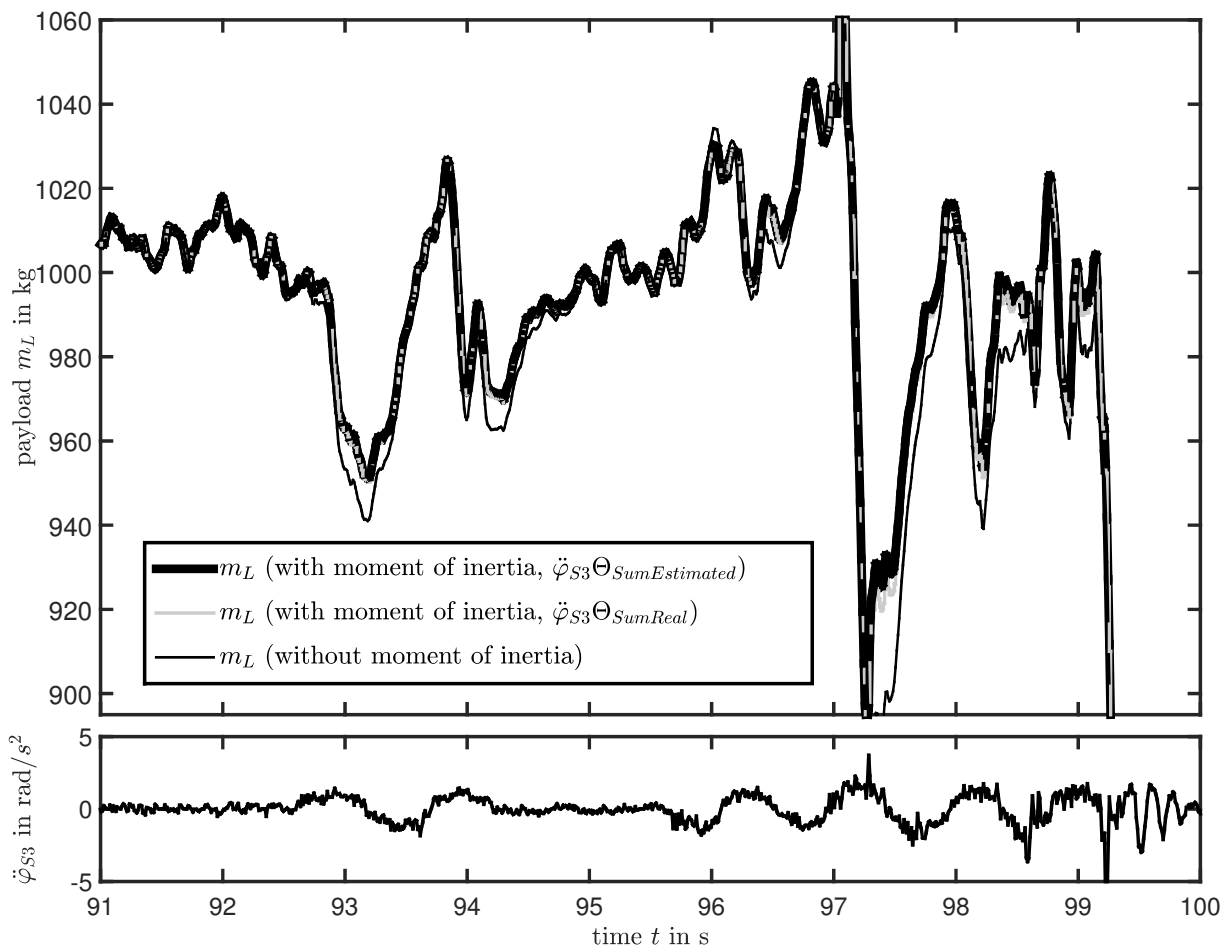
Figure 4.30: Payload measurement in extreme conditions with and without Θ_{Sum}

5 Results

This chapter discusses the characteristics of the "Dynamic Weighing System" (DynWeiSys) based on real measurements and compares the accuracy of the payload measurement for different system configurations. In addition, the DynWeiSys is compared to a common weighing system and the differences of the systems are pointed out. The **DynWeiSys is based on the reduced multi-body model** as described in chapter 4.6.1 with the parameters of appendix A.3. The common system is simulated by using the boom actuator forces and not considering the bucket actuator forces, as described in A.7.

5.1 Benchmark for the Accuracy of the Test Results

5.1.1 Accuracy Classes of Weighing Devices

Non-automatic weighing devices, such as mobile scales, are classified into four [DIN92] respectively five [Nat02] groups, which are defined by the value of the maximum weight capacity m_{max}, the value of the verification scale interval e (Eichwert), and the number of verification scale intervals $n = m_{max}/e$. The accuracy classes are used to determine the intended area of use for a particular scale. The classes are defined as follows:

- Class I is generally used for precision laboratory weighing.

- Class II scales are used for laboratory weighing, for instance, precious metals and gem weighing, grain test scales.

- Class III are all commercial weighing devices not otherwise specified, for instance, grain test scales, retail precious metals and semi-precious gem weighing, animal scales, postal scales, vehicle on-board weighing systems, etc.

- Class IIII includes, for example, wheel loader scales and portable axle load scales used for highway weight enforcement.

- Class IIIL is not subject of [DIN92] but subject of [Nat02]. It is a lower accuracy class than III. It includes vehicle scales and vehicle on-board weighing systems with a capacity greater than 30000lb$\approx$ 13.6t, as well as axle-load scales, railway track, crane scales, etc [Ame11].

Accuracy class III scales are generally used for industrial and commercial environments. Ordinary class IIII scales are only permitted for inexpensive goods such as sand or gravel.

Commercial goods of higher quality such as cereals are only weighed with class III scales [Bit09]. A detailed definition of the classes is given in table 5.1:

Class	Verification scale interval e	Minimum capacity m_{min}	Number of verification scale intervals n	
			n_{min}	n_{max}
I special	$0.001g \leq e$	$100e$	50000	-
II	$0.001g \leq e \leq 0.05g$	$20e$	100	100000
high	$0.1g \leq e$	$50e$	5000	100000
III	$0.1g \leq e \leq 2g$	$20e$	100	10000
medium	$5g \leq e$	$20e$	500	10000
IIII ordinary	$5g \leq e$	$10e$	100	1000
IIIL	$2kg \leq e$		2000	10000

Table 5.1: Scale accuracy classes [DIN92],[Ame11]

5.1.2 Required Accuracy of the Weighing System

As an example, a class IIII scale is given with the maximum capacity of $m_{max} = 2000$kg. The minimum number of verification scale intervals is defined by $n_{min} = 100$. This results in the largest, permitted verification scale interval $e = m_{max}/n_{min} = 20$kg. The tolerances of the initial verification are defined by [DIN92] for a class IIII scale with

- $\pm0.5e$ for a payload in the range of $0 < m_{payload} \leq 50e$,
  which results in ±10kg for a payload range of 0kg to 1000kg for the given example

- $\pm1e$ for a payload in the range of $50e < m_{payload} \leq 200e$,
  which results in ±20kg for a payload range of 1000kg to 4000kg for the given example.

The tolerances during operation while using the scale (Verkehrsfehlergrenzen) are twice the tolerances of the initial verification which result in $\pm2(0.5e) = \pm20$kg and $\pm2(1e) = \pm40$kg.

The maximum lifting capacity of the front loader used in this thesis is approximately $m_{max\,capacity} = 2000$kg. The 1% of the maximum lifting capacity (20kg) is equal to the tolerance of the initial verification interval for a payload range of $50e < m_{payload} \leq 200e$. Hence, the deviation of $0.01m_{max\,capacity}$ is used as a benchmark and marked as boundary lines in the following figures of this chapter. Additionally, the deviation of $0.01m_{payload}$ and the real payload $m_{payload}$ are evaluation criteria and marked as lines, as shown in the example of figure 5.1.
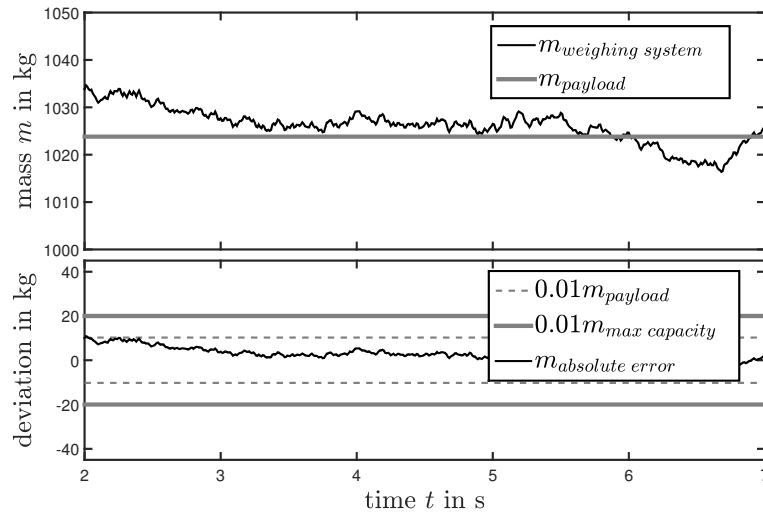
Figure 5.1: Example of benchmark lines

5.2 Dynamic Weighing vs. Common Systems

With a common system, as described in section 1.2.1 et sqq. (see also A.7), the payload measurement can be achieved with a deviation of $\approx 1\%$ of the maximum lifting capacity [Pro12b] (cf. section 1.2.8). This accuracy is only given, if the measurement is taken at a previously calibrated boom position during a boom up movement at a defined speed. The center of gravity of the payload has to be at a previously calibrated position and the machine must not oscillate during the measurement. Otherwise, the accuracy decreases significantly.

In contrast, DynWeiSys measures continuously as long as the cylinders are not in the end-stroke positions. Hence, the system deals with all working conditions, for example, oscillations of the machine or changes of the center of gravity position of the payload.

To illustrate the differences between the systems, the front loader lifts and lowers the boom with a known payload $m_{payload}$ at different cylinder velocities, as shown in figure 5.2.

During the measurement, the bucket cylinders do not move in order to keep the center of gravity position of the payload constant relatively to the boom.
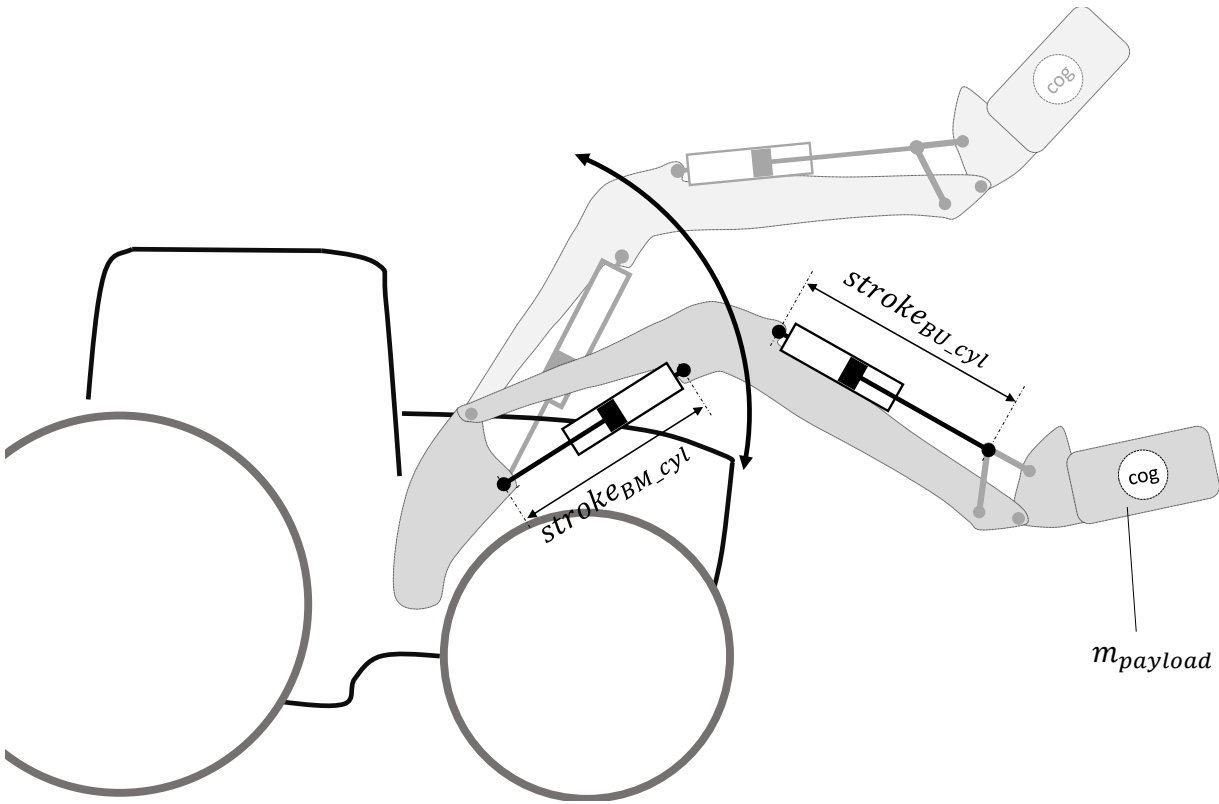

Figure 5.2: Test configuration 1: Lifting and lowering of the boom with a constant bucket cylinder position

Figure 5.3 shows a measurement of test configuration 1. At the top of figure 5.3 the payload readings of both systems are shown, which are displayed as mass over the time. The common system (m_{common}) takes the payload measurement only at a specific cylinder stroke while the DynWeigSys ($m_{DynWeiSys}$) measures continuously. The middle part of figure 5.3 shows the absolute deviation over the time and the $\pm 1\%$-boundary with respect to the maximum lifting capacity and with respect to $m_{payload}$. The measurement of the common system deviates strongly in different boom positions. Hence, the measurement is only taken at a certain boom cylinder stroke during the lifting of the boom. The deviation of the DynWeiSys is almost in the $\pm 1\%$-boundary, regardless of the boom position and movement. Deviations higher than 1% occur occasionally while lowering the boom. The deviations are effected by inaccuracies of the friction model. The common system is optimized for a boom up-movement at a specified actuator velocity. If the velocity or the direction of movement changes, the payload measurement deviates due to changing friction influences.
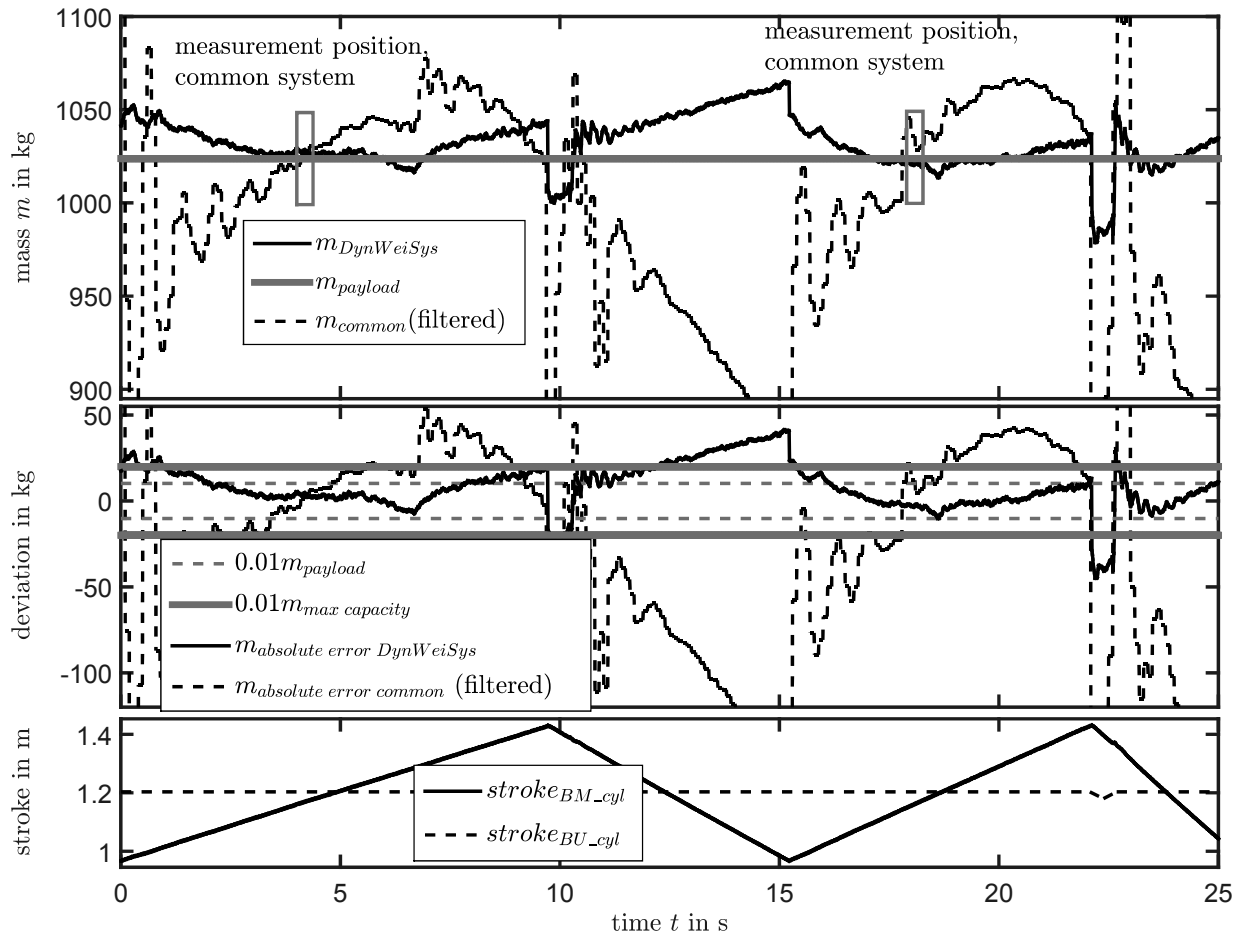
Figure 5.3: Dynamic weighing vs. common system for test configuration 1

Figure 5.4 shows the percentage of deviations with respect to the maximum lifting capacity of both systems over the cylinder stroke for several boom up-movements. The measurement of the DynWeiSys can be taken at any boom position with an accuracy loss of $\approx 1\%$. With the common system this accuracy of the payload measurement can only be achieved at a certain cylinder stroke, which is indicated by the small boxes in the top of figure 5.3.
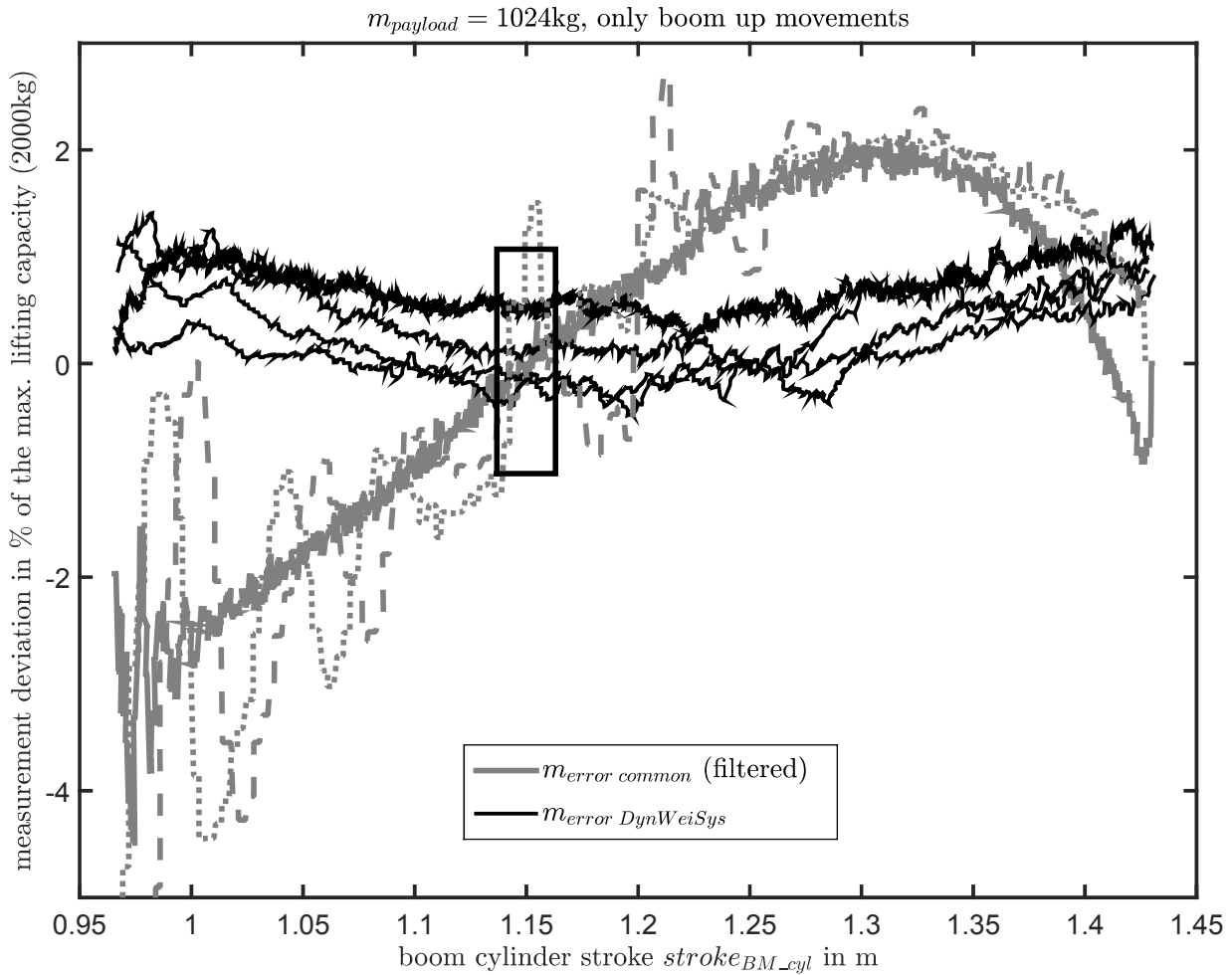
$$m_{payload} = 1024\text{kg, only boom up movements}$$

Figure 5.4: Dynamic weighing vs. common system for test configuration 1 - only boom up movements

In addition, the measurement results of DynWeiSys are independent of machine oscillations due to their compensation based on measured accelerations. This can be seen in figures 5.3 and 5.4 where the oscillations only affect the common system and do not affect the DynWeiSys. This will be discussed in greater detail in section 5.5.

5.3 Variation of the Payload's Center of Gravity Position

The DynWeiSys measures the payload independent of the center of gravity position of the payload. This is illustrated by two measurements. First, a known payload, $m_{payload} = 1724\text{kg}$, is connected to the tool carrier. By moving the carrier up and down the center of gravity of the payload changes its position relative to the boom and also relative to the machine, as shown in figure 5.5.
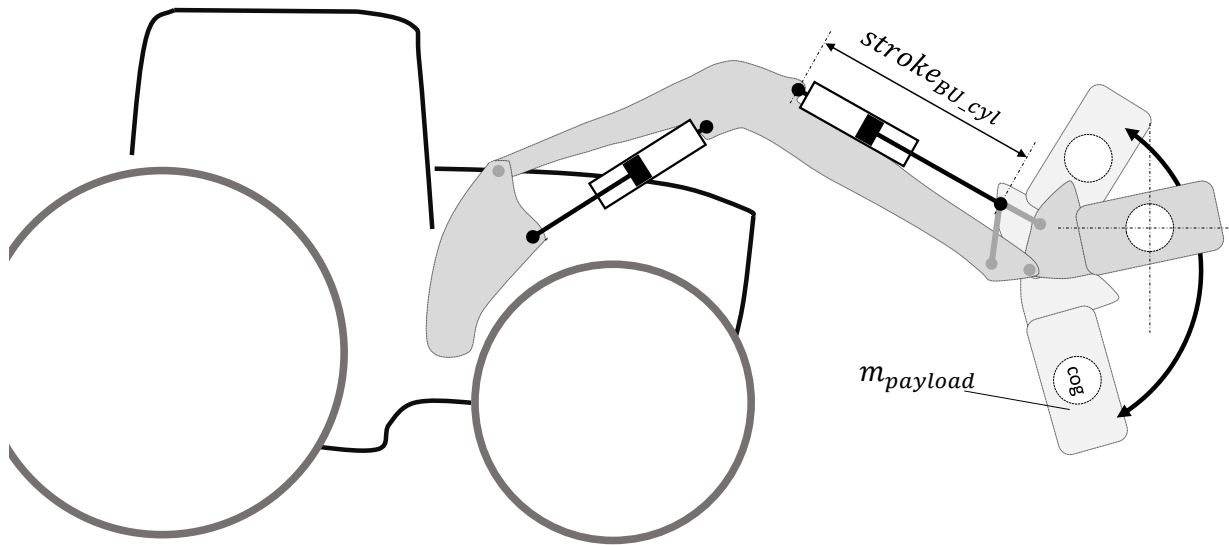
Figure 5.5: Test configuration 2: the tool carrier is moved up and down

The common system measures with a high accuracy as long as the center of gravity of the payload is in a previously calibrated position, usually in the bucket with the bucket cylinder at the minimum end-stroke position (rollback position). If the position varies, the payload measurement m_{common} deviates from the true payload $m_{payload}$. Figure 5.6 shows the payload measurement of test configuration 2 for the DynWeiSys and a common system. The payload measurement of the the common system is simulated by replacing $\vec{TQ}_2$ in equation (4.48) by a constant torque offset. This is equivalent to a common system which is calibrated at a defined bucket position. If the bucket cylinder is not close to the minimum end-stroke position, the payload measurement of the common system deviates more than 1% from the maximum lifting capacity. Otherwise, the deviation of the DynWeiSys is in the $\pm 1\%$-boundary.
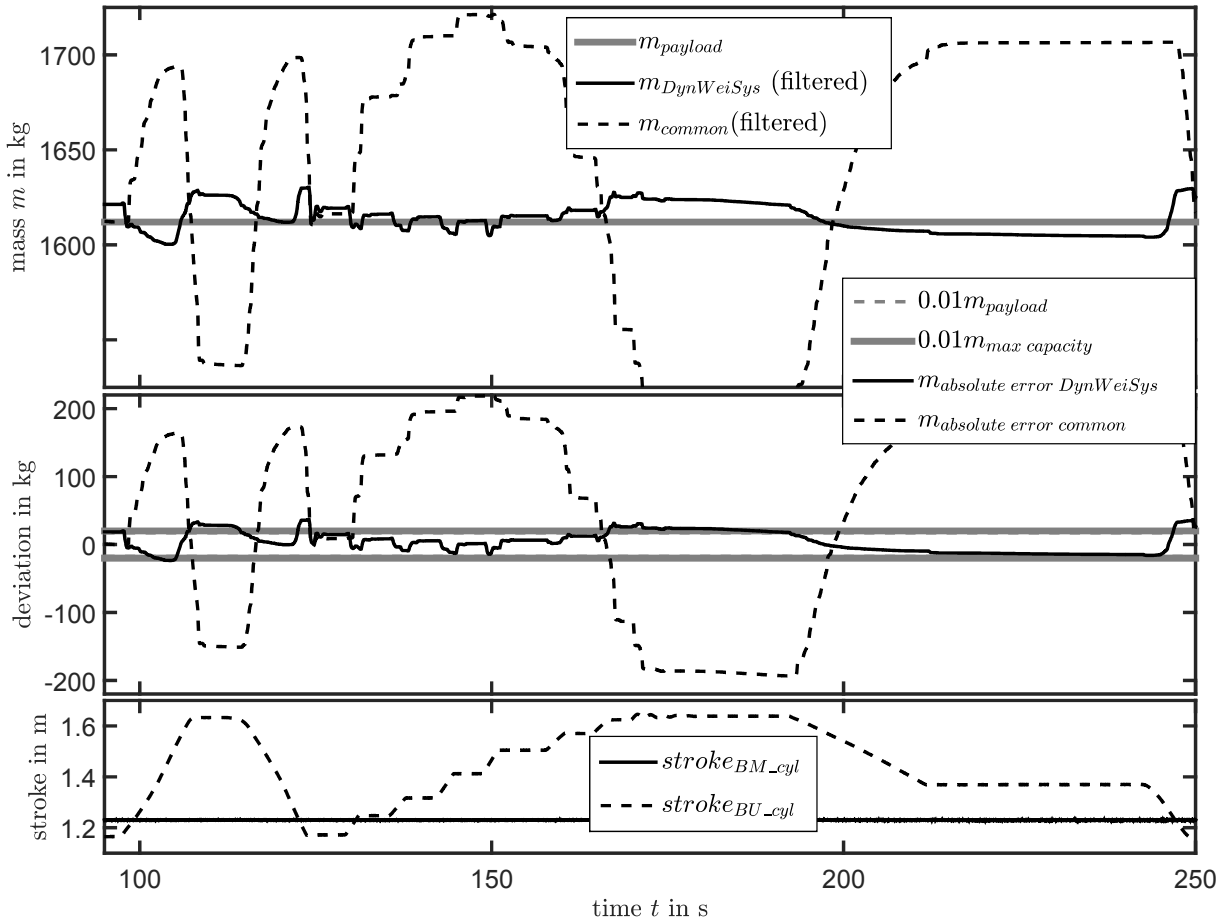
Figure 5.6: Variation of the center of gravity position of the payload for test configuration 2

For the second test, a long palette fork (242kg) is connected to the tool carrier. The fork is charged with a 65kg payload. The payload is shifted to five positions in a range of approximately 4m, as shown in figure 5.7. The common system does not work properly and measures a different payload m_{common} for each position, as seen in figure 5.8. The DynWeiSys measures the payload $m_{DynWeiSys}$ with a small deviation which lies within the $\pm 1\%$-boundary and also within the $\pm 1\%$-boundary of the payload. During this test, the front loader does not move.
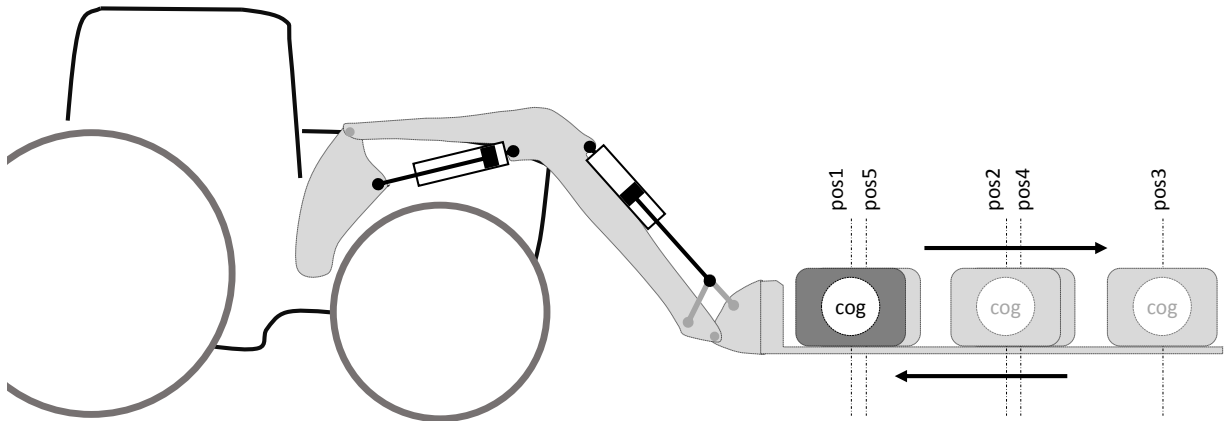
Figure 5.7: Test configuration 3: Variation of the center of gravity position of the payload
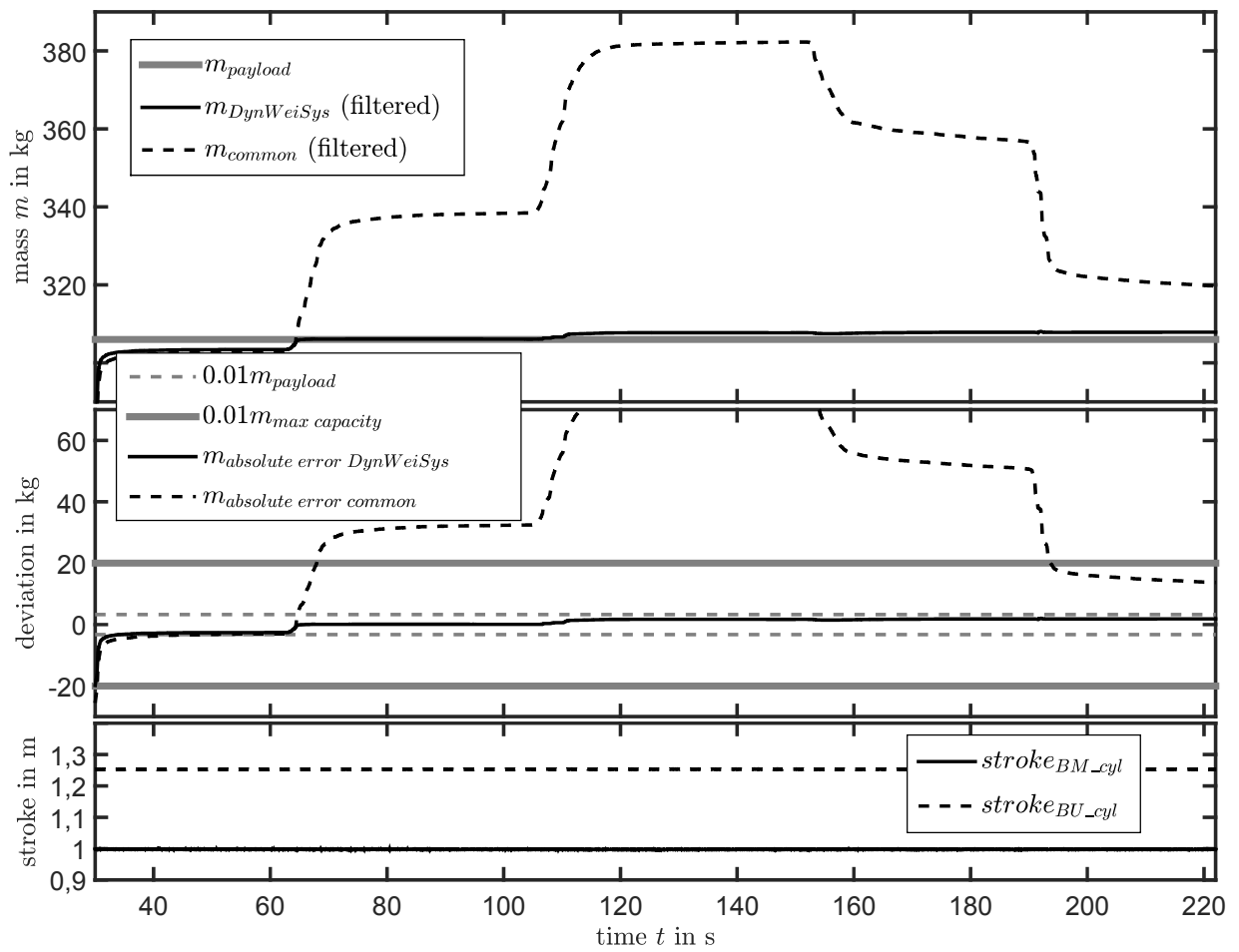

Figure 5.8: Variation of the center of gravity position of the payload for test configuration 3

5.4 Friction Compensation

The DynWeiSys compensates joint and cylinder friction during front loader movements, as described in chapter 4.1.2.2. In the following, two test configurations are provided to analyze the influence of friction on the payload measurement. At test configuration 4, there is no tool or payload attached to the front loader, therefore, $m_{payload} = 0$kg. The front loader performs several boom up and down movements at different cylinder velocities. The bucket actuators do not move. At test configuration 5, the front loader is charged with $m_{payload} = 1024$kg. It performs movements with the boom and bucket cylinders. Figure 5.9 shows the deviations of the payload measurement with and without (w/o) friction compensation at test configuration 4. Due to the increasing return pressure at increasing oil flow, the friction and also its influence on the payload measurement increases with the cylinder speed. Thus, the uncompensated payload measurement differs approximately 40kg from the true payload $m_{payload}$. If friction is considered, the deviation of the payload measurement lies inside the $\pm1\%$-boundary of the maximum lifting capacity.
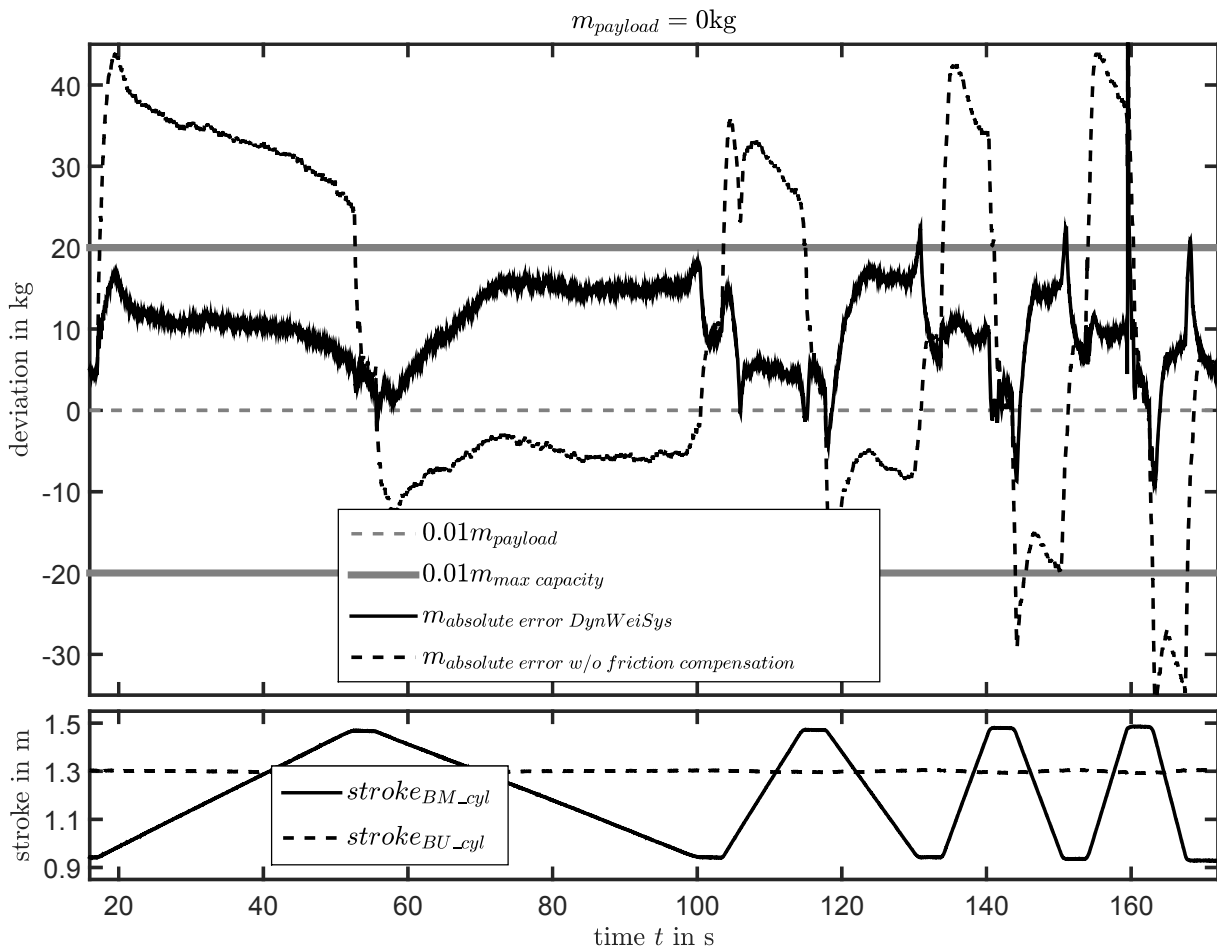

Figure 5.9: Influence of the friction compensation for test configuration 4 and $m_{payload} = 0$kg

In the following test, the front loader performs movements with the boom and bucket

actuators at test configuration 5. If the front loader is charged with a payload, the friction increases due to higher cylinder pressures. This is shown in figure 5.10, in which the uncompensated payload measurement deviates $\approx$ 75kg from the payload $m_{payload} = 1024$kg. Including friction compensation, the payload measurement is inside the $\pm 1\%$-boundary, except for down movements, where the deviation reaches the $\pm 1.5\%$-boundary of the maximum lifting capacity.
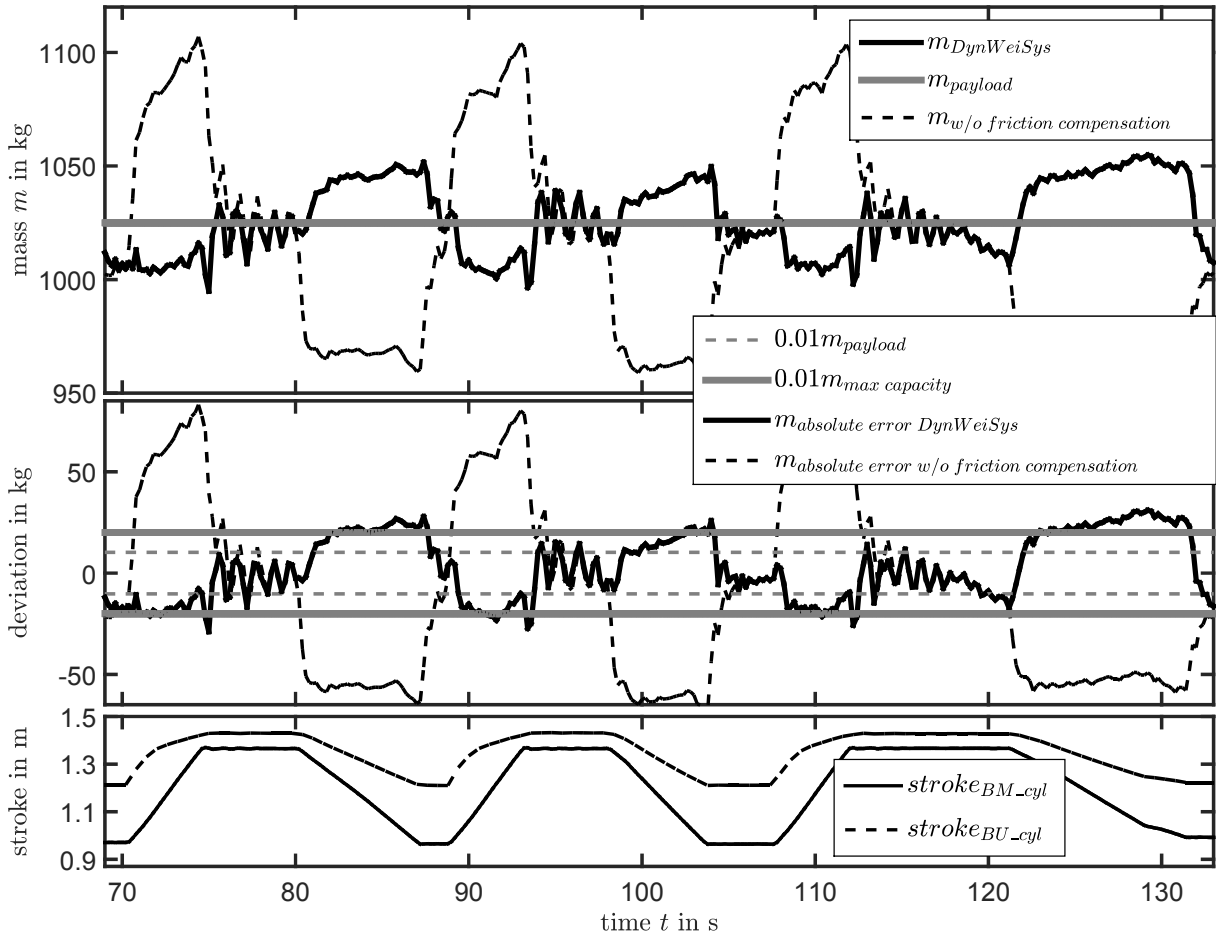

Figure 5.10: Influence of the friction compensation for test configuration 5 and $m_{payload} = 1024$kg

5.5 Accelerations and Oscillations of the Front Loader

The DynWeiSys compensates the influence of machine shaking and oscillations by measuring the actual accelerations. To calculate the payload, torques at the loader joints which are generated by cylinder forces are compared with torques which are generated by a multibody model, as described in chapter 4.3. In order to generate these torques, the multi-body model is fed with measured accelerations. If the machine or the front loader moves, the

cylinder forces oscillate and the torque does not remain constant. At the same time, the accelerations of the movements are measured with an IMU and the output of the multi-body model oscillates as well and compensates the oscillations in the payload measurement.

If the machine does not move, only gravity affects the front loader. Hence, it is possible to consider the accelerations as constant and feed the multi-body model only with the gravity. In this case, oscillations are not compensated. Figure 5.11 shows the differences of a payload measurement with measured accelerations by an IMU and the acceleration considered as constant (w/o IMU). The test is done under rough conditions and the boom movement is started and stopped abruptly to trigger oscillations of the machine. At the beginning ($t =$96s..98s), the machine is at standstill and only the gravity affects the front loader. Thus, the payload measurement is equal with and without IMU. Then, the loader starts to move. While the uncompensated payload measurement oscillates excessively the compensated payload measurement is almost in the $\pm 1\%$-boundary of the maximum lifting capacity. The acceleration output of the IMU is corrupted by noise, which is directly transferred to the payload measurement $m_{withIMU}$, as shown in figure 5.11. For $m_{w/oIMU}$ the acceleration is considered as constant, hence, the payload measurement is not corrupted by noise. For better comparability $m_{withIMU}$ is filtered and becomes $m_{withIMU}(\text{filtered})$.
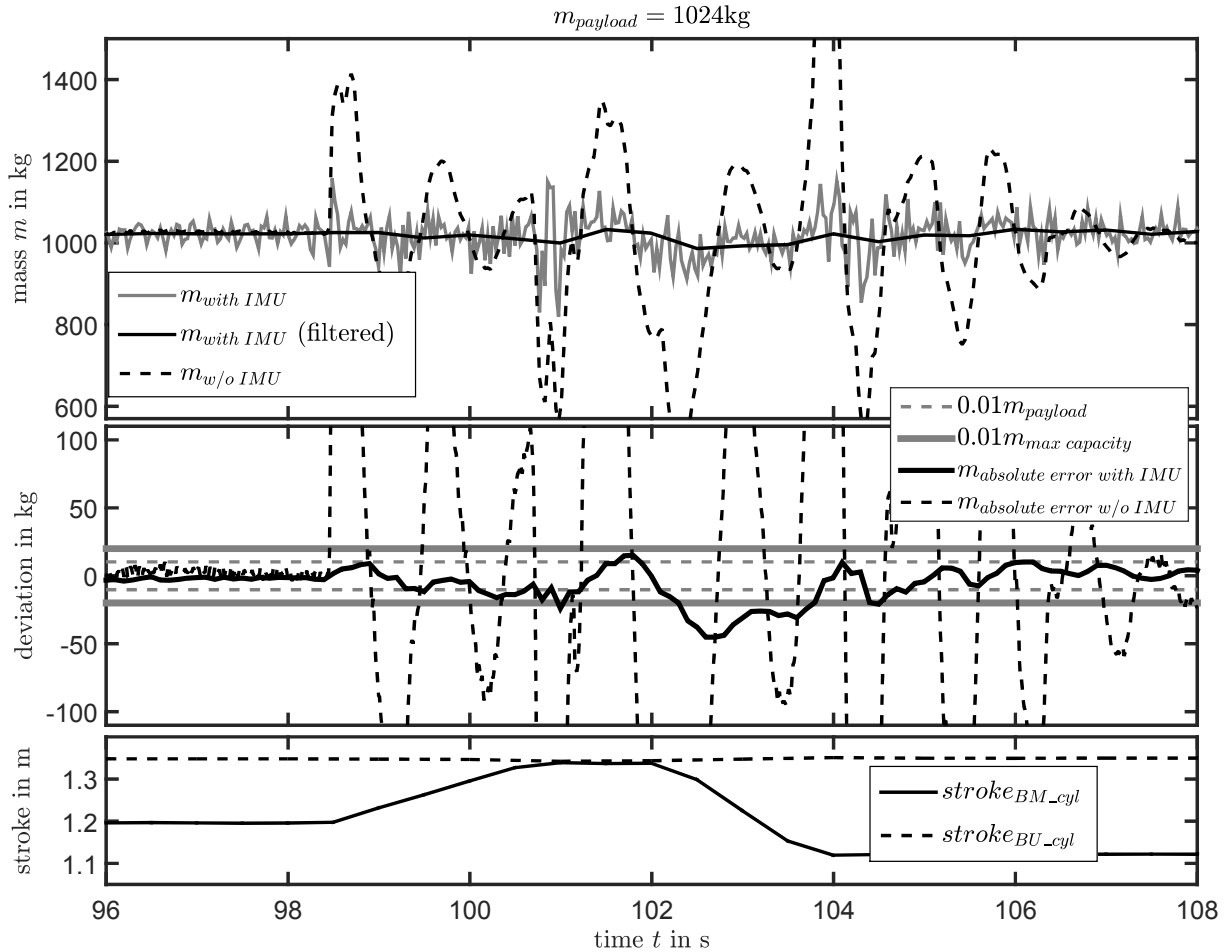
Figure 5.11: Oscillation compensation of rough movements with and without IMU

Nevertheless, it is possible to determine the payload without an IMU during oscillations by using statistics, for instance, the mean or median value over a longer time segment that contains several oscillations. But, as mentioned before, the goal is to determine the payload as fast as possible while working with the loader.

Figure 5.12 shows a detail of a payload measurement for loading cycles with a known payload at standard work conditions on horizontal ground with and without IMU. To evaluate the differences, a continuous median is calculated for each raw payload signal. In this case, continuous means that the range for calculating the median increases with every sample point and is reset at the time when the load is lifted from the ground. The bigger the range, the more the continuous median converges to the true payload value, as shown in the top graph of figure 5.12.
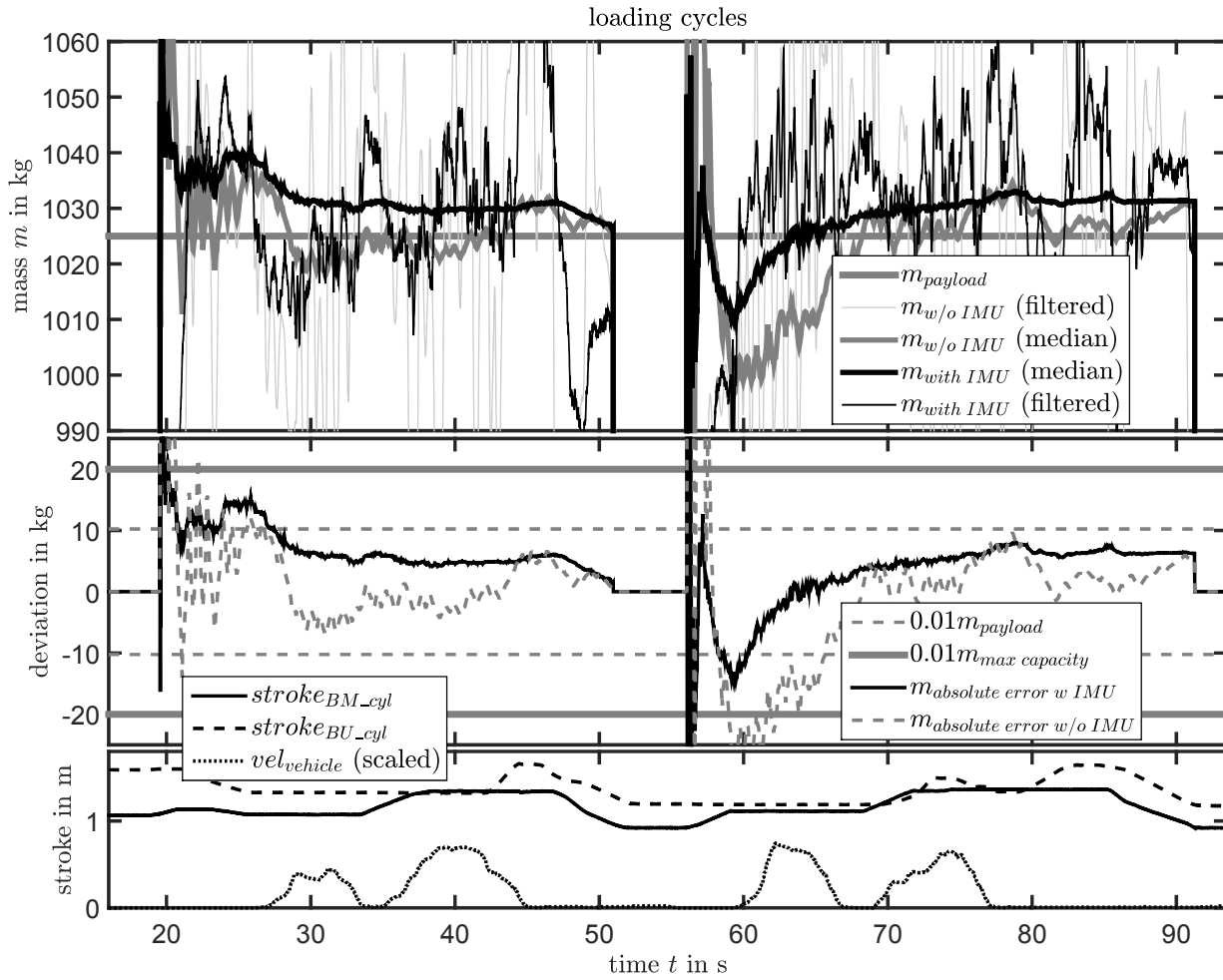
Figure 5.12: Oscillation compensation of standard loading cycles with and without IMU

Both configurations, with and without IMU, are benchmarked by the amount of time it takes until the payload is determined with an deviation of $\pm 1\%$ of the lifting capacity. Figure 5.13 shows the deviation of the median of the payload measurement for several loading cycles over the lifting time (5 loading cycles for $m_{payload} = 1024$kg and 6 loading cycles for $m_{payload} = 1724$kg). Each cycle starts at time $t = 0$ when the load is lifted from the ground.

relative deviation calculated by the root mean square of all cycles for a configuration
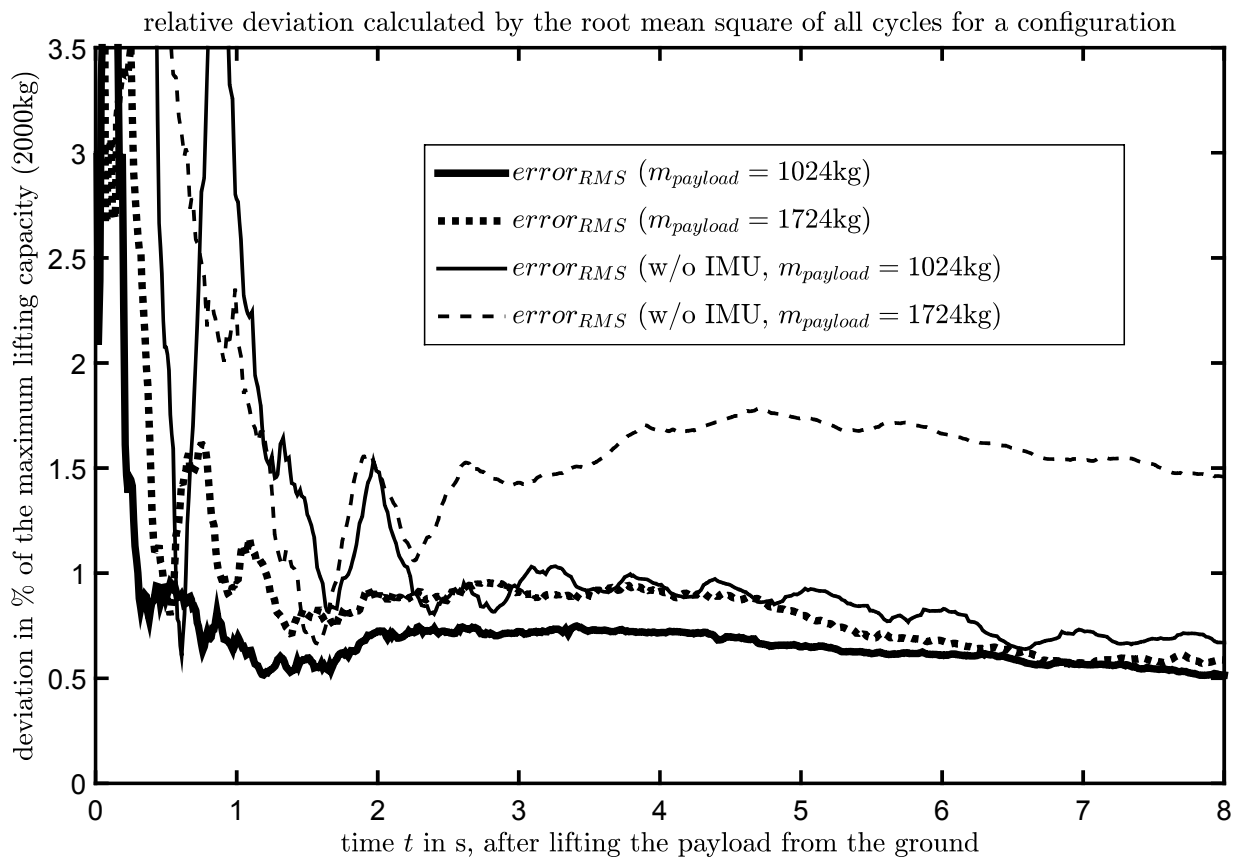

Figure 5.13: Benchmark of oscillation compensation of loading cycles with and without IMU

Figure 5.13 illustrates that with the use of an IMU the payload can be determined approximately one second after being lifted from the ground with an deviation of $\pm1\%$ of the maximum lifting capacity. Without an IMU, the value oscillates at least three seconds after the payload is being lifted from the ground. The higher offset in the graph "$error_{RMS}$ (rec119 w/o IMU, $m_{payload} = 1724$kg)" in figure 5.13 can be explained by deviations of the estimated gravity direction. The gravity direction is estimated as rectangular to the x-axis of the machine. If the loader lifts a high payload, the machine is pitched forward and the true gravity direction differs from the estimated one. With an IMU, the acceleration is measured as a vector with components measured at least in the x- and z-axis (cf. chapter 4.5.2.5).

5.6 Repeatability

This chapter analyses the repeatability of the DynWeiSys payload measurement during different loader work procedures. First, the accuracy of the payload measurement is analyzed for complete loading cycles and boom-lifting and -lowering cycles. Afterwards, the accuracy of the payload identification is investigated for receiving the payload value at any

time during a continuous measurement.

Because the measurements do not follow a normal distribution, the following statistics uses mainly medians and quartile ranges instead of mean values and standard deviations. The results are shown in a box-whisker-plot. The bottom of the box exemplifies the first quartile (25% quantile) whereas the top of the box represents the third quartile (75% quantile). The line inside the box is the second quartile (50% quantile), also known as the median. The whiskers have the length of 1.5 times of the inter quartile range (IQR), which is 1.5 times the height of the box. This corresponds to approximately $\pm 2.7\sigma$ and the coverage of 99.3% if data is normally distributed. Data outside the whiskers is defined as outliers. The width of the box is irrelevant, [Mat10].

5.6.1 Working Cycles

Several loading cycles are performed with a known payload that is permanently mounted to the tool carrier of the front loader. At first, the payload is lifted from the ground and fully supported by the front loader. While traveling forward, the load is fully raised, thus, all cylinders are moved to match the desired working situation. Then, the bucket cylinders are moved out simulating a dumping process onto a trailer. Finally, the bucket cylinders are moved in back, the machine travels back, and the payload is lowered to the ground. These cycles are performed several times with different known payloads while recording the payload measurement. In addition, several lifting and lowering cycles of the boom are included with different known weights to increase the number of measurements. To match the desired working situation the boom and bucket actuators are moved. Afterwards, a box-whisker-plot is generated and the median $\tilde{x}_i$ is calculated for each cycle, as displayed in figures 5.14, A.18, A.19, A.20, A.21.
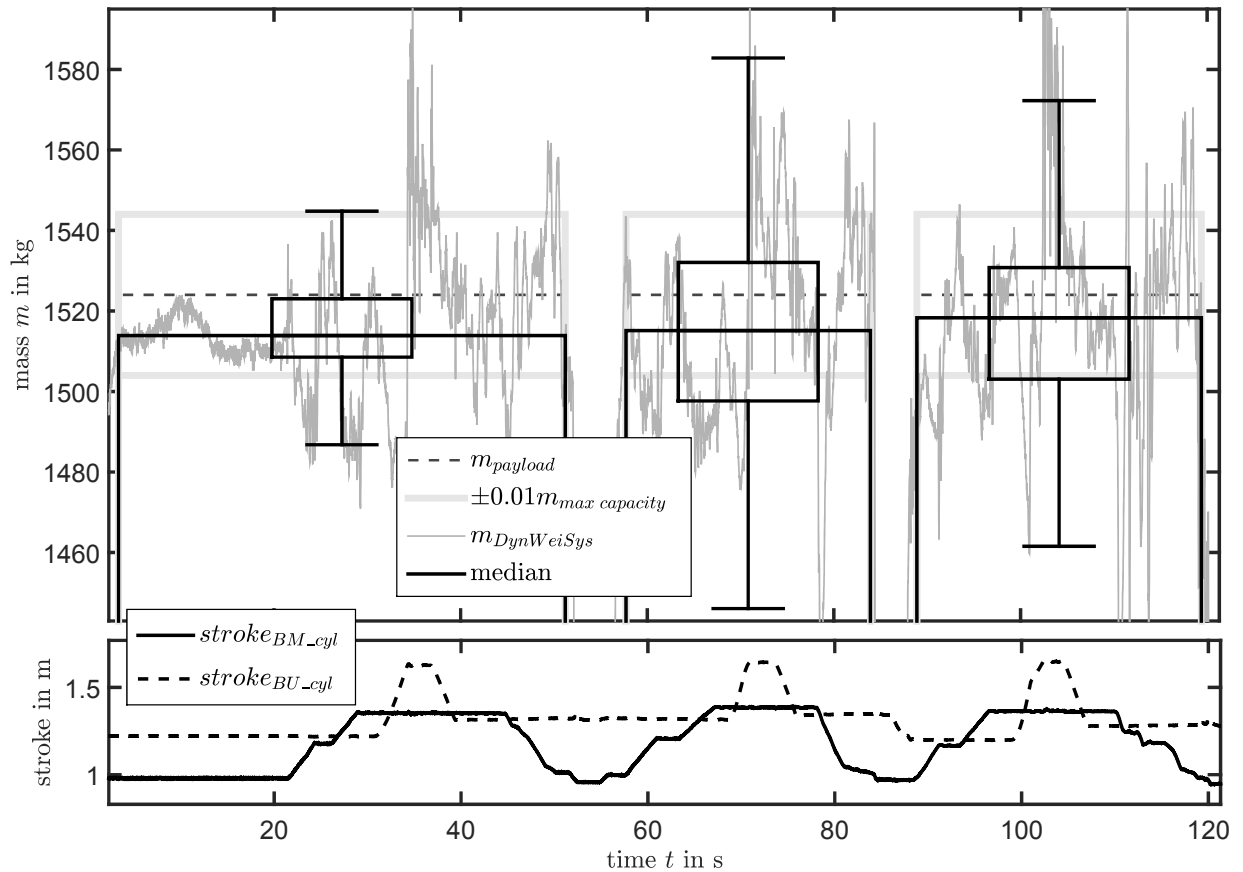
Figure 5.14: Calculating $\tilde{x}_i$ for loading cycles, $m_{payload}$=1524kg

In a next step, every deviation of the median from the true payload value is set in relation to the payload itself, $100\dfrac{|\tilde{x}_i - m_{payload}|}{m_{payload}}$, or set in relation to the maximum lifting capacity of the front loader, $100\dfrac{|\tilde{x}_i - m_{payload}|}{m_{max\ capacity}} = 100\dfrac{|\tilde{x}_i - m_{payload}|}{2000\text{kg}}$. Figure 5.15 shows the deviation for each cycle. For example, three cycles are performed with a payload of 1524kg. For each cycle, the deviation $|\tilde{x}_i - m_{payload}|$ is calculated. Hence, figure 5.15 displays three values for the mass $m_{payload}$=1524kg. As an additional example, seven lifting and lowering cycles are performed with a payload of 306kg. Hence, seven values for the mass $m_{payload}$=306kg are displayed.
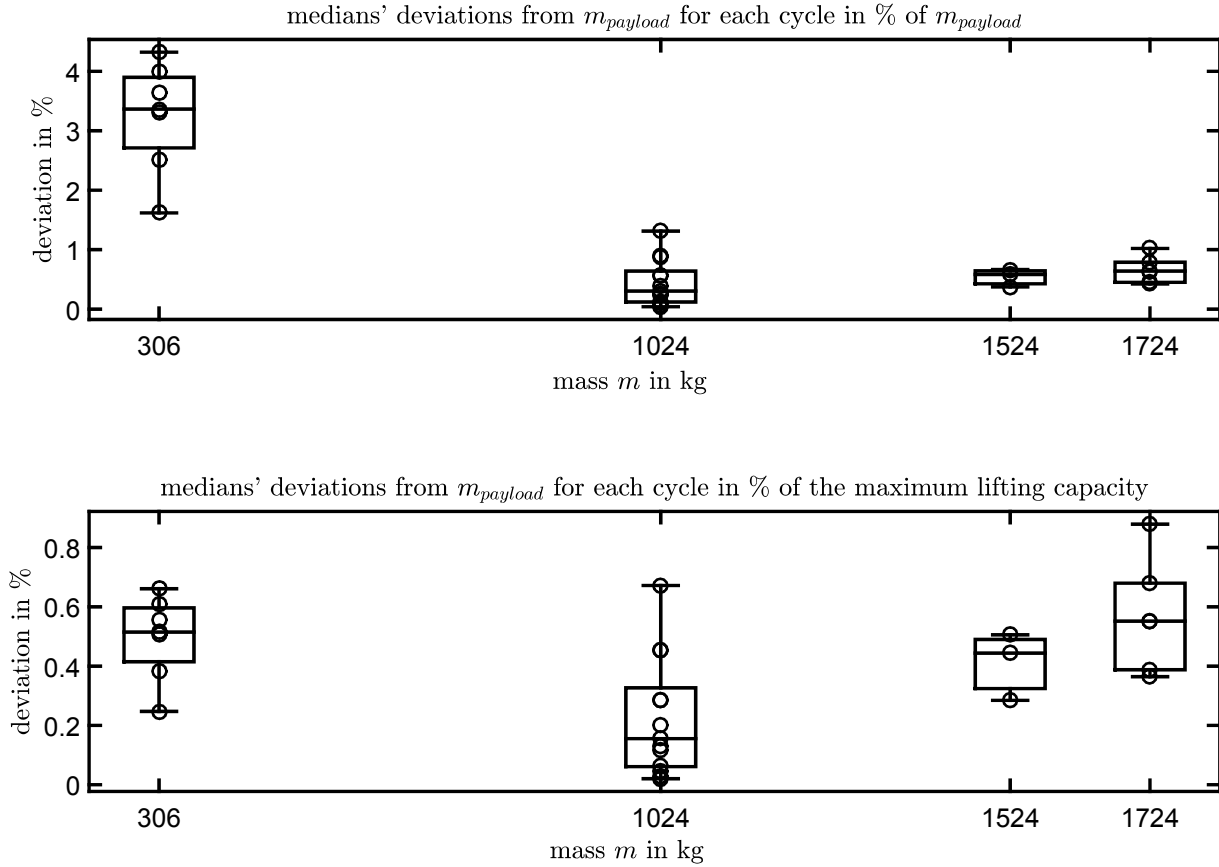
medians' deviations from $m_{payload}$ for each cycle in % of $m_{payload}$

medians' deviations from $m_{payload}$ for each cycle in % of the maximum lifting capacity

Figure 5.15: Deviation $|\tilde{x}_i - m_{payload}|$ in % for all cycles

For instance, at $m_{payload} = 306$kg, the highest deviation of the median is 4.32% of $m_{payload}$, which is equal to 0.66% of the maximum lifting capacity, which is approximately ± 13.2kg. Table 5.2 summarizes the relevant values of figure 5.15. It can be said that even the highest deviation from the true payload of the median of each cycle is less than 1% respective to the maximum lifting capacity of the loader.

$m_{payload}$ in kg	306	1024	1524	1724		**average**
	deviation in % of $m_{payload}$					
worst case	4.32	1.31	0.66	1.02		1.83
median	3.36	0.30	0.58	0.64		0.98
	deviation in **% of the maximum lifting capacity**					
worst case	0.66	0.67	0.51	0.88		0.54
median	0.51	0.16	0.44	0.55		0.33

Table 5.2: Relative deviation values for all cycles

5.6.2 Continuous Payload Measurement

The DynWeiSys gives the possibility to measure the payload in any condition at any time. Previous measurements, as in figure 5.11, have shown that even when compensating all disturbances the payload value still oscillates. Hence, it is obvious to determine the payload by filtering or by analyzing the payload readings over a short time. To evaluate the quality of the payload determination at any time, measurements with several lifting and lowering cycles of the boom are performed with a known payload $m_{payload}$. To match the working situation, the boom and bucket actuators are moved. The measurements are split into short segments of three seconds each in order to gather enough samples per segment for the following statistics. Then, the medians $\tilde{x}_i$ are calculated for each segment, as shown in figure 5.16.
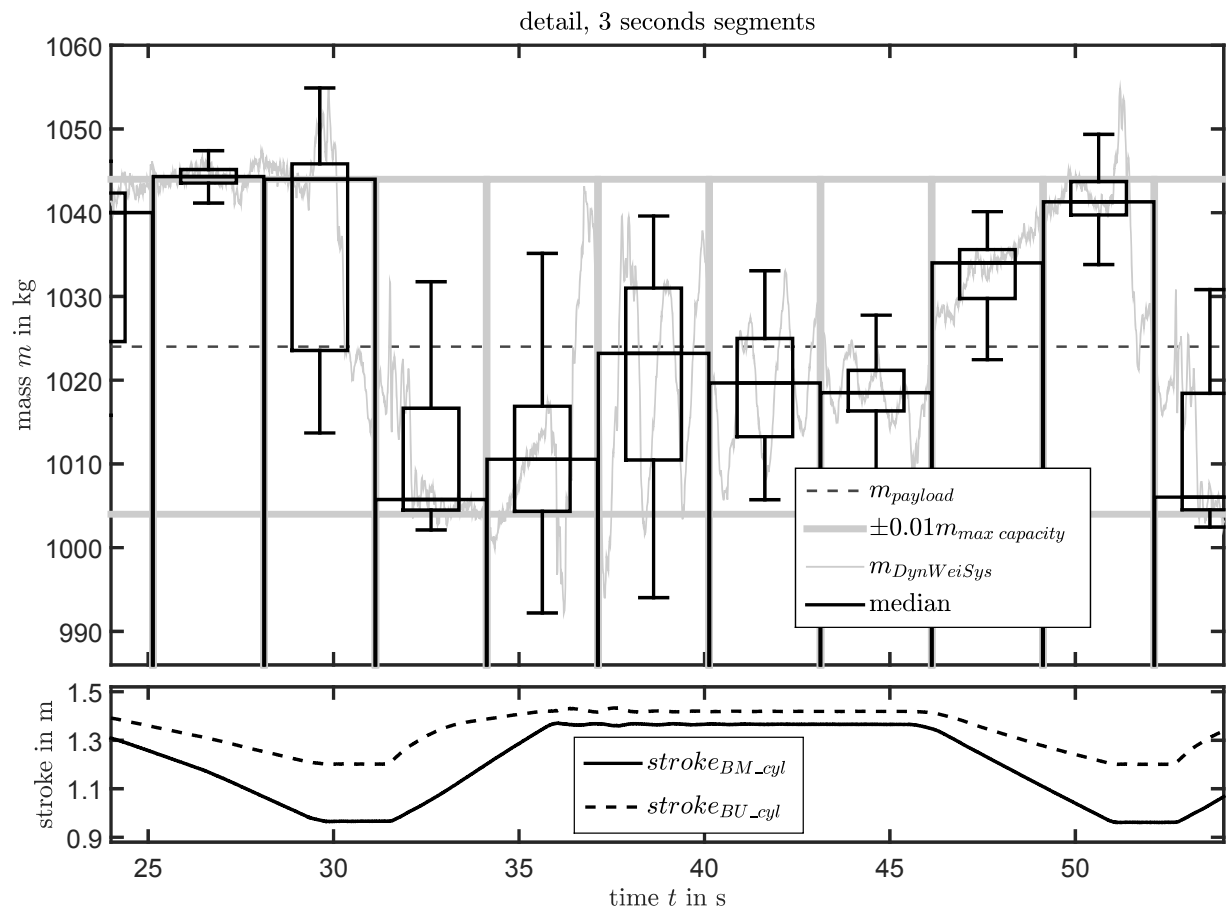

Figure 5.16: Calculating $\tilde{x}_i$ for lifting and lowering cycles, $m_{payload}$=1024kg

Finally, every deviation of the median from the true payload value is set in relation to the payload itself, $100\dfrac{|\tilde{x}_i - m_{payload}|}{m_{payload}}$, or set in relation to the maximum lifting capacity of the front loader, $100\dfrac{|\tilde{x}_i - m_{payload}|}{m_{max\ capacity}}$, as shown in figure 5.17.
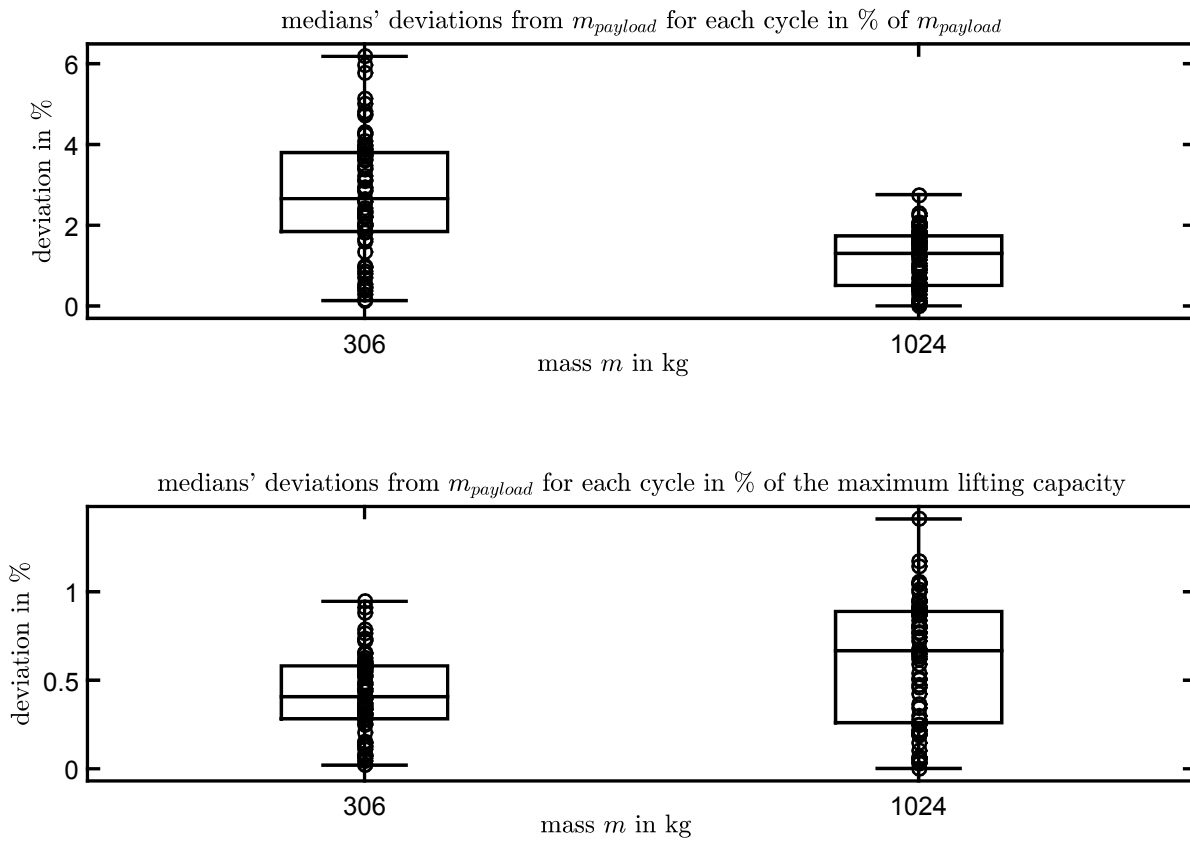
medians' deviations from $m_{payload}$ for each cycle in % of $m_{payload}$

medians' deviations from $m_{payload}$ for each cycle in % of the maximum lifting capacity

Figure 5.17: Deviation $|\tilde{x}_i - m_{payload}|$ in % for all segments

For $m_{payload} = 306$kg, the $\tilde{x}_i$ are allocated in a range of 20.6kg from 304.3kg to 324.9kg. This results in a worst case deviation of the median from the true payload value of $100\frac{|\tilde{x}_i - m_{payload}|}{m_{payload}} = 6.18\%$, or $100\frac{|\tilde{x}_i - m_{payload}|}{m_{max\ capacity}} = 0.95\%$ from the maximum lifting capacity (= 2000kg). The median $\tilde{x}$ of all medians of the segments $\tilde{x}_i$ is 314kg and the median of all deviations of the segments $|\tilde{x}_i - m_{payload}|$ is 2.66% of $m_{payload}$ or **0.41% of the maximum lifting capacity**.

For a higher payload, $m_{payload} = 1024$kg, the $\tilde{x}_i$ are spread from 1004.9kg to 1052.2kg in a range of 47.3kg. This results in a worst case deviation of the median of $100\frac{|\tilde{x}_i - m_{payload}|}{m_{payload}} = 2.75\%$ or $100\frac{|\tilde{x}_i - m_{payload}|}{m_{max\ capacity}} = 1.41\%$ of the maximum lifting capacity (= 2000kg). The median $\tilde{x}$ of all medians of the segments $\tilde{x}_i$ is 1018.8kg and the median of all deviations of the segments $|\tilde{x}_i - m_{payload}|$ is 1.3% of $m_{payload}$ or **0.67% of the maximum lifting capacity**.

This chapter presented and discussed the test results of the DynWeiSys. In addition, the procedure of testing was described in detail.

6 Conclusion and Outlook

This thesis deals with the research and development of a mobile loader scale, "Dynamic Weighing System" (DynWeiSys), which measures a lifted payload in every working situation. A prototype is developed for a front loader of an agricultural tractor that measures payload continuously with a deviation of $\pm 1\%$ of the maximum payload capacity regardless of the center of gravity position of the payload or whether the machine moves, travels, or bounces. The underlying theory combines a static model with a multi-body model.

The static model considers all front loader dimensions and transfers the measured actuator forces with the knowledge of the loader kinematics into torques at the joints of an open, planar kinematic chain. The chain consists of three major parts: chassis, boom, and tool carrier with two joints in between. The multi-body model is used to transfer measured accelerations into forces. The forces in connection with their respective levers generate torques at the joints as well. These torques are set into relation to each other. Since the multi-body model considers a front loader without a payload, the torques from the static model and the torques from the multi-body model differ from each other, which allows to calculate the payload.

The payload measurement is independent of the center of gravity position of the payload. This is achieved by considering the torques at both joints of the open planar kinematic chain, which implies the use of both boom and bucket actuator forces. Hence, the payload measurement is possible with any attached tool without an additional calibration. It is irrelevant whether the center of gravity of the payload is close to the machine, as for a bucket, or further away, for instance, in case of a bale clamp. This even applies to a tool with an additional moving arm such as a crane or excavator attachment.

Due to the cylinder and joint friction, the measured actuator forces deviate from the real actuator forces. Hence, friction is estimated with a friction model and is considered in the payload measurement. While working with the front loader, the measured actuator forces contain oscillations which are caused by the movements of the front loader and disturb the payload measurement. To compensate the influence of the movements on the payload measurement, the multi-body model is provided with accelerations that are measured with an inertial measurement unit (IMU). If the accelerations are not measured but considered as constant (gravity acceleration), the oscillations are directly transferred to the payload signal. Nevertheless, it is possible to determine the payload, but it takes more time due to filtering of the signal. If the acceleration is considered as constant (gravity), the direction

of the gravity is generally assumed as rectangular to the x-axis of the machine. A tilted machine, for instance while working on a slope, causes errors in the payload measurement because the direction of the gravity is still assumed as rectangular to the x-axis of the machine. These errors can be compensated with an additional tilt sensor. However, measuring the acceleration with an IMU compensates tilting of the machine anyway because the direction of the acceleration is measured as vector.

Although influences of the movements of the front loader are almost compensated, the payload signal still yields noises and oscillations, which are caused by sensor noises and time lags between the sensor signals. These effects are reduced by filtering the calculated payload signal with a low-pass filter to obtain a suitable signal.

The accuracy of the payload measurement strongly relies on the accuracy of the models. Developing an accurate multi-body model and identifying all its parameters is very time-consuming. Either the model and its parameters are derived from 3D-CAD data or a real front loader is taken apart and each parameter is measured in tests as done in this thesis. A model derived from 3D-CAD data underlies manufacturing tolerances and does not consider changes that are made on the front loader afterwards, such as adding an additional valve to the boom. Deriving the parameters of the multi-body model by tests, takes a lot of effort, but it is very accurate for one loader. Nevertheless, it has to be done for every machine.

This led to the development of a reduced multi-body model that obtains its parameters partly from 3D-CAD data and partly from a short calibration procedure. Thus, the reduced multi-body model is self-adjusting and covers all manufacturing tolerances. To consider changes that are made on the front loader afterwards, the calibration procedure can easily be redone.

To measure payload continuously at any time, the static model and the multi-body model require a continuous position detection of the front loader relative to the tractor. To obtain a reliable measurement system which is also easy to retrofit on existing loaders, the position detection is implemented with three IMUs connected to the chassis, boom, and tool carrier. The IMUs only consist of non-moving parts and can be mounted anywhere in a protected position. The accuracy of the position detection of the front loader and also the accuracy of the payload measurement is highly dependent on the accuracy of the IMUs. Tests showed that the acceleration measurements of the IMUs for different axis strongly deviate from the real acceleration due to tolerances. For instance, the signal deviates approximately 4% from the gravity during standstill. In this case, an additional calibration

is required to correct the output of the IMUs.

The payload should be determined as quickly as possible. Considering an average loading cycle which lasts 10 to 20 seconds only a fraction of that time allows to determine the payload. The remaining time is spent on picking up the load, dumping, and returning to the pick up place. If the signal processing contains a logic that counts loading cycles and determines payload of each cycle automatically, an instant payload signal is required. Finally, the DynWeiSys developed in this thesis generates a continuous payload signal which allows further analysis. The signal determines the weight of the payload as quickly as possible. Figure 5.13 in chapter 5.5 shows that it takes about one second after lifting the payload from the ground to determine the weight of the payload with an accuracy loss of $\pm 1\%$ of the maximum lifting capacity.

The DynWeiSys, as developed in this thesis, provides a continuous weight signal of the payload in every working situation after being lifted from the ground. To increase the benefit of the DynWeiSys, a "Weighing Logic" can be implemented that identifies loading cycles such as payload pick up, dumping, removing, or adding. The "Weighing Logic" counts the cycles and accumulates or subtracts the payload automatically and gives a comprehensive analysis of the handled material to the operator. This data allows the operator to evaluate or to bill the handled material immediately. Transferring this data continuously to a data processing server allows the mobile scale to be integrated and linked to the work environment, such as logistic, pricing, or payment systems. Also, service cycles of the front loader can be matched to the amount of the handled payload because a constantly used machine needs more service than a machine that is idle most of the time. Also, wear at the actuators or joints can be detected by deviations of the internal friction calculation.

In the following, several issues for further research are proposed to optimize the DynWeiSys as it is described in this thesis. In this regard, the friction model could be improved. During the movements of the front loader, the friction has a huge influence on the measurement accuracy. In this thesis, a pressure based friction model is applied with a friction behavior that is linearly proportional to the cylinder pressures. The parameters of this friction model are determined by measurements performed directly at the front loader itself. It is recommended to continue research by examining the friction behavior of hydraulic cylinders on a test bench and use the results to enhance the current friction model.

Currently, the DynWeiSys considers measured accelerations to calculate the payload. At standstill, these accelerations must be the gravity. Hence, it is suggested to detect stand-

still and calibrate the output of the IMUs to minimize tolerances. Additionally, switching between measured accelerations and a constant gravity serves as a possibility to avoid sensor noise.

To calculate the actuator forces, the pressures are taken at the hydraulic line just next to the cylinders. To minimize the influence of pressure drop due to oil flow, it is recommended to change the design of the cylinders to include pressure sensors that measure the pressures directly in the cylinder. This also decreases the influence of the oil viscosities due to changing temperatures.

A common working procedure is to operate the cylinders at the end-stroke positions. For instance, the bucket cylinders are frequently driven at the minimum end-stroke position, also known as the rollback position. If the hydraulic actuators are in the end-stroke positions, a determination of the actuator forces by hydraulic pressures is not possible. It is suggested to search for a solution either to avoid these positions or to provide actuator forces in these positions.

Heavy payloads cause elastic deformations on the structure of the front loader. This will change the dimensions, for instance, the distance between the main joints, chassis, boom, and tool carrier will decrease. It is suggested to continue research by compensating the elastic deformations of the structure by adjusting the dimensions of the static model in relation to the payload.

In this thesis, the DynWeiSys is shown as an example applied on a non self-leveling agricultural front loader. The next steps could be the transfer of the system to different loader kinematics such as mechanical self leveling loader kinematics or wheel loader kinematics.

A Appendix

A.1 Cylinder Center of Gravity Identification

The following procedure explains how to identify the single masses m_a, m_b and center of gravity positions x_{a1} of the cylinder and $(x_{min} - x_{b1})$ of the piston rod combination as they are used in the multi-body model. In order to achieve this, the oil is drained but the cylinder is not disassembled. Figure A.1 shows the cylinder in position 1 (left) and position 2 (right) with the center of gravity positions of the cylinder x_a and the piston rod combination x_b.
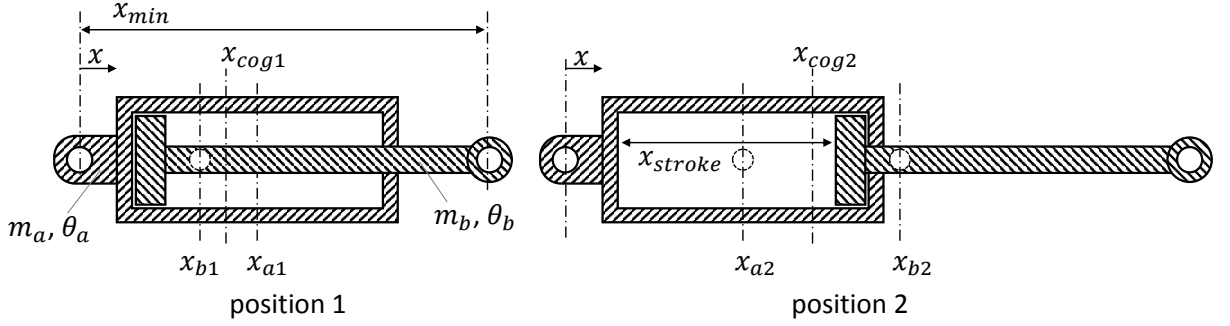

Figure A.1: Centers of gravity

The overall sum of both parts is given by:

$$m_{sum} = m_a + m_b \tag{A.1}$$

The center of gravity positions are set into relation:

$$x_{a2} = x_{a1}$$
$$x_{b2} = x_{b1} + x_{stroke} \tag{A.2}$$

The overall center of gravity of positions 1 and 2 are calculated as follows:

$$x_{cog1} = \frac{x_{a1}m_a + x_{b1}m_b}{m_{sum}} = \frac{m_1}{m_{sum}}x_{a1} + \frac{m_1}{m_{sum}}x_{b1} \tag{A.3}$$

$$x_{cog2} = \frac{x_{a2}m_a + x_{b2}m_b}{m_{sum}} \tag{A.4}$$

Equations (A.2) is combined with equation (A.4):

$$x_{cog2} = \frac{m_a}{m_{sum}}x_{a2} + \frac{m_b}{m_{sum}}x_{b2} = \left(\frac{m_a}{m_{sum}}x_{a1} + \frac{m_b}{m_{sum}}x_{b1}\right) + \frac{m_b}{m_{sum}}x_{stroke} \tag{A.5}$$

The bracket term of equation (A.5) is substituted by equation (A.3). Hence, it follows:

$$x_{cog2} = x_{cog1} + \frac{m_b}{m_{sum}} x_{stroke} \tag{A.6}$$

The overall center of gravity positions x_{cog1} and x_{cog2} are measured by balancing the piston at minimum and maximum stroke. m_{sum} is identified by weighing with a scale and x_{stroke} is measured with a ruler. Finally, equation (A.6) is solved to m_b:

$$m_b = \frac{x_{cog2} - x_{cog1}}{x_{stroke}} m_{sum} \quad \Rightarrow \quad m_a = m_{sum} - m_b \tag{A.7}$$

To define the overall moments of inertia Θ_1 and Θ_2, the cylinder is hung up as a pendulum at minimum and maximum stroke as described in chapter 2.8.

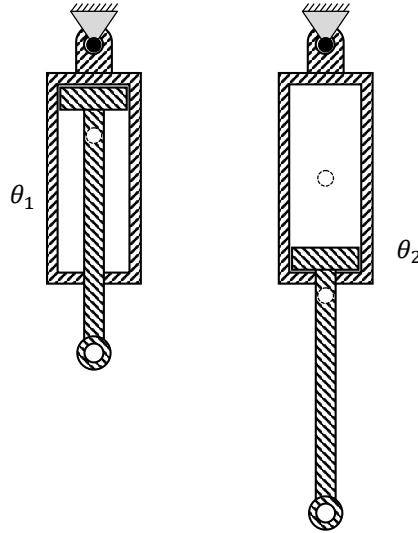**Figure A.2:** Moments of inertia

The moment of inertia of the pendulum is defined by the moments of inertia at the main axis Θ_a, Θ_b, and the Huygens-Steiner theorem.

$$\Theta_1 = \Theta_a + m_a x_{a1}^2 + \Theta_b + m_b x_{b1}^2 \tag{A.8}$$

$$\Theta_2 = \Theta_a + m_a x_{a2}^2 + \Theta_b + m_b x_{b2}^2 \tag{A.9}$$

The equations (A.2) are inserted into equation (A.9) as follows:

$$\Theta_2 = \Theta_a + m_a x_{a1}^2 + \Theta_b + m_b (x_{b1} + x_{stroke})^2 \tag{A.10}$$

Then, equation (A.10) is subtracted from equation (A.8):

$$
\begin{aligned}
\Theta_1 - \Theta_2 &= m_b x_{b1}^2 - m_b (x_{b1} + x_{stroke})^2 \\
&= -m_b (2 x_{b1} x_{stroke} - x_{stroke}^2)
\end{aligned}
\tag{A.11}
$$

And, finally, equation (A.11) is solved to x_{b1}:

$$
x_{b1} = \frac{\Theta_2 - \Theta_1}{2 m_b x_{stroke}} - \frac{x_{stroke}}{2}
\tag{A.12}
$$

The center of gravity position x_{a1} of the cylinder is obtained with equation (A.3).

A.2 Hardware

The front loader discussed in this thesis is a John Deere 683 NSL (Non Self-Leveling). All parameters were identified on this loader. To measure the weight of the loader's big parts a crane scale from Vetek (model: OCS-XZ-1t) was used, which measures in 0.5kg intervals. For the smaller parts (<80kg) a platform scale from Bosche was used, which measures in 0.05kg intervals. The oscillations at the moment of inertia test (cf. chapter 2.8) were measured with an inertial measurement unit in which the decaying angular velocity of the swinging part is used to identify the damping and oscillation period. All tests used inertial measurement units from Continental (Model SC06) and pressure sensors from Danfoss (Model MBS8250), which were connected to a DSPACE Microautobox2 installed at a John Deere 6534 Series Tractor.

A.3 Parameters

A.3.1 Mass, Center of Gravity, Inertia

Table A.2 shows all relevant parameters used for the multi-body model. The table shows the values for only one part. That means if more than one part is used, the value has to be multiplied with the amount of parts. For instance, the front loader uses two I-links, hence, $m_I = 2 * 4.4 kg$. The amount of parts is given in table A.1:

Part	Amount
boom	1
bucket	1
I-link	2
O-link	4
bucket actuator	2
boom actuator	2
pinIO	2

Table A.1: Number of parts

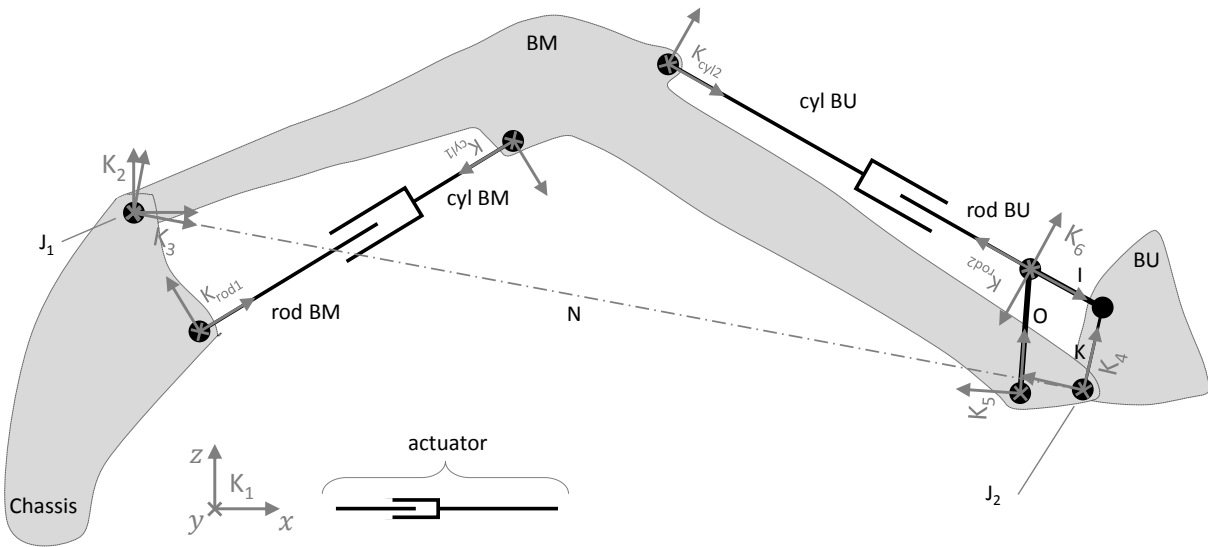Figure A.3 shows the location of the parts and their respective coordinate system.

Figure A.3: Front loader parts

Part	Coordinate System	Center of Gravity [x;y;z]	Mass	Moment of Inertia
	K	$\vec{r}_{cog\_}$ in m	$m\_$ in kg	$\Theta\_$ in kgm^2
BM (N) boom w/o Quick Coupler	3	[1.5240; 0; 0.3950]	348.3 - 6.5 = 341.8	166.20951
BU (K) bucket or tool carrier incl. pins	4	[0.1465; 0;-0.1050]	74+2(1+0.75) = 77.5	1.47337
I-Link	6	[0.1380; 0;-0.0140]	4.40	0.02194
O-Link	5	[0.1750; 0; 0.0525]	3.45	0.04206
O-Link incl. pinIO(=0.75kg)	5	[0.2063; 0; 0.0431]		
actuator BM min. stroke	cyl1	[0.4500; 0; 0.0000]	25.65	1.83430
actuator BM max. stroke	cyl1	[0.7100; 0; 0.0000]	25.65	4.62210
cyl BM	cyl1	[0.4100; 0; 0.0000]	14.15	
rod BM	rod1	[0.4160; 0; 0.0000]	11.5	
actuator BU min. stroke	cyl2	[0.5200; 0; 0.0000]	23.4	2.39591
actuator BU max. stroke	cyl2	[0.8150; 0; 0.0000]	23.4	5.42675
cyl BU	cyl2	[0.3920; 0; 0.0000]	10.38	
rod BU	rod2	[0.5130; 0; 0.0000]	13.02	
reduced model	3	[1.7508; 0; 0.3005]	$m_{Sum} = 541.5$	$\Theta_{Sum} = 339.98$

Table A.2: Parameters

In the following list, several notes are given related to the parameters of table A.2:

- Each moment of inertia is given for the main axis in y-direction.

- The parameters for the reduced model are calculated by:
  $m_{Sum} = m_{BM} + m_{BU} + 2m_I + 4m_O + 2m_{pinIO} + 2m_{BMcyl} + 2m_{BMrod} + 2m_{BUcyl} + 2m_{BUrod}$
  To estimate the moment of inertia, the loader is assumed as a square box with the length of the boom and a height of 0.3m. This results in the following equation:

$$\Theta_{Sum} = (m_{Sum} - m_{BU})(N^2 + 0.3^2)/12 = (m_{Sum} - m_{BU})(2.95^2 + 0.3^2)/12. \quad (A.13)$$

- Pins of the loader joints must be considered. In order to not consider a pin twice, it has to be determined to which part it belongs.

- A hydraulic cylinder that has different oil capacities at different strokes is considered as two parts, namely as cylinder and piston with rod. A procedure to identify the centers of gravity for rod and cylinder without disassembling the actuator, is discussed in section A.1. The mass of the oil volume in the cylinder is not considered.
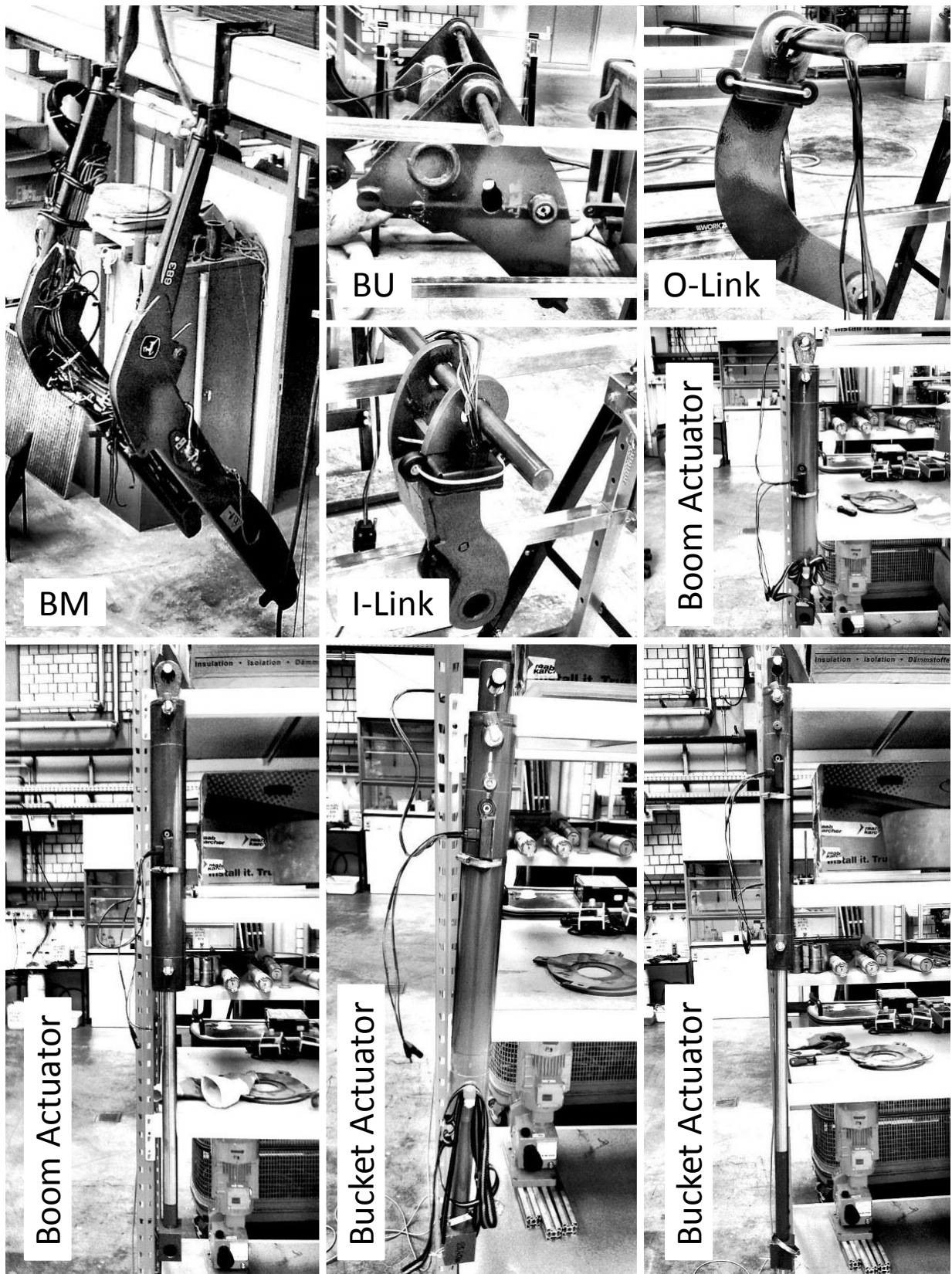
Figure A.4: Pictures of inertia identification

A.3.2 Dimensions

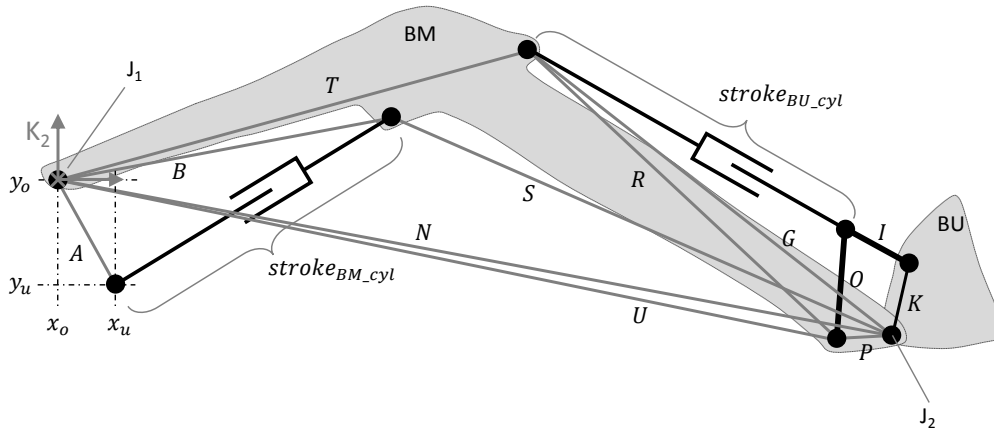The dimensions and distances used for the static model:

Figure A.5: Front loader dimensions

Distance	Value in m
A	0.415
B	1.160
G	1.590
I	0.250
K	0.227
N	2.950
O	0.350
P	0.229
R	1.413
S	1.913
T	1.700
U	2.724
x_o	0.415
x_u	0.600
y_o	0.991
y_u	0.621
$stroke_{BMcyl\_min}$	0.915
$stroke_{BMcyl\_max}$	1.495
$stroke_{BUcyl\_min}$	1.135
$stroke_{BUcyl\_max}$	1.665

Table A.3: Dimensions

A.3.3 IMU Mounting Positions

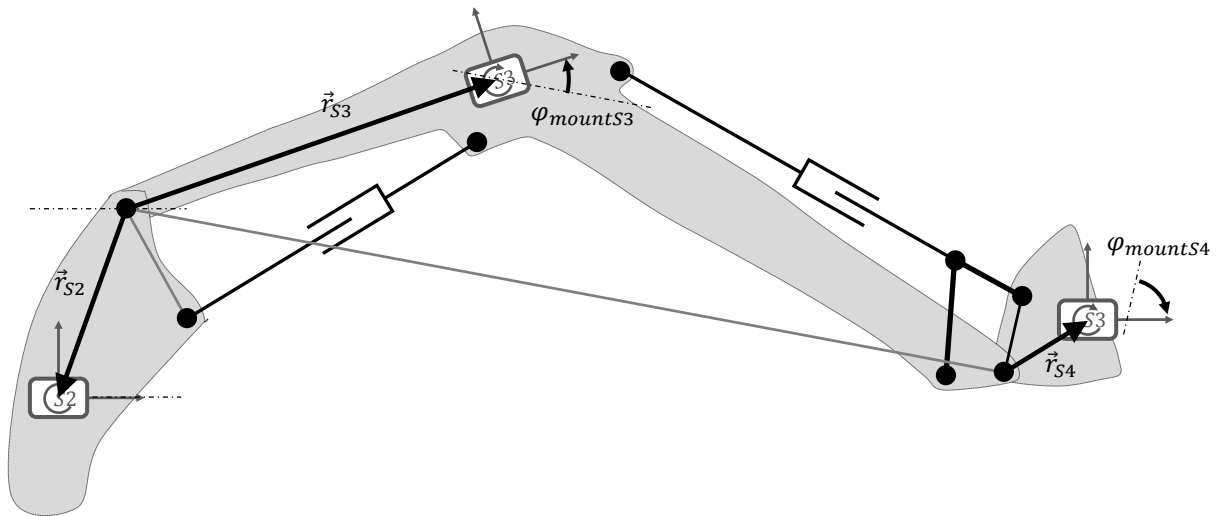The mounting positions of the inertial measurement units are given below:

Figure A.6: Inertial measurement unit positions

IMU	Mounted at	Coordinate System	Position [x;y;z]	Mounting Angle
$S\_$		K	$\vec{r}_S\_$ in m	$\varphi_{mountS\_}$ in rad
2	Tractor Chassis	2	[-0.246;-0.535;-0.640]	-0.0074
3	Boom	3	[0.513;-0.574; 0.317]	+0.5744
4	Bucket	4	[0.118;-0.442;-0.030]	-1.0144

Table A.4: Inertial measurement unit positions

A.3.4 Cylinder Dimensions

Dimensions of the boom and bucket cylinders of the front loader used in this thesis:

Position	Part	Variable	Diameter
			D in m
Boom	Piston	$D_{BMpiston}$	0.08
Boom	Piston	$D_{seal\_innerDiameter}$	0.06
Boom	Rod	D_{BMrod}	0.04
Boom	Rod	$D_{seal\_outerDiameter}$	0.05
Bucket	Piston	$D_{BUpiston}$	0.07
Bucket	Piston	$D_{seal\_innerDiameter}$	0.06
Bucket	Rod	D_{BUrod}	0.04
Bucket	Rod	$D_{seal\_outerDiameter}$	0.05

Table A.5: Actuator diameters

Notice, that two cylinders are used per function, two bucket cylinders and two boom cylinders.

A.4 Fluid Film Thickness

The assumptions to calculate the thickness of the lubrication film are as follows: the hydrodynamic pressure between seal and surface is in balance with the local seal load which is given by the mounting pre-load, its shape, and the hydraulic pressure within the cylinder. A detailed explanation of this is given in chapter 5 of reference [MN13].

A.5 Machine Tilt Angle

In this thesis, the angle φ_{tilt} is calculated by the angle φ_{acc_0}, which lies between vector $\vec{a}_{Sum}$ and vector $\vec{x}$ of the tractor coordinate system K_2.

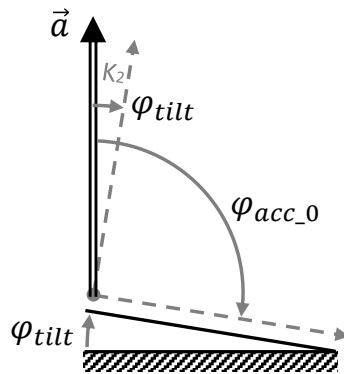$$\varphi_{tilt} = \varphi_{acc\_0} - \frac{\pi}{2} \tag{A.14}$$

Figure A.7: Machine tilt angle

A.6 Stiction - Settlement Effect

The friction model is only applied during front loader movements, as explained in section 4.1.2.1. If the front loader stops, friction changes to stiction. If the applied force is constant $F_{cyl} = F_{const}$ and the amount of stiction is constant, the cylinder force measured by pressures should be constant during standstill. But measurements have shown that the pressures as well as the cylinder force decrease over time. Thus, stiction changes during standstill and can not be predicted. Figure A.8 shows the decreasing force measured by pressures during standstill.
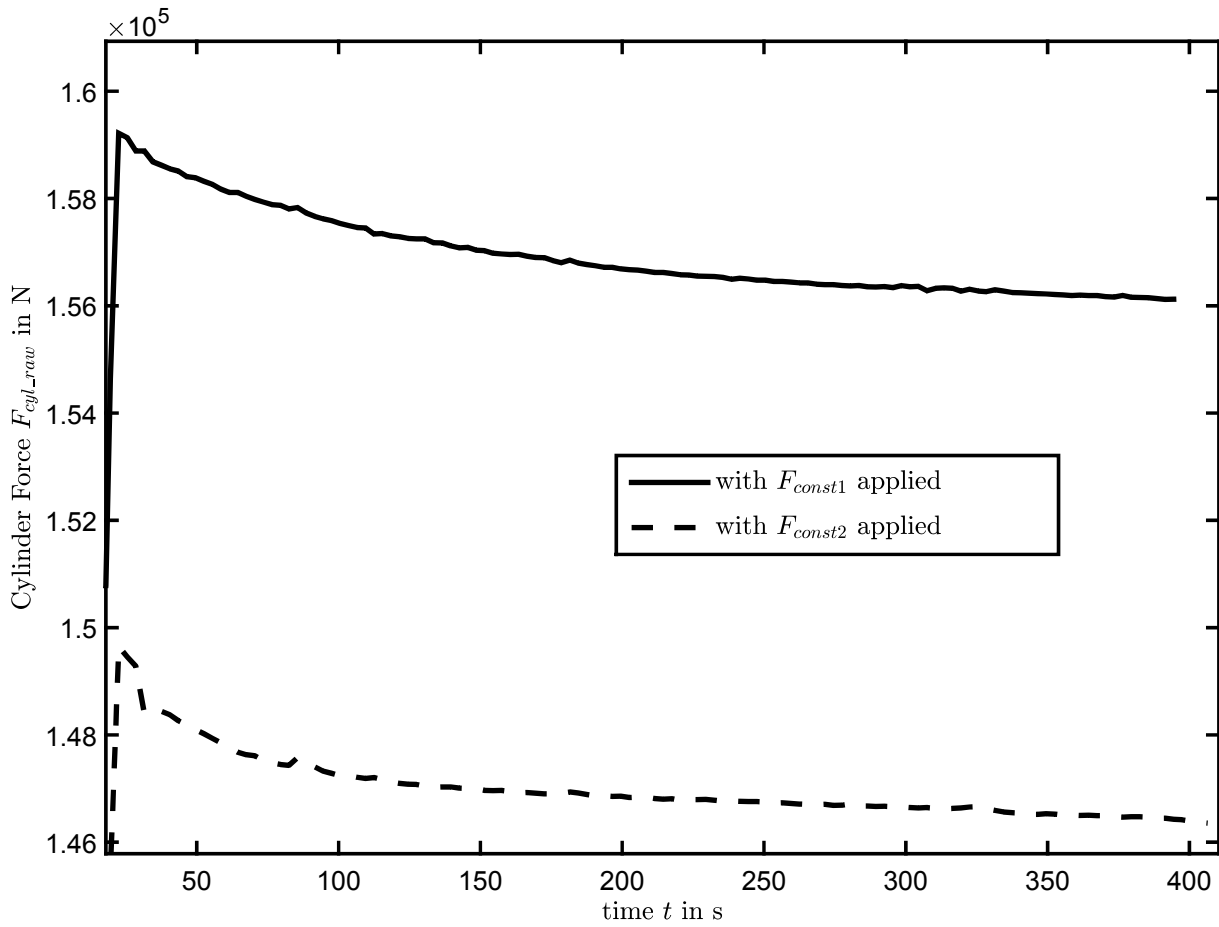
Figure A.8: Decreasing cylinder force

To examine this effect, two tests were performed. For the first test , a cylinder is loaded with a constant cylinder force F_{const1}. Additionally, the cylinder force F_{cyl_raw} is measured over time. For the second test , the cylinder is loaded with a constant cylinder force F_{const2} and the hydraulic line on the piston side "$_A$" is closed by a ball valve, as shown in figure A.9. Then, the rod side "$_B$" is loaded with $\Delta p_B \approx 200$bar, which also increases the pressure on the piston side by 150bar $\approx \Delta p_B \dfrac{D_{piston}^2 - D_{rod}^2}{D_{piston}^2}$.
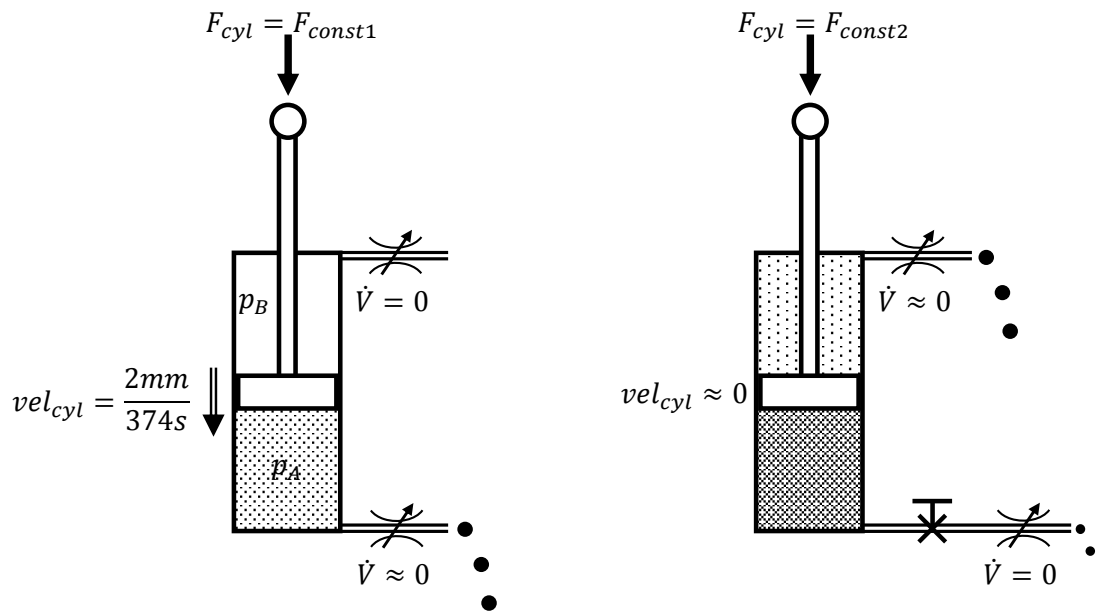
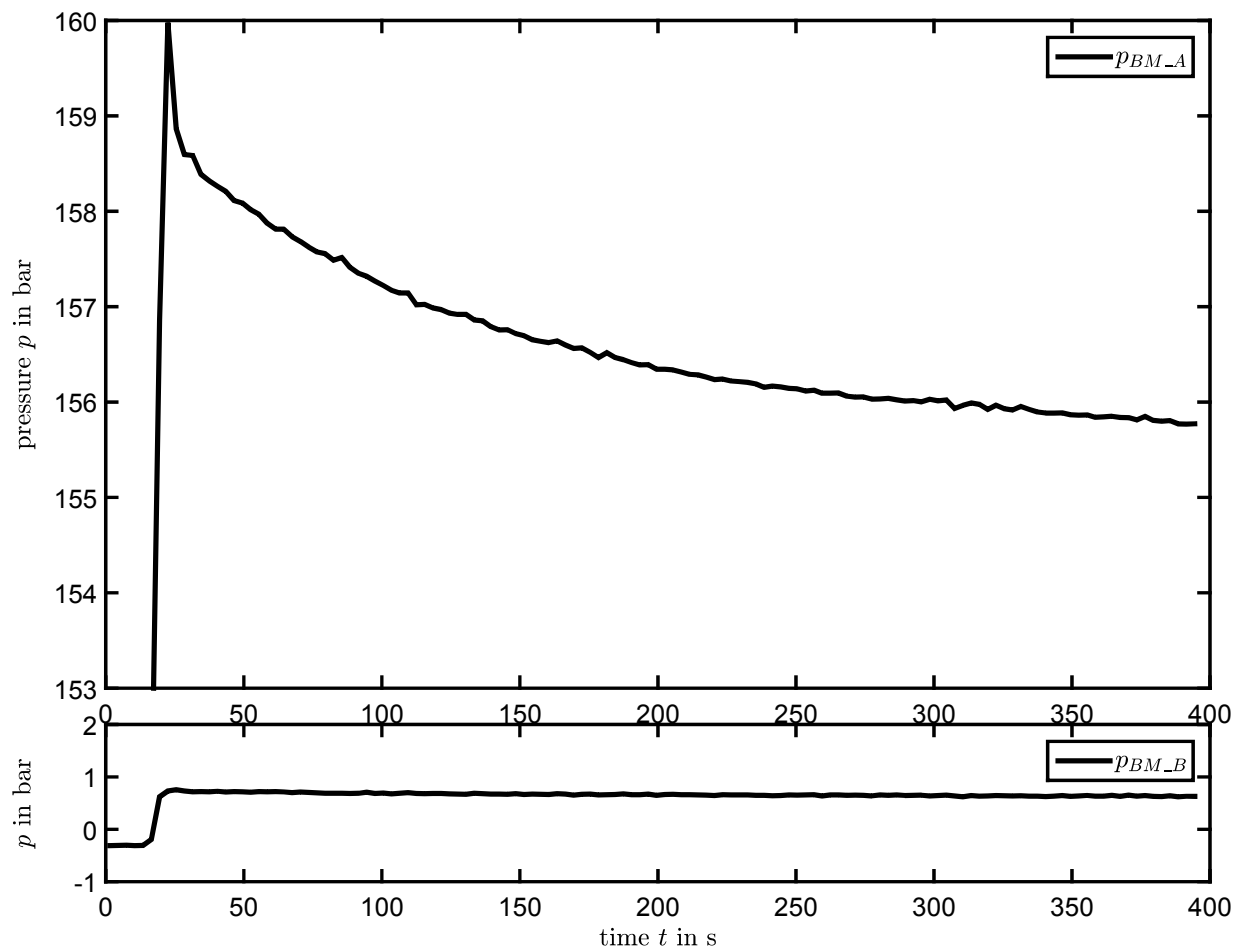**Figure A.9:** Configuration of the first and second test

Figure A.10: Decreasing cylinder pressures, first test

At the first test, the cylinder drifts slowly which is interpreted as leakage of the hydraulic valves. It is assumed that the reason for the decreasing pressure p_{BM_A} is an elastic "holding"-force F_{seal} of the seal that acts against F_{const1}, as shown in figure A.11. Or, the reason for the decreasing pressure p_{BM_A} could be a settling effect of the seal which enables higher friction forces.
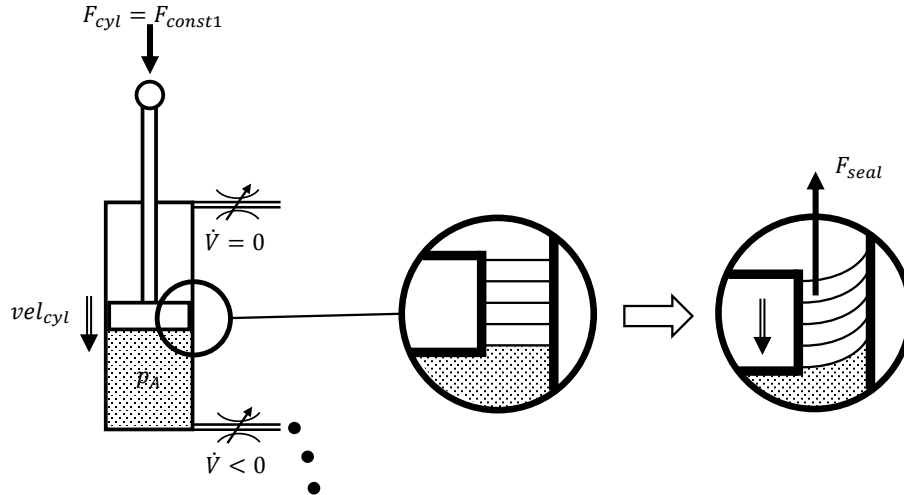

Figure A.11: Forces at the seal

Other tests have shown that the decreasing speed of the pressure is dependent on the temperature T and the pressure p which confirms the assumption of leakage, $\dfrac{\delta p}{\delta t} = f(T, p, ...)$. Because leakage is also depending on the tolerances of the valves, it is difficult to predict it for different machines.

The pressure levels of the second test are higher than of the first test and the seals are pressed with higher forces against their respective sliding partners. The pressures are decreasing on piston and rod side over time during standstill. Because the cylinder drift was not measurable by the used measurement equipment, it is assumed that oil mainly leaks through the rod side valve, as shown in figure A.9.
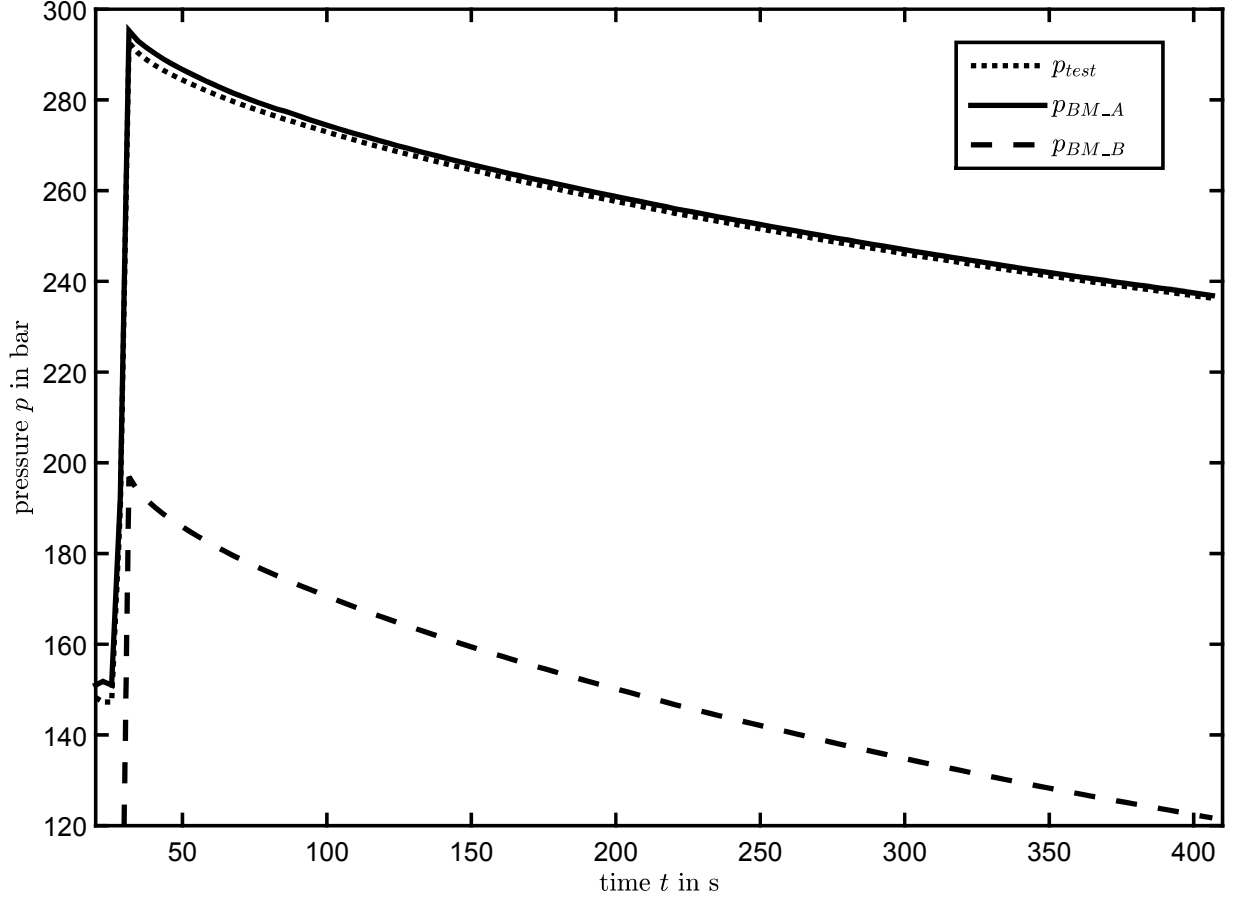
Figure A.12: Decreasing cylinder pressures, second test

The pressure decreases $\dfrac{\delta p_{BM\_A}}{\delta t}$ and $\dfrac{\delta p_{BM\_B}}{\delta t}$ of piston and rod side are mainly dependent on each other apart from a small deviation, as shown in the following equation, where p_{test} is nearly identical with p_{BM_A}.

$$p_{BM\_A} \approx p_{test} = \frac{4F_{const2}}{\pi D_{piston}^2} + p_{BM\_B}\frac{D_{piston}^2 - D_{rod}^2}{D_{piston}^2} \qquad (A.15)$$

The small deviation between p_{BM_A} and p_{test} is not constant over time and causes the decreasing cylinder force, as shown in figure A.8. To confirm the first assumption of the "holding"-force F_{seal}, it is assumed that there still is a minimal movement of the cylinder, which is not measurable. Due to high pressures, the seal becomes less elastic and the "holding"-force increases with less deflections. These tests have shown that the cylinder force measured by pressures decreases over time and is not predictable at this moment. The assumption of the "holding"-force F_{seal} still needs further proof.

A.7 Simulating a Common System

This work requires to simulate a common weighing system. In order to achieve this, only the raw boom actuator forces F_{BMcyl_raw} calculated by the hydraulic pressures without friction compensation are considered. The measurement is taken at previously defined actuator stroke positions and during a boom up movement. Finally, the payload is calculated by:

$$m_{common} = aF_{BMcyl\_raw@positionCommon} + b \tag{A.16}$$

with the actuators in position $stroke_{BM@positionCommon}$ and position $stroke_{BU@positionCommon}$. The constants a and b are determined by two force measurements, $F_{BMcyl\_raw@positionCommon0}$ and $F_{BMcyl\_raw@positionCommon1}$, with two known payloads, m_{L0} and m_{L1}.

An example is given for the test configuration 1 of chapter 5.2. The measurement is performed at the previously defined actuator stroke positions:

$$stroke_{BM@positionCommon} = 1.167\text{m}$$
$$stroke_{BU@positionCommon} = 1.202\text{m}$$

In these conditions, two force values are taken:

$$F_{BMcyl\_raw@positionCommon0} = 22850\text{N} \quad \text{for } m_{L0} = 0\text{kg}$$
$$F_{BMcyl\_raw@positionCommon1} = 111400\text{N} \quad \text{for } m_{L1} = 1024\text{kg}$$

Since $m_{L0} = 0$kg is a front loader without tool and payload, the force $F_{BMcyl\_raw@positionCommon0}$ is determined by the multi-body model. Finally, the constants are determined by:

$$a = \frac{m_{L1} - m_{L0}}{F_{BMcyl\_raw@positionCommon1} - F_{BMcyl\_raw@positionCommon0}} = 0.0116\text{kg/N}$$

and

$$b = m_{L0} - aF_{BMcyl\_raw@positionCommon0} = -264\text{kg}$$

A.8 Pressure Drop Identification

This section explains how to identify the pressure drop in the hydraulic lines for a given cylinder speed. The payload of the loader, which acts against the cylinder force, must not change during pressure drop identification.
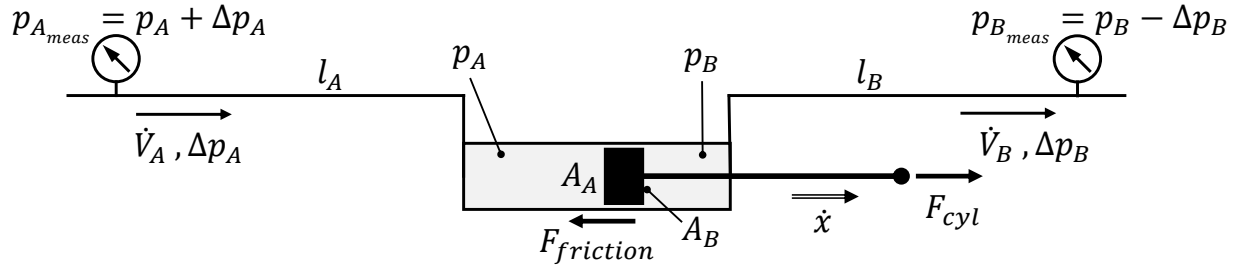

Figure A.13: Pressure drop identification

The cylinder ratio α is given by:

$$\alpha = \frac{A_A}{A_B} \tag{A.17}$$

The oil flow from piston and rod side are set into relation with the cylinder ratio:

$$
\begin{aligned}
\dot{V}_A &= A_A \dot{x} = A_B \alpha \dot{x} \\
\dot{V}_B &= A_B \dot{x} \\
\dot{V}_A &= \dot{V}_B \alpha
\end{aligned}
\tag{A.18}
$$

The pressure drop Δp is defined as a linear function of the oil flow $\dot{V}$ if the hydraulic line is assumed as a throttle, with the dynamic viscosity η, hose length l and diameter $2r$.

$$\dot{V} = \frac{\pi r^4}{8 \eta l} \Delta p = k_D \Delta p \tag{A.19}$$

If the diameter and length l of the hydraulic lines is assumed as $l_A = l_B$, the pressure drops of both sides could be set into relation:

$$
\begin{aligned}
\Delta p_B &= \frac{1}{k_D} \dot{V}_B \\
\Delta p_A &= \frac{1}{k_D} \dot{V}_A = \frac{1}{k_D} \dot{V}_B \alpha \\
\Delta p_A &= \Delta p_B \alpha
\end{aligned}
\tag{A.20}
$$

If the cylinder movement is very slow ($\dot{x} <<$) and only little oil flows, the pressure drop is

negligibly small, $\Delta p_A \approx \Delta p_B \approx 0$

$$p_{A_{meas1}} \approx p_A$$
$$p_{B_{meas1}} \approx p_B$$

$$(A.21)$$

At a fast cylinder movement $(\dot{x} >)$ the pressure drop disturbs the measurement, $\Delta p_A \neq 0$ and $\Delta p_B \neq 0$. The pressures at the sensor positions are defined as follows:

$$p_{A_{meas2}} = p_A + \Delta p_A \; \rightarrow \; p_A = p_{A_{meas2}} - \Delta p_A$$
$$p_{B_{meas2}} = p_A - \Delta p_B \; \rightarrow \; p_B = p_{B_{meas2}} + \Delta p_B$$

$$(A.22)$$

The force balance at the cylinder is given by:

$$\frac{F_{cyl}}{A_B} = p_A \alpha - p_B - \frac{F_{friction}}{A_B}$$

$$(A.23)$$

The force balances of the slow and fast movement are set into relation:

$$\frac{F_{cyl}}{A_B} = p_{A_{meas1}} \alpha - p_{B_{meas1}} - \frac{F_{friction}}{A_B} = (p_{A_{meas2}} - \Delta p_A)\alpha - (p_{B_{meas2}} + \Delta p_B) - \frac{F_{friction}}{A_B}$$

$$(A.24)$$

Due to the unchanged payload, the friction is assumed as equal for the slow and fast lifting cycle and is eliminated.

$$p_{A_{meas1}} \alpha - p_{B_{meas1}} = p_{A_{meas2}} \alpha - p_{B_{meas2}} - (\Delta p_A \alpha + \Delta p_B)$$
$$\alpha(p_{A_{meas1}} - p_{A_{meas2}}) - (p_{B_{meas1}} - p_{B_{meas2}}) = -(\Delta p_A \alpha + \Delta p_B)$$

$$(A.25)$$

Finally, the equation (A.25) is solved to Δp_B with $\Delta p_A = \Delta p_B \alpha$:

$$\frac{\alpha(p_{A_{meas2}} - p_{A_{meas1}}) - (p_{B_{meas2}} - p_{B_{meas1}})}{\alpha^2 + 1} = \Delta p_B$$

$$(A.26)$$

Note: Mobile scale manufacturers often generate different cylinder speeds for the calibration with different engine speeds and the joystick at full stroke.

A.9 Friction of Bearings

To evaluate the friction in the bearings, a real pendulum is created. The bucket linkage of the front loader is removed to allow the tool carrier to swing freely in its joints. Once the pendulum is started, the friction of the bearings is dampening the pendulum until its standstill. The air resistance is neglected.
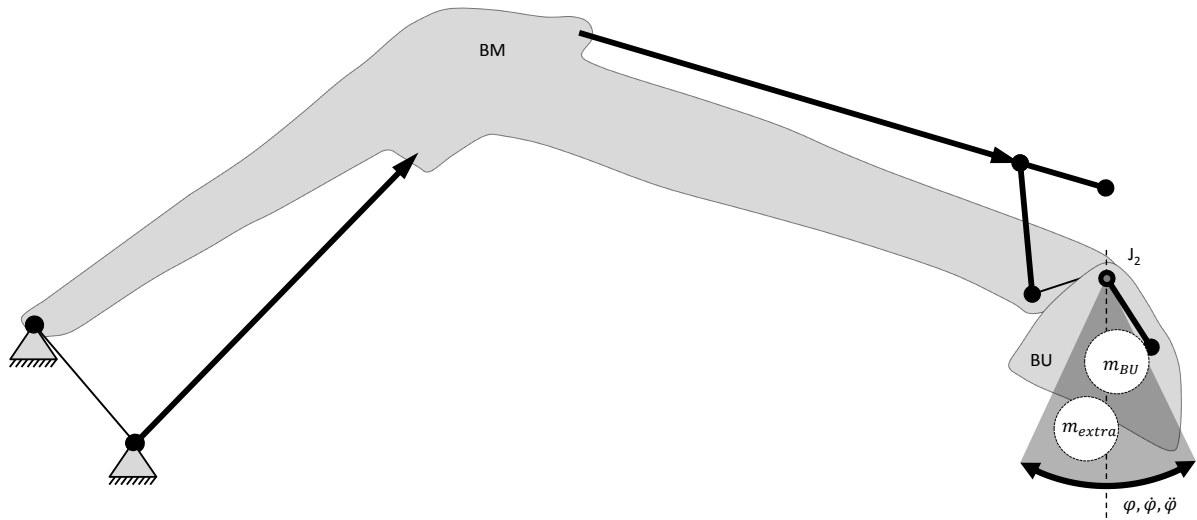

Figure A.14: Pendulum

During operation, the bearings run in boundary or mixed lubrication at low speed, as mentioned in chapter 2.9.3. For this reason, the tool carrier is loaded with an extra weight to increase the bearing load and to reduce the natural frequency. Figure A.14 shows the tool carrier (BU) as a pendulum around the second joint J_2 with its mass m_{BU} and the extra weight m_{extra}. The angle φ_{real}, angular velocity $\dot{\varphi}_{real}$, and angular acceleration velocity $\ddot{\varphi}_{real}$ are measured. Moreover, a mathematical model of the pendulum is created with an integrated friction model of the bearings. The parameters of the friction model were tuned in a way that the output ($\varphi_{model}, \dot{\varphi}_{model}, \ddot{\varphi}_{model}$) matches the real measurement, as shown in figure A.15. It turned out that it suffices to describe the friction of the joints only by Coulomb's friction law without considering any stiction.

$$F_{friction\_bearing} = \mu_{bearing} * F_{normal\_bearing} \tag{A.27}$$

The friction appears in the bearing ring. To convert the friction force into a Torque $TQ_{friction}$, it has to be multiplied by its lever $D/2$, which is half the diameter of the bearing.

$$TQ_{friction} = \mu_{bearing} * F_{normal\_bearing} * \frac{D}{2} \tag{A.28}$$
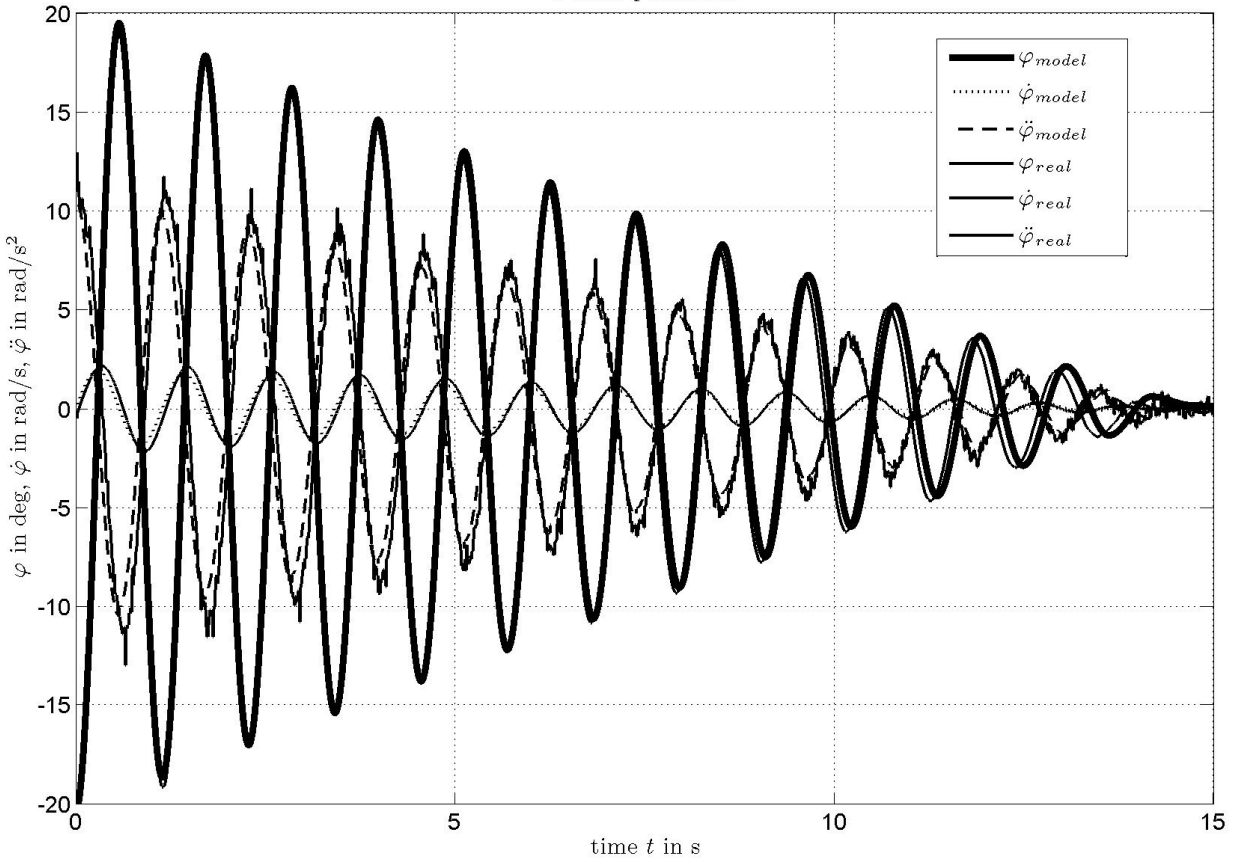
Figure A.15: Modeled pendulum versus real measurement

This is proved at the second joint J_2 of the front loader with a bearing that is lubricated with grease and a diameter of $D = 35$mm. The resulting friction coefficient is $\mu_{bearing} = 0.105$. The result is also valid for the other bearings due to the identical design.

A.10 Bearing Friction versus Total Friction

Figure A.16 shows a torque measurement at the joint J_1 between chassis and boom. Due to the friction, the raw value of TQ_1 differs between up and down movement for the same payload ($m_{payload} = 1024$kg). The friction compensated value of TQ_1 peaks almost at the same level. The small deviation is caused by inaccuracies of the overall friction model. The bottom window of figure A.16 shows the output of the overall friction model and the friction of joint J_1. The friction generated by the joint J_1 is approximately 10% of the overall friction.
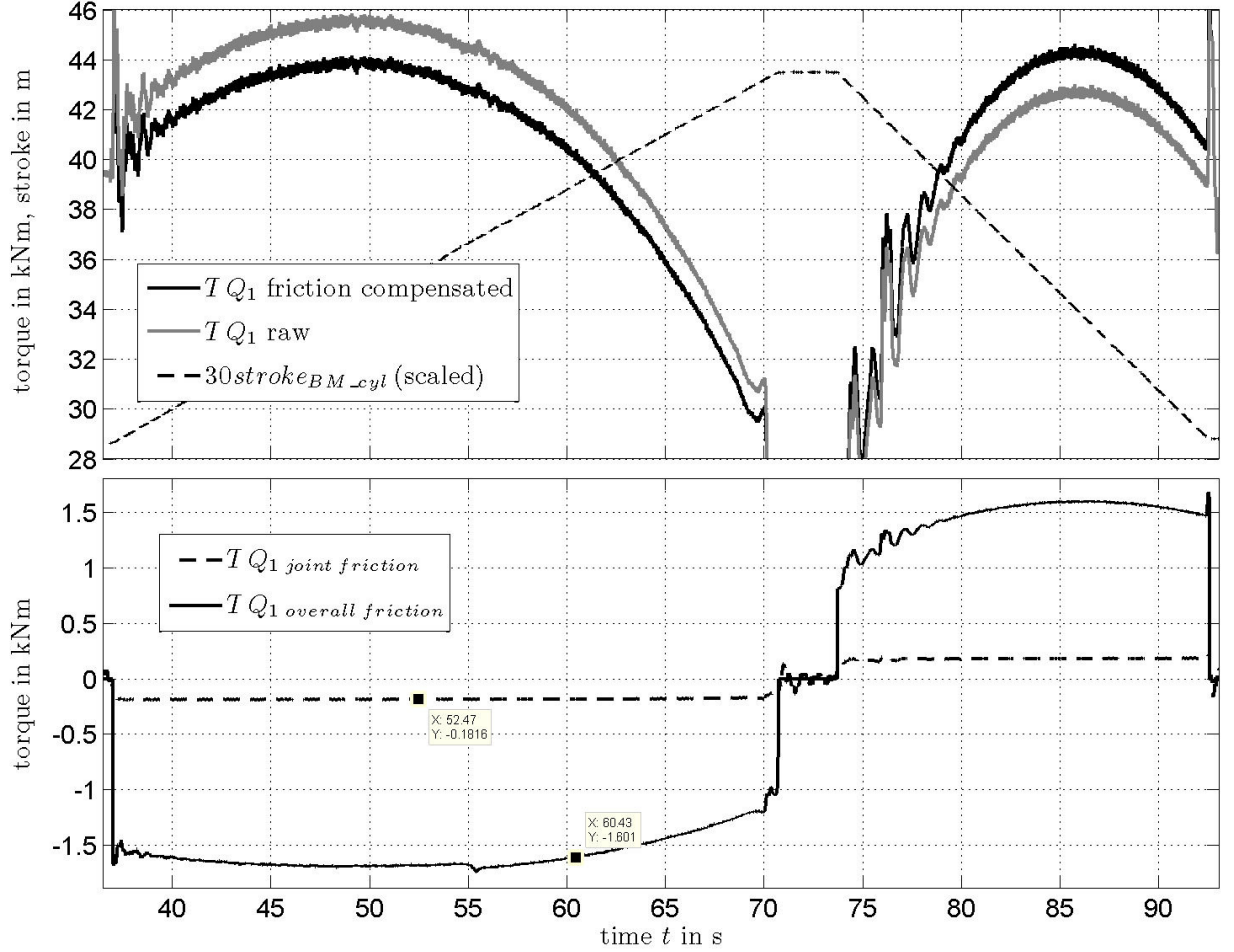
Figure A.16: Overall friction and joint friction

A.11 Inertial Forces of Boom Actuators

The boom actuator is mounted between the chassis and boom as illustrated in figure A.17. Hence, its inertial forces are supported by two joints. The joint between chassis and actuator as well as the joint between actuator and boom. The torque $[\vec{TQ}_{cylBM} + \vec{TQ}_{rodBM}]_{J1}$ at the loader main joint J_1 is only generated by the forces F_x and F_z that are supported at the upper actuator joint. The actuator splits into two parts, the rod and the cylinder. Each part generates inertial forces rectangular and parallel to the actuator. For the torque calculation, the rectangular forces of both parts and only the parallel force of the cylinder are considered.

$$\vec{TQ}_{actuator} = -m_{cylBM}(\vec{r}_{cog\ cylBM} \times \vec{a}_{cylBM}) - m_{rodBM}(\vec{r}_{cog\ rodBM} \times \vec{a}_{rodBM}) \qquad \text{(A.29)}$$

$$F_z = \frac{[\vec{TQ}_{actuator}]_y}{stroke_{BM\_cyl}} \qquad \text{(A.30)}$$

$$F_x = [-m_{cylBM}\vec{a}_{cylBM}]_x \qquad \text{(A.31)}$$

$$[\vec{TQ}_{cylBM} + \vec{TQ}_{rodBM}]_{J1} = \vec{r}_B \times \begin{bmatrix} F_x \\ 0 \\ F_z \end{bmatrix} \tag{A.32}$$
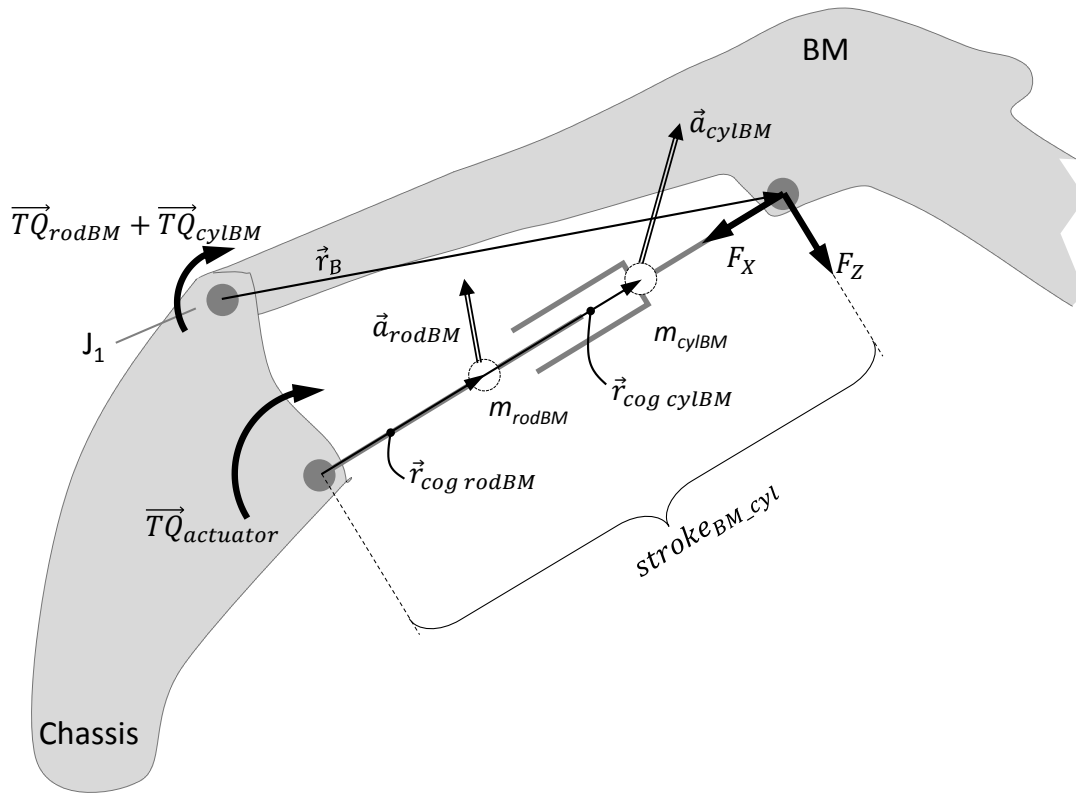

Figure A.17: Boom actuators

A.12 Measurements

This section contains additional measurement results that are mentioned in this work.
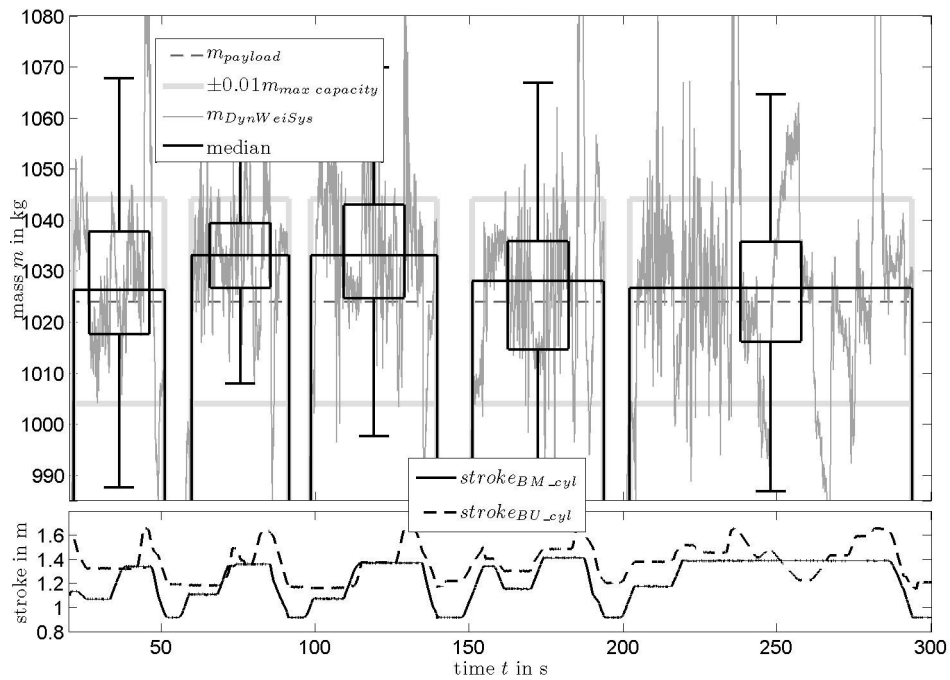

Figure A.18: Calculating $\tilde{x}_i$ for loading cycles, $m_{payload}$=1024kg
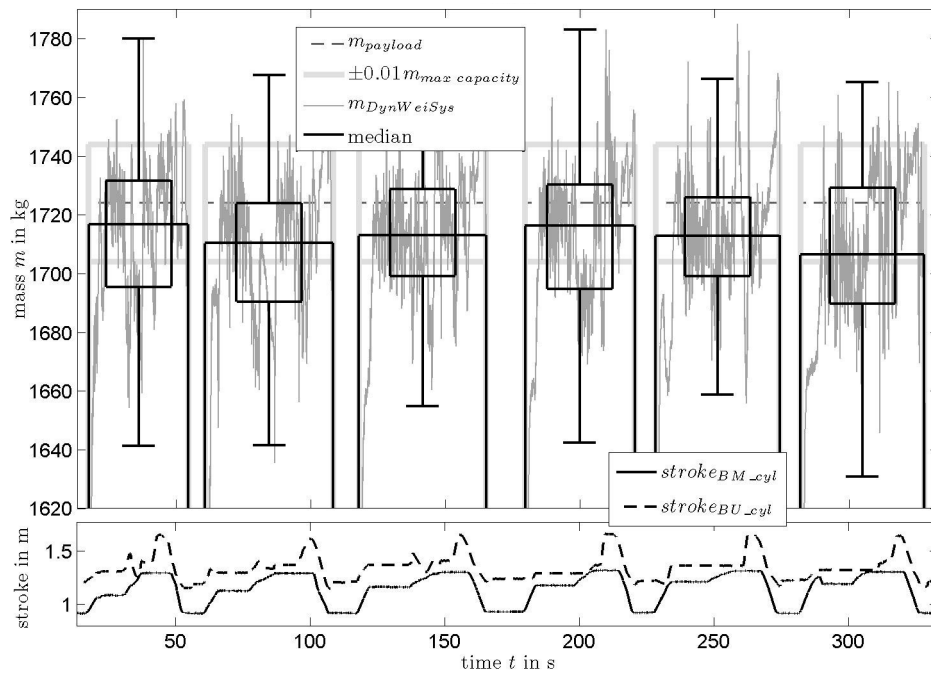

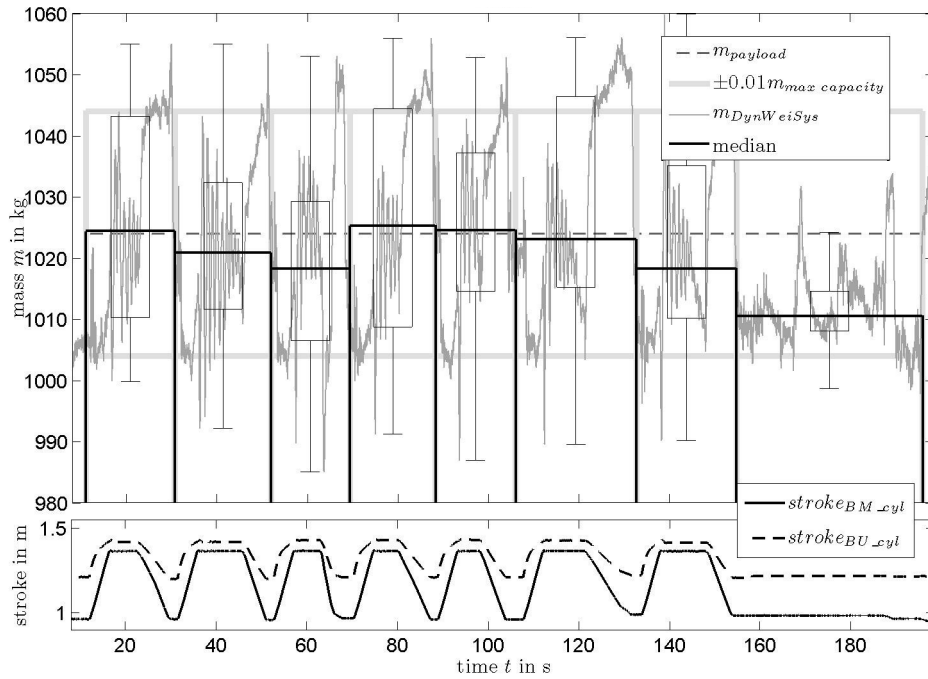**Figure A.19:** Calculating $\tilde{x}_i$ for loading cycles, $m_{payload}$=1724kg

Figure A.20: Calculating $\tilde{x}_i$ for lifting and lowering cycles, $m_{payload}$=1024kg

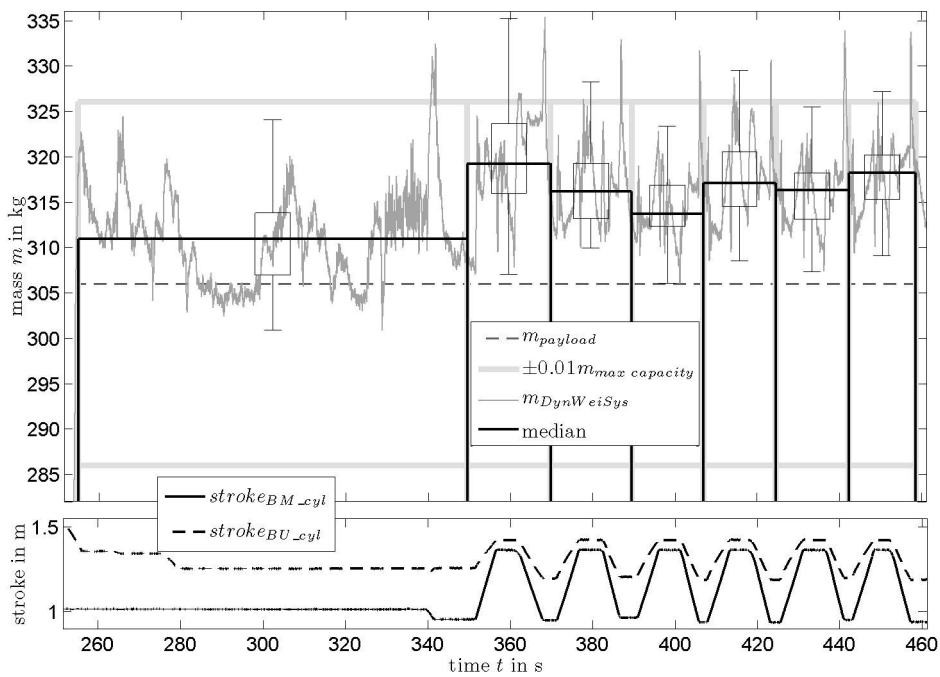**Figure A.21:** Calculating $\tilde{x}_i$ for lifting and lowering cycles, $m_{payload}$=306kg

Bibliography

[AdW08] K. J. Astroem and C. Canudas de Wit. *Revisiting the LuGre Model.* In: IEEE Control Systems Magazine 28, 6 (2008), Page 101-114, July 2008.

[Agg13] Aggregates Manager. *4 Simple Preventive Maintenance Steps to Help Ensure Accuracy of Your Onboard Weighing System.* online: `www.aggman.com`, 2013.

[AHDdW94] Brian Armstrong-Hélouvry, Pierre Dupont, and Carlos Canudas de Wit. *A Survey of Models, Analysis Tools and Compensation Methods for the Control of Machines with Friction.* Automatica (Journal of IFAC), Vol. 30, No. 7. pp. 1083-1138, Elsevier Science Ltd, July 1994.

[Ame11] American Weigh Scales, Inc. *Weighing Scale Terminology.* online: `http://www.awscales.com/support/terminology`, 2011.

[Ang07] Jorge Angeles. *Fundamentals of Robotics Mechanical Systems - Theory, Methods, and Algorithms.* Springer Science & Business Media, 2007. ISBN 0-387-29412-0.

[Arc53] J. F. Archard. *Contact and Rubbing of Flat Surfaces.* In: Journal of Applied Physics, 24, (1953), Page 981-988, 1953.

[ASB05] Sören Andersson, Anders Söderberg, and Stefan Björklund. *Friction models for sliding dry, boundary and mixed lubricated contacts.* Department of Machine Design, Machine Elements, Royal Institute of Technology, Sweden, online: `www.elsevier.com/locate/triboint`, 2005.

[BAR13] Fa. BARK. *Wiegesystem T400 für Teleskoplader.* BARK GmbH & Co.KG online: `www.bark-systeme.de`, 2013.

[Bau11] Gerhard Bauer. *Oelhydraulik: Grundlagen, Bauelemente, Anwendungen.* Springer-Verlag Berlin, Heidelberg, ISBN 978-3-8348-1464-7, 2011.

[BBU12] Andreas Bogala, Philipp Beerlage, and Alfred Ulrich. *Methodik zur modellbasierten Entwicklung von Mess- und Regelungssystemen bei mobilen Arbeitsmaschinen.* 5. Fachtagung Baumaschinentechnik, Dresden, Germany, 2012.

[BCR99] Adrian Bonchis, Peter Corke, and David Rye. *A Pressure-Based, Velocity Independent, Friction Model for Asymmetric Hydraulic Cylinders.* In Proceedings of the I999 IEEE, International Conference on Robotics & Automation, Detroit, Michigan 1999, May 1999.

[Bec14] Marco Becker. *Zünglein an der Waage.* In: Mobile Maschinen 3 (2014), Page 28-31, June 2014.

[Bit09] Ulrike Bitzer. *Genauigkeit von industriellen Wiegesystemen.* In: Mühle + Mischfutter Nr.18, online: `www.vms-detmold.de`, 2009.

[BM13] Frederic Ballaire and Steffen Müller. *Dynamic Weighing with a Front Loader.* In Proceedings of the 71st International Conference on Agricultural Engineering - Land Technik 2013, Hannover, Germany, Page 413-418, November 2013.

[BP82] Li Chun Bo and D. Pavelescu. *The friction-speed relation and its influence on the critical velocity of stick-slip motion.* In: Wear, Volume 82, Issue 3, Pages 277-289, 1982.

[BPH14] Frederic Ballaire, Ole Peters, and Klaus Hahn. *Arbeitsmaschine mit Hubvorrichtung und Wiegeeinrichtung.* European Patent Office, Patent DE102013203826, Assignee: Deere & Company, Filed: 06-March-2013, September 2014.

[BT39] F.P. Bowden and D. Tabor. *The Area of Contact between Stationary and between Moving Surfaces.* Proceedings of the Royal Society, London, doi: 10.1098/rspa.1939.0005, February 1939.

[Con14a] Continental AG. *Inertial Measurement Unit for ESC.* online: `www.conti-online.com`, October 2014.

[Con14b] Continental AG. *Sensor Cluster for sensing the Vehicle Dynamics.* online: `www.conti-online.com`, October 2014.

[Cra05] John J. Craig. *Introduction to Robotics Mechanics and Control.* Pearson Prentice Hall, ISBN 0-13-123629-6, 2005.

[Dee14a] Deere & Company. *Product Brochure: John Deere Frontlader der Serie 3.* online: `www.deere.com`, 2014.

[Dee14b] Deere & Company. *Product Brochure: John Deere K-Series Loaders.* online: `www.deere.com`, 2014.

[Dee15] Deere & Company. *Product Brochure: John Deere Frontlader der Serie H.* online: `www.deere.com`, 2015.

[DH11] Hans Dresig and Franz Holzweißig. *Maschinendynamik.* Springer-Verlag Heidelberg, Dordrecht, London, New York, ISBN 978-3-642-16009-7, 2011.

[DIN92]   DIN EN 45501:1992. *Metrological aspects of non-automatic weighing instruments - German version.* DIN German Institute for Standardization, The Joint Europeen Standards Organization, 11 1992.

[DIN13]   DIN ISO 8855. *Road vehicles - Vehicle dynamics and road-holding ability - Vocabulary.* Deutsches Institut für Normung e.V., Normenausschuss Automobiltechnik (NAAutomobil) im DIN, 2013.

[dSP14]   dSPACE GmbH. *Product Brochure: MicroAutoBox II.* online: `www.dspace.com`, 2014.

[Fin06]   Dietmar Findeisen. *Ölhydraulik - Handbuch für die hydrostatische Leistungsübertragung in der Fluidtechnik.* Springer, ISBN 10 3-540-23880-8, 2006.

[Föl94]   Otto Föllinger. *Regelungstechnik - Einführung in die Methoden und ihre Anwendung.* Hüthig GmbH Heidelberg ISBN 3-7785-2915-3, 1994.

[Fli11a]   Josef Fliegl. *Arbeitsmaschine mit Wiegeeinrichtung.* Deutsches Patent- und Markenamt, Patent DE102009051210, Assignee: Josef Fliegl, Filed: 29-October-2009, May 2011.

[Fli11b]   Fliegl Agro-Center GmbH. *Wiegeeinrichtungen und Elektronikbauteile.* online: `www.fliegl-agrocenter.de`, 2011.

[GHSW06]   Dietmar Gross, Werner Hauger, Jörg Schröder, and Wolfgang Wall. *Technische Mechanik 1.* Springer-Verlag Berlin, ISBN-10 3-540-34087-4, 2006.

[GRU11]   GRUNDFOS Holding A/S. *Shaft seal - Chapter4 - Tribology.* online: `http://machining.grundfos.com/technical-library`, 2011.

[GW66]   J.A. Greenwood and J.B.P. Williamson. *Contact of Nominally Flat Surfaces.* Proceedings of the Royal Society, London, doi: 10.1098/rspa.1966.0242, December 1966.

[HC12]   M. Hennecke H. Czichos. *Hütte 34. - Das Ingenieurswissen.* Springer Vieweg, ISBN 978-3-642-22849-0, 2012.

[HEN14]   HENNLICH GmbH & Co KG. *Wissenswertes - Auswahl von Dichtelementen - Wissenswertes.* online: `www.hennlich.at`, 2014.

[HO11]   Mads Hvoldal and Casper Olesen. *Master Thesis: Friction Modelling - and Parameter Estimation for Hydraulic Asymmetrical Cylinders.* Aalborg University - Electro Mechanical Systems Design, Denmark, 2011.

[Hol07]   Uwe Hollburg. *Maschinendynamik*. Oldenbourg Wissenschaftsverlag GmbH, ISBN 978-3-486-57898-0, 2007.

[Hon93]   Josef Honerkamp. *Klassische Theoretische Physik*. Springer-Verlag Berlin, Heidelberg, ISBN 3-540-55901-9, 1993.

[HSG99]   Werner Hauger, Walter Schnell, and Dietmar Gross. *Technische Mechanik 3 - Kinetik*. Springer-Verlag Berlin Heidelberg NY,ISBN 3-540-66117-4, 1999.

[Ise06]   Rolf Isermann, editor. *Fahrdynamik - Regelung Modellbildung, Fahrerassistenzsysteme, Mechatronik*. Vieweg Verlag ISBN 978-3-8348-9049-8, 2006.

[KK87]   Pradeep Khosla and Takeo Kanade. *An Algorithm to Estimate Manipulator Dynamics Parameters*. Department of Electrical and Computer Engineering, The Robotics Institute, Carnegie Mellon University, Pittsburgh, Pennsylvania, March 1987.

[Käm12]   Andreas Kämmerer. *Development of a semi-automatic front loader with weighing function by the example of the Fendt CARGO professional*. VDI, In Proceedings of the 70th International Conference on Agricultural Engineering - Land Technik 2012, Karlsruhe, Germany, Page 63-68, 2012.

[Krä84]   Erwin Krämer. *Maschinendynamik*. Springer-Verlag Berlin, Heidelberg, Tokyo, ISBN 3-540-12541-8, 1984.

[Loa13]   Trimble Loadrite. *Product Brochure: Wheel loader scales L-Series*. online `www.loadritescales.com`, 2013.

[Loa14a]   Loadrite. *Case study: Accurate and profitable dairy farming*. online: `http://www.loadritescales.com/loadrite-case-studies/accurate-and-profitable-dairy-farming`, 2014.

[Loa14b]   Loadrite. *Case study: Victorian dairy farm*. online: `http://www.loadritescales.com/loadrite-case-studies/victorian-dairy-farm`, 2014.

[Lun06]   Jan Lunze. *Regelungstechnik 2*. Springer-Verlag Berlin, Heidelberg, ISBN-13 978-3-540-32335-8, 2006.

[Lun08]   Jan Lunze. *Regelungstechnik 1*. Springer-Verlag Berlin, Heidelberg, ISBN 978-3-540-68907-2, 2008.

[Mar05]   Dan Marghitu. *Kinematic Chains and Machine Components Design*. Elsevier Academic Press, ISBN 0-12-471352-1, 2005.

[Mat10] MathWorks. *Matlab Documentation*. 1984-2010 The MathWorks, Inc, 2010.

[Mer14] Merkel Freudenberg Fluidtechnik GmbH. *Merkel - Technisches Handbuch*. online: `http://www.merkel-freudenberg.de/services/download-center/`, 2014.

[MN13] Heinz Müller and Bernard Nau. *Fachwissen Dichtungstechnik*. online: `www.fachwissen-dichtungstechnik.de`, 2013.

[NAS71] NASA SP-8063. *Space Vehicle Design Criteria (Structures) - Lubrification, Friction, and Wear*. National Aeronautics and Space Administration, Washington, D.C., 1971.

[Nat02] National Conference on Weights and Measures - Rice Lake Weighing Systems. *NTEP & Handbook 44*. NTEP, National Type Evaluation Program, online: `http://www.ncwm.net/`, 2002.

[Nol06] Wolfgang Nolting. *Grundkurs Theoretische Physik 1 - Klassische Mechanik*. Springer-Verlag Berlin, Heidelberg, New York, ISBN 3-540-34832-8, 2006.

[Oga02] Katsuhiko Ogata. *Modern Control Engineering*. Prentice Hall, ISBN 0-13-043245-8, 2002.

[Ols96] Henrik Olsson. *Control Systems with Friction*. Department of Automatic Control, Lund Institute of Technology, Sweden, 1996.

[Ove07] René M. Overney. *Introduction to Tribology*. Nanolab at the University of Washington, online: `http://depts.washington.edu/nanolab/ChemE554/Summaries%20ChemE%20554/Introduction%20Tribology.htm`, 2007.

[PFR14] PFREUNDT GmbH. *Product Brochure: Die PFREUNDT Radladerwaagen der pSerie*. online: `http://www.pfreundt.de/de/produkte/pSerie_Radladerwaagen.php`, 2014.

[Pro12a] Profi The Farm Machinery Magazine. *Nicht am langen Arm heben*. In: Profi - Energie, 2 (2012), February 2012.

[Pro12b] Profi The Farm Machinery Magazine, Anja Böhrnsen. *Volle Schaufeln wiegen*. In: Profi - Energie, 1 (2012), Page 78-83, January 2012.

[Pro14] Profi The Farm Machinery Magazin. *Fendt Frontlader Cargo 4X/80 Profi: Schlaue Schwinge*. In: Profi, 4 (2014), Page 71 ff., April 2014.

[RDS08]   RDS Technology Ltd. *Product Manual: Loadmaster 8000 - On Board Weighing System.* 2008.

[Sch07]   Prof. Dr. Florian Scheck. *Theoretische Physik 1 - Mechanik.* Number ISBN 978-3-540-71377-7. Springer-Verlag Berlin, Heidelberg, 2007.

[Str02]   Richard Stribeck. *Die Wesentlichen Eigenschaften der Gleit- und Rollenlager.* Zeitschrift des Vereins Deutscher Ingenieure, Vol. 46, pp. 1341-1348, 1902.

[Tan06]   Chin Pei Tang. *Lagrangian Dynamic Formulation of a Four-Bar Mechanism with Minimal Coordinates.* Retrieved 2014 online: `http://nonholonomic.com/research.html`, March 2006.

[TASLH08]   Luc Le Tien, Alin Albu-Schäffer, Alessandro De Luca, and Gerd Hirzinger. *Friction Observer and Compensation for Control of Robots with Joint Torque Measurement.* In Proceedings of the IEEE/RSJ International Conference on Intelligent Robots and Systems, Acropolis Convention Center Nice, France, September 2008.

[Tre02]   Peter Treue. *PHD Thesis: Potenziale und Grenzen teilflächenspezifischer N-Düngung in Schleswig-Holstein/Precision Agriculture.* Inst. für Pflanzenbau und Pflanzenzüchtung, Lehrstuhl Acker- und Pflanzenbau, Christian-Albrecht-Universität zu Kiel, Germany, 2002.

[Vei13]   Veigroup.com. *Case study Mongolia September 2013 Fuel Efficiency.* online: `www.veigroup.com`, September 2013.

[Vol14]   Volvo CE. *Product Brochure: Volvo Wheel Loader L45G and L50G.* online `www.volvoce.com`, 2014.

[Wat07]   Holger Watter. *Hydraulik und Pneumatik.* Vieweg Verlag, ISBN 978-3-8348-0190-6, 2007.

[WG08]   Dieter Will and Norbert Gebhardt. *Hydraulik - Grundlagen, Komponenten, Schaltungen.* Springer-Verlag Berlin, Heidelberg, ISBN 978-3-540-79534-6, 2008.

[Wil14]   Wilhelm Stoll Maschinenfabrik GmbH. *Product Brochure: Stoll FZ/Fs Profiline.* online: `www.stoll-germany.com`, 2014.

[Wis00]   Ludger Wissing. *Anordnung zum Wiegen von Nutzlasten.* Deutsches Patent- und Markenamt, Patent DE19901563A1, Assignee: Pfreundt GmbH, Filed: 16-January-1999, July 2000.

[WNB⁺06] Peter Wriggers, Udo Nackenhorst, Sascha Beuermann, Holger Spiess, and Stefan Löhnert. *Technische Mechanik kompakt - Starrkörperstatik Elastostatik Kinetik.* Teubner Verlag, ISBN 10 3-8351-0087-4, 2006.

Student Projects

Immanuel Deepan Morais
Force and Torque Analysis on Front- and Wheel Loader with Hydraulic Cylinders using an Optimal Controller Design for Trajectory Tracking, Master Thesis, 2014.

Christian Simonis
Userinterface und Statuserkennung für eine automatisierte Gewichtmessung am Traktorfrontlader, Studienarbeit, 2014.

Curriculum Vitae

Frederic Ballaire

Berufstätigkeit

seit 04/2011	Wissenschaftlicher Mitarbeiter,
	Lehrstuhl für Mechatronik in Maschinenbau und Fahrzeugtechnik
	Technische Universität Kaiserslautern
03/2007 - 03/2011	Ingenieur, Volvo Construction Equipment Germany GmbH

Hochschulbildung

09/2000 - 02/2007   Studium Maschinenbau und Verfahrenstechnik
Schwerpunktfach: Konstruktionstechnik
Technische Universität Kaiserslautern
Abschluss: Diplom-Ingenieur

Diplomarbeit: *Konzeption und Konstruktion eines leistungsverzweigten Getriebes mit hydraulischer Kupplung*

2. Studienarbeit: *Entwicklung der Hinterbaukinematik eines gefederten Mountainbikerahmens*

1. Studienarbeit: *Beschleunigungsmessungen an der Gleitringdichtung einer Kreiselpumpe*

Fachpraktikum: Keiper GmbH & Co.KG, Kaiserslautern
Versuch/Entwicklung, Prüfstandsoptimierung

Schulbildung

09/1990 - 06/2000   Rudi-Stephan-Gymnasium, Worms

Veröffentlichungen

BALLAIRE, F.; MÜLLER, S.: *Dynamic Weighing with a Front Loader.* In Proceedings of the 71st International Conference on Agricultural Engineering - LAND.TECHNIK 2013, Hannover, Germany, November 2013, Page 413-418.

SABZEWARI, K.; BALLAIRE, F.; MÜLLER, S.: *Energieeinsparpotenzial der Arbeitshydraulik durch die Elektrifizierung am Beispiel eines Frontladers.* In Proceedings of the 72nd International Conference on Agricultural Engineering - LAND.TECHNIK 2014, Berlin, Germany, November 2014, Page 449-458.

BALLAIRE, F.; PETERS, O.; HAHN, K.: *Arbeitsmaschine mit Hubvorrichtung und Wiegeeinrichtung.* European Patent Office, Patent DE102013203826, Assignee: Deere & Company, Filed: 06-March-2013, September 2014.

Neustadt an der Weinstraße, 01.09.2015